Spring 1-1-2016

Wave Coupling Between the Lower and Middle Thermosphere as Viewed from Quasi-Sun-Synchronous Satellites

Federico Gasperini
University of Colorado at Boulder, gasperini@colorado.edu

Wave Coupling between the Lower and Middle Thermosphere as Viewed from Quasi-Sun-Synchronous Satellites

by

Federico Gasperini

B.S., University of Pisa (Italy), 2010

M.S., University of Southern California, 2011

A thesis submitted to the

Faculty of the Graduate School of the

University of Colorado in partial fulfillment

of the requirements for the degree of

Doctor of Philosophy

Department of Aerospace Engineering Sciences

2016

This thesis entitled:
Wave Coupling between the Lower and Middle Thermosphere as Viewed from Quasi-Sun-Synchronous Satellites
written by Federico Gasperini
has been approved for the Department of Aerospace Engineering Sciences

Professor Jeffrey M. Forbes

Professor Maura E. Hagan

Professor Jeffrey P. Thayer

Professor Scott E. Palo

Professor Cora E. Randall

Date

The final copy of this thesis has been examined by the signatories, and we find that both the content and the form meet acceptable presentation standards of scholarly work in the above mentioned discipline.

Gasperini, Federico (Ph.D., Aerospace Engineering Sciences)

Wave Coupling between the Lower and Middle Thermosphere as Viewed from Quasi-Sun-Synchronous Satellites

Thesis directed by Professor Jeffrey M. Forbes

In a society increasingly dependent on space technology, space weather has become a prominent scientific paradigm. In the last decade evidence has shown that terrestrial weather significantly influences space weather. Periodic absorption of solar radiation in local time and longitude by tropospheric water vapor and stratospheric ozone as well as latent heat release in clouds generate a spatially- and temporally-evolving spectrum of global-scale atmospheric waves (i.e., tides, planetary waves and Kelvin waves). A subset of these waves propagates vertically, evolving with height due to wave-mean flow, wave-wave, and wave-plasma interactions, and driving electric fields of tidal origin in the dynamo region. While considerable improvements have been made on the understanding of MLT dynamics, driven in part by the development and deployment of new instruments and techniques, relatively little is known about the coupling of waves in the 120-300 km 'thermospheric gap' between satellite remote-sensing and in-situ wave diagnostics. The dissertation herein reveals vertical wave coupling in this height region and quantifies its role in determining thermospheric variability. This objective is accomplished by employing quasi-Sun-synchronous satellite measurements (i.e., TIMED, CHAMP, and GOCE) and state-of-the-art numerical modeling simulations (i.e., TIME-GCM/MERRA). Evidence is found for the vertical propagation from the lower to the middle thermosphere of the eastward propagating diurnal tide with zonal wave number 3 (DE3) and the 3-day ultra-fast Kelvin wave (UFKW), two major global-scale atmospheric oscillations of tropospheric origin. These waves are shown to nonlinearly interact and produce secondary waves responsible for significant longitudinal and day-to-day variability. For solar and geomagnetic quiet conditions, atmospheric waves are found to be responsible for up to 60% of the total variability, demonstrating lower atmosphere coupling as a key contributor to thermosphere weather, at least

in the absence of major solar-driven variability. Additionally, background atmospheric conditions (i.e., dissipation and zonal mean winds) and found to significantly impact the latitudinal-temporal evolution of upward propagating waves.

Acknowledgements

First and foremost, the author wishes to thank Dr. Jeffrey Forbes for the outstanding mentorship and continuous encouragement given through the years. The author would also like to thank Dr. Xiaoli Zhang for the help with data analysis issues, Dr. Sean Bruinsma for the direction and assistance at CNES, Dr. Eelco Doornbos for providing CHAMP and GOCE data, and all the members of the committee who generously gave their time and expertise to better my work.

Finally, the author thanks NASA for the support through grant NNX12AD26G to the University of Colorado under the U.S. Participating Investigator (USPI) Program for the GOCE Mission and NSF through the space weather grant ATM0719480, which made this dissertation research possible.

Contents

Chapter

Tables

Table

Figures

Figure

Chapter 1

INTRODUCTION AND BACKGROUND

The structure and dynamics of Earth's atmosphere are governed by a complex interplay of radiative, thermal, chemical, and electrodynamical processes, connected to variations in solar and geomagnetic activity, as shown in Figure 1.1. The processes occurring in the troposphere and stratosphere are studied under the field of meteorology, while the effects of solar and geomagnetic activity on the upper atmosphere are subjects of space weather research. The atmosphere as a whole system is continuously influenced by internal processes originating in the lower atmosphere, i.e., atmospheric waves [e.g., Fritts and Alexander, 2003 [57]; Kazimirovsky et al., 2003 [101]; Lastovicka, 2006 [113]; Forbes et al., 2009 [54]; Becker, 2011 [2]; Pancheva et al., 2012 [172]; Oberheide et al., 2015 [168]; Yigit and Medvedev, 2015 [224]] and space weather acting from above, i.e., magnetospheric, solar and geomagnetic processes [e.g., Thayer and Semeter, 2004 [208]; Johnson and Heelis, 2005 [96]; Kopp and Lean, 2011 [108]; Prölss, 2011 [178]]. Within the last decade, a new realization has arrived on the scene of upper atmosphere science: terrestrial weather significantly influences space weather. Space weather is responsible for electron density variability that translates to uncertainties in navigation and communications systems, and neutral density variability that translates to uncertainties in orbital and reentry predictions.

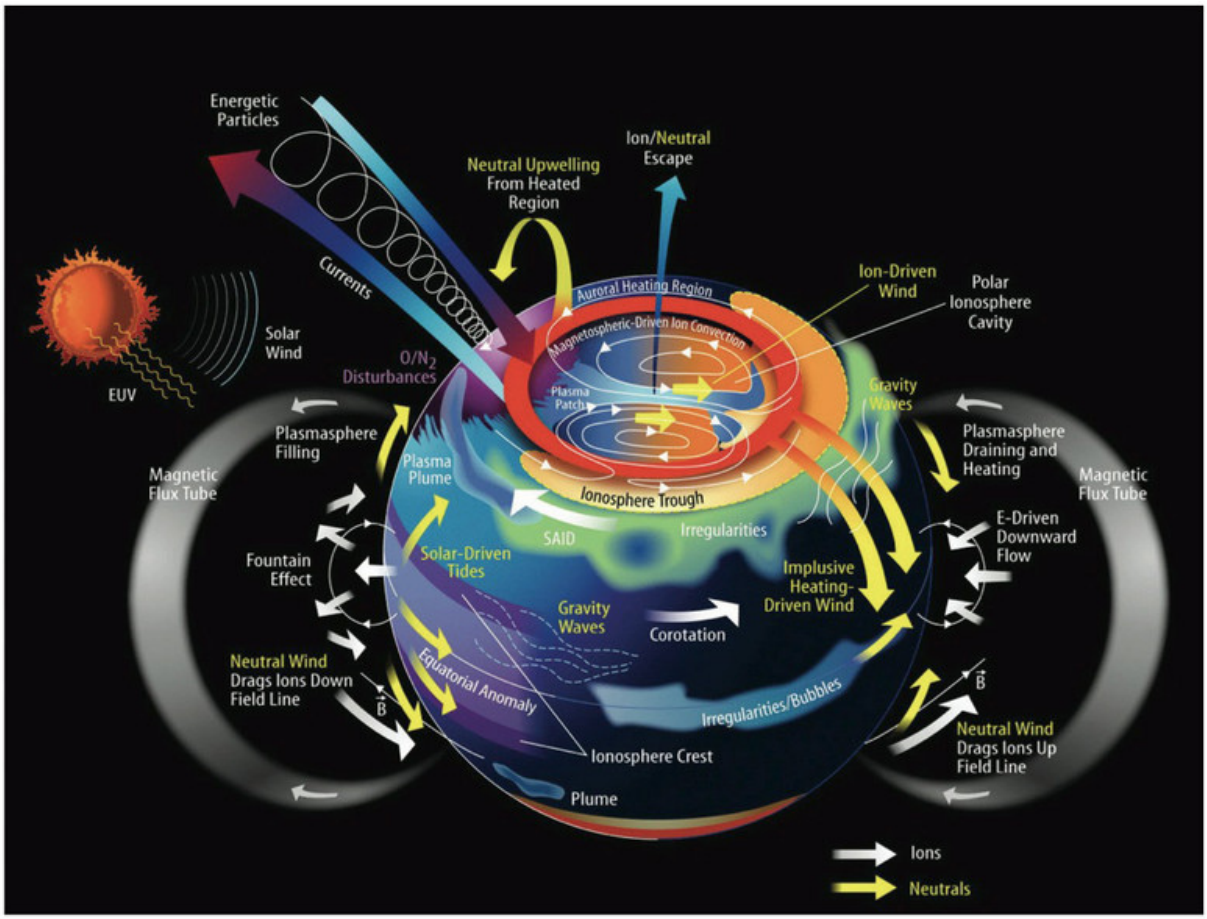

Figure 1.1: Illustration of the various processes occurring in the Ionosphere-Thermosphere-Mesosphere (ITM). The ITM region of the terrestrial atmosphere is a complex and dynamic environment influenced by solar radiation, energy transfer, winds, waves, tides, electric and magnetic fields, and plasma processes. In this figure processes involving electrically charged ions are colored in yellow, while neutral atmosphere mechanisms are in white. Figure from Grebowsky and Sibeck [2009] [65].

1.1 Waves in Earth's Atmosphere

The primary mechanism through which energy and momentum are transferred from the lower atmosphere (below 90 km) to the upper atmosphere (above 90 km) and ionosphere is through the generation and propagation of atmospheric waves. Periodic absorption of solar radiation in local time (LT) and longitude by tropospheric water vapor (H_2O) and stratospheric ozone (O_3) as well as

latent heat release in deep tropical clouds excites a spectrum of thermal tides. Surface topography and unstable shear flows excite planetary waves (PWs) and gravity waves (GWs). GWs have time scales of minutes to hours and horizontal wavelengths from a few km to several hundred km, while thermal tides have time scales from 1 to 1/3 of a solar day, planetary waves 2 to tens of days, and horizontal scales on the order of Earth's circumference. The subset of those waves that propagate vertically grow exponentially with height into an exponentially decreasing neutral mass density, ultimately achieving large amplitudes, mainly in the dissipative region between about 100 and 150 km (see Appendix A). Some fraction of these waves penetrates all the way to the upper thermosphere and exosphere [e.g., Forbes et al., 2009 [54]; Oberheide et al., 2009 [164]; Forbes et al., 2014 [53]]. Along the way, nonlinear interactions between different wave types occur, modifying the interacting waves and giving rise to secondary waves. Additionally, ionosphere-thermosphere (IT) wind perturbations associated with the waves can redistribute ionospheric plasma, either through the electric fields generated via the dynamo mechanism between 100 and 150 km, or directly by moving plasma along magnetic field lines at higher levels.

Sections 1.1.1 and 1.1.2 provide a brief description of atmospheric tides and Kelvin waves, respectively, two key wave types responsible for upper atmospheric variability. Appendix A presents an overview of the 'classical theory of atmospheric waves', including a mathematical formulation of the horizontal and vertical structure of global scale waves.

1.1.1 Atmospheric Tides

Atmospheric tides are global oscillations of temperature, density, and wind fields induced by the absorption of solar radiation, large-scale latent heat release, nonlinear interactions between particular sets of global-scale waves, and the gravitational pull of the Moon and Sun. At ground level, atmospheric tides can be detected as regular but small oscillations in surface pressure with periods of 24 and 12 hours. As tides propagate upwards, they experience exponentially decreasing density. In the absence of dissipation, kinetic energy is conserved and the amplitudes grow exponentially. Following this growth, atmospheric tides become so large that they dominate the dynamics of the

mesosphere and lower thermosphere (MLT, ∼80-150 km). Damping of these tidal perturbations mostly occurs in the MLT region due to the presence of eddy and molecular diffusion, and ion drag.

The primary mechanism of excitation of atmospheric tides is the periodic heating of the atmosphere by the Sun associated with Earth's rotation (the atmosphere is heated during the day and not heated at night). The absorption by the atmosphere of this regular diurnal cycle in heating generates tides with periods being subharmonics of one solar day (24 hours, 12 hours, and 6 hours). Solar energy is primarily absorbed by water vapor in the troposphere (∼0-15 km), ozone in the stratosphere (∼30-60 km) and molecular oxygen and molecular nitrogen between 120 km and 170 km in the thermosphere. A diagram showing the diurnal cycle of heating and its sources can be found in Figure 1.2. Variations in the global distribution and density of these species results in changes in the amplitudes of the solar tides. The tides are also affected by the environment through which they travel (e.g., zonal mean winds, see Section 1.2.2).

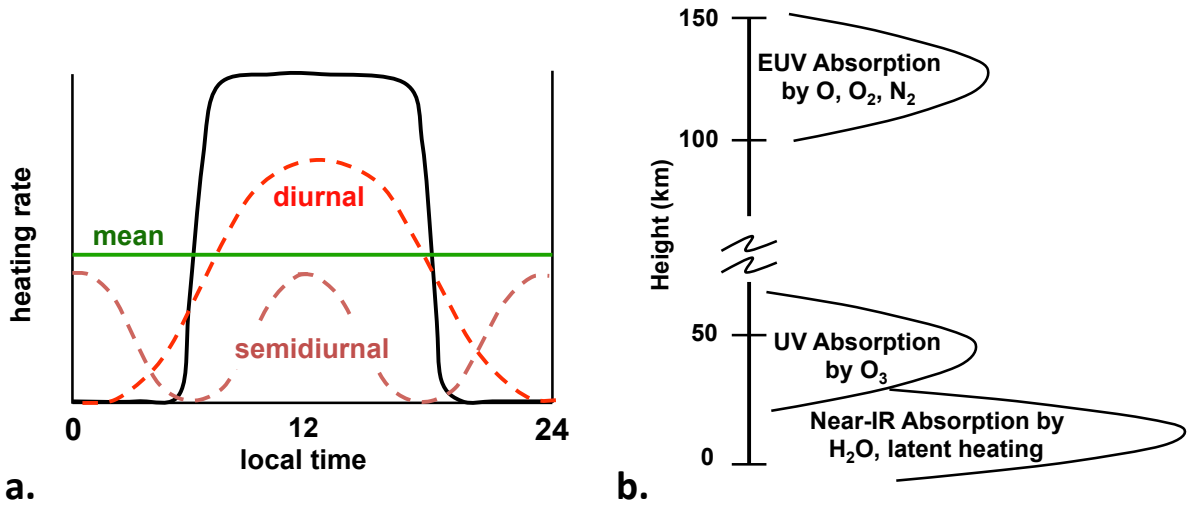

Figure 1.2: (a) Schematic of diurnal (dotted pink line), semidiurnal (dotted red line) solar thermal tidal harmonics excited by the diurnal cycle of heating (solid black line). (b) Absorption of solar radiation at different heights.

Assuming continuity in space and time around a latitude circle, solar thermal tides can be

described by the expression:

$$A_{n,s}cos(n\Omega t + s\lambda - \phi_{n,s}), \tag{1.1}$$

where t is time (days), Ω is the rotation rate of the Earth (2π/day), λ is longitude, n (= 1, 2, 3 for diurnal, semidiurnal, terdiurnal tides) denotes a sub-harmonic of a solar day, s (= ... ,-2, -1, 0, 1, 2, ...) is the zonal wavenumber, $A_{n,s}$ the amplitude, and $\phi_{n,s}$ the phase (defined as the time of maximum at zero longitude). Both $A_{n,s}$ and $\phi_{n,s}$ are functions of height and latitude. In this notation eastward (westward) propagation corresponds to s<0 (s>0). At each height and latitude the total tidal field is obtained as the sum over all n and s. In local time, $t_{LT} = t + \lambda/\Omega$ and Equation 1.1 becomes:

$$A_{n,s}cos(n\Omega t_{LT} + (s-n)\lambda - \phi_{n,s}). \tag{1.2}$$

Solar radiation absorption by a zonally symmetric atmosphere yields local time variations that are independent of longitude (so $s = n$), but propagating at the same speed as the apparent motion of the Sun to a ground-based observer. From (1.2), such components correspond to a zonal phase speed $C_{ph} = d\lambda/dt = -n\Omega/s = -\Omega$. These Sun-synchronous tidal components are referred to as migrating tides, whereas all other zonal harmonics are called non-migrating. With zonally asymmetric solar radiation absorption, the local time variations (at given latitude and height) are dependent on longitude. For this case, a Fourier decomposition of the lower-order harmonics (diurnal, semidiurnal, terdiurnal) must include zonal wavenumber of both signs, corresponding to eastward ($s < 0$) and westward ($s > 0$) propagating waves [Lindzen and Chapman, 1970 [130]].

In this dissertation we utilize the notation DWx or DEx to denote a westward- or eastward-propagating diurnal tide, respectively, with zonal wavenumber $x = s$. For semidiurnal and terdiurnal tides S and T would replace D. The standing oscillations ($s = 0$) are denoted D0, S0, T0, and stationary planetary waves (SPW, $n = 0$) with zonal wavenumber m are expressed as SPWm.

1.1.2 Kelvin Waves

Kelvin waves (KWs) are eastward and vertically propagating waves trapped at low latitudes by the Coriolis force. Any deviation toward the north (south) is brought back toward the equator because the Coriolis force acts to the right (left) of the direction of motion in the northern (southern) hemisphere. They satisfy geostrophic balance between zonal wind and meridional pressure gradient components of wave perturbations.

KWs were first observed in the atmosphere by Wallace and Kousky [1968] [213], and numerous theoretical studies on their origin followed [e.g., Holton, 1970, 1972, 1973 [85], [86], [87]; Chang, 1976 [16]]. KWs play a very important role in the dynamics of the low-latitude MLT. The source of these waves was identified with unsteady convective heating in the tropical troposphere [Holton, 1972 [86]]. They can propagate vertically, eventually dissipating in the thermosphere and depositing westerly momentum that affects the mean circulation. Holton [1992] [88] described KWs using linear theory in the absence of mean winds as oscillations with zero velocity across the equator and Gaussian symmetric structure in latitude and maxima in zonal wind, temperatures, and density at the equator.

A characteristic of KWs is that they are non-dispersive, that is, the phase speed of the wave crests is equal to the group velocity (see definition in Appendix A) independently from the frequency, and their phase velocity is positive (they always propagate eastward retaining their shapes). KWs are grouped into three classes [Wallace and Kousky, 1968 [213]]: slow Kelvin waves that occur in the stratosphere (∼15-50 km) at periods of 10-20 days, fast KWs found in the stratosphere and mesosphere (∼20-100 km) at periods of 6-10 days, and ultra-fast Kelvin waves (UFKW) with periods of 3-6 days that can propagate to higher altitudes given their longer vertical wavelength [Salby et al., 1984 [198], Canziani et al., 1995 [13]; Lieberman and Riggin, 1997 [121]; Forbes et al., 2009a [54]]. Using equatorial radar wind measurements from 1993 and 1997, Yoshida et al. [1999] [225] showed that UFKW amplitudes vary significantly throughout the year, with two annual peaks of increased activity: one around March-May and another around July-November. Using Global Scale Wave

Model (GSWM) simulations, Forbes [2000] [40] showed that a UFKW with period of 3 days and zonal wavenumber of 1 (eastward) can reach amplitudes of 10-25 K in temperature and 10-40 m/s in zonal wind in the lower thermosphere. Gu et al. [2014] [66] found similar UFKW amplitudes in temperatures from the Sounding of the Atmosphere using Broadband Emission Radiometry (SABER) instrument on the Thermosphere Ionosphere Mesosphere Energetics Dynamics (TIMED) satellite around 110 km.

1.2 Vertical Coupling of Waves between the Lower and Upper Atmosphere

The middle and upper atmosphere of Earth is a highly coupled system, where processes at one height strongly influence processes at other heights. Vertical wave coupling in the mesosphere-lower-thermosphere (MLT) region determines much of the dynamics of this region and of the middle to upper thermosphere due to the filtering of upward propagating disturbances. When a global-scale wave with sufficiently large amplitude and long wavelength propagates through the MLT region into the ionosphere, it can cause an electric current system to be driven with a period of the global-scale wave, through the dynamo action of tidal winds. These electric fields map along equipotential magnetic lines and drive E x B plasma drifts in the F-region, which cause the temporal and spatial variability in the E-region tides to transfer to the F-region plasma [e.g, Jin et al., 2008 [95]; Kil et al., 2007, 2008 [102], [103]; Liu et al., 2007 [138]; Liu and Watanabe, 2008 [139]]. The vertical propagation of some of these wave components to the upper thermosphere [300-400 km; Forbes et al., 2009b [41]; Hagan et al., 2009 [75]] also directly modulate neutral and plasma densities [He et al., 2011 [80]; England et al., 2010 [35]], deposit their momentum into the thermosphere and modify the mean circulation [Jones et al., 2014 [97]].

The general dynamical equations of atmospheric motions are nonlinear, coupled, and contain various dissipative terms. Neglecting mechanical forcing and dissipation, and assuming motionless zonal mean state that is horizontally stratified and isothermal, the dynamical equations of motion can be decoupled. This is the basis of the classical atmospheric wave theory discussed in Appendix A. Sections 1.2.1 and 1.2.2 provide a summary of the two main effects introducing departures from

classical theory: dissipation and zonal mean zonal winds. Note that in this dissertation zonal mean and longitude mean are synonymous, and also imply local time mean.

1.2.1 Dissipation Effects

Above about 100 km, molecular diffusion is the dominant dissipation mechanism for vertically-propagating waves. Therefore, to properly model global scale waves in the upper mesosphere and thermosphere diffusion of momentum and heat and planetary rotation must be included, making the horizontal and vertical structure equations (see Appendix A) inseparable in height and latitude (i.e., the height structures vary with latitude and the horizontal structures vary with height). This means that a solution to these equations can only be achieved numerically.

To estimate the relative time scales of diffusion and gain some understanding on the vertical structure of upward propagating waves subject to dissipation, Chapman and Lindzen [1970] [18] defined the quantity

$$\chi = \left| \frac{4\pi^2}{\lambda_z^2} \frac{\nu_D}{\sigma_D} \right| \tag{1.3}$$

for diffusion of momentum, to represent the ratio between diffusive and inertial forces, where σ_D is the Doppler-shifted frequency

$$\sigma_D = -\sigma + sU/(R_E cos\theta), \tag{1.4}$$

U is zonal mean zonal wind, R_E is Earth's radius, θ is latitude, ν_D is the molecular diffusion coefficient, and λ_z is vertical wavelength (for a definition of vertical wavelength refer to Appendix A). When $\chi \sim 1$ dissipation is considered important to the local physics of the wave, thus a wave entering this region transitions from an exponential growth (for propagating waves) or decay (for trapped oscillations) to asymptotically constant values in the thermosphere. The dependence of χ on λ_z^2 and σ_D (Equation 1.3) is such that the altitude at which the molecular processes dominate increases with vertical wavelength (as λ_z^{-2}) and wave frequency (as σ_D^{-1}). For diurnal

and semidiurnal tides, the altitude range at which $\chi \sim 1$ is approximately 100-170 km for vertical wavelengths in the range 30-150 km, and similar altitudes for the UFKW with λ_z ~50-70 km.

Lindzen [1968, 1970] [125][126] showed that the windless tidal equations still remain separable when including a height-dependent Newtonian cooling coefficient, and used this formulation to reveal some basic characteristics of waves propagating into a thermosphere where the dissipative time scale increases as ρ^{-1}. To gain some insights of how waves are affected by dissipation, Yanowitch [1967] [222] and Lindzen [1968, 1970] [125][126] defined the parameter

$$\beta = \frac{2\pi H}{\lambda_z}, \tag{1.5}$$

where H is the scale height ($H = \frac{kT}{mg}$, where T is the mean neutral temperature, k is the Boltzmann constant, m is the mean mass, and g is acceleration due to Earth's gravity) and λ_z is the vertical wavelength in the absence of dissipation, and obtained analytically the following results:

- The magnitude of reflection due to inhomogeneities is given by $e^{-\pi\beta}$.
- For $\beta \leq 2$, wave amplitudes increase roughly as $e^{x/2}$ (where x is in logarithm pressure coordinates) up to the region where $\chi \sim 1$, asymptotically approaching a constant above this level with little or no decrease in amplitude. This type of behavior is expected for the long-wavelength semidiurnal tidal modes (2,2) and (2,3) during low to moderate solar activity conditions (for a definition of tidal mode refer to Appendix A).
- For $\beta > 2$, wave amplitudes increase roughly as $e^{x/2}$ up to the region where $\chi \sim 1$, but then decrease considerably before asymptotically reaching a constant value. Common oscillations falling into this category include the (1,1) diurnal tide ($\lambda_z \sim 28$ km), and the (2,4) and (2,5) semidiurnal tides ($\lambda_z \sim$ 40-55 km).

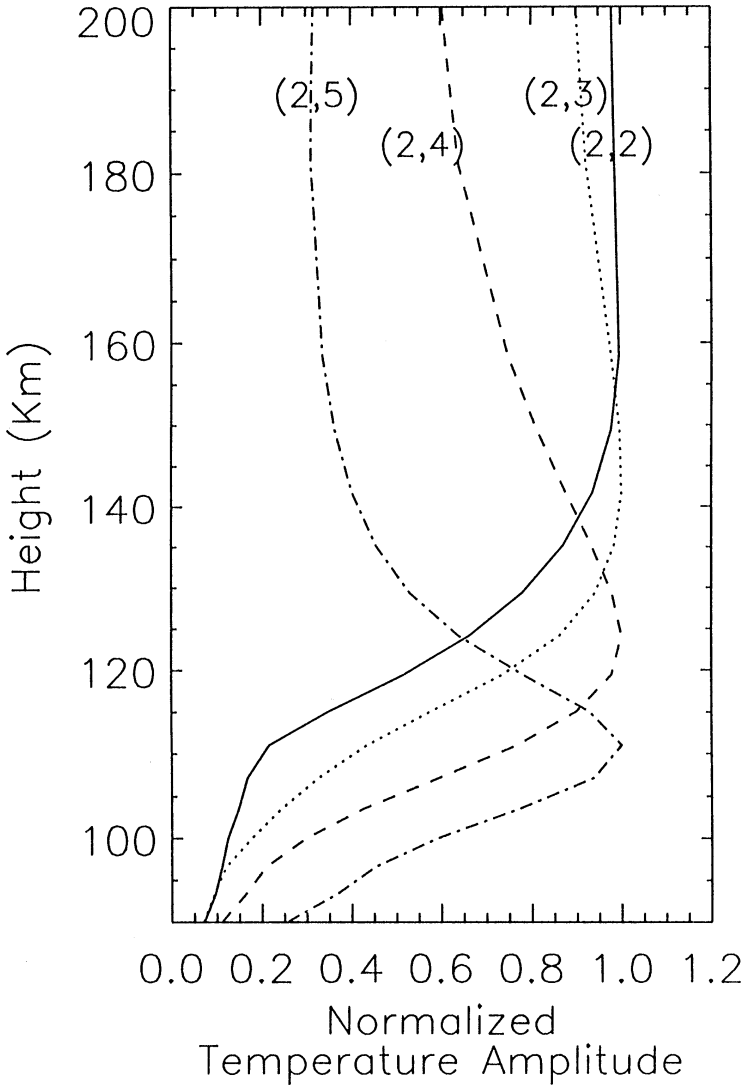

Figure 1.3: Thermospheric amplitude extensions of the semidiurnal temperature field at 42° latitude for the first 4 semidiurnal tidal oscillations with s = 2: (-2; 2; 2), solid line; (-2; 2; 3), dashed line; (-2; 2; 4), dashed-dot line; (-2; 2; 5), dashed line. All amplitudes are normalized to 1.0 K. The profile is derived from the Global Scale Wave Model (GSWM), that solves the linearized and extended Navier-Stokes equations for steady-state global temperature and wind perturbations, with no mean winds and medium solar activity (F10.7 = 110). Modes with lower longer vertical wavelength (lower modes) reach larger peak amplitudes and more easily penetrate to higher altitudes (figure adapted from Forbes, [2000] [40]).

Thus longer vertical wavelength waves more easily penetrate into the thermosphere, as shown in Figure 1.3 for different modes of SW2.

1.2.2 Zonal Mean Winds Effects

The linearized wave equations that include zonal mean winds and meridional temperature, density and pressure gradients are not separable in latitude and height, and thus numerical methods must be employed to derive solutions. Lindzen [1972] [127] and Lindzen and Hong [1974] [131] described some important effects of zonal mean zonal winds on atmospheric tides. The effects of mean winds can be viewed as a distortion of the response compared to a windless calculation. For scalar variables (i.e., temperature) this means that the combination of Hough modes required to reconstruct the response is different than the combination of Hough modes comprising the forcing. The phrase 'mode coupling' is utilized to describe the generation of modes (determined with orthogonal expansion of the calculated response) that are not forced directly by thermal excitation, but that arise due to the inseparability of the governing equations [Lindzen and Hong, 1974 [131]; Walterscheid and Venkateswaran, 1979a,b [217][216]; Walterscheid et al., 1980 [215]; and Forbes and Garrett, 1979 [44]].

It is often useful to consider the effects of mean winds simply by examining the implications of a Doppler shifted frequency $\sigma_D = -\sigma + sU/(R_E cos\theta)$. A Doppler-shifted complex frequency can be introduced into classical tidal theory to deduce some basic wave behavior due to dissipation and mean winds (e.g., Forbes and Vincent, [1988] [43]). For eastward propagating waves, the frequency is Doppler-shifted to higher absolute values in regions of westward wind (U $<$ 0) and to lower absolute values in regions of eastward wind (U $>$ 0). In regions where dissipation is important, waves with larger σ_D are less effectively damped than those with smaller σ_D (see Equation 1.3 and following discussion). Forbes and Vincent [1988] [43] also showed that a wave that is Doppler-shifted to higher (lower) absolute frequency experiences an increase (decrease) in vertical wavelength. For waves propagating in the same (opposite) direction as the mean wind, i.e., Doppler-shifting to lower (higher) absolute frequencies, h_n is reduced (increased) implying a shorter (longer) vertical wavelength. From Equation 1.3 one case see that lower (higher) frequencies and shorter (longer) results in higher (lower) χ , thus increased (decreased) damping. Note that the change in vertical

wavelength produces a reduction or increase in damping in the same direction as that expected for a change in the Doppler-shifted frequency (i.e., the effects work together).

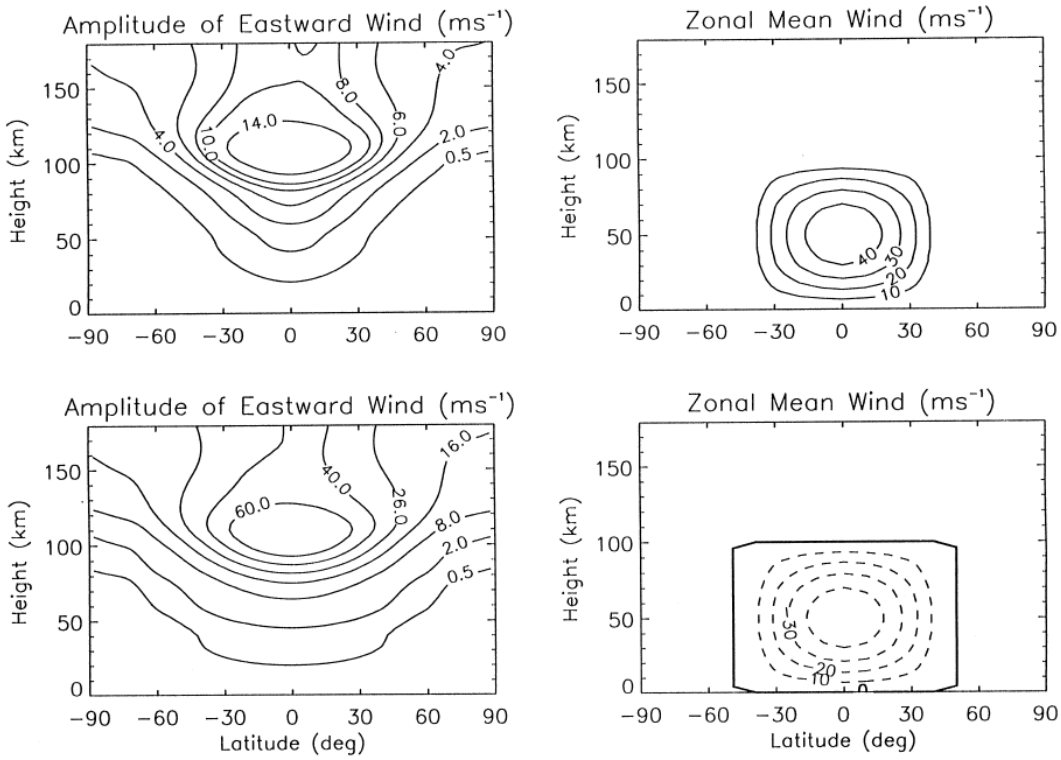

Figure 1.4: Effect of equatorial zonal mean zonal winds on the vertical structure of the eastward propagating 3-day Kelvin wave, derived from the GSWM simulations. The vertical wavelength for the case of eastward wind (top left panel) is ∼ 35 km, while that for westward winds (bottom left panel) is ∼ 70 km. Note that Doppler-shifting to lower (higher) frequencies and shorter (longer) vertical wavelengths, increases (decreases) the effectiveness of dissipation (figure from Forbes, [2000] [40]).

Figure 1.4 shows the effect of equatorial zonal mean zonal winds on the vertical structure of the eastward propagating 3-day UFKW, derived using GSWM simulations [Forbes, 2000]. Eastward (westward) zonal mean zonal winds Doppler-shifts to lower (higher) frequencies and shorter (longer) vertical wavelengths, increasing (decreasing) the effectiveness of dissipation, and leading to significant variations in wave amplitude. Ekanakaye et al. [1997] [34] also showed that the Doppler effect due to the presence of background mean zonal winds makes it possible for the diurnal nonmi-

grating tides of higher zonal wave numbers to propagate up into the middle to high latitude regions of both hemispheres.

Summarizing, the efficiency with which a given wave propagates from the troposphere to the MLT depends on its period, vertical wavelength and zonal wavenumber, the shorter-period, longer-wavelength waves being less affected by dissipation and therefore are more capable of propagating to high altitudes. Also important is the amplitude and direction of horizontal phase speed of the wave (inversely proportional to zonal wavenumber), compared to the wind speed of the background atmosphere through which it is propagating.

1.2.3 Solar EUV Effects

The peak altitude for an upward propagating wave coincides with that region where the time scale for molecular dissipation is of order the wave period, which occurs when

$$\chi = \frac{2\pi\mu_0}{\lambda_z^2\rho}T \sim 1, \tag{1.6}$$

where T is the wave period and μ_0 is molecular viscosity (Equation 1.6 is similar to Equation 1.3 but shows the explicit dependence on neutral density). From Section 1.2.1, we recall that this region is approximately 100-170 km for diurnal and semidiurnal tides with 30 km $< \lambda_z <$ 150 km and for the UFKW with λ_z ~50-70 km. An increase in solar EUV radiation leads to higher neutral density (the atmosphere 'expands'), resulting in lower χ values and thus higher peak heights.

Variations in solar heating are also responsible for variations in neutral temperature and thus changes in the scale height (the atmosphere 'expands' during solar high and 'compresses' during solar low). In particular, increased solar input results in a warmer atmosphere thus larger scale height $H = kT/mg$ (note that the mean molecular weight m also experiences an increase, but not as large as T). Recalling now the discussion of the β ratio ($\beta = 2H/\lambda_z$) in Section 1.2.1, increased scale height results in larger β values and hence a upward propagating wave experiencing an increased scale height will tend to decrease more considerably after the peak, before asymptotically reaching a constant value.

Summarizing, one can expect increased (decreased) solar radiation to cause increased (decreased) peak altitudes with larger (smaller) lower thermospheric amplitudes, but also significantly decreased (increased) middle-upper thermospheric amplitudes.

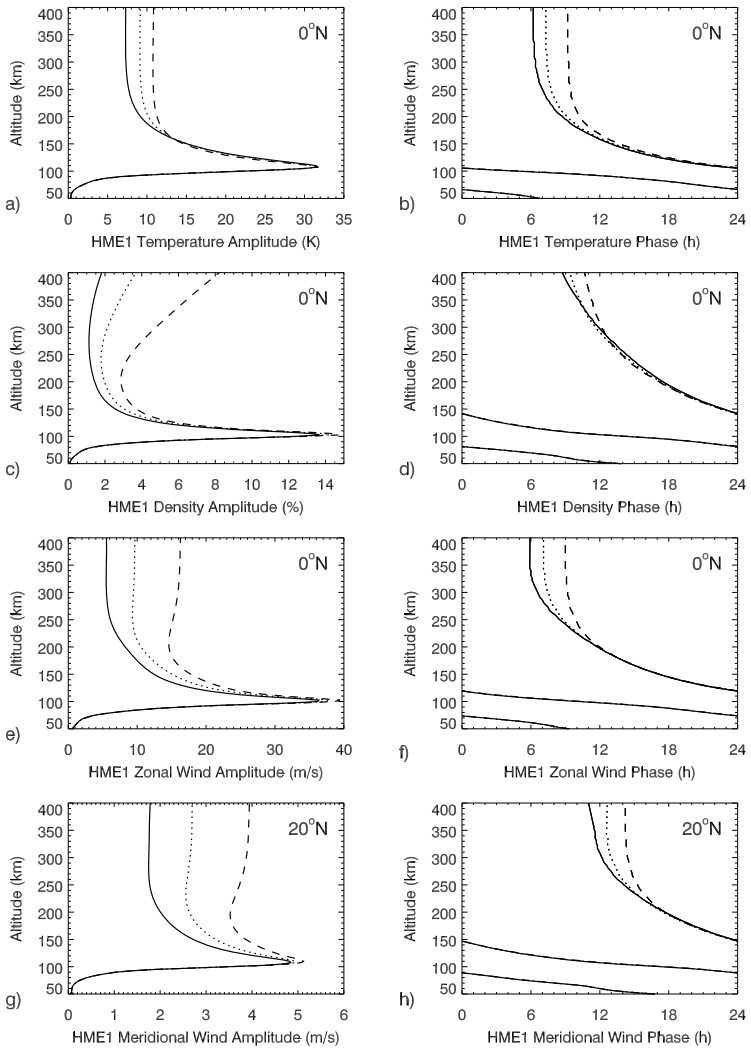

Figure 1.5: HME1 of DE3 for F10.7 of 170 sfu (solid curve), 110 sfu (dotted curve), 60 sfu (dashed curve). Shown is the latitude of maximum amplitude, and normalization is relative to a zonal wind amplitude of 10 m/s at 86 km. (a), (b) Temperature amplitude and phase. (c), (d) Density amplitude and phase. (e), (f) Zonal wind amplitude and phase. (g), (h) Meridional wind amplitude and phase [Oberheide et al., 2009 [164]]).

Oberheide et al. [2009] [164] computed the first symmetric Hough mode of DE3 (HME1) for three F10.7 radio flux levels: high (170 sfu), moderate (110 sfu) and low (60 sfu) for temperatures, densities, zonal winds and meridional winds (Figure 1.5). Oberheide et al. [2009] [164] showed that amplitudes are smallest for high solar flux and largest for low solar flux, and that temperature HMEs are less sensitive (with a 60% increase from 170 sfu to 60 sfu) than density (almost a factor of 5) and winds (a factor of 2-3) to solar flux variations.

1.3 Nonlinear Wave-Wave Interactions

Modulation of a tide by a PW is thought to occur through a nonlinear quadratic interaction that results in the generation of 'sum' and 'difference' secondary waves [Teitelbaum and Vial, 1991 [205]]. As explained by Teitelbaum and Vial [1991] [205], PW interactions with tides yield secondary waves defined by the sum and difference of the frequencies and zonal wavenumbers in the primary waves. This interaction occurs in the following manner:

$$[cos(\delta\Omega t + m\lambda) \cdot cos(n\Omega t + s\lambda)] = \frac{1}{2}cos[(n+\delta)\Omega t + (s+m)\lambda] + \frac{1}{2}cos[(n-\delta)\Omega t + (s-m)\lambda] \tag{1.7}$$

where $\delta\Omega$ and m are the PWs frequency and zonal wavenumber, respectively (see schematic in Figure 1.6). In a time-frequency spectrum, the secondary waves appear as two sidebands on either side of the tide with a shift in frequency equal to the planetary wave's frequency $\delta\Omega$. For example, in the interaction between the quasi-two-day-wave (2DW) (a normal mode or resonant oscillation of Earth's atmosphere, with frequency = 0.5 day^{-1} and $s = 3$) and the semidiurnal tide (frequency = 2 day^{-1} and $s = 2$), the primary waves are: $cos(0.5\Omega t + 3\lambda)$ and $cos(2\Omega t + 2\lambda)$, and the secondary waves generated by their interactions are: $cos(2.5\Omega t + 5\lambda)$ and $cos(1.5\Omega t - \lambda)$. Hence, the secondary waves generated by the quasi two-day-wave (2DW) and SW2 have periods of 9.6-hour and 16-hour, and zonal wavenumbers +5 and -1, respectively.

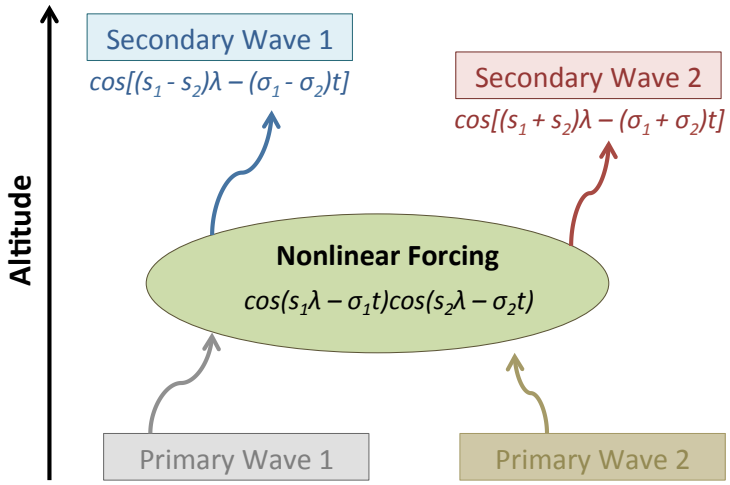

Figure 1.6: Schematic of nonlinear interaction between two waves and the secondary waves therein produced.

Spizzichino [1969] [199] was the first to report on the issue of nonlinear wave-wave interactions in the upper atmosphere. He hypothesized that 9.6-hour and 16-hour waves observed in meteor radar data near 95 km resulted from modulation of SW2 by the 2DW. Manson et al. [1982] [150] also argued that the 9.7-hour and 16-hour waves observed at Saskatoon were due to the nonlinear interaction between the 2DW and the semidiurnal tide. Teitelbaum et al. [1989] [206] provided the mathematical development and solution of a set of tidal equations demonstrating that TW3 could be generated through nonlinear interactions between DW1 and SW2, and the basic idea and model was extended to other wave interactions in Teitelbaum and Vial [1991] [205]. Teitelbaum and Vial [1991] [205] were the first to perform numerical simulations of nonlinear PW-tide interactions and develop a theoretical basis. These authors showed that secondary waves produced by nonlinear interaction can reach high amplitudes, even when the interacting waves are not strong, and showed the presence of nonlinear interactions in the MLT region using measurements taken over Garchy (47° latitude). Many studies followed this pioneering work, focusing on interactions between PWs and tides [Huuskonen et al., 1991 [90]; [Pancheva and Mukhtarov, 1994 [174]; and Clark and Bergin, 1997 [19]].

More recently, Palo et al. [1999] [169] numerically demonstrated the generation of secondary

waves due to the interaction between SW2 and the 2DW and their propagation into the thermosphere; Wang et al. [2011] [218] discuss generation of TW3 from DW1 and SW2; Hagan et al. [2009] [75] and Oberheide et al. [2011] [165] demonstrate the production of SE2 and SPW4 from the DE3-DW1 interaction; Moudden and Forbes [2013] [158] interpret the observations of terdiurnal nonmigrating tides in terms of interactions between diurnal and semi-diurnal nonmigrating tides; and Pedatella and Forbes [2010] [175] showed the generation of secondary waves due to SPW1-SW2 interactions and the atmosphere-ionosphere coupling mechanism in Figure 1.7; while Gasperini and Forbes [2014] [59] showed evidence of secondary waves produced by the interaction between lunar tide variability in the equatorial electric field and solar-driven variability in the E-region conductivity.

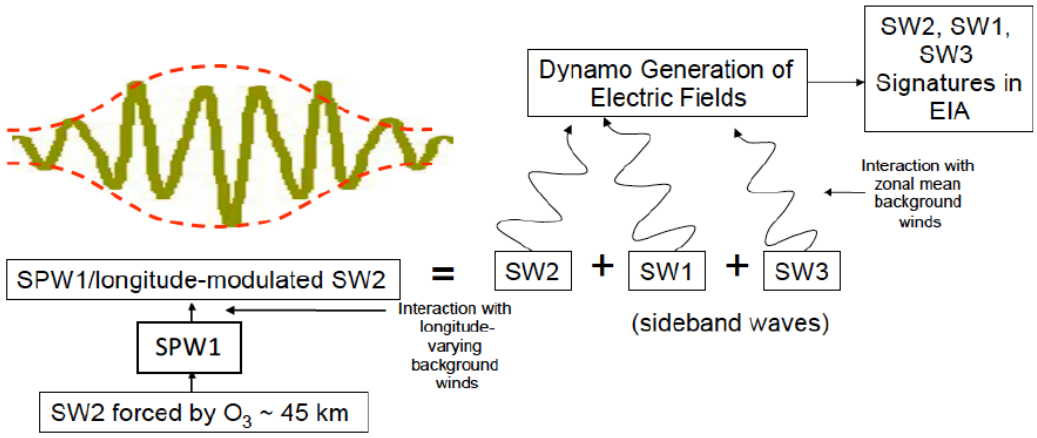

Figure 1.7: Schematic illustrating how SPW1 interacts with SW2 to produce SW1 and SW3 that extend globally and influence the ionosphere through the dynamo generation of electric fields.

Secondary waves generated by the interaction of a tide with a SPW (prominent feature of high-latitude winter in the Northern Hemisphere) have periods that are the period of the tide (since SPWs are time-independent) and zonal wavenumbers given by the sum and difference between the zonal wavenumbers of the tide and the SPW. For example, the interaction between SW2 and SPW1 generates SW3 and SW1 (sum and difference of zonal wavenumbers, respectively). A list of possible

tide-tide and tide-SPW nonlinear interactions can be found in Table 1.1.

Primary Waves	**DE3**	**DE2**	**D0**	**DW1**	**SW2**	**SE2**
SPW1	DE2, DE4	DE1, DE3	DE1, DE1	DW2, D0	SW3, SW1	SE1, SE3
SPW2	DE1, DE5	D0, DE4	DW2, DE2	DW3, DE1	SW4, S0	S0, SE4
DE3	SE6, ZM	SE5, SPW1	SE3, SPW3	SE2, SPW4	TE1, DW5	TE2, DW1
DE2		SE4, ZM	SE2, SPW2	SE1, SPW3	T0, DW4	TE4, D0
D0			S0, ZM	SW1, SPW1	TW2, DW2	TE2, DE2
DW1				SW2, ZM	TW3, DW1	TE1, DE3
SW2					QW4, ZM	Q0, SPW4
SE2						QE4, ZM

Table 1.1: Secondary waves arising from nonlinear interactions between "primary" waves (DE3, DE2, D0, DW1, SW2, SE2, SPW1, and SPW2). Interactions known to produce large secondary waves are highlighted in blue, while self interactions (probably not important) are in indicated in red.

Numerical simulations [Palo et al., 1999 [170]; Pedatella et al., 2012 [177]] and observations [Moudden and Forbes, 2013 [158]] demonstrate that the secondary waves propagate away from their sources as independent oscillations. Each secondary wave is affected differently by the background wind field depending on its zonal wavenumber and Doppler-shifted frequency (see Section 1.2). Therefore at some distance from the source, one of the secondary waves could be significantly larger than the other. Nguyen et al. [2016] [161]] also showed that the secondary wave response due to 2DW-DW1 interactions is most sensitive to the nonlinear forcing occurring in the lower and middle mesosphere, and not coincident with the regions of strongest nonlinear forcing. Additionally, the two secondary waves do not seem to be excited with equal efficiency in these interactions, and the underlying physical mechanism is a topic of current research.

1.4 Methods of Observing Atmospheric Waves

1.4.1 Ground-Based Methods

A large number of methods of observing atmospheric waves from ground-based measurements have been developed over the past few decades; the most common are:

- Medium-frequency (MF) and meteor radars: winds between 80 and 100 km in the MLT at various locations, nearly continuously.
- Passive optical methods: MLT temperatures and winds, but are restricted to nighttime and 'effective altitudes' associated with specific emission layers.
- Resonance lidars: measurements of temperatures and winds at nighttime (some also operate during the day), but not continuously and only at very limited locations.
- Incoherent scatter radars: MLT temperatures and winds in the 100-120 km range, only in intervals of 2 to 10 days and are available at only a handful of sites.

All the observing techniques listed above have their own advantages and drawbacks, whether it is in the continuity of its wind measurements (MF and meteor radars), measuring temperatures for long periods in remote polar locations (passive optical), providing good temporal and vertical resolution of the temperature field (lidars), or valuable measurements of the 100-120 km height region (incoherent scatter radars).

The major advantage of ground-based methods is the ability to distinguish various waves over a short period of time. They are often capable of providing detailed information on vertical structure, including vertical wavelengths and direction of propagation. The main disadvantage is the lack of information on the latitudinal and longitudinal structures and the inability to distinguish between global and local-scale signatures

1.4.2 Space-Based Methods

The massive amount of data collected by over a decade of satellite measurements has offered the unprecedented opportunity to gain a truly global perspective on the wave coupling problem. The obvious advantage of satellite-based atmospheric sampling, compared to any ground-based method previously described, is the latitude and longitude coverage that can be achieved. For a near-polar orbiting satellite in a ∼90-min period orbit, the ascending or descending segment of the orbit samples 15 longitudes per day at a nearly constant local solar time for any given latitude. The maximum latitude reached by the orbit is approximately equal to its inclination (i) with respect to the equatorial plane. Within a yaw cycle, ascending or descending measurements precess through about 12 hours of local time (common precession periods are greater than 60 days). For measurements taken during both day and night, coverage of 24 hours of local time can be attained by combining ascending and descending data together.

Assuming $i = 70°$ and that measurements are taken on both the ascending and descending parts of the orbit, one can fit those measurements with a function of the form

$$Q_0 + \sum_{n=1}^{N} \sum_{s=-M}^{M} a_{n,s} cos(n\Omega t_{LT} + s\lambda) + b_{n,s} sin(n\Omega t_{LT} + s\lambda), \tag{1.8}$$

and determine amplitude and phase of the different wave harmonics at each latitude and height. This is trivial for ground observations (at least for migrating tidal components), given the 24-hour local time coverage in a day, but determining short period waves (i.e., tides and UFKW) from slowly-precessing satellites presents several issues. These fall into the categories of sampling and aliasing.

- The sampling issue is caused by the inherent variability of the atmospheric system within the 24-hour local time precession period of the satellites: if the local time structure of the atmosphere evolves over the precession period the derived waves represent some sort of average over that period, but not a true average.

- The aliasing issue is due to the zonal mean and other longer-period waves aliasing into

the derived wave field. If the atmosphere is sampled by a satellite in a slowly precessing orbit, the changing zonal mean is perceived as a local-time change, leading to spurious wave harmonics. Evolving wave structures can alias into the mean, but this is a much smaller effect, since waves tend to cancel out when determining the mean [Forbes et al., 1997 [47]].

Different methods have been used to circumvent these issues [e.g., Lieberman, 1991 [119]; Forbes et al., 1997, 2003a [47], [45]; Talaat and Lieberman, 1999 [203]; Oberheide and Gusev, 2002 [166]], each one with its advantages and drawbacks. Lieberman [1991] [119] and Oberheide and Gusev [2002] [166] estimated daily diurnal tides by taking differences between ascending and descending node measurements that are 12 hours or less apart in local time. Using this method eliminates aliasing due to long-term trends, but leads to ambiguities in zonal wavenumbers (in particular for westward propagating tides). Similar issues occur when deriving tides from monthly averaged daytime-only data [Talaat and Lieberman, 1999 [203]]. When utilizing the full 24-hour local time precession period ($\sim$60 days for TIMED and $\sim$130 days for CHAMP, the Challenging Minisatellite Payload satellite), aliasing due to long-term trends can occur, as previously explained. In order to drastically reduce this aliasing between zonal mean and tides, Forbes et al. [1997, 2003] [47], [55] subtract a running mean from the data (i.e., 60-day running means), while Huang and Reber [2004] [89] fit data over a full year using functions that include annual and semiannual components in addition to the tides.

While the day-to-day variability of short-period waves is known to be very large according to ground-based observations, attribution of this variability to specific wave components on a global basis has been practically impossible due to (a) inadequate latitude-longitude distribution of ground-based observing sites, and (b) the slow local time precession of single satellites. For (b) only wave fields averaged over 30-60 days or more can be retrieved, leading to observational wave climatologies with significant amplitude and day-to-day variability suppression.

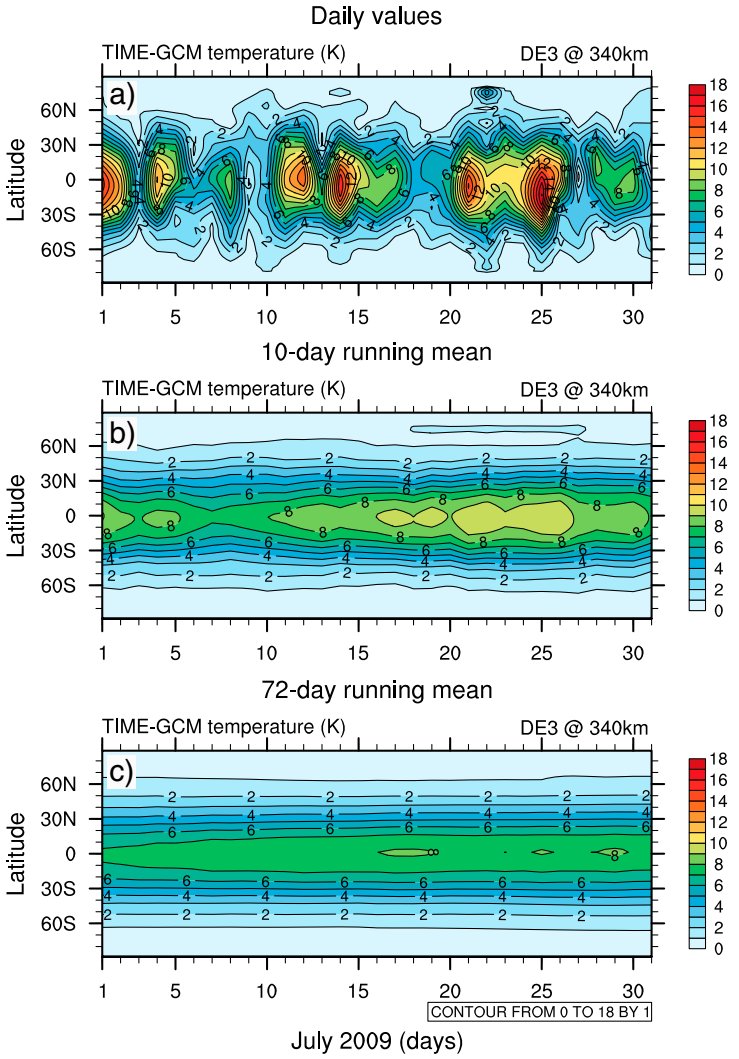

Figure 1.8: Contours of TIME-GCM/MERRA DE3 temperature amplitudes (K) versus latitude and days in July 2009 at 340 km altitude. Shown are (a) the daily values, (b) a 10 day running mean moved forward in time by 1 day, and (c) a 72 day running mean moved forward in time by 1 day. Figure from Häusler et al. [2015] [77].

Figure 1.8 (from Häusler et al. [2015] [77]) shows an example of the daily variability for DE3 temperature amplitudes for July 2009 as function of latitude at 340 km altitude, derived using the National Center of Atmospheric Research (NCAR) Thermosphere Ionosphere Mesosphere Electrodynamics General Circulation Model (TIME-GCM) with Modern Era Retrospective-Analysis for Research and Applications (MERRA) forcing at the lower boundary. The day-to-day variations

are in the 4-18 K range. Figure 1.8b (Figure 1.8c) shows the same DE3 amplitudes with 10 day (72-day) running means, moved forward in time by 1 day. The averaging over several days and weeks drastically reduces the DE3 amplitudes by up to 50% for the 10 day means and more for the 72 day means, and the large day-to-day variations present in the daily values are smoothed out. This suggests that the averaging involved with extracting the tidal field from slowly precessing satellite measurements generates large errors both in terms of inherent variability and amplitude maxima and minima.

1.5 Research Objective and Science Questions

The objective of this dissertation work is to **reveal and understand the nature of vertical wave coupling in the thermosphere and quantify its role in determining the variability of the thermosphere system**. This objective is achieved using quasi-Sun-synchronous satellite measurements (i.e., TIMED, CHAMP, and GOCE) and numerical modeling simulations (i.e., TIME-GCM), and by addressing the the following scientific questions:

Q1 What do satellite-based measurements reveal about the nature, origins, and consequences of wave coupling between the lower and middle thermosphere?

Q2 What are the most prominent low to mid-latitude global-scale waves participating in this coupling?

Q3 What are the physical processes that determine the nature of this coupling?

Q4 To what degree does vertical wave coupling contribute to the overall variability of the middle thermosphere for solar and geomagnetic quiet condtions?

In answering **Q1**, the unique perspectives of quasi-Sun-synchronous satellite observations is identified and applied to the wave coupling problem, and a new method for quantifying wind structures from satellite measurements of atmospheric density is revealed. Answering **Q2** involves

the analysis of GOCE winds and neutral densities, and TIMED-SABER temperatures, with particular attention to short-term variability, for evidence of global-scale vertical wave coupling. For **Q3**, satellite measurements are complemented with TIME-GCM simulations to study the physics governing the vertical coupling of waves and its relationship to: (a) mean winds, (b) nonlinear wave-wave interactions, (c) dissipation, (d) solar EUV radiation. Secondary waves generated by nonlinear wave-wave interactions are identified and their seasonal, interannual, solar cycle variability is studied. In answering **Q4**, the thermosphere variability associated with solar and geomagnetic changes is quantified and compared with that due to upward-propagating waves for solar low and geomagnetic quiet conditions. The contributions of secondary waves to thermosphere variability are also quantified as part of addressing **Q4**.

In the past decade, there have been considerable improvements in our understanding of MLT dynamics, driven in part by the development and deployment of new instruments and techniques. An area of wave coupling research that still require significant advancements is the study of short-term (days to weeks) variability of atmospheric waves. This work has a special emphasis on this topic.

1.6 Outline of Thesis

This dissertation is organized into 7 chapters. Chapter 2 provides a summary of the data, models and methods used to analyze wave coupling from quasi-Sun-synchronous satellite measurements and TIME-GCM simulations; Chapter 3 discusses the importance of winds in the wave coupling problem and presents a new method of extracting both zonal and meridional winds from neutral and electron density satellite measurements and these wind fields are employed to reveal several aspects of vertical wave coupling in the thermosphere; Chapter 4 focuses on vertical wave coupling due to DE3 and UFKW and their relative contribution to the overall thermospheric variability; Chapter 5 provides evidence of nonlinear interactions between DE3 and the UFKW and offers a study of the latitude-longitude and day-to-day variability of the secondary waves; Chapter 6 provides physical insights into the wave-coupling problem using a MERRA-forced TIME-GCM

simulation; while Chapter 7 summarizes results, conclusions and opportunities for future research.

Chapter 2

DATA, MODELS, METHODS

In Chapter 1 we provided some background information on atmospheric waves, i.e., physics of upward propagating waves and their nonlinear interactions, reviewed the relative merits of ground-based and space-based methods to investigate wave coupling, and presented the overall objective of this study and the science questions it seeks to address. The purpose of this chapter is to review the data, models, and methods employed. It is organized as follows: Section 2.1 describes the observational data used (i.e., quasi-Sun-synchronous satellite measurements from the TIMED, CHAMP, and GOCE missions), Section 2.2 reviews the models implemented (i.e., TIME-GCM numerical simulations with GSWM and MERRA lower boundary forcing), Section 2.3 explains the procedure adopted to extract daily tidal amplitudes from satellite measurements, while Section 2.4 presents the method used to study nonlinear wave-wave interactions.

2.1 Quasi-Sun-synchronous Satellite Measurements

Satellite observations are a crucial component of research into the coupling processes that link the upper atmosphere to the lower atmosphere and provide a unique perspective due to their sampling patterns (i.e., spatially global but temporally asynoptic). In this section we provide a description of the quasi-Sun-synchronous satellite measurements from the TIMED (Section 2.1.1), CHAMP (Section 2.1.2), and GOCE (Section 2.2.3) missions that we employ to investigate wave coupling. Note that 'quasi-Sun-synchronous' refers to orbits that slowly precess with respect to local time, i.e., in the present context slowly precessing and quasi-Sun-synchronous are used inter-

changeably.

Figure 2.1 [Doornbos, 2014 [26]] shows altitudes and coplanar events (i.e., the same local solar times) between the CHAllenging Minisatellite Payload (CHAMP), Gravity Recovery and Climate Experiment (GRACE), and Gravity Field and Steady-State Ocean Circulation Explorer (GOCE) satellites from January 2009 to March 2013. The Thermosphere Ionosphere Mesosphere Energetics Dynamics (TIMED) satellite, not shown, is currently operational at ∼625 km and its instrument SABER still provides valuable limb-view measurements in the ∼20-120 km height region.

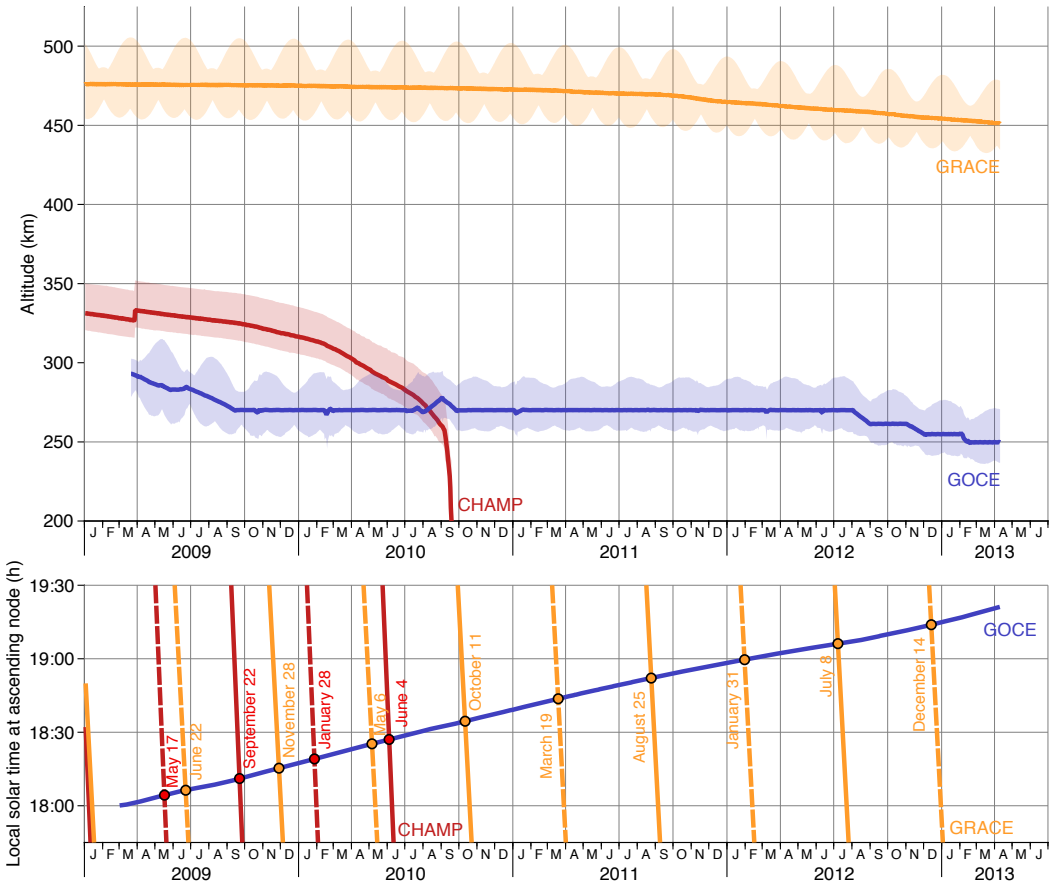

Figure 2.1: Altitude (top panel) and local time at ascending node (bottom panel) of CHAMP (red line), GOCE (blue line), and GRACE (orange line) between January 2009 and March 2013. On the bottom panel coplanar events between GOCE and CHAMP (GRACE) are marked as red (orange) dots [Doornbos, 2014 [26]].

2.1.1 TIMED-SABER

The TIMED satellite is a NASA Solar-Terrestrial Probe (STP) mission dedicated to study the dynamics and energetics of the Ionosphere-Thermosphere-Mesosphere (ITM) portion of the Earth's atmosphere, with the primary goal of providing data needed to advance our understanding of the fundamental processes governing the energetics, chemistry, dynamics, and transport in the mesosphere and lower thermosphere. TIMED was launched 7 December 2001 into a 625 km i=73° inclination orbit with a 2-year planned mission but it is still operative and fully functional. SABER is one of four instruments on TIMED and observes the atmosphere perpendicular to the satellite velocity vector. Latitude coverage for each day is about 53° latitude in one hemisphere and 83° in the other. This viewing geometry alternates once every 60 days due to 180° yaw maneuvers. Within a yaw cycle, SABER covers about 22 hours of local time, when including data from both the ascending and descending portions of the orbit (data near noon are not recorded by SABER).

Together with other parameters, SABER provides kinetic temperature estimations (derived from the CO_2 15 μm emission measured by the 10-channel broadband limb-scanning infrared radiometer) from approximately 20 km to 120 km of altitude, during both day and night, and extending up to ±83° latitude. This type of coverage offers an unprecedented opportunity to study tides and planetary waves, and their roles in coupling the troposphere, stratosphere, mesosphere, and thermosphere. The method of deriving kinetic temperatures from CO_2 emissions is detailed by Mertens et al. [2001] [154]. One of the main difficulties is the determination of kinetic temperatures under conditions of nonlocal thermodynamic equilibrium (non-LTE), typical of heights above about 70 km. In the version V1.04 of SABER temperatures used in this study, non-LTE temperatures utilize simultaneous determinations of CO_2 densities from the two CO_2 15 μm channels (narrow and wide bandpass channels). With this method (as explained by Zhang et al., [2006] [229]) a major source of uncertainty is eliminated, since CO_2 is not well mixed above 75 km and hence cannot be described in terms of volume mixing ratio. Temperature estimated with this procedure are subject to errors up to 4-5 K in the 80-120 km region, according to Mertens et al. [2001] [154].

2.1.2 CHAMP

The CHAMP satellite was launched on 15 July 2000 into an almost circular, near polar ($i = 87°$) orbit with an initial altitude of 454 km, and re-entered Earth's atmosphere on 19 September 2010. Due to atmospheric drag the altitude decreased over the 10-year mission life, such that in 2010 it was around 300 km (note: the orbit was raised 4 times over the course of the mission). Given the almost circular nearly-polar orbit and slow precession rate (considering ascending and descending nodes 24 hours of local time are sampled in ∼130 days), CHAMP provided a homogeneous and complete global coverage of the Earth's sphere for atmospheric studies.

Along with other instruments, CHAMP carried onboard the Spatial Triaxial Accelerometer for Research (STAR) accelerometer provided by the Centre National dEtudes Spatiales (CNES). Its measurements allowed the retrieval of total mass densities according to the method detailed below (a more complete description can be found in Bruinsma et al. [2004] [8]).

The acceleration due to drag experienced by an accelerometer onboard an orbiting satellite can be modeled as

$$\vec{a}_{DRAG} = -\frac{\rho}{2M}\sum_{i=1}^{15}[A_i C_{Di}(\vec{v}_{rel}\cdot\hat{n}_i)\vec{v}_{rel}], \tag{2.1}$$

where C_{Di} is the drag coefficient of plate i (15 plates for CHAMP, oriented in inertial space using STAR camera observations), A_i is the area of plate i, M the mass of the satellite, $\vec{v}_r$ the satellite velocity vector relative to a corotating atmosphere, $\hat{n}_i$ = unit vector perpendicular to plate i, and ρ the total mass density of the atmosphere. Neutral density can be calculated from Equation 2.1, after non-gravitational forces due to solar radiation pressure, Earth's albedo, and IR radiation are removed (through the use of models) from the raw acceleration data. As noted by Bruinsma et al. [2004] [8], uncertainty in the drag coefficient is about 5-15% and it is the most important systematic error. Errors relating to calibration, resolution, attitude, mass, and the macromodel are all less than 1% for both systematic and noise errors. The largest source of error in inferring densities from in-track accelerations is due to neutral winds that modify the relative velocity vector $\vec{v}_r$ in

(2.1) and thus the effective area of CHAMP. These errors were evaluated by Bruinsma et al. [2004] [8] as follows: zonal and meridional winds calculated from the TIE-GCM model over a range of conditions were added to the corotating atmosphere, the differences in modeled acceleration (and hence density) were computed and translated into an estimated density error.

The triaxial accelerometer onboard CHAMP also enabled estimation of thermosphere winds in the cross-track direction [Doornbos et al, 2008, 2010 [37], [28]]. Deriving winds from accelerometer measurements presents a significant challenge. At CHAMP altitude, the cross-track wind determination is highly dependent on the accuracy of the solar radiation pressure model. Radiation pressure modeling errors are the largest source of uncertainty and have the greatest effect when the orbital plane is near dawn-dusk, and are minimal for a noon-midnight orbital configuration. Doornbos [2011] [25] estimated the errors in accelerometer-derived cross-track winds to be mainly caused by uncertainties in the solar radiation pressure acceleration model and by accelerometer calibration biases. Both of these are dependent on the orientation of the orbital plane with respect to the Sun (i.e., solar local time) and on the level of neutral density, such that when densities are low (i.e., high altitudes and low solar and geomagnetic activity) the errors can become as large as a few hundred m/s, and when densities are high (i.e., during high solar and geomagnetic activity) the errors are of the order of a few tens of m/s. The in-track accelerations are by far dominated by accelerations due to neutral density (i.e., drag), and thus it is not feasible to separate out the in-track wind.

CHAMP also carried onboard a Digital Ion Drift Meter (DIDM) [Cooke et al., 2003 [22]; Roth, 2004 [194]], which was provided by the Air Force Research Laboratory. It consisted of two different measurement components, an ion drift meter (DM) and a Planar Langmuir Probe (PLP). The DM was a first flight demonstration of a new digital microchannel plate (MCP) approach to imaging the ion distribution function from which ion drift could be determined. The DM sustained significant damage at launch, rendering the data unusable for precision measurements. The PLP, on the other hand, functioned as per design, measuring the spacecraft potential, electron density, and electron temperature from the front panel of the spacecraft (aligned with the forward axis of

the spacecraft). McNamara et al. [2007] [152] estimated the errors in electron density retrieval to be up to 4% at low- to mid-latitudes.

2.1.3 GOCE

GOCE was launched on 17 March 2009 into a near-circular and quasi-Sun-synchronous orbit ($i = 96.5°$) at around 270 km, and remained in orbit until 10 November 2013. GOCE was the first European Space Agency (ESA) Earth-Explorer core mission [Drinkwater et al., 2003 [30]]. The objective of the mission was high-resolution mapping of the gravity field of the Earth, to which end GOCE was equipped with an ensemble of six three-axis accelerometers (the highest precision for the time) constituting the main part of the gravity gradiometer instrument. GOCE provided a total mass density product different than that of CHAMP due to the spacecraft's lower altitude (270 km vs 400 km) and dawn-dusk orbit. The nearly constant altitude and local solar time over each measurement phase made the GOCE mission profile particularly interesting for upper atmosphere studies, i.e., seasonal and solar cycle variations are not mixed with local time variations (this comes at the cost of local time coverage).

Neutral densities and cross-track winds were derived from GOCE using ion thruster data combined with accelerometer and star camera data products [Doornbos et al., 2014 [26], Doornbos et al., 2013a, 2013b [29], [27]; Bruinsma, 2014 [9]], following five steps: (1) estimation of the biases in the gradiometer common-mode accelerations using GPS tracking data, (2) conversion of ion thruster activation data to accelerations, (3) modeling of radiation pressure accelerations based on orbit and attitude information, (4) removal of radiation pressure and ion thruster accelerations from the acceleration data, and (5) iterative adjustment of wind direction and density inputs of an aerodynamic model of the satellite until the modeled aerodynamic accelerations match the observations.

The largest error sources in the GOCE density derivation are the gas-surface interaction, modeling of the satellite geometry, the calibration scale factor for the in-track accelerometer component, and the knowledge of the atmospheric in-track wind speed, composition and temperature.

Total mass density accuracy is estimated to be 10%, and the precision to 1-2% [Doornbos et al., 2014 [26]]. The dominant source of errors in the crosswind data are due to acceleration errors in the spacecraft body-fixed Y-direction. These errors are mainly due to accelerometer biases, radiation pressure variability, and thruster activations. The level of these acceleration errors with respect to the aerodynamic acceleration determines the level of crosswind error. GOCE's low orbit, where aerodynamic accelerations are very strong, is therefore a big advantage for obtaining high accuracy crosswind data. The error in this wind product is estimated to generally be less than 10 m/s [Doornbos et al., 2014 [26]].

2.2 Numerical Models

Recent modeling activity has been directed toward providing insights into the identity of the upward propagating waves, their form and amplitude variations with height. These investigations are focused toward resolving what Oberheide et al. [2011] [165] labelled the 'thermospheric gap', the lack of global observations between 120 km and 400 km, and how the lower and upper atmosphere are coupled. In this dissertation work, we employ TIME-GCM simulations to help diagnose the behavior of atmospheric waves propagating vertically from the lower to the middle thermosphere, and to validate the methodology used to infer neutral winds from CHAMP neutral and electron density measurements (see Chapter 3 and Appendix B).

2.2.1 TIME-GCM

TIME-GCM is the latest in the series of 3-dimensional time-dependent NCAR models developed to simulate the circulation, temperature, electrodynamics, and compositional structure of the upper atmosphere and ionosphere. TIME-GCM is a global grid point model that calculates neutral gas heating, dynamics, photoionization, electrodynamics, and composition of the middle and upper atmosphere and ionosphere from first principles for a given solar irradiance spectrum which varies with solar activity. It predicts global neutral winds, constituents, electron and ion densities, temperatures and drifts, and the dynamo electric field. TIME-GCM inherently accounts for at-

mospheric tides that are excited by the absorption of ultraviolet and extreme ultraviolet radiation in the middle and upper atmosphere. Upward-propagating waves excited in the troposphere are specified at the ∼30 km lower boundary (i.e., MERRA, GSMW see following subsections). TIME-GCM provides the best available global simulation of the vertical evolution of the wave spectrum through the middle atmosphere, thermosphere and ionosphere, and its effects on the ionosphere. We refer the reader to Roble et al., [1988] [193], Richmond et al., [1992] [182], Roble and Ridley, [1994] [192] and references therein for a more complete description of the TIME-GCM.

2.2.2 MERRA

In order to gain insights on wave coupling processes and to close the 'thermospheric gap' aforementioned, we employ a TIME-GCM simulation covering all of 2009 that is forced by interpolated 3-hourly MERRA dynamical fields at the lower boundary of ∼30 km, as described in Häusler et al. [2015] [77]. This simulation uses the high-resolution version of TIME-GCM, corresponding to 2.5° x 2.5° in latitude and longitude, four grid points per scale height in the vertical direction, and 60-second time step, although only hourly histories are archived (the high-resolution simulation is necessary to resolve nonlinear interactions). The 10.7 cm solar radio flux (F10.7) values along with hemispheric power and cross-cap potential values based on Kp indices are used to represent solar radiative and auroral forcing during solar minimum and for geomagnetically quiet conditions.

MERRA is a NASA satellite-era reanalysis that uses a major new version of the Goddard Earth Observing System Data Assimilation System Version 5 (GEOS-5) [Rienecker et al, 2011 [184]]. MERRA is a physics-based model with a horizontal resolution of 1.25°, temporal resolution of 3 hours and 42 vertical levels ranging from 1000 hPa to 0.1 hPa (∼64 km). For this work, we choose MERRA due to its comprehensive nature, especially in terms of the hydrological cycle (relevant to lower wave forcing), and because it provides 3-hourly data enabling both diurnal and semidiurnal tides to be extracted on a daily basis. A number of studies have used MERRA to study regional and global climate, various types of wave coupling, precipitation, stratospheric water vapor, global energy and water budgets. Additionally, Lindsay et al. [2014] [124] analyzed 7 different reanalysis

products (including various versions of NCEP and ECMWF), finding MERRA to out-perform the other models. The MERRA lower boundary condition provides the best method to specify the upward-propagating wave spectrum (with periods of 12 hours or greater) at 30 km altitude.

2.2.3 GSWM

For the purpose of validating the method used to derive zonal and meridional wind from neutral and electron density, we use TIME-GCM with GSWM-09 at the lower boundary (identical simulations to those analyzed by Jones et al. [2013, 2014] [99][100]). The simulations are static monthly values, i.e. TIME-GCM is run for 1 day in the middle of the month until the model reaches a diurnally reproducible state.

GSWM [Hagan et al., 1995, 1999 [74][70]; Hagan, 1996 [69]; Hagan and Forbes, 2002, 2003 [72][73]] is a 2-dimensional linearized, steady state numerical tidal model. GWM solves the linearized wave equations; for a given frequency and zonal wavenumber and excitation of a particular oscillation (and given a specification of the zonally-averaged atmospheric state), zonal, meridional, and vertical wind components as well as temperature perturbation are resolved as function of latitude ($\pm 87^{\circ}$) and altitude (from the ground to the thermosphere). GSWM includes all the processes known to be important to the calculation of the global atmospheric wave response: surface friction, mean winds and meridional gradients in scalar atmospheric parameters, radiative cooling, eddy and molecular diffusion, Rayleigh friction, and ion drag. In this study we use the 2009 version of GSWM (GSWM-09) [Zhang et al., 2010ab [226][228]], for which solar thermal forcing is updated using ISCCP (International Satellite Cloud Climatology Project) radiative heating, TRMM (Tropical Rainfall Measuring Mission) latent heating, and SABER mean zonal winds (derived from SABER geopotential data and mean temperatures).

2.3 Daily Tides from Ascending-Descending Differences

As discussed in Section 1.4.2, short-term variations in tides can be inferred from differences between ascending and descending measurements nearly 12 hour apart. This method was first

formulated by Hitchman and Leovy, 1985 [84]. Lieberman [1991] [119] and Oberheide et al. [2000] [167] demonstrated that amplitude and phase of DW1 could be estimated from the vertical structure of the zonal mean component of the ascending-descending difference pattern. Oberheide et al. [2000] [167] also discussed the complexities associated with the recovery of nonmigrating tides using this method. A diurnal tide with zonal wavenumber s is viewed by the satellite as a stationary zonal wavenumber $k_s = s - 1$ for westward propagation and $k_s = s + 1$ if eastward propagating. Thus, an integer-valued k_s in an ascending-descending node spectrum represents the juxtaposition of a westward propagating diurnal tide with $s = k_s + 1$ and an eastward propagating diurnal tide with $m = k_s - 1$. Below we present the mathematical formulation of this method.

A tidal component with period n/Ω can be represented as

$$A_{n,s}cos(n\Omega t + (s-n)\lambda - \phi_{n,s}). \tag{2.2}$$

The ascending (descending) leg of a satellite measures the tidal component at local time t_A (t_D), thus we can write:

$$A = A_{n,s}cos(n\Omega t_A + (s-n)\lambda - \phi_{n,s}) \tag{2.3}$$

$$D = A_{n,s}cos(n\Omega t_D + (s-n)\lambda - \phi_{n,s}) \tag{2.4}$$

If we use the two sum-to-product trigonometric identities

$$cosA - cosB = -2sin\Big(\frac{A+B}{2}\Big)sin\Big(\frac{A-B}{2}\Big) \tag{2.5}$$

and

$$cosA + cosB = 2cos\Big(\frac{A+B}{2}\Big)cos\Big(\frac{A-B}{2}\Big) \tag{2.6}$$

we can write

$$\frac{A-D}{2} = -A_{n,s} sin\Big(n\Omega\frac{t_A - t_D}{2}\Big) sin\Big(n\Omega\frac{t_A + t_D}{2} + (s-n)\lambda - \phi_{n,s}\Big). \tag{2.7}$$

and

$$\frac{A+D}{2} = A_{n,s} cos\Big(n\Omega\frac{t_A - t_D}{2}\Big) cos\Big(n\Omega\frac{t_A + t_D}{2} + (s-n)\lambda - \phi_{n,s}\Big). \tag{2.8}$$

Since at low-mid latitudes most satellites (e.g., TIMED and GOCE) satisfy the relationship: $(t_A - t_D)/2 = \pm 12$ hour, we can write $n\Omega(t_A - t_D)/2 = \pi/2$, thus Equation 2.7 can be written as

$$\frac{A-D}{2} = \mp A_{n,s} sin\Big(n\Omega\frac{t_A + t_D}{2} + (s-n)\lambda - \phi_{n,s}\Big). \tag{2.9}$$

$$\frac{A+D}{2} = \mp A_{n,s} cos\Big(n\Omega\frac{t_A + t_D}{2} + (s-n)\lambda - \phi_{n,s}\Big). \tag{2.10}$$

Each day (for ∼14 orbits/longitudes), we can fit wave $s-n$ in $(A-D)/2$ and $(A+D)/2$ to get the amplitude $A_{n,s} = A'$ and phase $\phi_{n,s} = \phi' + n\Omega(t_A + t_D)/2$.

This method allows for extraction of tidal amplitudes and phases on a daily basis. The daily resolution is very valuable, but the main shortcoming as previously mentioned is that waves with the same $s-n$ alias into each other, and hence cannot be distinguished. For instance, when estimating DE3 from wave 4 ($s-n=4$) of ascending minus descending differences the main source of error is represented by aliasing of TE1 and DW5, which cause uncertainties ranging from ∼5% during the Northern Hemisphere summer to ∼30% during the Northern Hemisphere winter at low latitudes and altitudes of ∼100 km (according to Oberheide et al., [2011] [165]). Another drawback to this technique is that semidiurnal tidal components can alias into the diurnal tidal estimates, when the ascending and descending nodes are not exactly 12 hours apart. More information on this issue is provided on Chapter 4.

2.4 Nonlinear Interactions from Pseudolongitude Spectra

The mathematical formulation of nonlinear wave-wave interactions and their relevance to the wave coupling problem was provided in Section 1.3. This section presents the method developed by Moudden and Forbes [2010] [157] to study PW-tide and tide-tide nonlinear interactions from quasi-Sun-synchronous satellite measurements.

Using the theory formulated by *Teitelbaum and Vial* [1991] [205], *Moudden and Forbes* [2010] [157] showed that the modulation of a tide by a PW generates two secondary waves with longitudinal wavenumbers $(s - n) \pm (m - \delta)$, while *Forbes and Moudden* [2012] [48] demonstrated that the effect of slow local time precession is negligible. For instance, the 6.5-day modulation of DE3 produces eastward-propagating waves with periods 20 and 28 hours, and zonal wavenumbers $s = -2$ and $s = -4$. These signals are outside the Nyquist limits of a daily sampling, and thus extracting them from satellite measurements would not possible. However, a new method developed by Forbes and Moudden [2012] [48] enables PW-tide coupling to be revealed in data from satellites precessing too slowly in local time to resolve tides over time scales much less than PW periods.

In this method, instead of ordering data sequentially in universal time, data is ordered in 'pseudo-longitude', which is simply longitude incremented by 2π each day ($\sim$14 longitudes are sampled each day on both ascending and descending parts of the orbit). Pseudolongitude P is defined as: $P = \lambda + 2\pi c$, where λ is longitude and c is the number of cycles around Earth. In other words, an increment of 2π is added to the real longitudes every time the initial longitude (that of the first orbit in the time series) is crossed again by the satellite. In a pseudolongitude spectrum, PW peaks are located at $|m - \delta|$, tides at $|s - m|$, and secondary waves due to PW-tide modulation at $|(s - n) \pm (m - \delta)|$. For the case of DE3 (n = 1, s = -3) modulated by the 6.5-day PW ($\delta = 0.15$, m = 1), the DE3 peak would occur at $k_s = 4$, the PW peak would occur at $k_s = 0.85$, and secondary peaks should occur at $|-4 \pm 0.85|$, that is $k_s = 3.15$ and $k_s = 4.85$. These peaks are sufficiently different from anything else in the spectrum that they can easily be identified and extracted.

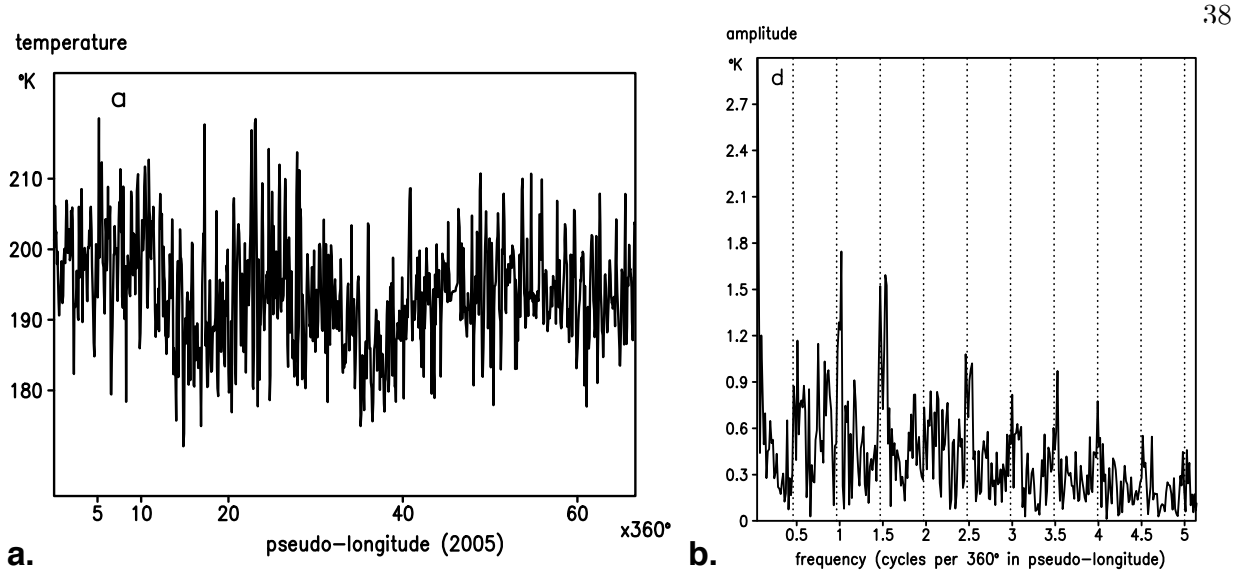

Figure 2.2: (a) Temperature time series at 30° S latitude and 80 km altitude from TIMED-SABER profiles collected during January 2006, arranged using pseudo-longitudes. (b) Spectral analysis of the time series in (a). All the peaks at half-integers are evidence of secondary waves generated by the QTDW (with $\delta = 0.5$ and $m = 3$) interacting with solar tides (integers), except for the peak at 2.5 showing the QTDW. From Forbes and Moudden [2012] [48].

Figure 2.2 (from Forbes and Moudden [2012] [48]) shows an example of TDW-tide interactions in TIMED-SABER temperatures for 2005 using the method explained above. The peaks associated with integer values are signatures of tides or stationary planetary waves since among all possible values of $s - n$, $m - \delta$, and $s \pm m - n \mp \delta$ only $s - n$ are integers (δ necessarily satisfies $\delta < 1$ since PW periods are longer than one day, unless they are stationary). The half-integer peaks can be due either to PWs ($m - \delta$) or secondary waves ($s \pm m - n \mp \delta$) resulting from PW-tide modulation. In Figure 2.2, the recurring peaks at half-integer values suggest the value of 0.5 for δ, or a PW period of 2 days and show that the 2DW has a predominant zonal wavenumber 3 ($m = 3$) and therefore its amplitude corresponds to the peaks located at $m - \delta = 2.5$. The remainder of the peaks can only be explained by the interaction of the 2DW with solar tides.

Chapter 3

VERTICAL WAVE COUPLING FROM SYNTHETIC THERMOSPHERE WINDS

In Chapter 1 we introduced the problem of atmospheric wave coupling, while in Chapter 2 we presented the data, models, and methods employed in this dissertation. In this chapter we discuss the importance of horizontal winds in governing the dynamics of the thermosphere system, and present a new method for revealing latitude-local time and latitude-longitude wind structures arising from vertical wave coupling from quasi-Sun-synchronous satellite measurements. Chapter 3 is organized into 6 sections: Section 3.1 provides an historical introduction to thermospheric wind measurements and an overview on the importance of horizontal winds as a key element of vertical wave coupling; Section 3.2 presents the data and models used in this work; Section 3.3 details the innovative method of using neutral and plasma densities measured by the CHAMP satellite to infer zonal and meridional ('synthetic') winds; Section 3.4 validates the methodology by showing that neutral and electron densities output from TIME-GCM can be used to derive solutions to the momentum equations that replicate reasonably well the winds self-consistently calculated within the TIME-GCM; Section 3.5 discusses the uncertainties in the derived synthetic winds taking advantage of the same TIME-GCM simulations used for validation; while Section 3.6 reveals the seasonal and local time dependencies of zonal and meridional wind latitude-longitude structures, compares CHAMP synthetic winds with CHAMP cross-track winds and empirical estimates from HWM14, and shows examples of new science that can be conducted using this dataset. An interested reader may refer to Appendix B for the complete validation, which also includes scale and error analyses.

The contents of this chapter are derived from the JGR-Space Physics paper first published online on April 25, 2016 and referenced in the Bibliography as Gasperini et al. [2016] [60].

3.1 Introduction

Wind, temperature, and composition are the fundamental parameters of thermosphere dynamics and structure; from knowledge of composition and temperature one can determine pressure and total mass density using the ideal gas law. In a hypothetical windless atmosphere, temperature, composition, pressure, and density are rather easily related through the hydrostatic law, and this forms the basis for most empirical models of the thermosphere. The addition of winds elevates the complexity of the system considerably, since vertical and horizontal winds modify composition by redistributing chemical species, and can affect temperature through vertical motions (adiabatic heating and cooling). In addition, the bulk wind field responds to changes in pressure as well as collisional momentum transfer with the ionospheric plasma, and momentum deposition due to dissipating waves. In particular, the meridional wind component modifies the ionosphere by moving plasma up and down magnetic field lines, and serves to transport neutral minor constituents. The meridional wind field can also close with vertical winds on both local and global scales, thus contributing to the thermal structure through adiabatic heating and cooling effects. However, the meridional wind field has not been well measured, especially on a global scale.

Thermosphere wind measurements are relatively sparse. Some measurements are possible from the ground using Fabry-Perot interferometers [Meriwether, 2006 [153]] or incoherent scatter radars [Salah and Holt, 1974 [196]]. Low-latitude meridional winds at 130-330 km were estimated using ionization gauge data from the Streak mission, but only for the dusk sector [Clemmons et al., 2013 [20]]. There have also been some attempts to derive meridional winds through their self-consistency with other observed parameters. Given the proportional relationship between the winds and the height of the F2-layer peak, magnetic meridional winds can be derived from ionospheric F2-layer peak height (hmF2) and peak density (NmF2) [Rishbeth, 1967 [186]; Rishbeth et al., 1978 [190]]. Thermospheric meridional winds extracted from ionosonde data have been used to

investigate diurnal, seasonal, solar cycle and latitudinal variability [Buonsanto, 1990, 1991 [11][12]; Liu et al., 2003, 2004 [140][141]], and study changes in the meridional circulation associated with magnetically-disturbed conditions [Forbes et al., 1988 [43]]. Luan and Salomon [2008] [145] derived magnetic meridional winds from hmF2/NmF2 measurements taken by the Constellation Observing System for Meteorology, Ionosphere, and Climate (COSMIC) satellites, validated this dataset using ISR and FPI measurements, and found evidence of longitudinal variation of meridional winds induced by magnetic declination effects associated with the zonal wind. More recently, Lomidze et al. [2015a] [142] used the Global Assimilation of Ionospheric Measurements Full Physics (GAIM-FP) model and COSMIC data to infer magnetic meridional winds consistent with observed ionospheric conditions, and Lomidze et al. [2015b] [143] estimated climatological zonal and meridional winds with the Thermospheric Wind Assimilation Model (TWAM), which combines GAIM-FP magnetic meridional winds with a thermospheric neutral wind model that uses an implicit Kalman filter method.

Some measurements of thermosphere winds were taken as part of the Atmosphere Explorer, Dynamics Explorer, SETA, UARS, C/NOFS missions, but these also provided coarse coverage either due to duty cycle, local time and latitude restrictions, or limited solar cycle sampling. What we currently know about thermosphere wind behavior is embodied in the Horizontal Wind Model 14 (HWM14) empirical model [Drob et al., 2015 [32]], which is a massive multi-parameter fit to essentially all of the relevant wind measurements to date. Simultaneous measurements of winds, temperature and composition are even more rare than wind measurements themselves, yet global simultaneous observations of these fields, and their temporal evolution in response to measured external forcing, are what is really needed to truly understand the physical mechanisms responsible for the dynamics of the thermosphere system.

Despite the somewhat dim perspective laid out above, a remarkable degree of new insights have resulted just from the total mass density measurements derived [Doornbos et al., 2008, 2010 [37][28]] from accelerometer measurements made on the CHAMP and GRACE satellites over the past decade. These span a broad spectrum of topics, including thermosphere variations due to

traveling atmospheric disturbances [Bruinsma, 2010 [7]], the response to solar flares [Sutton, 2005 [201]] and magnetospheric energy inputs [Lühr et al., 2004 [148]; Liu and Lühr, 2005 [134]], the solar terminator [Forbes et al., 2008 [42]; Liu et al., 2009 [137]], signatures of plasma-neutral coupling at low latitudes [Liu et al., 2007 [133], Lühr et al., 2007 [146]], the semiannual variation [Guo et al., 2008 [67]], solar coronal holes and recurrent geomagnetic activity [Thayer et al., 2008 [207]; Lei et al., 2008, 2010 [115][114]], upward-propagating solar and lunar tides [Forbes et al., 2013 [51]], density connections to various solar wind characteristics [Kwak et al., 2009, 2011 [112][111] ; Deng et al., 2009 [23], Knipp et al., 2013 [107]], and the deep solar minimum of 2008-2009 [Bruinsma and Forbes, 2010 [7]; Lei et al., 2011 [118]].

The triaxial accelerometer on CHAMP have also enabled some estimate of thermosphere winds in the cross-track direction [Doornbos et al, 2010, 2011 [28][25]; Liu et al., 2006 [136]; Haüsler et al., 2007 [79]]. As explained in Section 2.1.2, deriving winds from accelerometer measurements presents a significant challenge. The in-track accelerations are dominated by accelerations due to the neutral density, and it is not feasible to separate out the in-track wind. At the high altitudes of CHAMP, the cross-track wind determination is highly dependent on the accuracy of the solar radiation pressure model. The radiation pressure force in fact dominates in the cross-track direction at GRACE altitudes (∼500 km), precluding any reasonable wind extraction. For CHAMP, radiation pressure modeling errors are the largest when the orbital plane is near dawn-dusk, and are minimal for a noon-midnight orbital configuration. Since thermosphere winds are especially large at high latitudes, some success has been achieved in establishing polar-region wind patterns and even their dependence on solar wind magnetic field configuration [Förster et al, 2008 [56]; Lühr et al., 2007a [147]]. At lower latitudes, with careful data processing and significant averaging, some information on the longitude variability of thermosphere winds has been achieved, including that due to non-migrating tides propagating upwards from the lower atmosphere [Häusler and Lühr, 2009 [78]; Lühr et al., 2007a [147]; Liu and Watanabe, 2008 [139]].

In the 1960's and 1970's, before satellite-based wind measurements were made, insights into global patterns of thermosphere wind behavior were obtained by solving the horizontal momentum

equations [Challinor, 1969 [15]; Geisler, 1966, 1967 [62], [63]], with pressure gradient terms approximated from empirical density and temperature models based on satellite drag [e.g., Jacchia, 1964, 1971 [93], [92]] and crude models of the ionosphere and magnetic field geometry. These steady-state models mainly showed how ion drag tended to cause cross-isobaric flow in contrast to geostrophic flow, and gave some impression about the diurnal behavior of the wind system, and in some cases its height dependence. Total mass densities derived from CHAMP accelerometer measurements and in-situ electron densities measured from a Langmuir probe can be used to specify the pressure gradient and ion drag terms in the eastward and northward momentum equations of the thermosphere, and thus obtain wind estimates ('synthetic winds') for thermosphere studies. A distinct advantage of this method is that meridional winds are produced in addition to zonal winds.

3.2 Data

In this work we use neutral densities and zonal (cross-track) winds from CHAMP's Spatial Triaxial Accelerometer for Research (STAR) accelerometer [Bruinsma et al., 2004 [10]; Doornbos et al., 2010 [28]; Doornbos, 2011 [25]], and electron densities from CHAMP's Digital Ion Drift Meter (DIDM) instrument [Cooke et al., 2003 [22]; Roth, 2004 [194]]. We also employ the Thermosphere, Ionosphere, Mesosphere, Electrodynamics General Circulation Model (TIME-GCM) with GSWM-09 at the lower boundary to validate the methodology adopted to derive winds from neutral and electron density measurements. [For more information on CHAMP and TIME-GCM refer to Sections 2.1 and 2.2.]

Analyzing the noise in the 10-sec (15-sec) CHAMP neutral (electron) density measurements and using a 3° latitude bin, we determined that latitude-longitude wind structures can be effectively derived by using 10-day means. For each latitude-longitude bin we determined that averaging ∼60 data points (6 measurements per latitude bin for 10 days) is sufficient to beat down the noise (in part caused by geomagnetic activity effects) and leads to a clean wind product, without compromising the fixed local time assumption (CHAMP precesses 1 hour in ∼11 days; see Section 3.5 for error estimates). For CHAMP's 10-year lifetime, we identified 115 geomagnetically quiet 10-day periods,

defined as the 10-day periods that include a minimum of 8 days with Ap≤10, and we calculated an average F10.7 of 99 sfu and standard deviation of 22 sfu for these 115 periods. Defining low solar activity days with F10.7≤77, in this paper we restrict our attention to only 63 of these 115 10-day periods that are both at solar minimum and in geomagnetically quiet conditions and span all months at various local times. These prove to be sufficient to study the seasonal and local time variability in the derived winds, as discussed in Section 3.6. We limit our analysis to low- to mid-latitudes (±45°), where the effects of convection electric fields on the neutral dynamics are minimal (at higher latitudes we would expect larger errors in the derivation method due to the effect of unmodeled ionosphere-thermosphere coupling processes).

3.3 Methodology

In this section we describe the methodology used to derive synthetic winds from CHAMP neutral and electron density measurements, including all the assumptions and limitations. The procedure consists of three major steps: (1) deriving temperatures and ion drag values from neutral and electron density measurements, (2) inferring pressure gradients from neutral density and temperature, and (3) solving the 2-D momentum equations for the zonal and meridional wind components. Details for each step are provided below.

Step 1 *Deriving temperatures and ion drag values from neutral and electron densities.*

Approach

(i) Starting from CHAMP total mass densities derived from accelerometer measurements, we use the NRLMSISE00 empirical model of the thermosphere and iterate on the F10.7 solar flux index until the model density converges on the measured density (with a margin of ±1%), yielding the equivalent exosphere temperature from the model. This procedure is possible due to the parametric dependence between exospheric temperature and F10.7. The idea of parametrically relating thermosphere densities and temperatures is basic to all empirical models to date, because the vertical distribution

of thermosphere density is assumed to follow the barometric law. When temperature is basically independent of height (i.e., for CHAMP at ∼300 km) the scale height of each constituent is constant, and a simple exponential dependence with height applies (see also Forbes et al. [2009] [54] and Weimer et al. [2016] [219] for application of this method).

(ii) We infer ion drag coefficients (λ's) from plasma densities measured in-situ by CHAMP's Langmuir probe. The Lorentz force, which represents the influence of the ionized plasma on the neutrals, can be expressed as [Richmond, 1971 [181]]

$$\left[\frac{\vec{J}\times\vec{B}}{\rho}\right]_{\phi} = -\lambda_x(u-u^e) + \lambda_y cos\theta(v-v^e) \tag{3.1}$$

for the zonal direction ϕ, and in the latitudinal direction θ as

$$\left[\frac{\vec{J}\times\vec{B}}{\rho}\right]_{\theta} = -\lambda_x(v-v^e) - \lambda_y cos\theta(u-u^e) \tag{3.2}$$

where $\vec{J}$ and $\vec{B}$ are the Pedersen current and the magnetic field respectively, u (v) is neutral zonal (meridional) velocity, u^e (v^e) is zonal (meridional) electrodynamic drift velocity, $\lambda_x = \sigma_1 B^2(\theta)/\rho$, and $\lambda_y = \sigma_2 B(\theta) B_{pole}/\rho$ are the ion drag coefficients, σ_1 (σ_2) is the Pederson (Hall) conductivity, and ρ is neutral density. If we then assume that plasma drifts are negligible (see Appendix B for the error analysis), and that the masses of ions and neutrals are equal, we can write

$$\lambda_x \approx \frac{N_i}{\rho}\frac{\nu_{ni}}{1+(\nu_{ni}/\omega_i)^2} \tag{3.3}$$

$$\lambda_y \approx \frac{\nu_{ni}}{\omega_i}\lambda_x \tag{3.4}$$

where N_i is ion density, ω_i ion gyrofrequency, and ν_{ni} neutral-ion collision frequency, where we then use the approximation $\nu_{ni} = 2.610^{-9}(N/M^{0.5})$ in cgs units [Chapman, 1956 [17]; Rishbeth and Garriott, 1969 [191]; Forbes and Garrett, 1979 [44]].

Step 2 *Inferring pressure gradients from neutral density and temperature.*

Approach

(i) Pressure (p) is inferred from neutral density (ρ) and temperature (T) derived in Step 1. If we assume ideal gas conditions (very good approximation for the thermosphere, especially under geomagnetic quiet conditions), we can solve the ideal gas law $p = \rho R_{spec} T$, where R_{spec} is the specific gas constant ($\approx$ 129.9 $Jkg^{-1}K^{-1}$ for atomic oxygen) to derive pressure values.

(ii) Pressure gradients in the eastward and northward directions are derived by calculating derivatives with respect to longitude ϕ (PGX) and latitude θ (PGY), respectively:

$$PGX = \frac{1}{R_E \rho cos\theta} \frac{\partial p}{\partial \phi} \tag{3.5}$$

$$PGY = \frac{1}{\rho R_E} \frac{\partial p}{\partial \theta} \tag{3.6}$$

where R_E is Earth's radius. Note that any longitudinal or latitudinal *mean* biases possibly introduced by the use of MSISE in Step 1 are largely eliminated in the pressure gradients by taking derivatives with respect to longitude and latitude.

Step 3 *Solving the 2-D momentum equations for the horizontal wind field.*

Approach The complete 2D momentum equations (ignoring vertical velocity effects) in the zonal and meridional directions can be written as [*Dickinson et al.*, 1981]:

$$\begin{aligned} \frac{\partial u}{\partial t} = & \frac{\mu}{\rho} \frac{\partial^2 u}{\partial z^2} + f^{cor} v + \lambda_x (u^e - u) + \lambda_y (v^e - v) - \vec{v} \cdot \vec{\nabla} u + \frac{uv}{R_E} tan\theta \\ & - \frac{1}{R_E \rho cos\theta} \frac{\partial p}{\partial \phi} - w \frac{\partial u}{\partial z} \end{aligned} \tag{3.7}$$

$$\begin{aligned} \frac{\partial v}{\partial t} = & \frac{\mu}{\rho} \frac{\partial^2 v}{\partial z^2} - f^{cor} u + \lambda_x (v^e - v) + \lambda_y (u^e - u) - \vec{v} \cdot \vec{\nabla} v + \frac{uu}{R_E} tan\theta \\ & - \frac{1}{R_E \rho} \frac{\partial p}{\partial \theta} - w \frac{\partial v}{\partial z} \end{aligned} \tag{3.8}$$

where u and v are the zonal and meridional velocities, z is height, μ is the viscosity coefficient, f^{cor} is the Coriolis parameter, and u^e (v^e) is the zonal (meridional) plasma drift

velocity. Looking at Equations 3.7 and 3.8, we can say that the time rate of change in the horizontal velocity on the left hand (1^{st} term) side is equal to the forcing terms on the right hand side. The forcing terms are in the following order: vertical viscosity (2^{nd} term), Coriolis force (3^{rd} term), ion-drag force ($4^{th} + 5^{th}$ term), nonlinear horizontal advection (6^{th} term), curvature momentum force (7^{th} term), pressure gradient force (8^{th} term), and vertical advection (9^{th} term). If we neglect (1) vertical viscosity, (2) plasma drift velocities and parallel ion drag, and (3) non-linear horizontal and vertical advection and momentum force (second order terms), and we consider the relationships: $f^{cor} = 2\Omega sin\theta$, $\lambda_y = \lambda_x sin^2 I = \lambda sin^2 I$ (where I is the magnetic dip angle), where Ω is Earth's rotation rate, we can simplify Equations 3.7 and 3.8 to the following:

$$\frac{\partial u}{\partial t} = 2\Omega v sin\theta - \lambda u - \frac{1}{\rho R_E cos\theta}\frac{\partial p}{\partial \phi} \tag{3.9}$$

$$\frac{\partial v}{\partial t} = -2\Omega u sin\theta - \lambda v sin^2 I - \frac{1}{\rho R_E}\frac{\partial p}{\partial \theta} \tag{3.10}$$

The left hand side of Equation 3.9 (3.10) shows the time derivative of zonal (meridional) wind with respect to time. The issue is now understanding the relationship between UT time, longitude, and local time in CHAMP's measurements. For each day and latitude CHAMP provides a global longitudinal coverage with a resolution of $\sim 24°$. Additionally, CHAMP possesses a slow precession rate (24 hours of local time are covered in $\sim$260 days), so that we can effectively approximate data for a 10-day period to be at a fixed local time (in reality local time varies by $\sim$4 minutes every 24 hours). Thus, given CHAMP's precession, we can reformulate (3.9) and (3.10) in a latitude vs. longitude frame for each 10-day period (*case a*) and in a latitude vs. local time frame (at specific longitudes, or as a longitudinal mean) using 130 days of data including both the ascending and the descending nodes (*case b*).

If we consider the linear relationship between universal time (UT) and local time (LT),

such that $\delta t_{UT} = \delta t_{LT} - \frac{\delta\phi}{\Omega}$, we can rewrite Equations 3.9 and 3.10 for *case a* ($\delta t_{LT} = 0$, so $\delta t_{UT} = -\frac{\delta\phi}{\Omega}$) as:

$$\frac{du}{dt_{UT}} = -\Omega\frac{\partial u}{\partial\phi} = -\frac{1}{\rho R_E cos\theta}\frac{\partial p}{\partial\phi} + 2\Omega v sin\theta - \lambda u \tag{3.11}$$

$$\frac{dv}{dt_{UT}} = -\Omega\frac{\partial v}{\partial\phi} = -\frac{1}{\rho R_E}\frac{\partial p}{\partial\theta} - 2\Omega u sin\theta - \lambda v sin^2 I \tag{3.12}$$

and for *case b* ($\delta t_{UT} = 0$, so $\delta t_{LT} = \frac{\delta\phi}{\Omega}$) as:

$$\frac{du}{dt_{LT}} = \Omega\frac{\partial u}{\partial\phi} = -\frac{1}{\rho R_E cos\theta}\frac{\partial p}{\partial\phi} + 2\Omega v sin\theta - \lambda u \tag{3.13}$$

$$\frac{dv}{dt_{LT}} = \Omega\frac{\partial v}{\partial\phi} = -\frac{1}{\rho R_E}\frac{\partial p}{\partial\theta} - 2\Omega u sin\theta - \lambda v sin^2 I \tag{3.14}$$

Using Equation 3.11 and solving for v as function of u, we can write:

$$v = -\frac{1}{2sin\theta}\frac{\partial u}{\partial\phi} + \frac{1}{2\Omega R_E\rho sin\theta cos\theta}\frac{\partial p}{\partial\phi} + \frac{\lambda u}{2\Omega sin\theta} \tag{3.15}$$

If we then substitute (3.15) into (3.12) we can write

$$\frac{\Omega}{2sin\theta}\frac{\partial^2 u}{\partial\phi^2} - \frac{1}{R_E\rho sin(2\theta)}\frac{\partial^2 p}{\partial\phi^2} - \frac{\lambda}{2sin\theta}\frac{\partial u}{\partial\phi}(1 + sin^2 I) - u(2\Omega sin\theta + \frac{\lambda^2 sin^2 I}{2\Omega sin\theta}) = -\frac{1}{R_E\rho}\frac{\partial p}{\partial\theta} \tag{3.16}$$

Equation 3.16 is a second order partial differential equation for u, of the kind $a\frac{\partial^2 x}{\partial y^2} + b\frac{\partial x}{\partial y} + cx + d = 0$, with a, b , c, d as known values, in the only variables of longitude and latitude. We solve (3.16) using the IDL function IMSL-PDE-MOL, which implements the method of lines to represent the solution as cubic Hermite polynomials, and use this calculated value of u to solve for v in Equation 3.12. The same procedure is also applied to solve Equations 3.13 and 3.14.

Of the three assumptions used to simplify the momentum equations, the more questionable ones are neglecting vertical viscosity and the drift velocities. We neglect vertical viscosity assuming this force to be small compared to pressure gradient and ion drag (as suggested by Geisler [1966] [62]); the main role of vertical diffusion is to maintain the horizontal wind field (determined by the pressure gradient and ion drag forces) approximately constant with height. There are some situations where this could be violated; e.g. see Section 3.6.2. We also neglect drift velocities (similar to models such as GSWM) under the assumption that these have a small effect on the ion drag term at low to middle latitudes. For validation and error analyses that bear on these assumptions refer to Section 3.4, Section 3.5, and Appendix B.

3.4 Validation

In order to validate the methodology described in the previous section, we implement TIME-GCM simulations for September at solar minimum (F10.7 value of 70 sfu), identical to those analyzed by Jones et al., [2013], [2014] [99][100]. The simulations are static monthly values (i.e., the TIME-GCM is run for one day in the middle of the month until the model reaches a diurnally-reproducible state) and uses GSWM-09 to specify tidal components at the lower boundary (i.e., 10 mb or 30 km). GSWM-09 includes updated background temperature and wind fields derived from measurements made by the SABER instrument onboard the TIMED satellite, as well as new radiative and latent heating rates derived from the International Satellite Cloud Climatology Project (ISCPP) and Tropical Rainfall Measuring Mission (TRMM) data, respectively [Zhang et al., 2010ab [226][228]]. The GSWM-09 boundary includes migrating and non-migrating diurnal and semidiurnal tidal components with zonal wavenumbers ranging between ±6. Appendix B provides additional comparisons for December at solar medium conditions with and without tides at the lower boundary, and including and neglecting ion drifts.

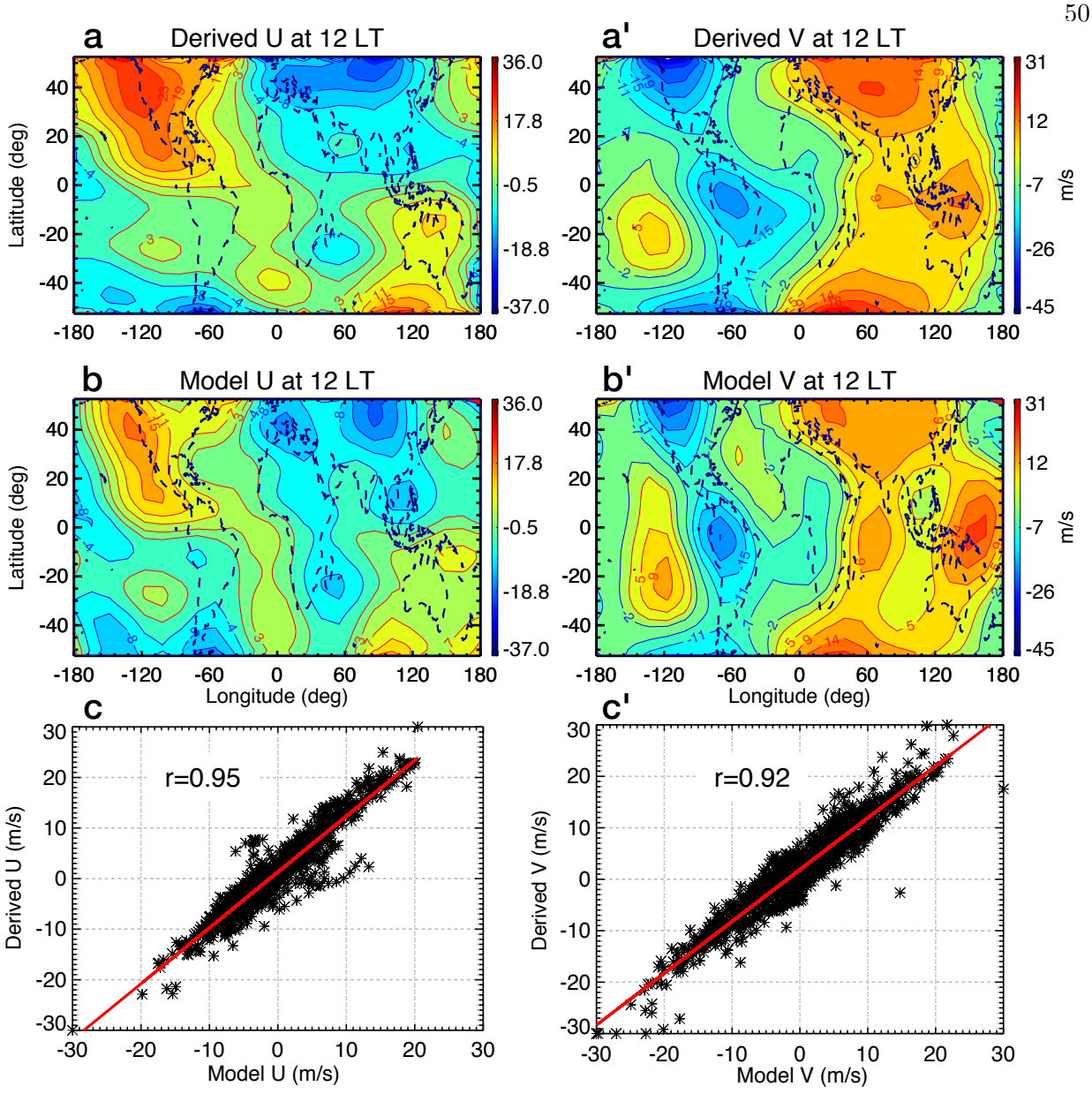

Figure 3.1: Zonal (panels a-c) and meridional (a′-c′) latitude-longitude wind structures at 12 LT derived from TIME-GCM neutral and electron densities (panels a and a′) and as self-consistently output from the model (panels b and b′). A scatter plot between derived and model winds is also included (panels c and c′). The model simulation used is for September at solar minimum with tides at the lower boundary. The longitudinal mean was removed to facilitate the comparison. Correlation coefficients of ∼0.95 and ∼0.92 are found for the zonal and meridional winds, respectively.

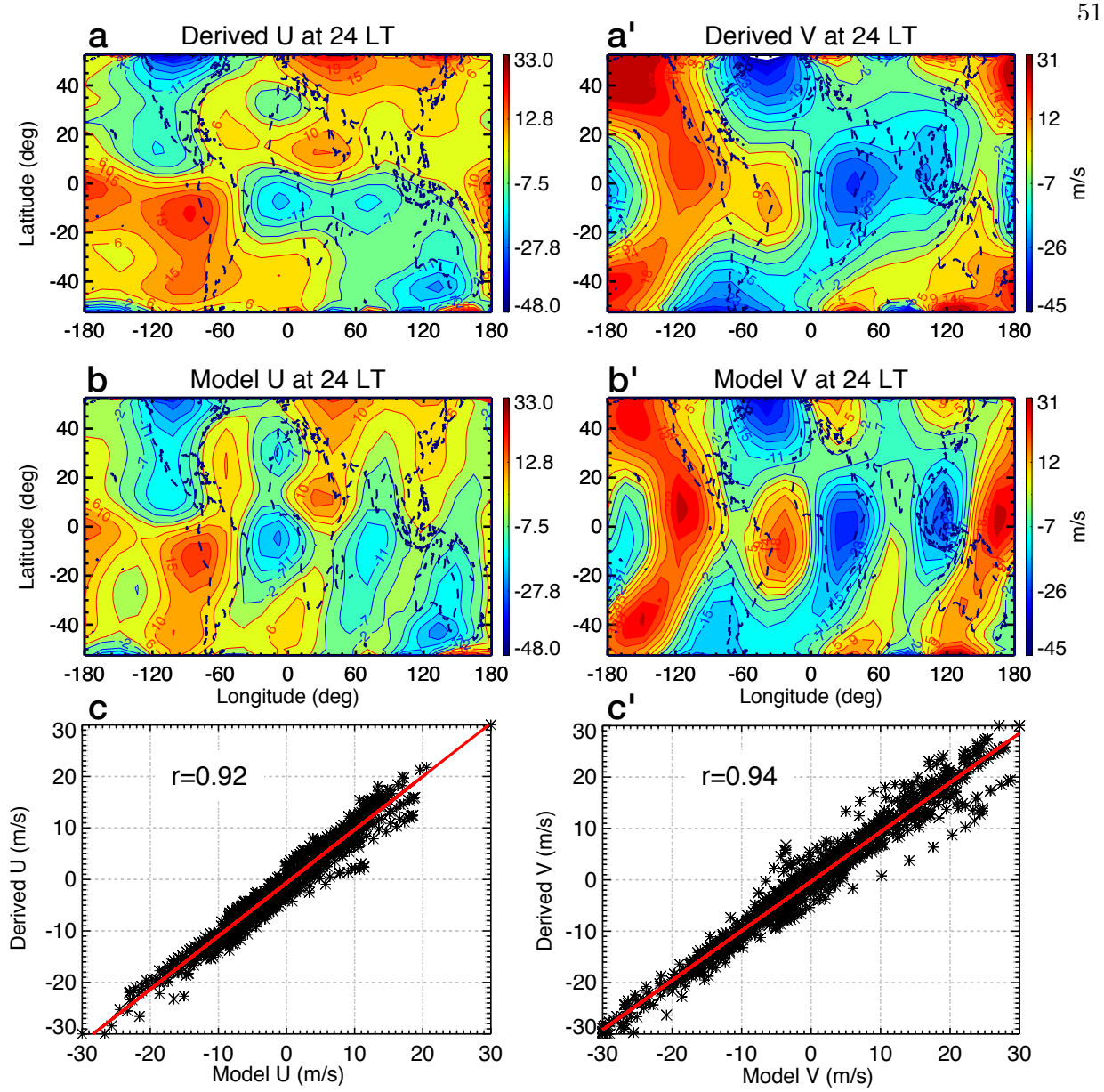

Figure 3.2: Similar to Figure 3.1, but for 24 LT. Note correlation coefficients of ∼0.92 (∼0.94) for the zonal (meridional) wind component.

Neutral and electron densities from TIME-GCM are converted to pressure gradients and ion drag values, according to the method detailed in Section 3.3 (Step 1 and Step 2), and used to derive solutions to the horizontal momentum equations (Step 3). Figure 3.1 (Figure 3.2) shows a comparison between the derived (panels a and a') and model (panels b and b') zonal and meridional winds in a latitude-longitude format for 12 LT (24 LT). A scatter plot between the derived and model

zonal and meridional wind components is provided in Figure 3.1c and Figure 3.1c'. Comparing Figure 3.1a (Figure 3.1b) and Figure 3.2a (Figure 3.2b) with Figure 3.1a$'$ (Figure 3.1b$'$) and Figure 3.2a$'$ (Figure 3.2b$'$), one can see that the large majority of the longitude-latitude variability in the model winds is effectively replicated by the derived winds. To quantify this, correlation coefficients (r's) are included in the scatter plots. We report correlation coefficients $\geq$0.92 for both zonal and meridional winds at 12 LT and 24 LT, demonstrating that the derived winds capture $\sim$85% of the latitude-longitude variability in the model winds.

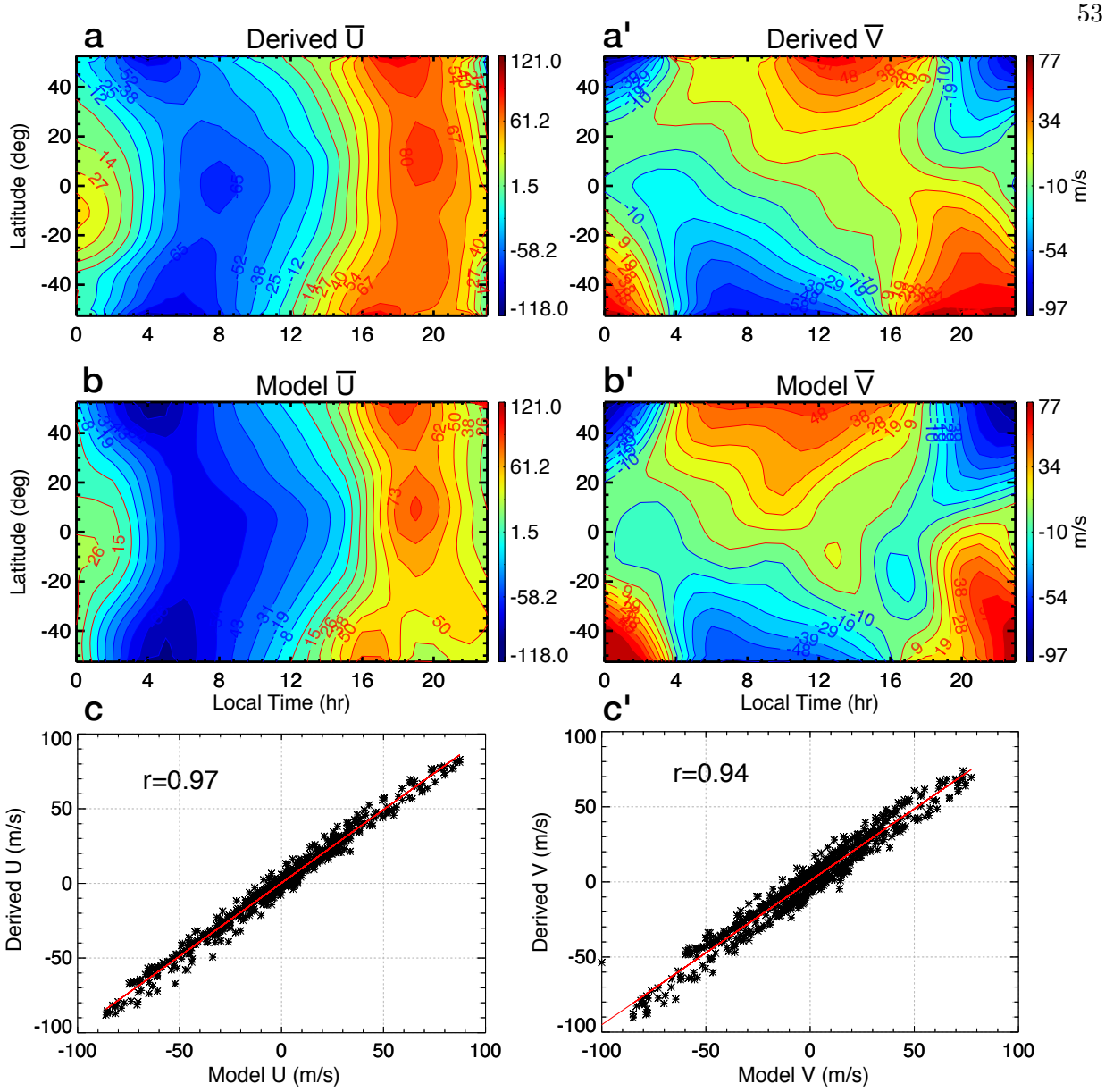

Figure 3.3: Latitude vs. local time comparison between synthetic (panel a) and model (panel b) zonal winds (longitudinal mean, $\overline{U}$), and derived (panel a′) and model (panel b′) meridional wind (longitudinal mean, $\overline{V}$). Panel c (c′) shows the scatter plot between synthetic zonal (meridional) winds and model zonal (meridional) winds. The TIME-GCM model run used is the same as in Figures 3.1 and 3.2. Note correlation coefficients of ∼0.97 (∼0.94) for zonal (meridional) winds. The minimum in model meridional winds at 10-30° S around 16-18 LT not captured by the derived winds is likely due increased pressure gradient and/or ion drag retrieval errors around sunset for relatively low wind speeds (±15 m/s).

As discussed in Section 3.3, the horizontal momentum equations can also be solved to reveal the local time variation, when approximating the solution to be UT time-independent. To validate this assumption we implement the same TIME-GCM simulations used to validate latitude-longitude structures. Given the linear relationship between UT time, longitude, and local time (the model runs have a time and longitude resolution of 1 minute and 2.5°, respectively), local time is resolvable in the model with a resolution of 1 hour. Figure 3.3 shows the comparison between derived (panel a and a') and model (panel b and b') zonal and meridional wind structures in a latitude vs. local time format as longitude means. Note the strong local time dependence of the longitude-mean winds, with values ranging from 116 m/s to -94 m/s for the zonal component ($\overline{U}$) and 77 m/s to -97 m/s for the meridional component ($\overline{V}$) . To quantify the extent to which the derived winds can reproduce the latitude and local time variability in model winds, a scatter plot between the two is provided in panels c and c', showing r≈0.97 (r≈0.94) for zonal (meridional) winds, which translates to a variance of ∼94% (∼88%). No biases between model and derived winds was found. Similar results (not shown here) are found for different geophysical conditions (i.e., December at solar medium conditions, see Appendix B) and longitudes.

3.5 Estimated Errors

There are 3 main sources of error that affect the synthetic winds derived from CHAMP measurements. These are: (a) errors due to simplifications made in solving the momentum equations, (b) errors in the retrieval of neutral and electron densities from CHAMP accelerometer data, and (c) errors generated by the assumption of constant local time in a 10-day period (only for latitude-longitude structures). The TIME-GCM simulations used to validate the methodology provide the opportunity to estimate the errors due to (a). This is performed for each step in the derivation method outlined in Section 3.3, and for the overall wind estimates. To accomplish this, we assume the model pressure gradients, ion drag values, and winds as truth, and interpret the differences from the derived pressure gradients, ion drag values, and winds as the errors. For a comprehensive error analysis on the wind derivation method, an interested reader may refer to Appendix B. Here

below we provide a brief summary of the errors due to (a), (b), and (c).

By performing a scale analysis of the momentum equations, we estimated that neglecting vertical viscosity, horizontal advection, curvature momentum force, and vertical advection in the momentum equations leads to uncertainties of only ∼2% in the calculation of the $\frac{du}{dt}$ term. Errors in the derivation of ion drag from electron densities are estimated to be up to 14%, mainly due to the effect of ion drifts (∼12%), while errors in the retrieval of pressure gradients from neutral densities are found to be less than 4% (biases in the MSISE-derived temperatures are largely removed by using longitude-latitude derivatives). Correlation coefficients between the model winds and the winds derived from electron and neutral densities as function of local time and latitude at different local times, or as function of local time and latitude at different longitudes (or as longitudinal means) are greater than 0.9 for all the model simulations analyzed. This means that over 80% of the latitude-longitude variability in the zonal and meridional winds can be reproduced by starting from neutral and electron densities alone (as discussed for Figures 3.1 and 3.2 in Section 3.4). Errors in the retrieval of neutral and electron densities from CHAMP accelerometer data are also a factor in the overall errors of the derived winds. Errors in the derivation of electron densities from the DIDM are estimated to be ∼4%, while errors in the retrieval of neutral densities from accelerometer measurements are generally less than ∼10%. In-track (meridional) winds can impact the quality of the derived neutral densities [Doornbos et al., 2010 [28]] and cause errors up to ∼5% (for meridional winds of ∼200 m/s). Additionally, CHAMP local time precession of ∼4 min/day yields errors up to 4% in the derived latitude-longitude wind products when assuming fixed local time.

Summarizing, the overall error in the derived winds is estimated to be up to ∼30%, although we would expect the real value to be lower due to biases in the derived temperatures being removed by applying derivatives when calculating pressure gradient values, and because we do not expect the total error to be the simple sum of (a), (b), and (c), although this provides a worst case estimate.

3.6 Results

In this section, first we discuss the method adopted to derive the full 24-hour local time variability by averaging data for 43 days; second (Section 6.2) we show latitude vs. longitude synthetic wind structures at various local times and comparisons with acceleration-derived cross-track winds and HWM14 empirical model winds; next we analyze the winds in latitude vs. local time (Section 6.3) and local time vs. longitude (Section 6.4) formats; in Section 6.5 we analyze the latitudinal variability of wave-4; while in Section 6.6 we discuss seasonal and local time dependencies in the winds. Note that all the results presented in this section refer to low- to mid-latitudes ($\pm 45°$), and data are binned in 3° latitude, 24° longitude, and 1 hour local time.

3.6.1 Local Time Reconstruction

As mentioned in Section 3.2, analyzing CHAMP's 10-sec (15-sec) neutral (electron) density measurements we determined that, for a 3° latitude bin, averaging 10 days of data is sufficient to beat down the noise without compromising the fixed local time assumption. Of the 63 geomagnetically quiet 10-day periods that are also at low solar activity, we found 7 to be concentrated within the 43-day period between 1 August and 12 September spanning the years 2007-2009 (see Table 3.1). Using data from both ascending and descending nodes, and by considering each 10-day period at a fixed local time, for each 3° latitude bin we fit using an equation of the form $A_{n,s}cos[n\Omega t_{LT} + (s-n)\lambda - \Phi]$, all the waves (diurnal n=1, semi-diurnal n=2, and terdiurnal n=3, with s=$\pm$4) in the variables of local time (t_{LT}) and longitude (λ), where $A_{n,s}$ is the amplitude of the wave with frequency $n\Omega^{-1}$ and zonal wavenumber s, and Φ is the phase (defined as the time of maximum at zero longitude). In the following we refer to this 43-day period, for which all latitudes, longitudes, and local times are adequately sampled to perform the above fit, as an 'equivalent day'. The main advantage of averaging data for only 43 days, as opposed to using the ~130 days needed for CHAMP to cover all local times, is an expected amelioration of amplitude suppression due to averaging and possible mixing of seasons (130 days span over 4 months).

SLT Asc. (Dsc.) Node	Date (day/month/year)	Avg. F10.7
03 (15)	30/08/07 - 09/09/07	69
04 (16)	20/08/07 - 29/08/07	71
10 (22)	04/08/09 - 13/08/09	68
17 (05)	03/09/08 - 12/09/08	67
18 (06)	24/08/08 - 02/09/08	67
19 (07)	12/08/08 - 22/08/08	67
20 (08)	01/08/08 - 11/08/08	67

Table 3.1: Periods selected for the local time reconstruction.

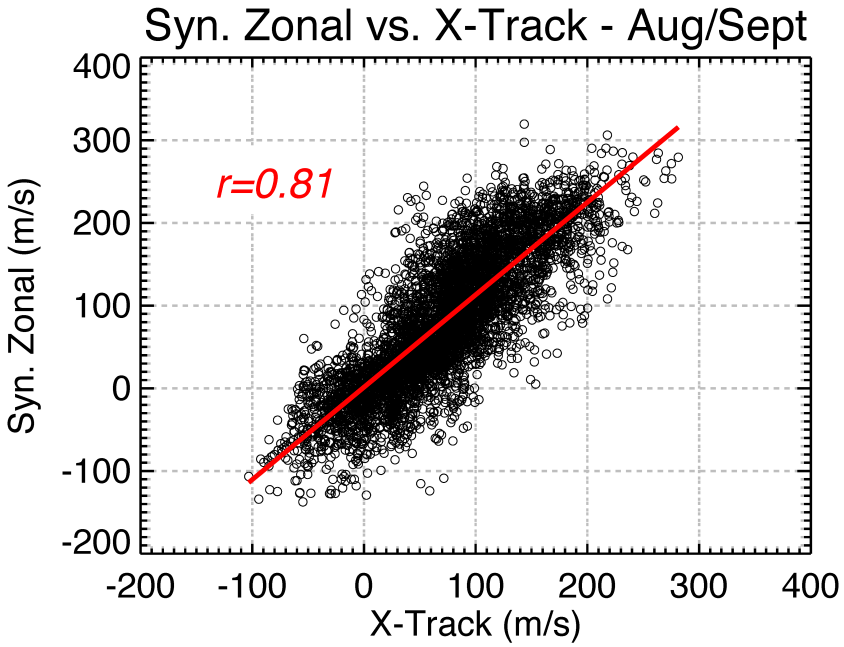

Figure 3.4: Scatter plot between synthetic zonal winds and cross-track winds for the seven 10-day periods between 1 August and 12 September. For this plot, which includes 3150 data-points (14 local times × 15 points in longitude × 15 points in latitude), we report a correlation coefficient of 0.81, which means that the synthetic zonal and cross-track winds share over 65% of the variance. No bias between the two quantities was detected.

In order to compare the synthetic zonal winds with CHAMP accelerometer-derived cross-track winds, we generated a scatter plot between the two wind estimates (Figure 3.4) that includes data for the 10-day periods listed in Table 3.1. Figure 3.4, consisting of 3150 data-points (14 local times, 15 longitudes, and 15 latitudes), shows strong correlation between synthetic zonal winds and cross-track winds, with r$\sim$0.81. This means that the synthetic zonal and cross-track winds share over 65% of the variance in latitude-longitude structures, with no detectable biases between the two quantities. The large number of points and strong correlation further reassures us of the quality of the synthetic wind product. More comparisons between cross-track winds and synthetic zonal winds are presented in the following sections.

3.6.2 Latitude vs. Longitude

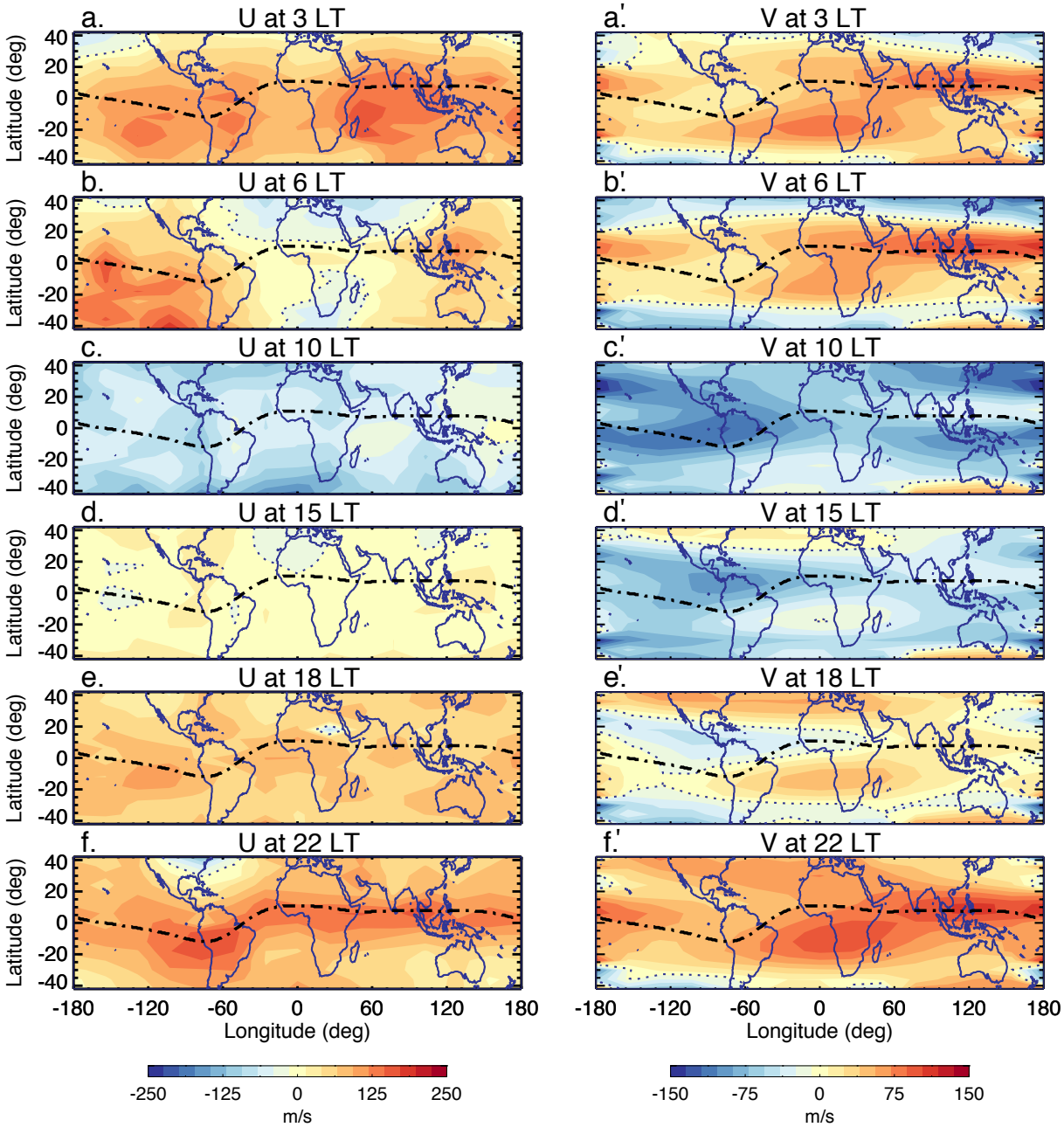

Figure 3.5: Latitude vs. longitude comparisons for synthetic zonal and meridional winds at 3 LT (panels a and a′), 6 LT (panels b and b′), 10 LT (panels c and c′), 15 LT (panels d and d′), 18 LT (panels e and e′), 22 LT (panels f and f′). The dotted line is the geomagnetic equator. Note the significant local time variability in the latitude-longitude wind structures, and the geomagnetic effects in the zonal winds at 22 LT.

A view of the synthetic zonal and meridional winds in a latitude vs. longitude format is offered in Figure 3.5 for a variety of local times, chosen on the basis of displaying the range of structures that exist for a 24-hour LT period during the equivalent day. Figure 3.5 shows significant local time dependency in both zonal and meridional winds. We find eastward zonal winds up to ∼200 m/s in the evening (i.e., 22 LT), and westward winds of ∼100 m/s around noon (i.e., 10 LT and 15 LT). Low-latitude meridional winds are primarily northward at nighttime (from 18 LT to 6 LT) with speeds up to 75 m/s, and become southward around noon (i.e., 10 LT and 15 LT) with speeds of ∼50 m/s. This general behavior in wind structures agrees with what is found by *Luan and Solomon* [2008] in winds extracted from COSMIC radio occultation measurements and estimated by the TIE-GCM. From a closer inspection of Figure 3.5, one can see that at 18 LT (panel e') the meridional flow is mainly directed toward the equator for latitudes ±20° and poleward at higher latitudes (particularly evident for longitudes -180° to 60°), which may reflect the effect of the equatorial ionization anomaly (EIA) on the neutral dynamics. As discussed by Clemmons et al. [2013] [20], heating associated with EIA crests enhances the neutral pressure, and the resulting pressure gradients drive equatorward and poleward flow away from the pressure maxima. Additionally, from Figure 3.5 one can see that the zonal (eastward) winds tend to maximize around the geomagnetic equator (dotted black line), in the evening hours (i.e., 22 LT; panel f). This effect is linked to the evening prereversal enhancement of the vertical plasma drift and the uplifting of the F-region and is discussed below for 19 LT.

Figure 3.6 presents zonal (cross-track, synthetic, and HWM14) and meridional (synthetic and HWM14) winds in a latitude vs. longitude frame at ∼19 LT, for post-sunset conditions. Examining Figure 3.6, we note that (1) synthetic zonal and cross-track winds share the majority of the salient features, with large eastward speeds up to 250 m/s; (2) zonal winds tend to maximize around the geomagnetic equator (black dotted line); and (3) HWM14 zonal winds show similar latitude-longitude patterns, but significantly underestimate the observed speeds.

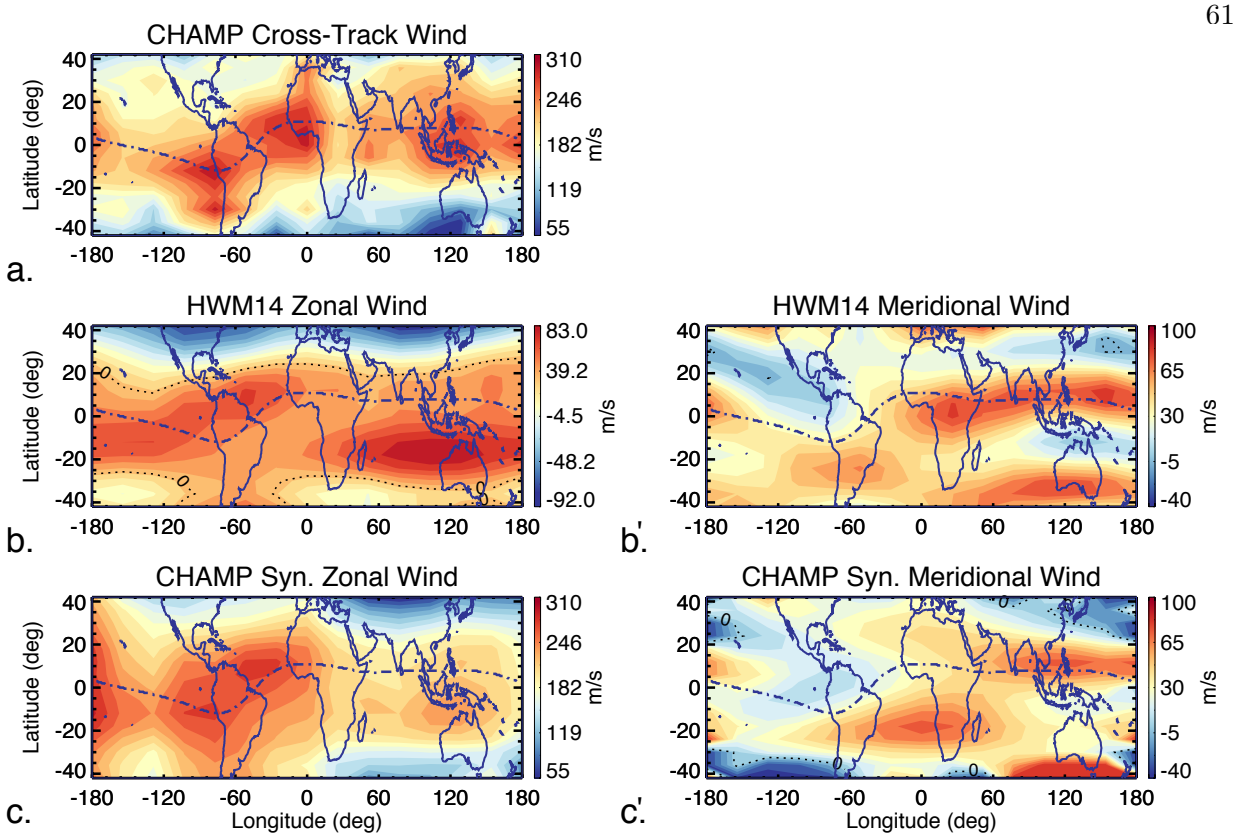

Figure 3.6: Latitude vs. longitude comparisons between CHAMP cross-track wind (panel a), HWM14 zonal (b) and meridional (b′) wind, and CHAMP synthetic zonal (c) and meridional (c′) wind for the 10-day period 12-22 August 2008 at 19 LT. The salient features in the synthetic zonal latitude-longitude wind structures compare well with those found in the cross-track winds. The maxima in zonal winds are located around the geomagnetic equator, with speeds up to 250 m/s. Note the poor comparison with HWM14 winds and the different colorbar scale.

For (1), we note similar latitude-longitude variability in the synthetic zonal winds (Figure 3.6c) and cross-track winds (Figure 3.6a). Eastward winds up to to 250 m/s (similar to Liu et al. [2006] [136] during September equinox for geomagnetically quiet and solar low conditions) found in the synthetic zonal winds around the geomagnetic equator are also present in the cross-track winds. From a closer examination of Figure 3.6, one can see sharper gradients (in both latitude and longitude) for cross-track winds than synthetic zonal winds. This is likely due to the effect of smoothing introduced when calculating pressure gradients from neutral densities prior to calculating

synthetic winds. Comparing panels c and a, one can also see that the synthetic zonal winds in the low-latitude 60^{deg} to 180^{deg} longitude sector are smaller (by up to 20%), than the cross-track winds. This feature is not present for other local times, suggesting that this is not a systematic error in the synthetic zonal winds, but rather a random effect. We also recall that radiation pressure modeling errors in the retrieval of cross-track winds (from accelerometer data) are the largest at dawn-dusk. In addition to larger variances in the cross-track winds, we can also expect greater errors in the derivation of the synthetic winds for dusk conditions. As discussed in Section 3.5, neglecting vertical viscosity in the derivation of synthetic winds causes errors that are generally smaller than 2%. On the other hand, the reduction in ion drag force at dusk (for more details see the following paragraph) together with the small low-latitude Coriolis force, suggests that for this case vertical viscosity could play a larger role [Killeen and Roble, 1984 [104]; Walterscheid and Crowley, 2015 [214]] and be responsible for larger uncertainties in the synthetic winds [Miyoshi et al., 2012 [156]]. Thus some of the differences between the synthetic zonal winds (Figure 3.6c) and the cross-track winds (Figure 3.6a) can be explained by larger variances in both cross-track and synthetic winds around dusk.

Regarding (2), Figure 3.6a and 3.6c shows a clear enhancement in the eastward winds around the geomagnetic equator. This strong low-latitude eastward jet is typical for post-sunset hours (i.e., 19 LT), and is due to the combined effect of intensified eastward ion drifts due to vertical electric fields and the rapid increase in height of the ionosphere driven by the evening prereversal enhancement of the vertical plasma drift. Zonal winds in the low-latitude F-region evening ionosphere generate nearly vertical electric fields (polarization electric fields) that cause the ionospheric plasma to drift in the zonal direction with a velocity approaching that of the neutral wind [Rishbeth, 1971 [187]; Miyoshi et al., 2012 [156]]. This motion of the plasma together with the neutrals drastically reduces the ion drag, which opposes the pressure gradient and acts to limit the wind speed. At low latitudes, where the Coriolis force is small and the balance is mainly obtained between pressure gradient and ion drag, the reduction in ion drag associated with the post-sunset uplifting of the F-layer results in enhanced eastward wind speeds. This phenomenon occurs toward sunset,

because this is when the pressure gradient force increases in the eastward direction. Richmond et al. [1992] [182] demonstrated that both the uplift of the ionosphere due to the prereversal enhancement [Anderson and Roble, 1974 [1]], and the small difference between the neutral wind and the plasma drift [Rishbeth, 1971 [187]] are responsible for the strong eastward wind in the evening. The west-to-east prevailing wind motion of the upper atmosphere, that is both longitude and diurnal mean, is referred to as 'superrotation' [King-Hele, 1964 [105]]. King-Hele and Walker [1983] [106] estimated from satellite orbital analysis superrotation speeds of 100 m/s, whereas Wharton et al. [1984] [220] found speeds of 20 m/s in Dynamics Explorer 2 (DE-2) data at high solar flux level, and more recently Rishbeth [2002] [189] calculated values of 47 m/s using the TIE-GCM model. Using CHAMP data at 400 km, Liu et al. [2006] [136] found the superrotation speed to be highly dependent on solar flux level, geomagnetic conditions, and season, with speeds ranging from 10 m/s during solar low and geomagnetic quiet conditions to 60 m/s for solar high and geomagnetically perturbed days. The latitudinal variation of diurnally and longitudinally averaged synthetic zonal winds for the equivalent day is shown in Figure 3.7. We note the bell-like distribution partly skewed towards the south hemisphere (probably due to the use of geographic instead of geomagnetic coordinates), with maxima around the equator. From Figure 3.7 we report superrotation speeds of ∼27 m/s, significantly larger than the 11 m/s found by Liu et al. [2006] [136] for similar geophysical conditions (summer solstice, solar minimum, and geomagnetically quiet conditions). This apparent inconsistency is likely due to the different method used by Liu et al. [2006] [136] to derive zonal winds from accelerometer measurements compared to the Doornbos et al. [2010] [28] method used in this work. Liu et al. [2006] [136] used a direct approach, where the lift and sideways forces are neglected or are modeled and removed from the acceleration beforehand, so that only the observed acceleration due to drag remains. While Doornbos et al. [2010] [28] used an iterative approach, where an algorithm is used to make the modeled aerodynamic acceleration match the direction and magnitude of the aerodynamic acceleration observed by the accelerometer. Doornbos et al. [2010] [28] reports significant error reduction through the iterative method. Additionally, amplitude suppression caused by the ∼130-day averaging performed by Liu et al. [2006] [136] could play a role.

The superrotation speeds found in this study are in reasonably good agreement with those reported by Richmond et al. [1992] [182], Fuller-Rowell et al. [1997] [58], and Rishbeth [2002] [189] using model simulations.

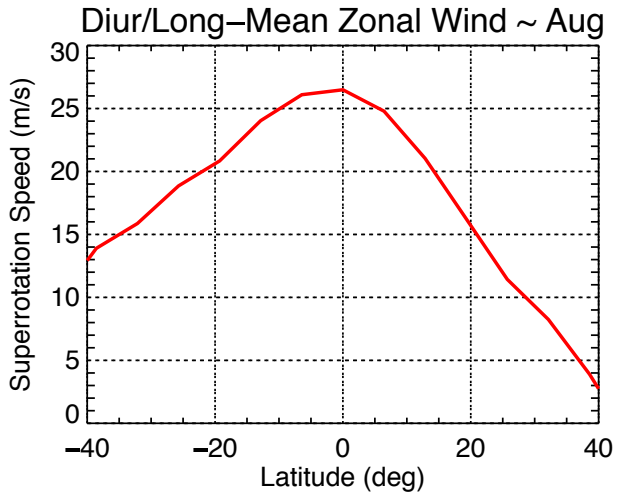

Figure 3.7: Diurnal and longitude mean zonal winds ('superrotation') for the equivalent day as a function of latitude. Note the peak around the equator with maximum of 27 m/s.

With respect to (3), note that HWM14 zonal winds (Figure 3.6b) largely underestimates CHAMP synthetic zonal (Figure 3.6c) and cross-track (Figure 3.6a) winds. HWM zonal winds show similar latitude-longitude structures, but with speeds less than ~50% of those observed from CHAMP. This is not surprising considering that HWM wind estimates at 300 km are primarily based on DE-2s WATS measurements taken between August 1981 to February 1983 [Hedin et al., 1991 [81]]. Since the majority of DE-2 measurements were made at solar maximum, the model values are less representative for low solar flux levels, leading to large differences with CHAMP observations [Liu et al., 2006 [136]]. Additionally, the DE-2 orbit was such that it took it one year to cover all local times, hence season and local time are locked, with dawn-dusk coverage only in early summer and winter months [Coley et al., 1994 [21]]. Thus, since Figure 3.6 refers to the 10-day period 12-22 August 2008, limited DE-2 sampling could explain the model errors. Some of the differences are also likely due to vertically propagating waves measured by CHAMP, but not

captured by the empirical model. On the other hand, HWM meridional winds compare well with the synthetic winds both in speed and latitude-longitude structures (Figure 3.6b′ and 3.6c′). The following sections offer more comparisons of CHAMP synthetic winds with HWM14 and CHAMP cross-track winds.

3.6.3 Latitude vs. Local Time

A different perspective on the winds can be obtained by looking at a latitude vs. local time frame. In such a frame one can study the local time variability for a single longitude or as a longitude mean. Figure 3.8 shows longitudinally-averaged ($\overline{U}$ and $\overline{V}$) latitude vs. local time structures in synthetic zonal and meridional winds, HWM14, and cross-track winds. Panels a and a' show 130-day means (130 days are used to resolve the full 24-hour local time variability) for the synthetic zonal and meridional winds, respectively. Panels b and b' show zonal and meridional synthetic winds for the equivalent day; whereas panels c and c' show HWM14 zonal and meridional winds and panel d illustrates cross-track winds for the same equivalent day. As discussed in Section 3.6.2, we found large local time variability in both zonal and meridional winds. Eastward winds up to ∼250 m/s and northward winds up to ∼100 m/s are found at nighttime (with maxima at 2 LT). Westward winds up to ∼100 m/s are found around noon (i.e., 10-16 LT), when meridional winds of ∼45 m/s are mainly southward. Figure 3.8 (panels a and b) also shows the smoothing effect of 130-day averages on the zonal wind, with speeds reduced by up to 30% when compared to the ∼40-day means. On the other hand, Figure 3.8 (panels a' and b') also shows that 130-day average meridional wind has similar speeds to the 40-day averages (or even larger wind speeds for 8-16 LT). Note that any difference between the local time-latitude distribution of cross-track wind presented by *Liu et al.* [2006] and what shown by Figure 3.8 can be explained by the different method adopted by Liu et al. [2006] [136] (direct approach vs. iterative approach). Additionally, Figure 3.8 shows that HWM14 fails to reproduce most of the observed local time and latitude variability in the winds. Similar conclusions can be drawn for latitude vs. local time wind structures at specific longitudes, but these results are not shown here.

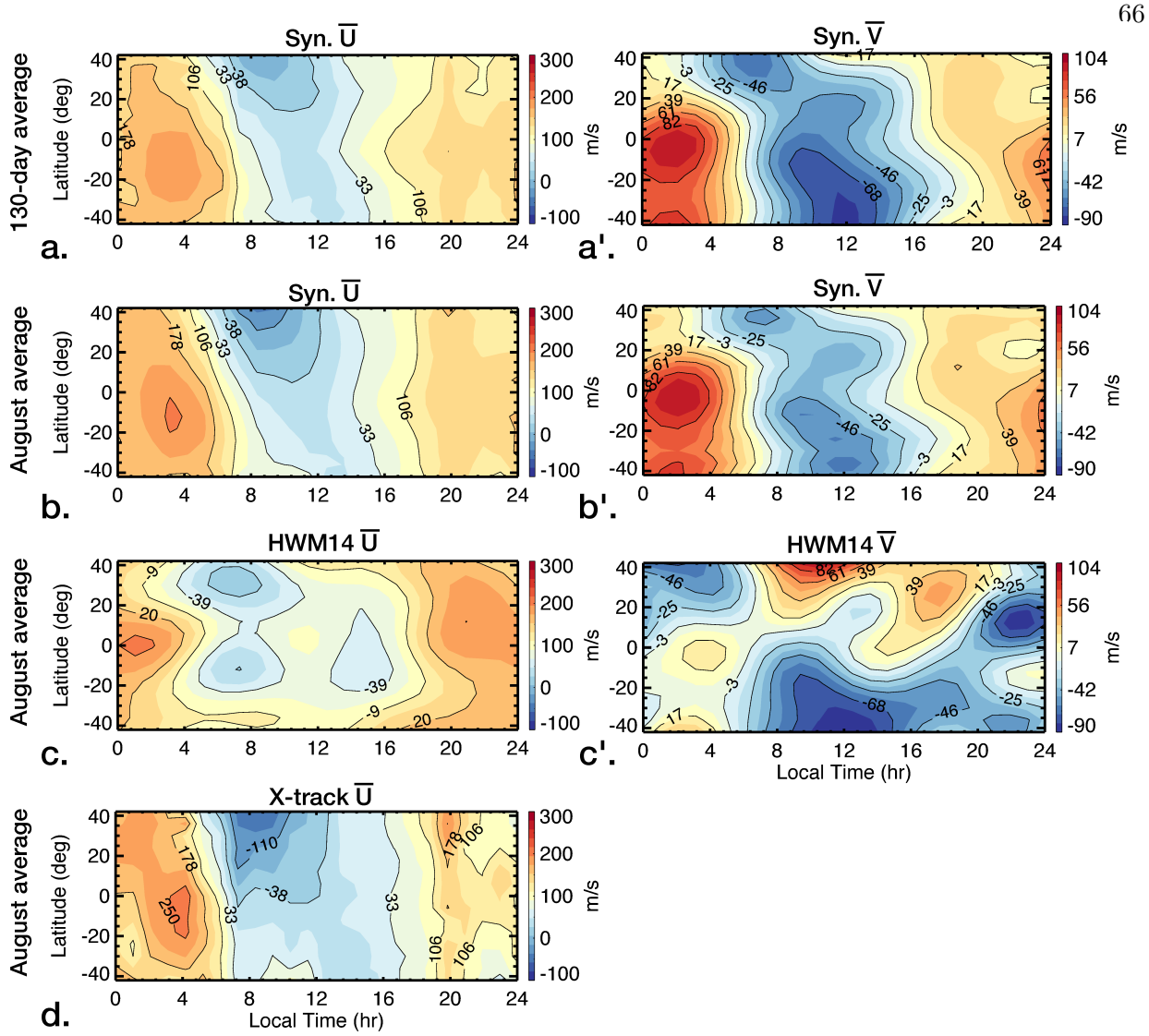

Figure 3.8: Latitude vs. local time plot of 130-day mean and ∼40-day mean (equivalent day) synthetic zonal (panels a and b) and meridional (panels a′ and b′) winds, 40-day mean HWM14 zonal (c) and meridional (c′) winds, and 40-day mean (equivalent day) cross-track (d) winds. Note the many similarities between synthetic zonal and cross-track winds, with HWM14 winds differing significantly from CHAMP synthetic and cross-track winds.

3.6.4 Local Time vs. Longitude

New insights on thermospheric winds can also be acquired by analyzing wind structures in a local time vs. longitude frame at a fixed latitude. This frame of reference is preferential to

investigate the presence and effect of atmospheric tides

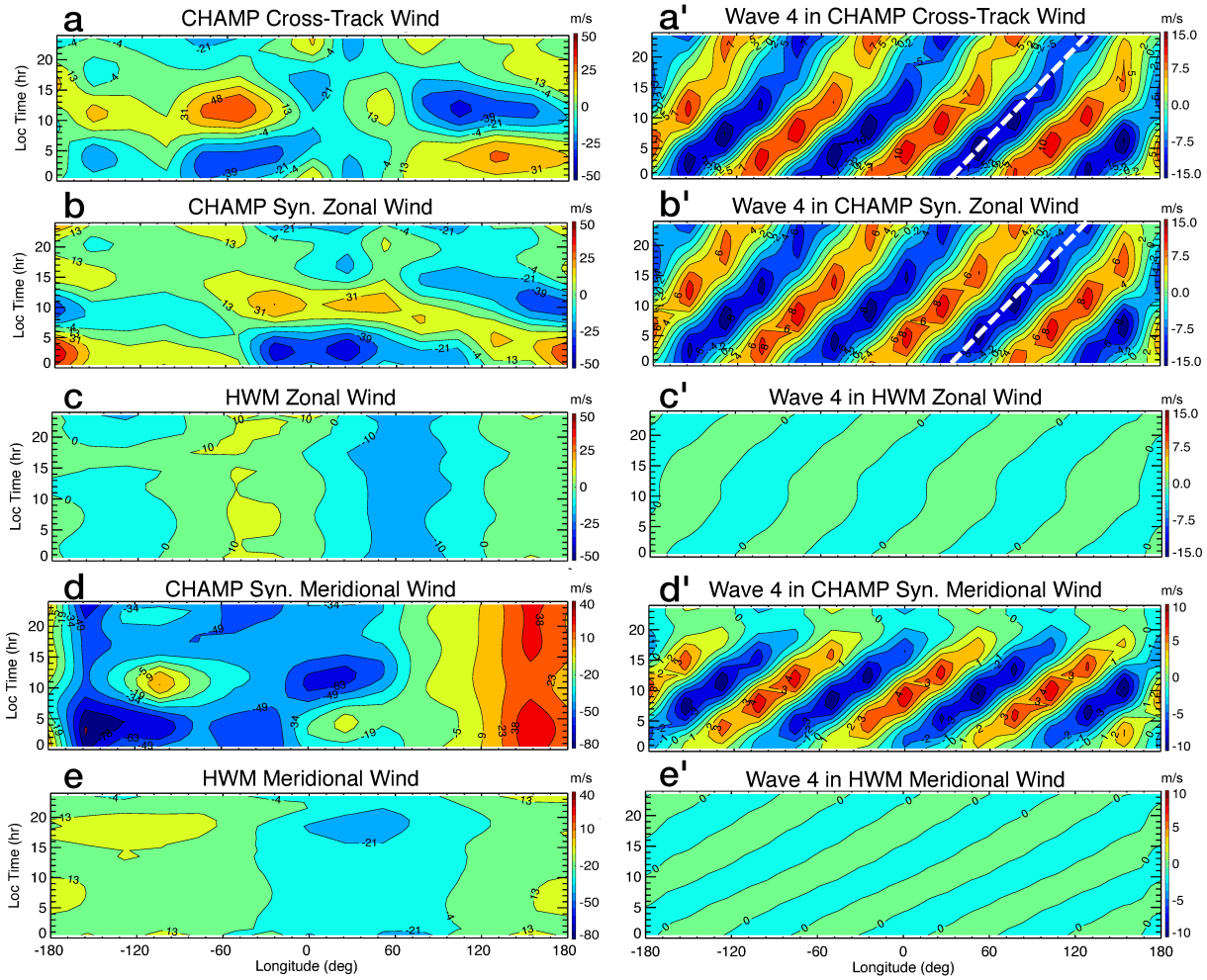

Figure 3.9: Local time vs. longitude structures in cross-track winds (panel a), synthetic zonal winds (b), HWM14 zonal winds (c), synthetic meridional winds (d), and HWM-14 meridional winds (e) for the equivalent day. Panels a′-e′ show the wave-4 component of each plot in panels a-e. The zonal mean was removed from panels a-e to help the comparison. Note the poor comparison with HWM, which shows very little longitude variability. The white dashed line (a′ and b′) shows eastward propagation of ∼90° in 24-hr LT, consistent with DE3.

Figure 3.9 (panels a-e) shows a comparison of synthetic, cross-track, and HWM14 winds in a local time vs. longitude frame at the equator, for the 43-day equivalent day. Cross-track and synthetic equatorial zonal winds agree for the majority of the observed longitude and local time

variability and show evidence of strong diurnal and semi-diurnal components. Both zonal and meridional wind estimates from HWM14 poorly replicate the longitude and local time variability observed in CHAMP. Analyzing the local time vs. longitude structures for the equivalent day, we found evidence of a strong wave-4 signal in both the zonal and meridional winds (Figure 3.9a′ and Figure 3.9e′). Wave-4 amplitudes of ∼12 m/s (∼14 m/s) in synthetic zonal (cross-track) winds and ∼10 m/s in synthetic meridional winds are found. Among the non-Sun-synchronous (non-migrating) tidal components, DE3 and SE2 are some of the largest wave components in the MLT. From a Sun-synchronous satellite perspective, DE3 and SE2 produce 4 longitudinal peaks, and are the main contributors to the wave-4 structure observed in the ionosphere [i.e., England et al., 2006 [36]; Lin et al., 2007 [123]; Pedatella et al., 2008 [176]], and thermosphere [i.e., Hagan et al., 1997 [71]; Hagan and Forbes, 2002 [72]; Oberheide et al., 2011b [165], Gasperini et al., 2015 [61]]. The local time vs. longitude pattern of wave-4 in zonal winds shows clear eastward propagation of ∼90° in 24-hr LT, as indicated by the white guiding line. This phase propagation is indicative of the presence of the nonmigrating tide DE3, and thus suggests DE3 to be the cause for the observed wave-4 structure in the zonal wind. Wave-4 in meridional winds propagates ∼120° to the East in 24-hr LT, and can be explained by the presence of both SE2 and DE3. The following section shows the latitudinal profile of DE3 and SE2 extracted from CHAMP winds, along with comparisons with the Climatological Tidal Model of the Thermosphere (CTMT) [Oberheide et al., 2011a [163]].

3.6.5 Example of Wave Decomposition

By analyzing local time vs. longitude equatorial wind structures for the 43-day equivalent day, we determined wave-4 to be the largest oscillation in zonal winds and among the largest in meridional winds (only surpassed by wave-1), and suggested a link to DE3 and SE2. The presence of a strong wave-4 in the neutral atmosphere is known to impose significant longitudinal variability in the ionosphere, either by modulation of the E region dynamo and F region fountain [Sagawa et al., 2005 [195]; Immel et al., 2006 [91]], or by direct penetration into the F region [Forbes et al., 2009 [54]; Häusler and Lühr, 2009 [78]; Oberheide et al., 2009, 2011a [164][163]; Talaat

and Lieberman, 2010 [204]]. Using F2-layer peak density and the peak height extracted from the COSMIC data set, He et al., [2011] [80] found that the generally accepted mechanism of DE3 modulation of E region dynamo only accounts for the daytime symmetric components, while the antisymmetric components are likely due to transequatorial neutral winds associated with the SE2 tide. Meridional SE2 winds transport plasma along geomagnetic field lines upwards (downwards) in the upwind (downwind) hemisphere, thus raising the F2-layer peak height at the upwind side and lowering it at the downwind side [Rishbeth, 2000 [188]], causing ionospheric asymmetry. Oberheide et al. [2011b] [165] originally anticipated the role of SE2 meridional winds in producing ionospheric asymmetries about the equator.

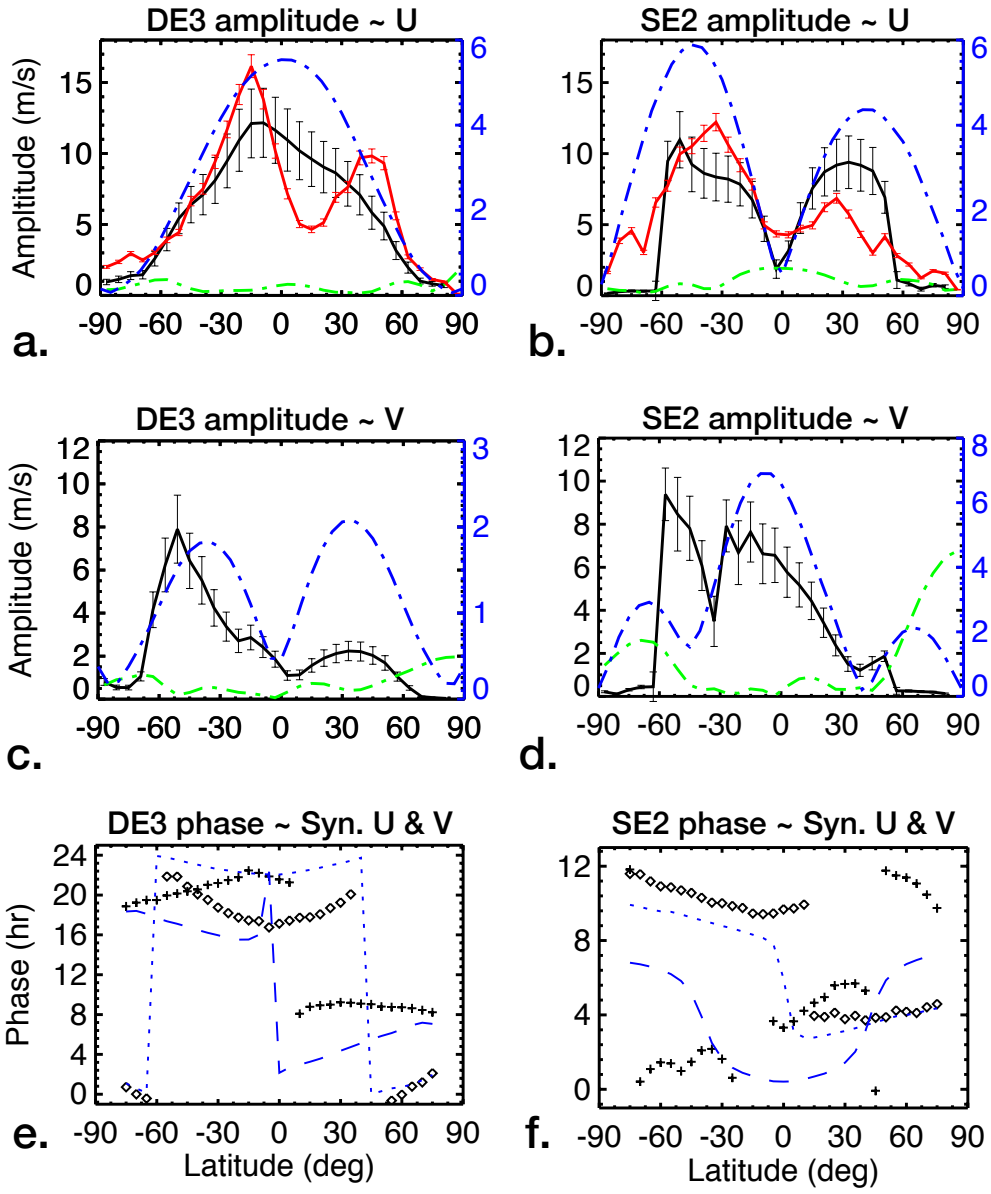

Figure 3.10: (a) and (b). Latitudinal profile of DE3 and SE2 in zonal winds for the equivalent day; (c) and (d) are the same as (a) and (b), but for meridional winds; (e) and (f) the latitudinal profile for both zonal and meridional winds of DE3 and SE2, respectively. In (a)-(d), the black line refers to synthetic winds, the red line to cross-track winds, the green line to HWM14 winds, and the blue line shows the amplitude of DE3 and SE2 in CTMT winds for August at 300 km (note the blue y-axis on the right side of each plot). In (e) and (f), black crosses (squares) represent synthetic zonal (meridional) wind phases, while the dotted (dashed) blue line shows CTMT zonal (meridional) wind phases. Error bars are included for synthetic and cross-track wind amplitudes, with estimated errors of ∼20% and ∼5%, respectively. Note the small amplitudes in HWM-14 and significant departure of DE3 and SE2 latitudinal structures from that of CTMT.

Figure 3.10 shows DE3 and SE2 amplitudes and phases as a function of latitude in synthetic winds (black line), cross-track winds (red line), and HWM14 winds (green line), retrieved from least square fitting the local time vs. longitude at different latitudes for the 43-day equivalent day. DE3 and SE2 amplitudes in zonal and meridional winds according to CTMT are also plotted (blue line). CTMT is an empirical thermospheric model of upward propagating migrating and nonmigrating diurnal and semidiurnal tides. It provides amplitude and phase for each tidal perturbation from 80 to 400 km and pole-to-pole, and is based on HMEs fits to SABER-measured MLT temperatures and winds for the years 2002 to 2008 [Oberheide et al., 2011a [163]]. As shown in Figure 3.10, we found DE3 maxima of ∼12 m/s in equatorial zonal winds and ∼8 m/s in meridional winds around 45°S, while SE2 reaches maxima of ∼10 m/s in mid-latitude zonal winds and ∼8 m/s in equatorial meridional winds. These amplitudes of DE3 in the zonal winds (i.e., 12 m/s) are comparable to those found by Häusler and Lühr [2009] [78] for August in similar geophysical conditions.

Further analyzing Figure 3.10, one can see similarities between the latitudinal profile of DE3 and SE2 amplitudes and phases in synthetic winds and the amplitudes predicted by CTMT. For the amplitudes, we find one major peak centered around the equator in DE3 zonal winds, two 'symmetric' peaks at low latitudes (±45°) in SE2 zonal winds and DE3 meridional winds, and one major peak around the equator and two secondary peaks at higher latitudes (±60°) in SE2 meridional winds. For the phases, DE3 zonal (meridional) winds are mostly symmetric (anti-symmetric) about the equator, whereas SE2 zonal winds are mostly anti-symmetric and SE2 meridional winds have a more complex latitudinal structure. More interestingly though, we also find large differences between SE2 and DE3 in CHAMP winds and those predicted by CTMT. First, the amplitudes of DE3 and SE2 in CTMT winds are ∼50-70% smaller than the ones found in CHAMP (note the different y-axis for CTMT); this effect is likely due to amplitude suppression caused by CTMT's multi-year averaging. Second, the latitudinal shape of observed DE3 and SE2 is significantly different from that of CTMT. To understand the cause of this difference we need to consider that CTMT tidal predictions at 300 km are based on the vertical extrapolation of HMEs, and neglects any tide-mean flow interactions (or nonlinear wave-wave interactions). As shown in Figure 3.10a,

DE3 in zonal winds is dominated by its hemispherically symmetric mode, consistent with what is found by Truskowski et al. [2014] [209] at the base of the thermosphere (110 km). DE3 is known to be generated in the tropical troposphere by latent heat release, and its first symmetric mode (which is a Kelvin wave) has been shown to propagate high into the thermosphere due to its vertical wavelength of ∼56 km [Oberheide et al., 2011a [163]]. A careful analysis of Figure 3.10*a* also reveals the presence of a non-negligible anti-symmetric component of DE3 zonal winds (the amplitudes are party skewed toward the southern hemisphere). Looking at panel *c*, we find DE3 in meridional winds to be not purely anti-symmetric (as predicted by HMEs, and shown by CTMT), but significantly skewed towards the southern hemisphere (similarly to DE3 in zonal winds, and SE2 in meridional winds). One possible explanation for the presence of this anti-symmetric component is given by mode coupling, wherein a given mode (i.e., symmetric mode) interacts with the mean flow to contribute to the generation of other modes (e.g., anti-symmetric modes). Despite mode coupling, individual modes tend to retain their properties in terms of vertical propagation [Lindzen, 1977 [132]]. The first anti-symmetric mode of DE3 has a vertical wavelength of ∼30 km [Truskowski et al., 2014 [209]], and does not propagate to CHAMP heights. Thus, if DE3 is symmetric at ∼100 km, then its distortion is due to mode coupling occurring between ∼100 km and ∼300 km. We know that for eastward propagating waves (such as DE3 and SE2), the frequency is Doppler-shifted to higher absolute values in regions of westward wind and to lower absolute values in regions of eastward wind. In regions where dissipation is important, waves with large Doppler-shifted frequency are less effectively damped than those with smaller Doppler-shifted frequency; thus a wave exhibits larger amplitudes if Doppler-shifted to higher absolute frequencies. With this in mind, our results would indicate the presence of stronger eastward winds in the northern hemisphere, or westward winds in the southern hemisphere, in the ∼100-300 km height region (refer to the TIME-GCM results in Chapter 6). The situation is more complicated for SE2, which can be generated in-situ by nonlinear interactions between DE3 and DW1 [Oberheide et al., 2011a [163]], in addition to propagating upwards from lower altitudes.

3.6.6 Seasonal and Local Time Variability

In this section we provide a small sampling of latitude-longitude wind structures obtainable from the CHAMP database to provide a perspective on potential scientific applications not directly addressed in this paper. We begin by demonstrating that both the latitude-longitude variation and magnitude of the winds highly depend on season and local time. Figure 3.11 shows latitude-longitude structures in synthetic zonal wind for the months of March, June, September, and December at 0 LT, 6 LT, 12 LT, and 18 LT, and give an overview of seasonal and local time dependency of the winds for low solar flux levels and geomagnetic quiet conditions. Note the significant seasonal dependency in the longitudinal structures, with the strong presence of wave-1 in March (0 LT and 12 LT), wave-2 in March (6 LT and 18 LT), September (5 LT, 13 LT, and 17 LT) and December (6 LT, 11 LT, and 23 LT), and wave-4 in September (1 LT and 5 LT). Various tidal perturbations can generate a wave-2 longitude structure in the zonal winds (i.e., DW3, DE1, SW4, S0, and SPW2). Forbes et al.'s [2014] [53] findings indicate that SW4 is likely the main contributor to the observed wave-2 structure. This non-migrating tidal component is also known to maximize around September-March [Forbes et al., 2014 [53]], thus explaining the strong wave-2 in March, September, and December. For September at 1 LT (which refers to the 10-day period 25 August - 5 September 2007) we see the clear presence of wave-4 around the equator (i.e., DE3) and at mid low-latitudes (i.e., SE2, with greater amplitudes in the south hemisphere, consistent with what is shown in Figure 3.10). A rather common feature in the seasonal variation is that the average wind velocities (both eastward and westward) are about 20-30% smaller around December than in other seasons. This is particular evident for 11 LT and 18 LT, with speeds of $\pm$100 m/s in March/June, but limited to $\pm$50-70 m/s in December.

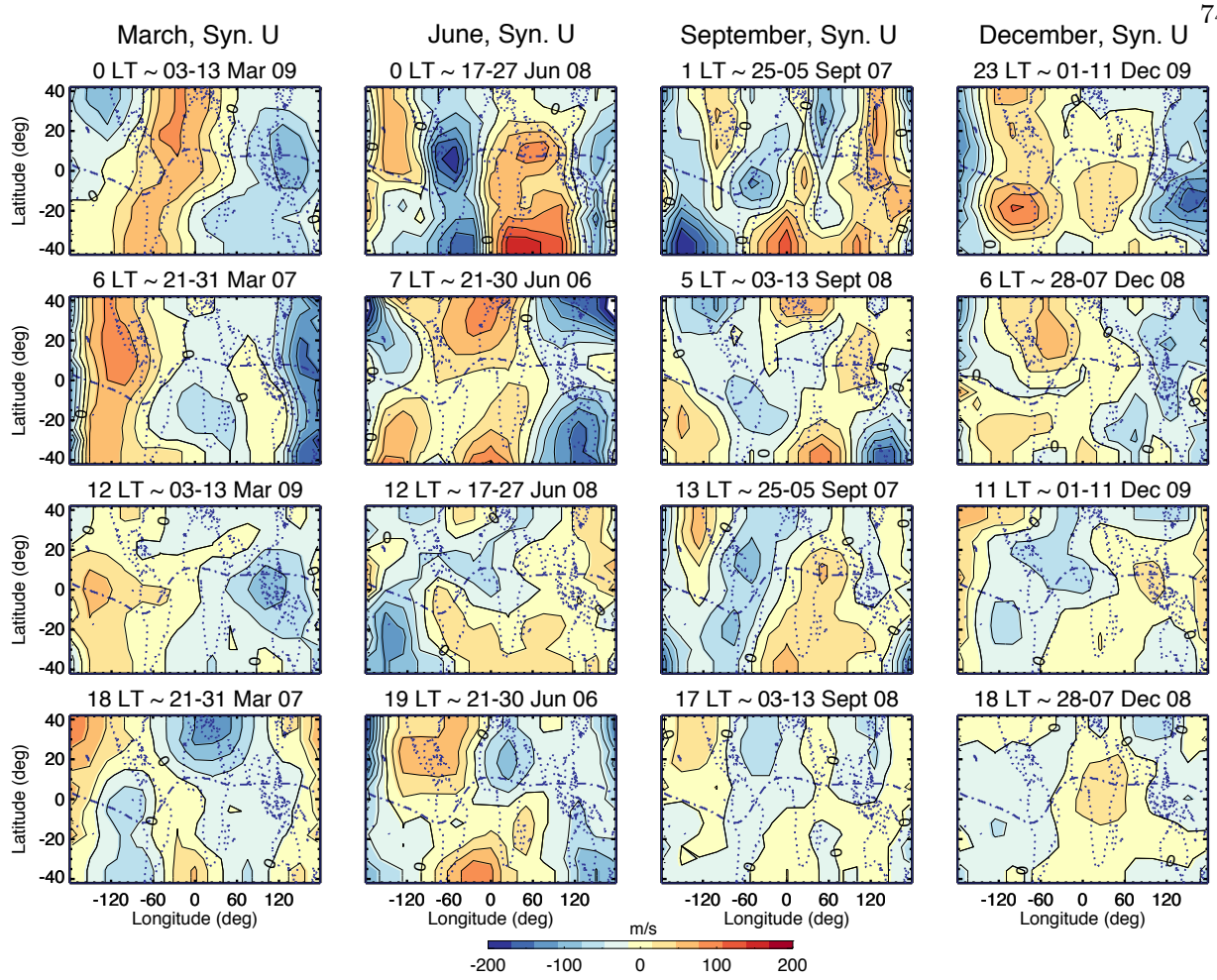

Figure 3.11: Latitude-longitude structures in the synthetic zonal wind for the months of March, June, September and December around noon (i.e., 12 LT), midnight (i.e., 0 LT), dawn (i.e., 6 LT), dusk (i.e., 18 LT). Note strong seasonal and local time variability in the winds, and the significant presence of wave-2, wave-3, and wave-4.

The meridional latitude-longitude wind structures (Figure 3.12) show significant dependency on local time, similarly to the zonal winds, but not much variability with season. For all seasons, at dusk (i.e., 18 LT) the winds tend to be southward in the south hemisphere and northward in the north hemisphere, while this pattern is reversed at dawn (i.e., 6 LT). The midnight meridional winds possess little longitudinal variability, and are mainly northward at low-mid latitudes ($\pm 25^\circ$) for all seasons but December (when they are southward). Note how the the absolute speeds of the meridional winds is generally $\sim \pm 100$ m/s.

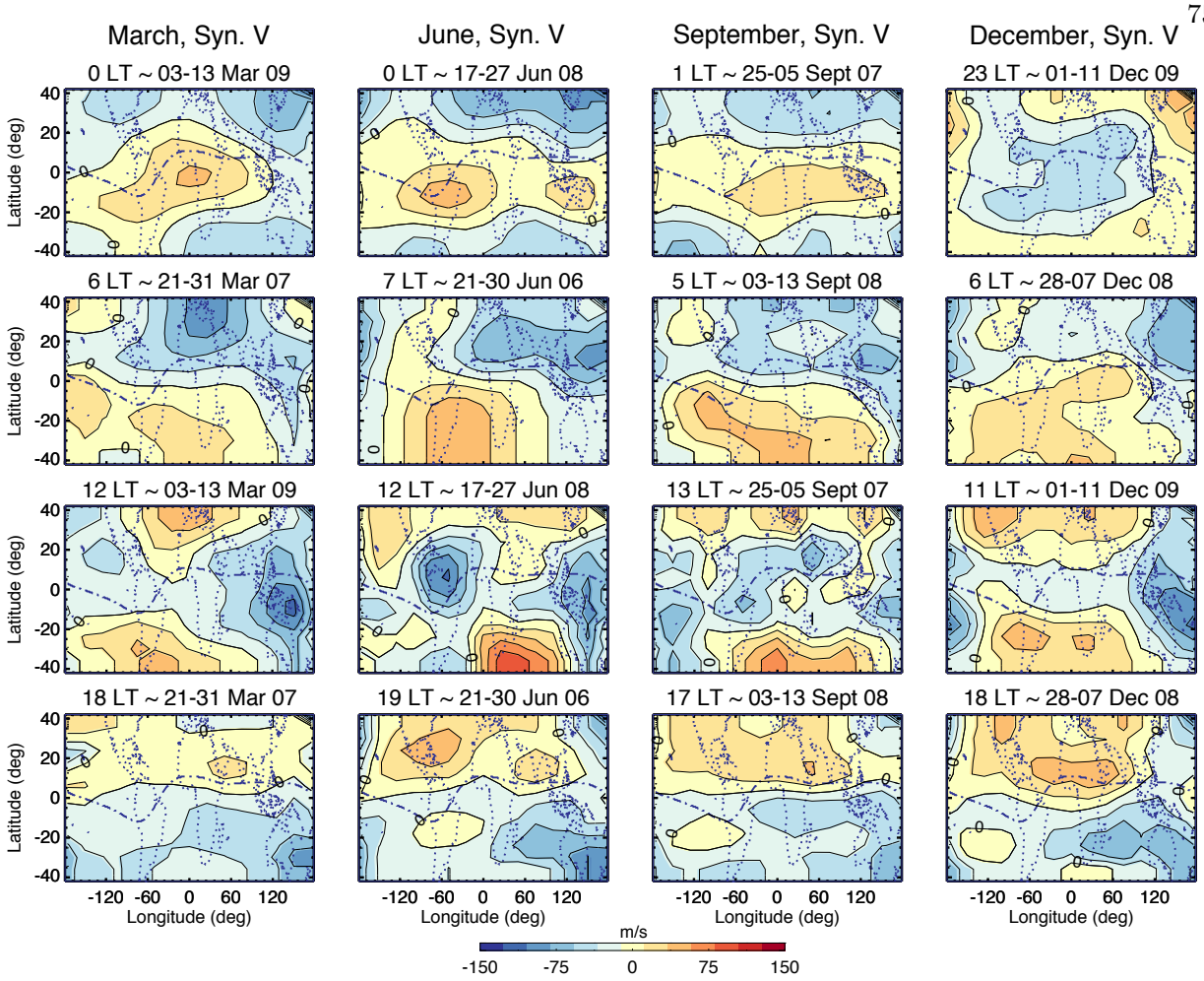

Figure 3.12: Similar to Figure 3.11, but for meridional synthetic winds. The seasonal dependency in the meridional winds is not as strong as for the zonal winds. Note the strong longitudinal wave-1 structure, and absence of wave-3 and wave-4 structures.

As one can see by comparing Figure 3.12 with Figure 3.11, the latitude-longitude structures in meridional winds are simpler compared to those present in the zonal winds. The longitudinal structure of the meridional winds (Figure 3.12) does not possess much wave-3 and wave-4, and is dominated by wave-1 for most seasons and local times. This is similar to what is found by Clemmons et al. [2013] [20] in meridional winds derived from Streak ionization gauge measurements. The small wave-3 and wave-4 can be explained by the fact that DE2 and DE3 are quasi-Kelvin waves, and thus are known to have substantially smaller meridional winds than zonal winds. From a nearly

fixed local time perspective, several tidal perturbations can be responsible for a wave-1 longitude modulation (all the ones with the same |s-n|, as discussed in Section 6.4): SPW1, D0, DW2, SW1, and SW3. We know that SPW1 modulation of DW1 (n = 1, s = 1) yields the secondary products D0 (n = 1, s = 0) and DW2 (n = 1, s = 2), and that SPW1 modulation of SW2 (n = 2, s = 2) yields the secondary products SW1 and SW3 [Forbes et al., 2012 [48]]. Thus, if the meridional winds have large DW1 and SW2 in the geographic frame, and this structure is tilted into the geomagnetic frame, then we can expect D0, DW2, SW1 and SW3 to be significant components in a geographic frame perspective. A combination of these tidal perturbations due to the effects of the magnetic field is likely to be responsible for the observed wave-1 structure shown in Figure 3.12.

3.7 Summary and Conclusions

The neutral wind field is a fundamental parameter defining the state and dynamics of the ionosphere-thermosphere system, yet global-scale wind measurements are scarce. Vertical and horizontal winds are responsible for redistributing chemical species, and altering the bulk temperature field through adiabatic heating and cooling. Zonal winds are responsible for the generation of electric fields via the F-region dynamo mechanism, while meridional winds modify the ionosphere by moving plasma up and down magnetic field lines.

CHAMP's slowly precessing orbit provides a unique perspective and different types of insights into the dynamics of the thermosphere than those obtainable from the ground. In this work, we used neutral and electron densities measured by the CHAMP satellite around 300-350 km to derive pressure gradients and ion drag values. We then solved the horizontal momentum equations of the thermosphere for solar low and geomagnetically quiet conditions to infer zonal and meridional winds. We limited our analyses to mid-low latitudes (±45°), where winds driven by convection electric fields are generally negligible. To provide reassurance on the credibility of the derived wind field, we validated our methodology by showing that neutral and electron densities output from the NCAR TIME-GCM model can be used to derive solutions to the momentum equations that well replicate (with uncertainties up to ∼15%) the winds self-consistently calculated within TIME-

GCM. We estimated the total uncertainty in the synthetic winds to be ∼±30%, mainly due to errors in the derivation of ion drag (∼ ±14%) and pressure gradient (∼ ±4%) from CHAMP electron and neutral densities. We also compared latitude-longitude synthetic wind structures with CHAMP cross-track winds and found that they share over 65% of the variance, with no detectable bias. We then used synthetic winds to highlight the longitude, latitude, local time, and seasonal variability and presented comparisons with CHAMP cross-track and HWM14 winds in various formats. The main findings from these analyses can be summarized as follows:

- We found evidence of a strong eastward jet in the post-sunset hours around the geomagnetic equator due to decreased ion drag associated with the combined effect of intensified eastward ion drifts due to vertical electric fields and the rapid increase in height of the ionosphere driven by the evening prereversal enhancement of the vertical plasma drift. We also calculated superrotation speeds of 27 m/s at the equator.

- We found that the HWM14 empirical model largely underestimates (by over ∼50%) the latitude, longitude, and local time variability in CHAMP synthetic winds. This is likely due to DE-2's poor sampling at solar minimum and the presence of upward propagating tides not captured by the empirical model.

- We found evidence of vertical wave coupling due to DE3 and SE2, with maximum amplitudes of ∼12 m/s in zonal winds (DE3) and ∼9 m/s in meridional winds (SE2). Significant asymmetry in the latitudinal variation of DE3 and SE2 are consistent with the presence of higher order modes likely due to the effect of mean winds.

- We found large low-latitude meridional SE2 winds, with amplitudes greater than 8 m/s. These results are supportive of Oberheide et al.'s [2011b] [165] and He et al.'s, [2011] [80] theories that SE2 transequatorial neutral winds are responsible for the anti-symmetric component of the ionospheric wave-4.

- We found strong seasonal and local time dependency in both zonal and meridional winds.

Zonal winds show significant latitude-longitude variability for all seasons and local times, whereas meridional winds feature a simpler longitude structure dominated by wave-1. This is explained as due to the combined effect of small DE3 and SE2 meridional winds (both are quasi-Kelvin waves), and the SPW1 modulation of DW1 and SW2 associated with the displacement between geographic and geomagnetic coordinate systems.

Chapter 4

VERTICAL WAVE COUPLING FROM TIMED AND GOCE

The vertical propagation of waves is the main coupling process in the atmosphere. By conveying momentum from lower altitudes (i.e., troposphere, stratosphere, mesosphere) to high altitudes (i.e., thermosphere) waves link different altitude regimes in Earth's atmosphere. The importance of wave coupling on the dynamics of the thermosphere system was reviewed in Chapter 1, while an example of wave coupling through CHAMP-derived synthetic winds was presented in Chapter 3. In this chapter, TIMED-SABER temperature measurements at 110 km and GOCE neutral density and cross-track wind measurements around 260 km are employed to reveal the vertical coupling of waves during 2010-2012 for solar low and geomagnetic quite conditions. For this 3-year period, DE3 and a 3-day UFKW are found to be prominent oscillations in both the lower and middle thermosphere.

Chapter 4 is organized as follows: Section 4.1 contains an overview of thermospheric variability produced by DE3 and UFKW coupling; Section 4.2 reviews the data and methods herein adopted; Section 4.3 (1) presents evidence of the vertical propagation of DE3 and UFKW over daily and monthly time scales, (2) discusses their seasonal and interannual variability, and (3) investigates the effect of solar radiation on the vertical propagation; while Section 4.4 summarizes the main conclusions obtained with this study.

Some of the contents of this chapter are derived from the JGR Space Physics paper issued online on 24 August 2015 and referenced in the Bibliography as Gasperini et al., 2015 [61].

4.1 Introduction

In the past decade a lot of progress has been made on improving our understanding of what are the main tidal components, their climatology (i.e., month to month variability, see Truskowski et al., [2014] [209]), what waves are capable of propagating into the thermosphere [e.g., Forbes et al., 2014 [53]; Oberheide et al., 2009, 2011 [164][165]], and what subset of these waves are primarily excited in the troposphere [e.g., Zhang et al., 2010a,b [226][228]]. This has been made possible thanks to very large amount of data collected by the TIMED, CHAMP, GRACE, and GOCE satellite missions. As already extensively discussed in Chapters 1-3 a topic of wave coupling research that still requires significant advancement is the study of short-term (days to weeks) variability of atmospheric tides. From ground-based observations we know that the day-to-day variability of tides is significant, but attributing this variability to specific tidal components on a global basis is made impossible due to (a) the sparse latitude-longitude distribution of ground-based observing sites, and (b) the slow local time precession of single satellites, such that only tidal fields averaged over 60 days or more can be retrieved. For these reasons, there is still a lack of understanding on how tides vary globally on day-to-day and weekly time scales. As explained below, this study takes advantage of a method to extract tides on a daily basis and reveal wave coupling on short time scales.

Analyzing SABER temperatures at 110 km and GOCE densities and cross-track winds around 260 km during 2010-2012, the highest-impact global waves in the spectrum are found to be DE3 and a 3-day UFKW. DE3 is a large source of variability in the MLT and is sometimes the single largest tidal component above the mesopause [Forbes et al., 2008 [42]; Oberheide and Forbes, 2008 [162]; Mukhtarov et al., 2009 [159]; Pancheva and Mukhtarov, 2010 [173]], and the main sources of the longitudinal wavenumber-4 structure in the ionosphere [Immel et al., 2006 [91]]. DE3 is excited in the tropical troposphere by latent heat release in deep convective clouds [Hagan et al., 1997 [71]; Hagan and Forbes, 2002 [72]; Oberheide et al., 2011 [165]]. Its first symmetric mode (Kelvin wave) is the largest component [Truskowski et al., 2014 [209]] and is known to propagate higher into the thermosphere due to its vertical wavelength of ∼56 km [Oberheide et al., 2011 [165]]. The strongest

DE3 tends to occur during July-November with maximum eastward winds near the equator of 15 m/s [Talaat and Lieberman, 1999 [203]; Forbes et al., 2003b [55]]. DE3 also affects the mean states of the ionosphere and thermosphere. Forbes et al. [1993] used the NCAR TIGCM to simulate tidal influence on ionosphere and thermosphere and found that the upward propagating migrating tides can accelerate, heat, and mix composition in the coupled ionosphere-thermosphere system. Jones et al. [2014] simulated the impacts of vertically propagating tides on the mean state of the ionosphere and thermosphere and found that the non-migrating tide DE3 can also affect the ionospheric mean state.

Kelvin Waves are equatorially-trapped planetary waves that travel eastwards with respect to the background winds. They propagate upwards away from their sources in the troposphere where they are excited by the latent heat release associated with tropospheric convection [Holton, 1973 [87]; Salby and Garcia, 1987 [197]]. UFKW can reach large amplitudes in the MLT where they can be a significant part of the motion field [Forbes et al., 2009 [54]; Forbes, 2000 [40]]. UFKW in the MLT have been investigated in a limited number of studies using meteor and MF radars [e.g. Riggin et al., 1997 [185]; Kovalam et al., 1999 [109]; Sridharan et al., 2002 [200]; Pancheva et al., 1994 [174]; Lima et al., 2008 [122]], satellites [e.g. Canziani et al., 1994 [14]; Lieberman and Riggin, 1997 [121]; Forbes et al., 2009 [54]], and models [e.g. Forbes, 2000 [40]; Miyoshi and Fujiwara, 2006 [155]]. UFKW have been suggested to play a key role in driving the Intraseasonal Oscillations (ISOs) with peaks at periods of 60 days, 35-40 days and 22-25 days that are observed in the MLT zonal mean temperatures and winds at low latitudes [Eckermann and Vincent, 1994 [33]]. [A more comprehensive review on Kelvin waves is provided in Section 1.1.2.]

4.2 Data and Methodology

For this study, we use global temperatures (version 1.07) at 110 km from the SABER instrument aboard the TIMED satellite, and density and zonal wind at 260 km from GOCE accelerometers [Rebhan et al., 2000 [179]]. As noted by Zhang et al. [2006] [229] and mentioned in Chapter 2, unmodeled atomic oxygen variations can also introduce errors into the retrieved temperatures, and

for this reason results above 100-110 km contain errors of unknown magnitude due to this source and should be viewed with due caution. However, we can say that no unusual or unexpected tidal behavior is evident in any of our results at 110 km. We perform our analysis for the 3-year period 2010-2012 and focus on latitudes between $\pm 45^{\circ}$, where DE3 and the UFKW reach their largest amplitudes and sampling is not affected by yaw maneuvers for TIMED, leading to an an almost continuous time series coverage in UT and longitude.

In order to highlight the thermosphere variability associated with waves and at least partially quantify solar and geomagnetic influences, we use multiple linear regression to fit the raw data to daily S10.7 and 3-hour ap values in 15-day windows, stepping forward 1 day at a time ('running windows'). We then remove these fits from the raw data and analyze the resulting residuals for wave content. S10.7 has been shown to be better proxy for EUV variability than the commonly used F10.7 solar flux, especially for day-to-day variations during solar low conditions [Tobiska et al., 2008 [110]]. S10.7 is derived by normalizing and converting to sfu through linear regression with F10.7 measurements of the 26-34 nm solar EUV emission from the Solar Extreme-ultraviolet Monitor instrument aboard the NASA/ESA Solar and Heliospheric Observatory research satellite [Bowman et al., 2008 [4]]. Figure 4.1 shows an example of the fit for a geomagnetically active period, where ap-S10.7 effects account for $\sim$28% and $\sim$39% of the total variability at 260 km in the winds and densities, respectively. These fits are then used in Chapter 5 to assess the relative importance of thermosphere variability attributed to waves from below versus that are connected to solar and geomagnetic forcing.

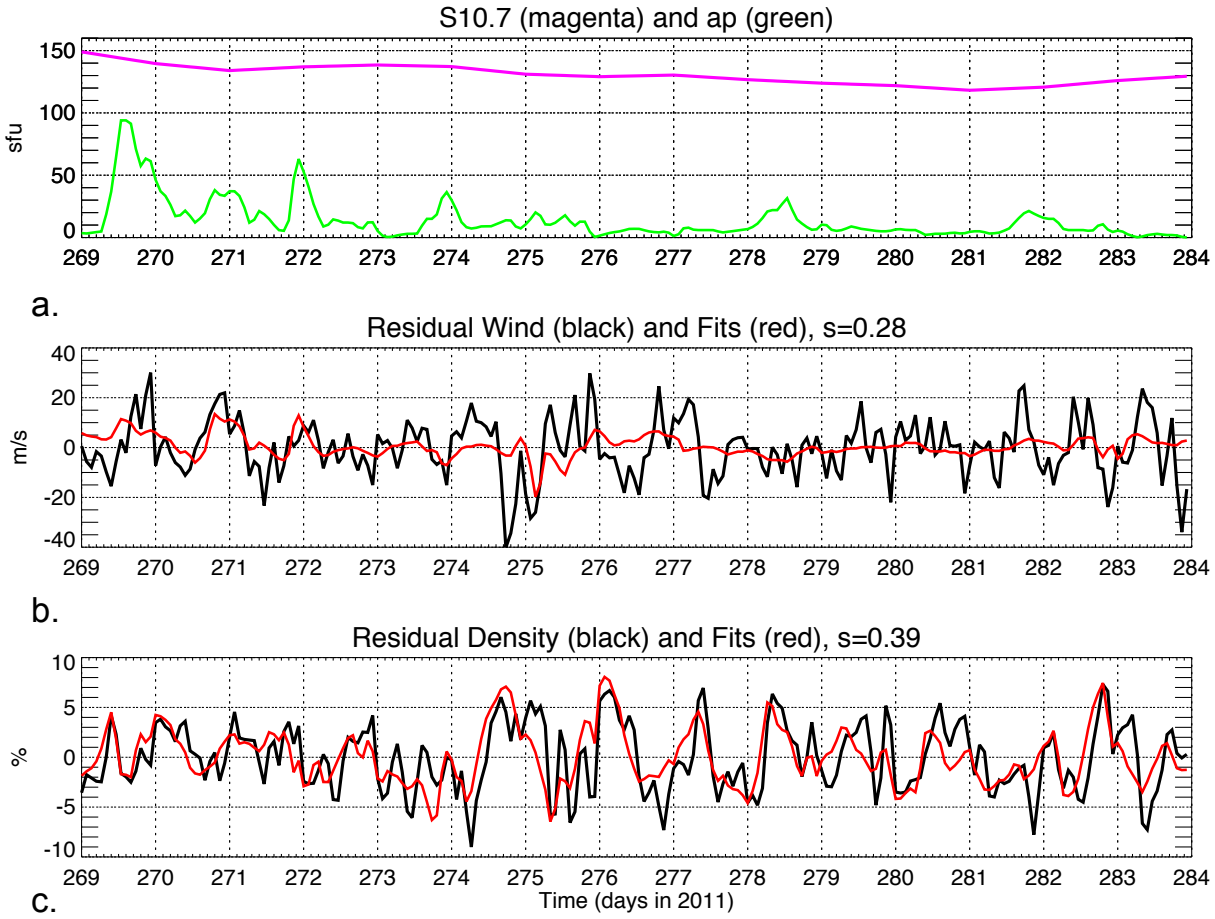

Figure 4.1: Example of fits to GOCE residuals and daily F10.7 and 3-hour ap indices for a geomagnetic active period (DOY 269-284 in 2011), around the equator (latitude ±12°). The top panel (a) illustrates the S10.7 (magenta line) and ap (green line) values. The residual winds (black line) and their fits (red line) are shown in panel b and panel c, respectively. In this 15-day period, the variance captured by the fits to wind (density) is 0.28 (0.39), indicating that at least ∼28% (∼39%) of the variance in the winds (densities) is linked to geomagnetic and/or solar effects.

The slow local time precession of most low-orbiting satellites represents a major limitation of utilizing satellite-based measurements to study the short-term variability of atmospheric tides. To counteract this shortcoming, we employ a similar method to that of Lieberman [1991] [119] and Oberheide and Gusev [2002] [166] to SABER and GOCE residuals (i.e., data after the removal of ap-F10.7 fits) to infer 'daily' DE3 amplitudes. The method, which involves taking differences

between measurements at the ascending and descending nodes and least-squares fitting wave-4, is presented in Section 2.5 of Chapter 2. Extracting DE3 amplitudes according to this method, the main source of error is represented by aliasing of TE1 and DW5 into the wave-4 structure, causing uncertainties ranging from ∼5% during the Northern Hemisphere summer to ∼30% during the Northern Hemisphere winter at low latitudes (±45°) for heights ∼100 km (according to Oberheide et al., [2011] [165]). Although this method can be applied to derive DE3 amplitudes on a daily basis, in this work we average 5 days of data to extract an amplitude value for each day. We find this averaging necessary based on the noise level on the raw data. In the following, we refer to these DE3 values as 'daily' amplitudes, although the reader should keep in mind that these values are actually 5-day means.

UFKW amplitudes are derived by least-squares fitting SABER and GOCE residuals in 15-day running windows (15-day means shifted one day at the time), using the expression $y(t,\lambda) = \overline{y} + A\ cos[2\pi\ (t/T - \lambda m)]$, where t is UT time, λ is longitude (in radians), $\overline{y}$ is the zonal mean, A the amplitude, T the period (i.e., 3 days), and m the zonal wavenumber (i.e., -1). The length of the window is chosen such that at least 5 full cycles are required to fully capture a wave with a 3-day period.

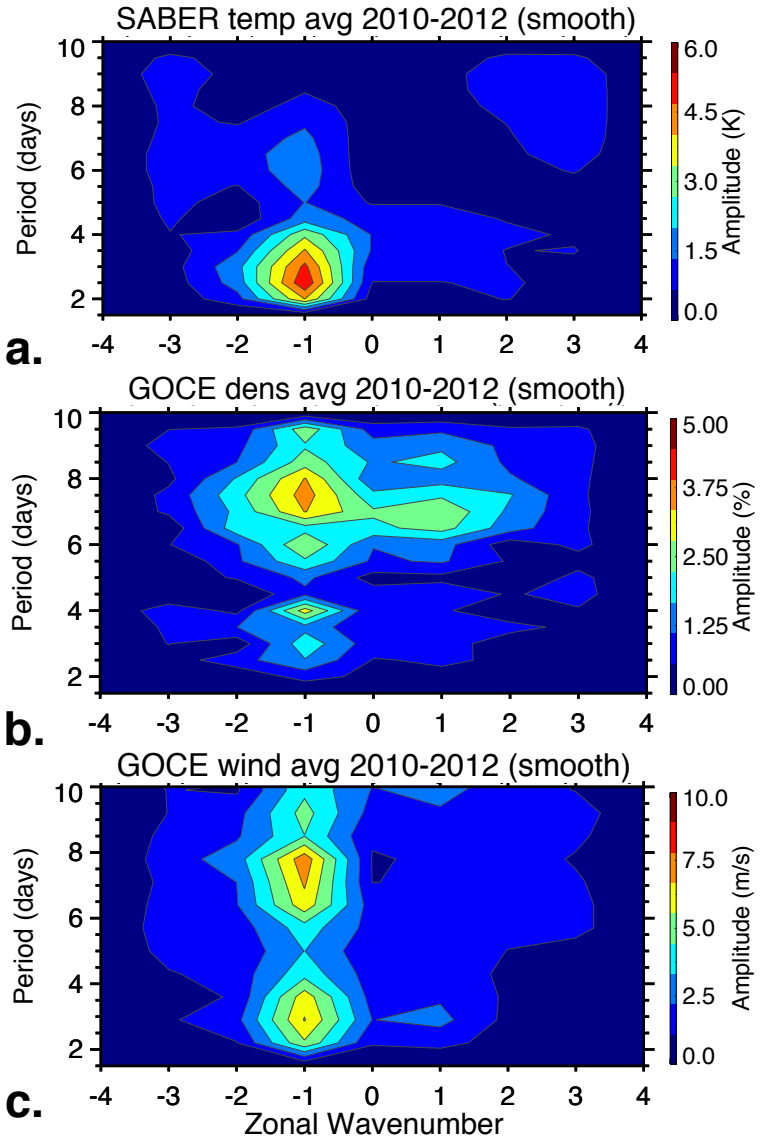

Figure 4.2: Three-year average period vs. zonal wavenumber spectrum, with ap/S10.7 fits removed, after the repeated 1-2-1 smoothing to the original spectrum is removed from the original spectrum for SABER temperature (panel a), GOCE density (panel b), and GOCE wind (panel c). Note a strong 3-day UFKW at both 110 and 260 km, and 6-9 day Kelvin waves at 260 km.

Figure 4.2 shows the period vs. zonal wavenumber spectrum for 2010-2012 around the equator (±12° latitude), produced by least-squares fitting for the 3-year period residuals after removing ap-S10.7 effects. The multi-year spectrum of Figure 4.2 has the 'background energy', obtained by repeated 1-2-1 smoothing to the original spectrum, removed from the original spectrum. This

method is the same that Wheeler and Kiladis [1999] [221] applied to outgoing longwave radiation (OLR) data in the tropics to highlight several convectively-generated waves, and that Forbes et al. [2009] [54] applied to SABER temperatures to reveal Kelvin waves and other equatorial oscillations over the altitude range 20-120 km. Figure 4.2 presents evidence of a strong 3-day UFKW with s = -1 in SABER temperature (panel a), and Kelvin waves (s = -1) with periods ranging from 3 to 9 days in GOCE density (panel b) and GOCE wind (panel c). The 3-year average UFKW amplitude is ∼5 K in SABER temperature, and ∼4% and ∼7 m/s in GOCE density and wind, respectively. Note that the 6-9 day Kelvin waves present in GOCE data are not found in SABER, suggesting that these thermospheric oscillations arise from in-situ excitation, possibly due to secondary waves generated by nonlinear wave-wave interactions and/or interactions with the longitudinal structure of ion drag (i.e., magnetic control of ion-neutral interactions, see Jones et al. [2013] [99]). It would be beyond the scope of the present study to further investigate the origin and nature of these oscillations present at 260 km but not at 110 km; thus this analysis is left for future work. Additionally, for the year 2011 we found a large 10-day periodicity with zonal wavenumber 0 both at 110 km and 260 km (result not shown here). This oscillation is significantly reduced in the spectrum by removing ap-S10.7 fits, suggesting a link to geomagnetic and solar effects. In fact, this periodicity is likely related to recurrent geomagnetic activity and high-speed solar wind streams near 9-day period, the signature of which has been reported in both TIMED temperature data near 110 km [Jiang et al., 2014 [94]] and CHAMP density data near 400 km [Lei et al., 2008 [116]].

4.3 Results

4.3.1 Evidence of Vertical Propagation

Figure 4.3 shows daily DE3 amplitudes in SABER temperatures at 110 km (Figure 4.3a) and GOCE densities (Figure 4.3b) and winds (Figure 4.3c) at 260 km for 2010-2012. Amplitudes up to 20 K are found in the temperatures, 8% in the densities, and 10 m/s in the winds. The intraseasonal variability of DE3 is very similar at 110 km and 260 km, with maxima at low latitudes. The presence

of DE3 at both heights, the common intraseasonal variability, and the similar amplitudes are a clear indication that vertical propagation is occurring. In addition we do not know of any source for DE3 between 110 km and 260 km. The vertical propagation of DE3 is even more apparent when looking at Figure 4.4, which shows 30-day running means of the daily values plotted in Figure 4.3. For each day (and latitude bin) we calculated 30-day means and created an array of means by stepping forward 1 day at the time (if gaps exist at least 15 days are needed to produce an output value). Eliminating a lot of day-to-day variability, this method provides a quasi-steady-state view. The latitudinal structures are somewhat smoothened by applying monthly means, giving the impression that for this case the maxima occur closer to the equator than for the daily values. Additionally, most of the day-to-day variability is removed and the amplitudes are reduced by up to 50%. The apparently different latitudinal structures can only be attributed to the fictitious effect introduced by taking monthly means, and no contamination by other wave components is possible. The correlation coefficients between SABER temperature and GOCE density is 0.67 for daily values and 0.73 for the 30-day running means (see Table 4.1). No link with season, level of geomagnetic activity, or zonal mean winds is found. Generally (see Truskowski et al. [2014] [209] and references therein), DE3 tends to have a symmetric latitudinal structure with maxima around the equator due to the prevalence of its first symmetric mode (which is a Kelvin wave and thus is symmetrical around the equator). The presence of other Hough modes, such as the first anti-symmetric mode, can alter such symmetric structure and give rise to maxima at low latitudes, instead of the equator [Forbes et al., 2003a [45]]. This is likely the cause of the low-latitude non-equatorial peaks present in Figure 4.3.

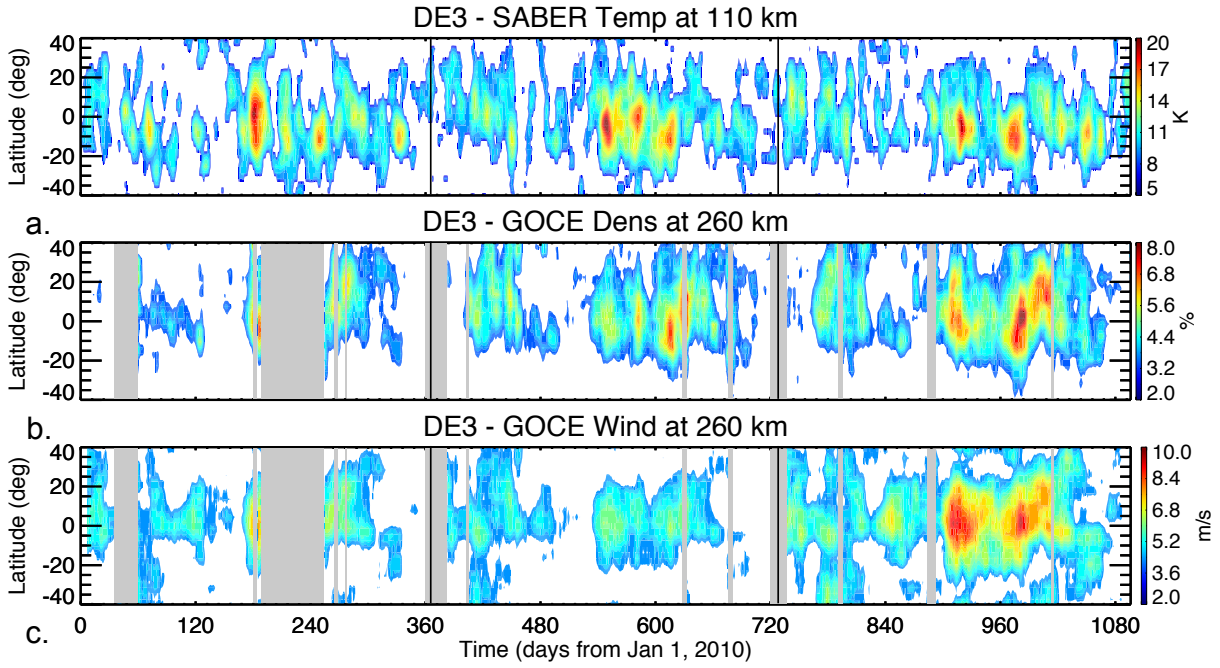

Figure 4.3: Time series of daily DE3 amplitudes for SABER temperature (panel a), GOCE density (panel b), and GOCE wind (panel c) for 2010-2012. Large day-to-day and seasonal variability at both heights is present, with low-latitude maxima. Amplitudes up to 20 K are found in the temperatures, 8% in the densities, and 10 m/s in the winds. Based on the noise level in the extracted DE3 amplitudes, values smaller than 5 K, 2%, 2 m/s are not shown (white spaces), while gaps in the raw data are colored in gray. The similar intra- and inter-seasonal variability and amplitudes, and the absence of any known source for DE3 between 110 km and 260 km, is clear indication of the vertical propagation of DE3 from 110 km to 260 km.

Correlation	**DE3 Daily**	**DE3 Monthly**
Temperature and Density	0.67	0.73
Density and Wind	0.81	0.84
Temperature and Wind	0.63	0.71

Table 4.1: Correlation coefficients of daily and monthly DE3 in SABER temperature, GOCE density, and GOCE wind, calculated around the equator (±12° latitude) for 2010-2012.

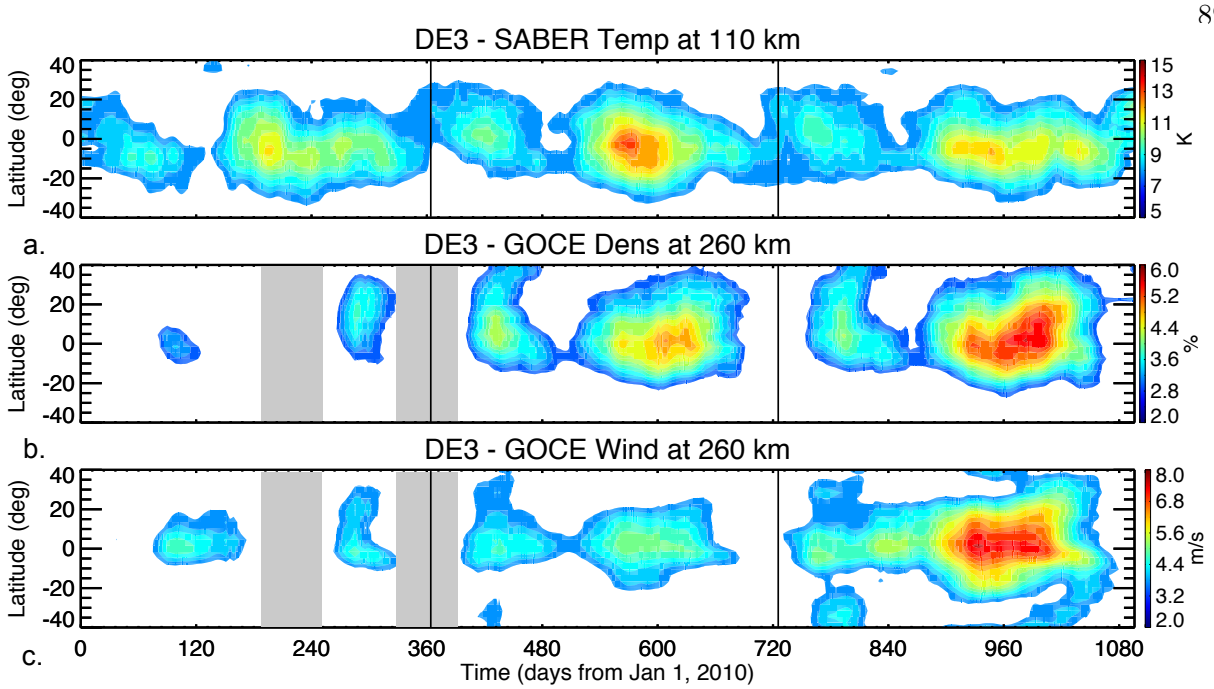

Figure 4.4: Time series of 30-day running means of daily DE3 amplitudes for GOCE density (a), GOCE wind (b), and SABER temperature (c). Similar to Figure 4.3 amplitudes smaller than the noise level are not shown, while gaps in the data are in gray. Vertical propagation of DE3 is even more evident than in Figure 4.3, given the quasi-steady-state approximation. Note the distinct annual and semi-annual oscillations in DE3 amplitudes at both heights.

As discussed in Section 4.1, after the removal of the ap-S10.7 fits from the raw data, the UFKW with 3-day period emerges as a prevalent short-period global wave both at 110 km and 260 km. Figure 4.5 shows daily UFKW amplitudes for GOCE at 260 km and SABER at 110 km. Amplitudes up to 15 K are found in the temperatures (Figure 4.5a), 8% in the densities (Figure 4.5b), and 10 m/s in the winds (Figure 4.5c), with maxima around the equator. The common intra-seasonal latitude-time variability of the amplitudes between SABER and GOCE, and the absence of any known UFKW source between 110 km and 260 km, is indication that vertical propagation is occurring. [Note that although daily values are presented, the UFKW is calculated using 15-day moving windows, and thus every latitude-day bin combines data from 15 days.] Similar to DE3, the comparison is improved by looking at 30-day running means, which

are shown in Figure 4.6. Table 4.2 lists the correlation coefficients between the UFKW in SABER and GOCE. Correlation coefficients of 0.61 for daily values and 0.70 for running means are found between UFKW temperatures at 260 km and UFKW densities at 110 km.

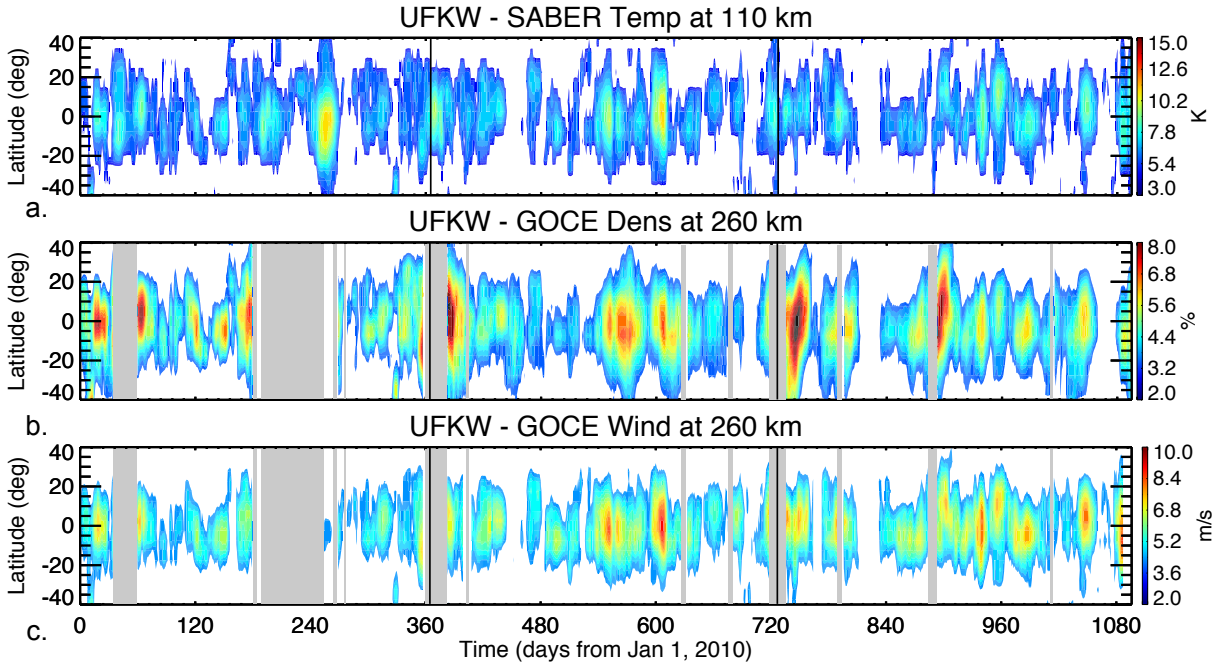

Figure 4.5: Same as Figure 4.3, but for the UFKW with period of 3 days and zonal wavenumber -1. Amplitudes up to 15 K are found in the temperatures (panel a), 8% in the densities (panel b), and 10 m/s in the winds (panel c), with maxima at low latitudes.

Correlation	**UFKW Daily**	**UFKW Monthly**
Temperature and Density	0.61	0.70
Density and Wind	0.79	0.86
Temperature and Wind	0.59	0.67

Table 4.2: Same as Table 4.1, but for the UFKW. Note correlation coefficients of 0.70 (0.67) between temperatures and densities (winds) for the 30-day means.

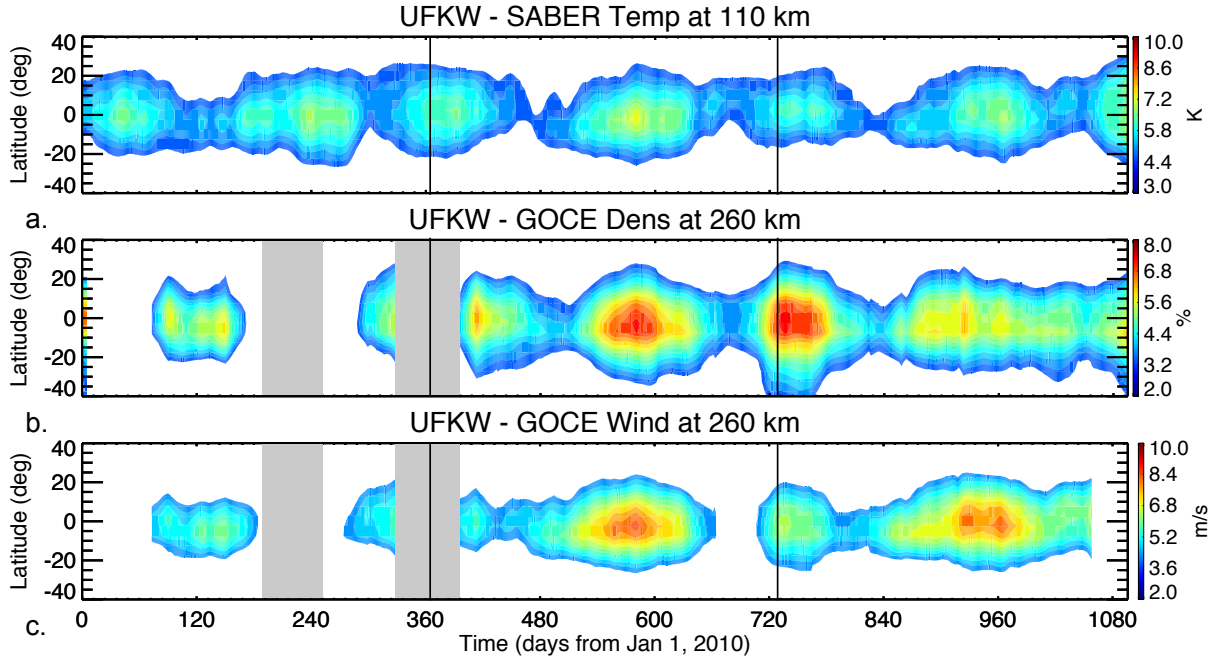

Figure 4.6: Same as Figure 4.4, but for the UFKW; similar to the case of DE3, vertical propagation is more evident when taking monthly means.

Note that the DE3 amplitudes presented in Figure 4.3 have much higher temporal resolution than ever before presented (5-day averages compared to means of 60 days or more). The high correlation between the latitude-temporal variability of DE3 and UFKW structures at 110 km and that at 260 km is clear evidence that vertical propagation between the heights is occurring for both waves.

4.3.2 Seasonal and Interannual Variability

Comparing the latitude-temporal variability of DE3 and UFKW structures for different years (see Figures 4.3-4.6), one can investigate the extent to which this variability repeats from year to year. Significant repeatability for the salient features of DE3 is found at both 110 km and 260 km. Correlation coefficients between different years calculated around the equator ($\pm 12^\circ$ latitude) are reported in Table 4.3.

Correlation Coefficient for DE3	SABER temperature	GOCE density
2010 - 2011	0.75	0.61
2010 - 2012	0.71	0.63
2011 - 2012	0.74	0.69

Table 4.3: Correlation coefficients between different years for DE3 in SABER temperature at 110 km and GOCE density 260 km. This table refers to the daily amplitudes shown in Figure 4.3 and is calculated around the equator (±12° latitude). Note values greater than 0.7 for SABER and 0.6 for GOCE, indicating strong year-to-year repeatability.

As listed in Table 4.3, correlation coefficients greater than 0.7 and 0.6 are found at 110 km and 260 km, respectively. This level of correlation is evidence of significant year-to-year repeatability, but also indication of some degree of interannual variability. Interannual variations are not unexpected and can be explained by variability in tropospheric forcing (i.e., latent heat release) and propagation conditions (i.e., changes in zonal mean winds). Changing mean winds in the 110-260 km height region would also explain less year-to-year coherence at 260 km than at 110 km.

Correlation Coefficient for UFKW	SABER temperature	GOCE density
2010 - 2011	0.54	0.51
2010 - 2012	0.56	0.49
2011 - 2012	0.51	0.53

Table 4.4: Similar to Table 4.3, but for the UFKW. Note values greater than 0.5 for SABER and GOCE, indicating some year-to-year repeatability, but also significant interannual variability.

Table 4.4 lists the correlation coefficients between different years of daily UFKW amplitudes. Values no larger than 0.56 are found at both 110 km and 260 km, indicating some year-to-year repeatability, but also significant interannual variability. Similar to DE3 (Table 4.3), the correlation coefficients at 260 km are smaller than those at 110 km, and may be explained by interannual

variations in zonal mean winds between 110 km and 260 km that can increase (i.e, eastward zonal mean winds) or decrease (i.e., westward zonal mean winds) susceptibility to dissipation, resulting in less year to year coherence at 260 km than at 110 km. Additionally, Table 4.4 indicates that the UFKW has less annual repeatability than DE3, with correlation coefficients up to 0.75 for latter and only 0.54 for the former. The exact reasons of this difference are not known, although variations in year-to-year forcing and zonal mean wind effects for the two waves are the likely cause. Both these effects will be further investigated in Chapter 6.

In addition to strong interannual variability, DE3 and UFKW also present significant seasonal variations. Figure 4.7 (Figure 4.8) shows the latitude-temporal evolution of DE3 (UFKW) amplitudes at 110 km and 260 km obtained combining data for the 3 years. Averaging 3 years of data shows the variability that repeats from year to year, and thus highlights seasonal patterns. This averaging is performed in 5-day chunks, moved forward 1 day at the time, as a 3-year vector average (i.e., accounting for the phase). Note that these DE3 amplitudes have much higher temporal resolution than ever before presented (5-day averages, instead of means of 60 days or more).

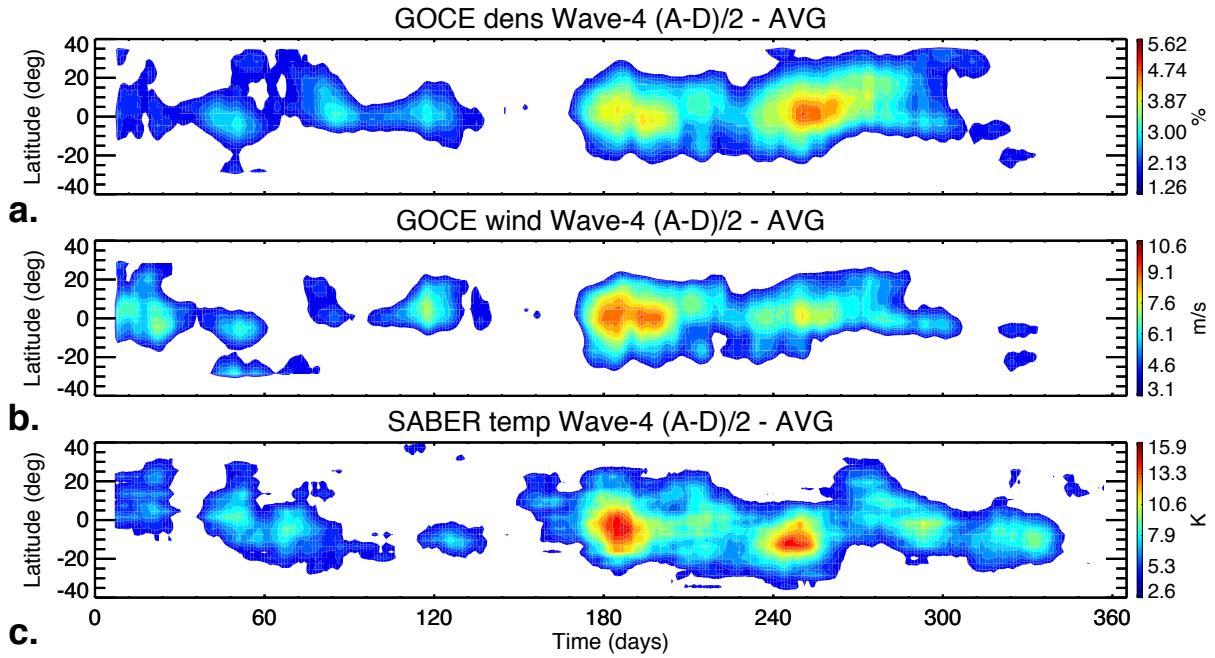

Figure 4.7: Comparison between DE3 in GOCE density and wind (panels a and b), and DE3 in SABER temperature (panel c), obtained by combining 3-year of data before the fit with wave-4. Significant seasonal variability in DE3 at both 110 km and 260 km, with the largest DE3 amplitudes (6%, 10 m/s, 16 K) observed at DOY 170-200 and DOY 240-260 and a secondary amplification at DOY 20-120 (3%, 6 m/s, 8 K). Amplitudes smaller than 2.6 K, 3.1 m/s, 1.26%, based on the noise level on the raw data, are not plotted.

As shown in Figure 4.7, the seasonal course of DE3 at both 110 km and 260 km is dominated by an annual oscillation with maxima between DOY 170 and DOY 300. The largest DE3 amplitudes, observed around DOY 170-200 and DOY 240-260, are ∼16 K at 110 km and ∼10 m/s (∼6%) at 260 km, while those of the secondary amplification around DOY 20-120 are ∼8 K at 110 km and ∼6 m/s (∼3%) at 260 km. On average, summer (DOY 170-265) DE3 amplitudes in the southern hemisphere are slightly larger than those in the northern hemisphere. Signatures of a semi-annual oscillation can be distinguished, with maxima around DOY 20-140 and DOY 170-300. The seasonal variability in DE3 outlined above is similar to what is reported by Truskowski et al. [2014] [209] and Forbes et al. [2014] [53]. Forbes et al. [2014] [53] exploited the local time coverage offered by combining CHAMP and GRACE data together and derived tides in terms of 72-day mean values.

As discussed in Chapters 1 and 2, previous tidal analyses with CHAMP were performed in terms of perturbation density and consisted of 130-day mean values due to the slow local time precession of the CHAMP orbit, likely suppressing the amplitudes and significantly smearing month-to-month variability. In this study, we further reduced the amplitude suppression by looking at 5-day means. As a result, the unprecedented temporal resolution attained reveals much more intra-seasonal variability in DE3, as shown in Figure 4.7, than ever shown before in satellite observations [e.g., Forbes et al., 2014 [53]].

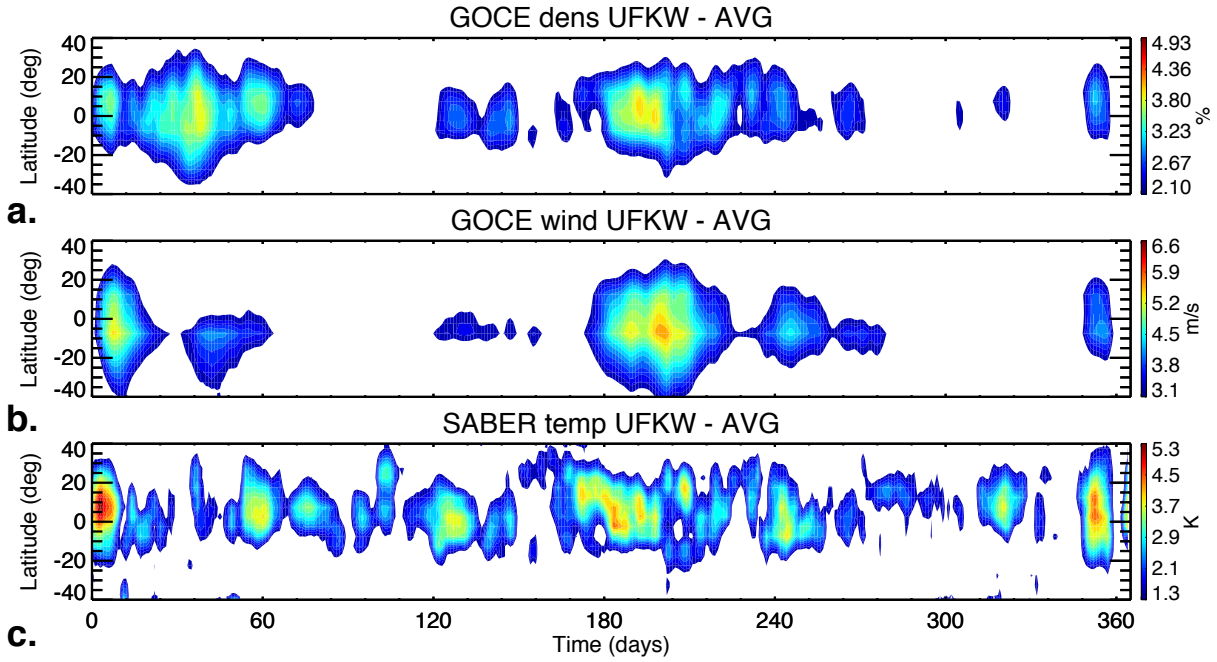

Figure 4.8: Similar to Figure 4.7, but for the UFKW. Note a significant semi-annual variation with maxima around DOY 1-60 and DOY 170-260 at 260 km, but no identifiable seasonal pattern at 110 km.

Figure 4.8 presents UFKW amplitudes, vector averaged over 2010-2012, for SABER and GOCE in a latitude versus DOY format. The UFKW shows a very distinct semi-annual variation at 260 km, with maxima of ∼4% and ∼6 m/s around DOY 1-60 and DOY 170-260. A less defined seasonal pattern can be seen at 110 km, where maxima of 6-7 K are found throughout the year. This seasonal modulation of the UFKW at 260 km, not present at 110 km, ought to be explained

by the effect of dissipation and zonal mean winds acting between 110 and 260 km. This topic will be further examined in Chapter 6. The results in Figures 4.7 and 4.8 can be summarized as follows:

- DE3 maximizes around ±15° latitude both at 110 km and 260 km, and can be detected in the ±30° latitude range, while the UFKW maximizes around ±25° latitude at 110 km and possesses non-negligible amplitudes up to ±40° latitude at 260 km. Latitudinal asymmetries and non-equatorial maxima for DE3 and the UFKW represent departure from HME solutions (see Oberheide et al. [2011] [165] for DE3 and Forbes [2000] [40] for the UFKW) and can be explained by the effect of zonal mean winds.

- While the seasonal course of the DE3 tide is dominated by strong maxima around DOY 170-300 and secondary maxima around DOY 20-120 both in the lower and middle thermosphere, the UFKW shows weak seasonal dependence at 110 km but a strong semi-annual oscillation at 260 km, possibly introduced by the intervening wind field.

- Significant latitudinal asymmetry is found in both DE3 and the UFKW, which is likely associated with the combined effect of dissipation and zonal mean winds.

4.3.3 Solar EUV Effects on Vertical Coupling

In Sections 4.3.1 and 4.3.2 we presented evidence of the vertical propagation of DE3 and UFKW from the middle to the upper thermosphere and analyzed their interannual and seasonal variability. In this subsection, we investigate the effect of solar EUV variations embedded in the S10.7 index on vertical wave coupling. We do this by analyzing DE3 variability in relation to S10.7 variations. We limit the analysis to DE3, given that this wave component exhibits stronger correlation between the lower and middle thermosphere (see Section 4.3.1). Note that the conclusions derived from the results presented below can be generalized to include the UFKW. [For background information on solar EUV effects on vertical propagation refer to Chapter 1 (Section 1.2.3).]

To better characterize the impact of solar EUV radiation on vertical coupling, we decompose DE3 into its equatorially symmetric and anti-symmetric components. The first anti-symmetric

mode of DE3 is a Kelvin wave that is known to propagate high into the thermosphere due to its long vertical wavelength [Oberheide et al., [2011] [165] and Truskowski et al., 2014 [209]]. As shown in Section 3.6.5 of Chapter 3, the first anti-symmetric mode of DE3 can have significant effects on the latitudinal profile of DE3 in the lower thermosphere and impose departure from its otherwise primarily equatorially symmetric structure. The first anti-symmetric mode of DE3 has a vertical wavelength of around 30 km [Truskowski et al., 2014 [209]] and thus is less likely to vertically propagate to the middle thermosphere compared to the first symmetric mode with $\lambda_z \sim$56 km. Also, the anti-symmetric component can be introduced in-situ by mean winds. [For a review of vertical wavelengths, tidal modes, and the effect of mean winds and dissipation refer to Chapter 1 and Appendix A.] Therefore, isolating the symmetric component of DE3 that is known to propagate high into the thermosphere facilitates studying the impact of solar radiation on vertical wave coupling.

To effectively compare DE3 amplitudes at 110 km with those at 260 km, we convert SABER DE3 temperatures at 110 km to DE3 densities using the ratio between the two given by Hough Mode Extensions. As discussed in Appendix A, HMEs represent the global solution to the linearized dynamical equations of the atmosphere for an oscillation of given frequency and zonal wavenumber, taking into account dissipative effects above the forcing region. The perturbation fields (i.e., u, w, v, T, ρ) output from the HMEs maintain internally self-consistent relative amplitude and phase relationships, thus enabling the estimation of DE3 densities from DE3 temperatures. The HMEs are the same as in Oberheide et al. [2009] [164], computed as detailed by Svoboda et al. [2005] [202] using a stripped-down version of the Global Scale Wave Model), calculated for three F10.7 radio flux levels: high (170 sfu), moderate (110 sfu) and low (60 sfu). Oberheide et al. [2009] [164] found strong solar flux dependence in thermospheric DE3 amplitudes in the thermosphere, with smallest amplitudes for high solar flux and largest for low solar flux (mainly owing to the temperature dependence $\sim T^{2/3}$ of molecular thermal conductivity, see Forbes and Hagan [1982] [46] and Chapter 1 for details). Temperature HMEs are the least sensitive to solar cycle effects with a 60% increase from 170 sfu to 60 sfu, while density (almost a factor of 5) and winds (a factor

of 2-3) are more affected. The HME solar flux dependence in the MLT region is small with only a few percent (density, winds) or even less (temperature). Figure 4.9 shows the latitude versus solar flux dependence in the ratio between DE3 temperatures and DE3 densities derived by linearly interpolating HMEs for the 3 solar flux levels previously described. As shown in Figure 4.9, the ratio is not significantly affected by solar flux or latitude at 110 km, with values varying from 1.7 for F10.7 ∼60 to 1.8 for F10.7 ∼200, while at 260 km the ratio has a strong solar flux dependence, with values from 3 for F10.7 ∼60 to 8 for F10.7 ∼200. In both cases the ratios are maxima around the equator and decrease quadratically with latitude. We use the ratios shown in Figure 4.9 to convert DE3 temperatures to DE3 density perturbations at 110 km, accounting for latitude and solar flux variations. We then use these calculated DE3 density perturbations at 110 km to compare with DE3 density perturbations at 260 km derived from GOCE accelerometer measurements.

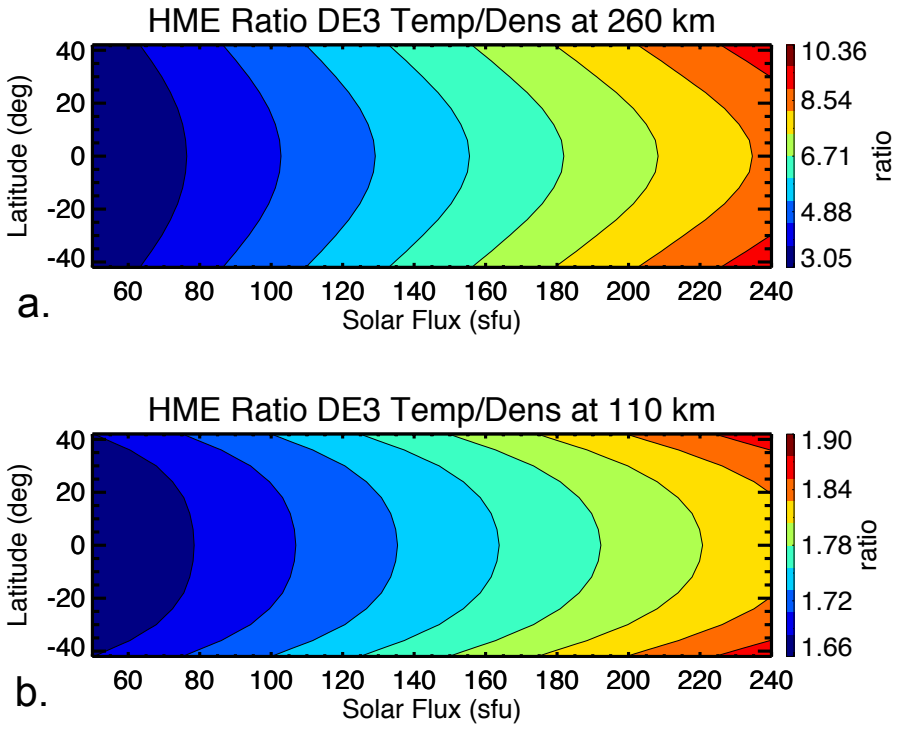

Figure 4.9: Ratio between DE3 in temperatures and DE3 densities for the first symmetric mode at 110 km (panel a) and 260 km (panel b), calculated using HMEs, as function of solar flux and latitude.

Figure 4.10 presents the latitude-temporal evolution of DE3 symmetric density amplitudes (derived as described above) at 110 km (panel a) and 260 km (panel b), where the red line in both plots represents the S10.7 solar EUV index. From Figure 4.10 one can see that the amplitude of DE3 at both heights is comparable and is up to ∼10% with maxima at the equator. This is different from what shown by Forbes et al. [2014] [53], where DE3 at 260 km is much smaller than DE3 at 110 km, probably due to amplitude suppression caused by the 72-day running means. Significant day-to-day variability in DE3 is present at both 110 km and 260 km. While many similarities between the two heights are evident in the temporal evolution of the maxima, the latitude structures at 260 km are broader than those at 110 km. This latitudinal spread is a feature imposed by molecular dissipation (see Forbes and Vincent [1989] [50]). The correlation coefficients between the variability of symmetric DE3 at 110 km and that at 260 km calculated around the equator (±12° latitude) is 0.75, which is larger than what shown in the previous section for the symmetric plus antisymmetric component (r=0.67). Larger correlation and more one-to-one matching is expected since the first symmetric mode of DE3 has longer vertical wavelength than its first anti-symmetric mode (56 km versus 30 km, see Section 4.3.1 and Truskowski et al., [2014] [209]) and hence is less subject to dissipation as it propagates upwards (see Chapters 1 and 6, and Appendix A). The high correlation between the latitude and day-to-day structures in DE3 symmetric at the two heights is evidence that the majority of DE3 at 260 km is the vertical extension of DE3 at 110 km. As previously discussed, the not exact agreement is likely caused by the effects brought on by wave dissipation, the presence of zonal mean winds, wave-wave interactions, and inherent transience.

In order to verify the effect of solar radiation on the vertical coupling of DE3 at different time scales, Figure 4.11 presents symmetric DE3 density perturbations at 110 km (blue line), 260 km (black line), and S10.7 (red line) around the equator (±12° latitude) as daily values (panel a), 81-day running means (panel b) and residuals from 81-day means (panel c). No significant correlation between the short and long term variability in DE3 and that in S10.7 is found at either height over the 3-year period analyzed.

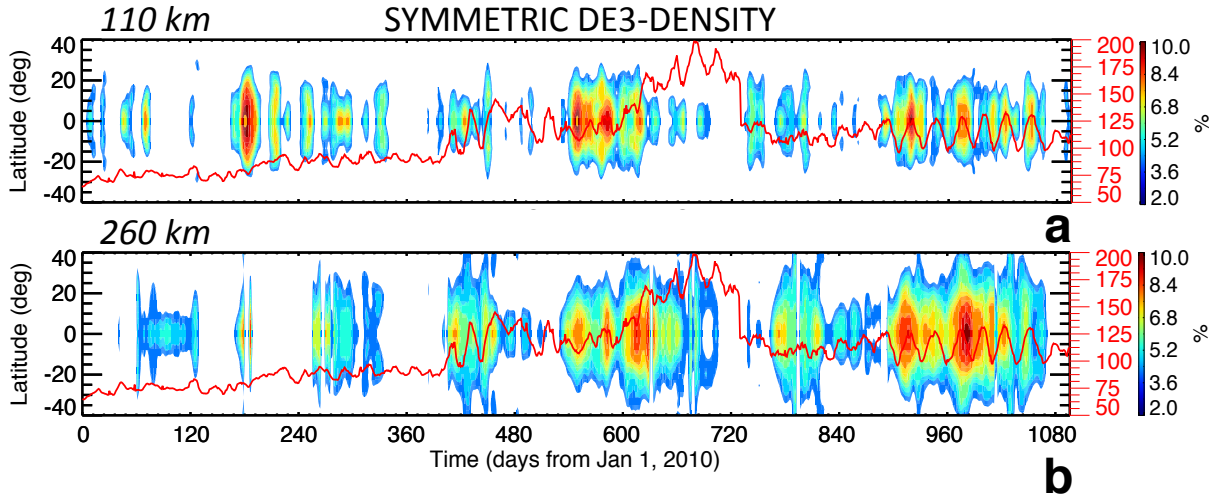

Figure 4.10: Comparison of DE3 symmetric density perturbations between 110 km and 260 km for 2010-2012. DE3 temperatures at 110 km are converted to DE3 densities using the HME ratios shown in Figure 4.9. The superposed red line represents the S10.7 index. Note broader latitudinal structures at 260 km and no apparent correlation between DE3 and S10.7 at the two heights.

One of the issues in investigating the effect of solar radiation on the vertical propagation is separating the effect of decreased amplitudes at 260 km due to less generation at lower heights from solar radiation influence on vertical propagation. In order to focus on the effect of EUV radiation on the vertical propagation between 110 km and 260 km, we analyze the time series of the ratio of daily symmetric DE3 density amplitudes between 110 km and 260 km, as shown in Figure 4.12a. Figure 4.12b shows the 81-day running mean, highlighting longer period trends, and Figure 4.12c shows the residuals from the same 81-day running mean (daily values minus 81-day means), isolating shorter-period variability.

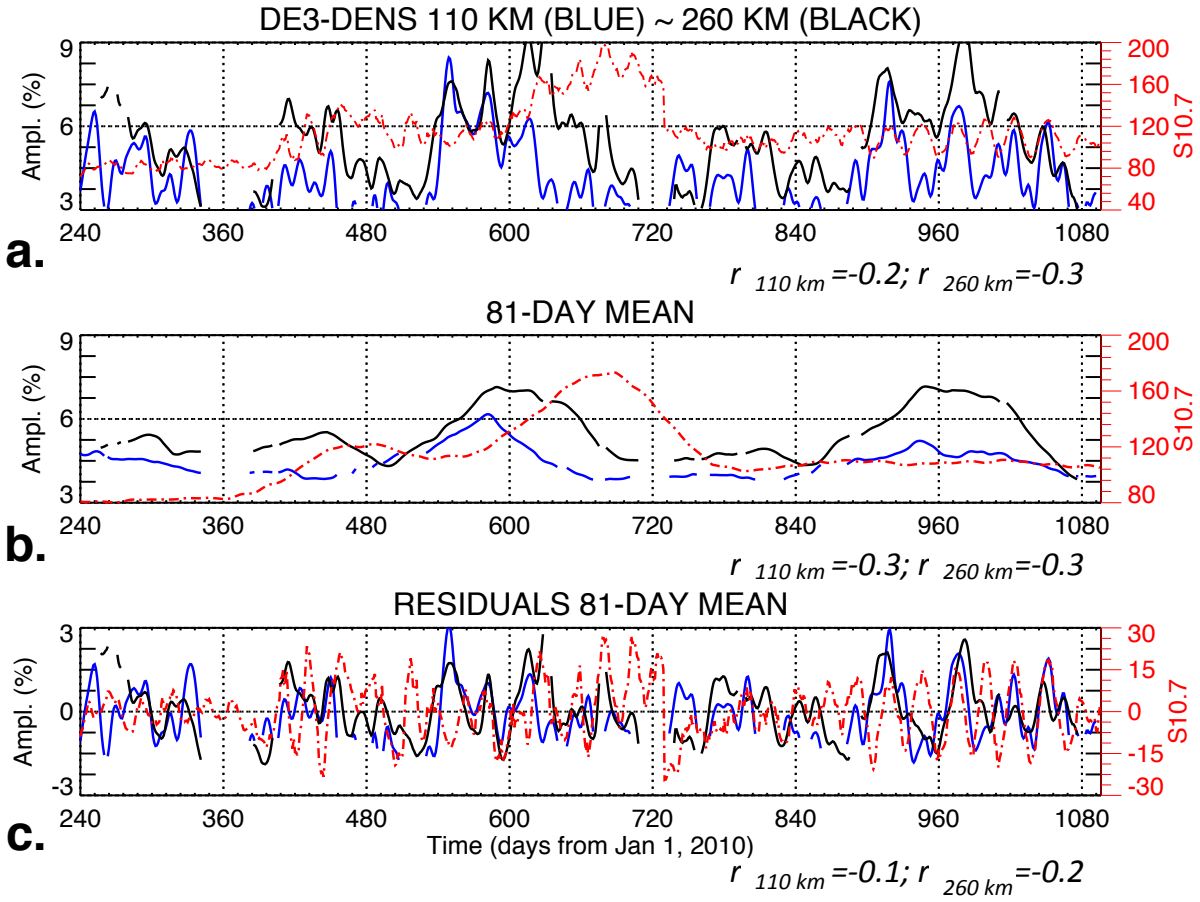

Figure 4.11: Time series around the equator (±12° latitude) of DE3 density at 110 km and 260 km (panel a), the 81-day running mean (panel b), and residuals calculated from the 81-day running mean (panel c). The first 240 days of 2010 are not shown due to large gaps in GOCE raw data. The black (blue) line refers to DE3 at 260 km (110 km), while the red line represents S10.7 (see separate y-axis on the right side of the plot). Correlation coefficients for the 3-year period between DE3 and S10.7 are included and indicate no significant correlation.

Although DE3 is not clearly correlated with S10.7 at 110 km or 260 km, as previously discussed and shown in Figure 4.11, the ratio between DE3 at 260 km and DE3 at 110 km shows some degree of anti-correlation with r=-0.63 for daily values (Figure 4.12a) and r=-0.69 for 81-day means (Figure 4.12b).

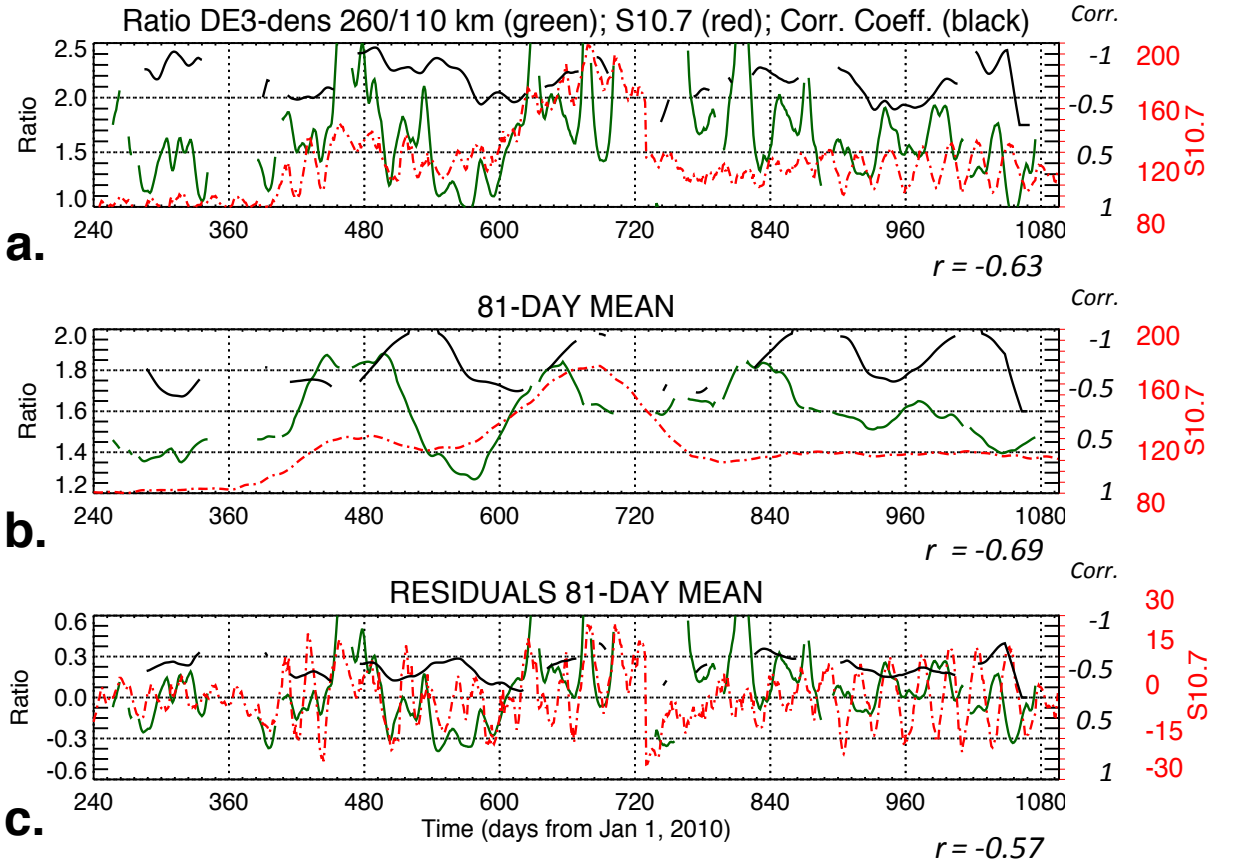

Figure 4.12: Ratio (green line) between DE3 density at 260 km and 110 km (panel a), 81-day running mean (panel b), and residuals from the 81-day means (panel c). The red line is S10.7, while the black line is the moving correlation coefficient (see separate axes for S10.7 and the correlation coefficients on the right side of the plot). Note strong anti-correlation between the ratios and S10.7 with average values of -0.63 for daily values and -0.69 for 81-day running means.

Negative correlation between S10.7 and DE3 ratios is not unexpected. This is because, as explained in Chapter 1 (Section 1.2.3), variations in solar heating are responsible for variations in neutral temperature and thus changes in the scale height. In particular, increased solar input results in a warmer atmosphere thus larger scale heights (H = kT/mg). An upward propagating wave experiencing an increased scale height will tend to decrease more considerably above the peak, before asymptotically reaching a constant value (i.e., hence smaller amplitudes in the middle thermosphere). So one can expect increased (decreased) solar radiation to cause increased (de-

creased) peak altitudes with larger (smaller) lower thermospheric amplitudes, but also significantly decreased (increased) middle-upper thermosphere amplitudes. As a result, for increased S10.7 value the ratio between DE3 at 260 km and DE3 at 110 km decreases. Figure 4.12b and Figure 4.12c also show that the ratio is more anti-correlated with S10.7 over longer time-scales (r=-0.69), and less anti-correlated with S10.7 over shorter time-scales (r=-0.57).

4.4 Conclusions

Using SABER temperatures near 110 km and GOCE winds and densities near 260 km, DE3 and a 3-day UFKW are identified as dominant sources of longitudinal variability during 2010-2012. We determined that over 60% of the variance in DE3 and the UFKW at 260 km can be traced back to variability occurring at 110 km. This level of correlation, and the absence of any known DE3 and UFKW source between 110 km and 260 km, serves as evidence that both DE3 and the UFKW propagate from the lower to the middle thermosphere. The not perfect agreement between the two heights is ascribable to additional complexities introduced by wave dissipation, the presence of zonal mean winds, wave-wave interactions, and inherent transience.

By combining the 3 years of data, we found that the seasonal course of the DE3 tide is dominated by strong maxima around DOY 170-300 and secondary maxima around DOY 20-120 at both 110 km and 260 km, while the UFKW shows weak seasonal dependence at 110 km but a strong semi-annual oscillation at 260 km. Significant latitudinal asymmetry is also found in both DE3 and the UFKW, which is likely associated with the combined effect of dissipation and zonal mean winds.

By analyzing the ratio of DE3 density perturbations between 260 km and 110 km and S10.7, we found significant anti-correlation that points to the importance of solar EUV radiation in the vertical propagation of waves in the thermosphere. In particular we found that higher S10.7 results in decreased propagation, which is in line with the theory outlined in Chapter 1.

Chapter 5

NONLINEAR WAVE-WAVE INTERACTIONS FROM TIMED AND GOCE

As discussed in Chapter 1, over the past decade numerous modeling and observational studies have demonstrated that atmospheric tides and other global-scale waves interact nonlinearly to produce secondary waves, which propagate away from their sources as independent oscillations. The modulation of tides by a PW introduces temporal and spatial variability in the thermosphere and significantly contributes to wave coupling. The manifestations and impacts of these waves are still poorly understood.

In Chapter 1 we reviewed the theory of nonlinear wave-wave interactions and presented an up-to-date synopsis of the literature, while in Chapter 4 we provided evidence of coupling associated with the vertical propagation of DE3 and a 3-day UFKW, two prominent global atmospheric waves. In this chapter, we utilize SABER temperatures at 110 km and GOCE densities and cross-track winds at 260 km to investigate the impact of nonlinear interactions between DE3 and the UFKW on the thermospheric system. This chapter is organized as follows: Section 5.1 contains an introduction to wave coupling associated with nonlinear wave-wave interactions and reviews the method adopted to examine nonlinear interactions from quasi-Sunsynchronous satellite measurements; Section 5.2 presents evidence of secondary waves generated by DE3-UFKW coupling; Section 5.3 investigates the longitudinal variability associated with these secondary waves; Section 5.4 compares the relative importance of upward propagating waves and geomagnetic/solar-driven variability; while Section 5.5 presents the conclusions.

Some of the contents of this chapter are derived from the JGR Space Physics paper issued

online on 24 August 2015 and referenced in the Bibliography as Gasperini et al., 2015 [61].

5.1 Introduction and Methodology

As reviewed in Chapter 1, there is increasing evidence that different components of the wave spectrum interact with each other to produce secondary waves. Each secondary wave is affected differently by the background wind field depending on its zonal wavenumber and Doppler-shifted frequency (see Chapter 1, Chapter 6, and Appendix A). At some distance from the source, one of the sideband waves could be significantly larger than the other, either due to different propagation conditions or because the two waves are not excited with equal efficiency. The modulation of tides by a PW introduces temporal and spatial complexity by virtue of the secondary waves, which have different periods and zonal wavenumbers than the primary waves. For instance, Palo et al. [1999] [170] demonstrate the generation of secondary waves due to the interaction between SW2 and the Q2DW; Wang et al. [2011] [218] discuss generation of TW3 from DW1 and SW2; Hagan et al. [2009] [75] and Oberheide et al. [2011] [165] demonstrate the production of SE2 and SPW4 from the DE3-DW1 interaction; and Moudden and Forbes [2013] [51] interpret the observation of terdiurnal nonmigrating tides in terms of interactions between diurnal and semidiurnal nonmigrating tides.

In Chapter 4, using SABER temperatures at ∼110 km and GOCE winds and densities at ∼260 km, we presented evidence for the vertical propagation of DE3 and a 3-day UFKW from the lower to the middle thermosphere, two major global-scale atmospheric oscillations. Using the same dataset, in this chapter we reveal evidence of nonlinear interactions between DE3 and the UFKW and investigate their effects on thermospheric variability. The theory of nonlinear interactions was reviewed in Section 1.3 (see also Teitelbaum and Vial [1991] [205]), while the method to examine such interactions was discussed in Section 2.4. Below we provide a brief description of this method in the context of UFKW-DE3 interactions.

Due to their quasi-Sunsynchronous orbits, the TIMED and GOCE satellites sample the atmosphere in a way that does not allow direct time-domain determination of wave-tide interactions. To counteract this shortcoming, we take advantage of the pseudolongitude method developed by

Moudden and Forbes [2010] [157] for Mars (and later applied to Earth, Forbes and Moudden, [2012] [48]]), and reviewed in Section 2.4. In a pseudolongitude spectrum PW peaks are located at $|m$ - $\delta|$, tides at $|s$ - $n|$, and secondary waves due to PW-tide modulation at $|(s$ - $n) \pm (m$ - $\delta)|$. Accordingly, the 3-day UFKW (m = -1, δ = 0.33) and DE3 (s = -3, n = 1) interact to produce secondary peaks at |(-3 -1) ± (-1 -0.33)| = |-4 ∓ 1.3| = 2.67 (sideband 1, or k_1) and 5.33 (sideband 2, or k_2). Sideband 1 has a period of $(n$ - $\delta)^{-1}$ = (1 - 0.33)$^{-1}$ = 1.5 days and zonal wavenumber of $(s$ - $m)$ = (-3 + 1) = -2, while sideband 2 has a period of $(n + \delta)^{-1}$ = (1 +0.33)$^{-1}$ = 0.75 days and zonal wavenumber $(s + m)$ = (-3 -1) = -4.

In Chapter 4 we provided evidence that DE3 and a 3-day UFKW are prominent oscillations both in the lower and middle thermosphere and propagate from 110 km and 260 km. In the following section we investigate whether DE3 and the UFKW undergo nonlinear interactions and produce secondary waves in this height regime, in Section 5.2 we analyze their impact on longitudinal variability, while in Section 5.3 we seek to quantify the total contributions of upward propagating waves to the total density and wind variability measured by GOCE.

5.2 Evidence of Nonlinear Interactions

Utilizing the method of Moudden and Forbes [2010] [157], we analyzed the SABER and GOCE data looking for evidence of nonlinear interactions between DE3 and the UFKW. In a fixed local time frame DE3 appears as a longitudinal wave-4 (|s - n| = |-3 -1| = 4), hence creates a peak at 4 cycles in a pseudolongitude spectrum, while the UFKW with $\delta = 3^{-1}$ day^{-1} and s = -1 generates a peak near 1.3 cycles (|m - δ| = |-1 - 3^{-1}| ≈ 1.3). The modulation of DE3 by the UFKW produces two sidebands given by the sum and differences of the zonal wavenumbers and frequencies [Forbes and Moudden, 2012 [48]]. In a UT-longitude frame [Teitelbaum and Vial, 1991 [205]] the sideband waves are the sum (k_2) and difference (k_1) waves with periods of 0.75 and 1.5 days and zonal wavenumbers -4 and -2, respectively. As previously described, in a pseudolongitude spectrum these waves appear as one peak near 5.3 cycles (k_2) and another near 2.7 cycles (k_1).

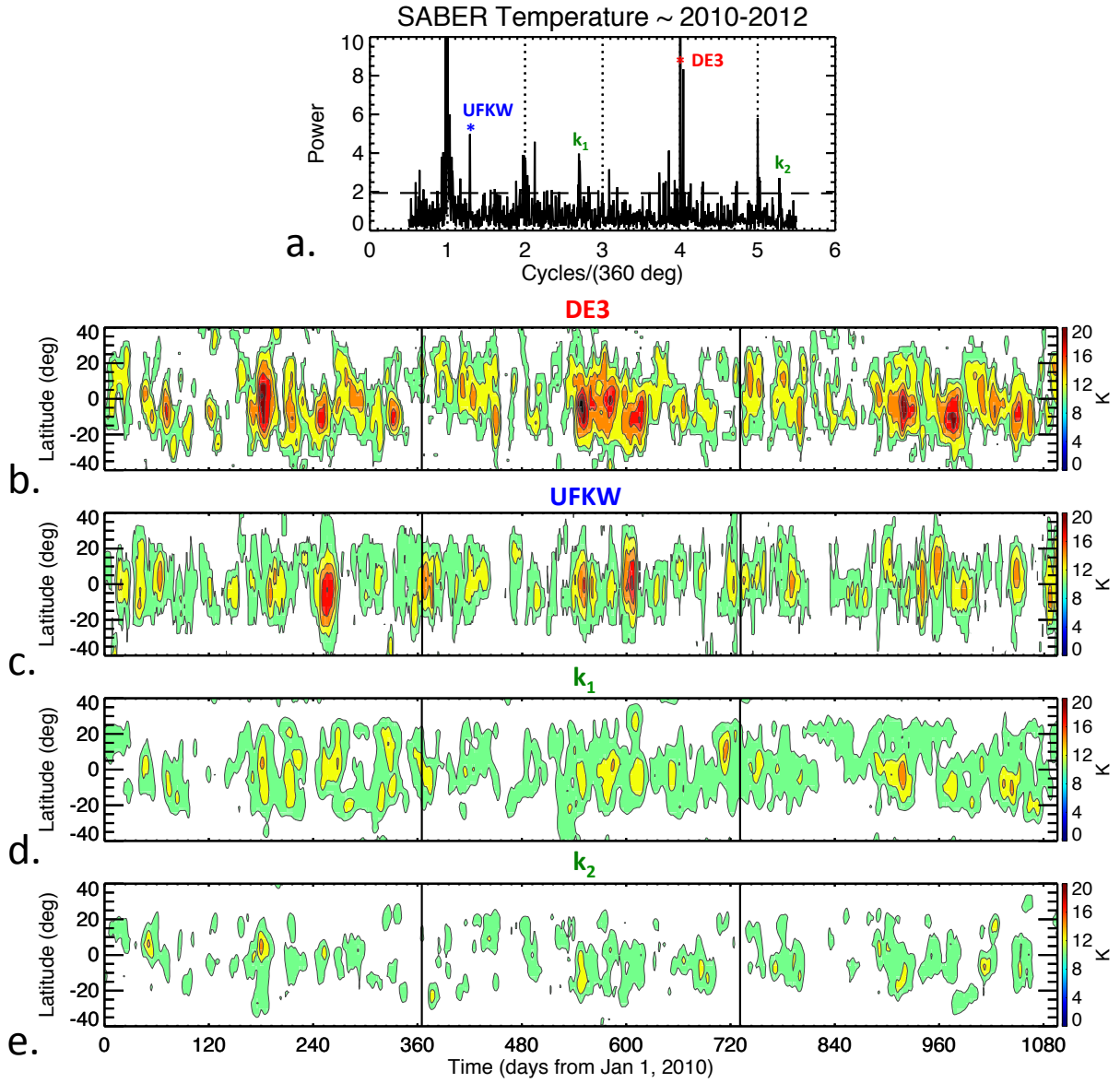

Figure 5.1: SABER-temperature 3-year average pseudolongitude spectrum (panel a), time series of DE3 (panel b), UFKW (panel c), k_1 (panel d), and k_2 (panel e). The interaction between DE3 (peak at 4 cycles, marked in red) and the UFKW (peak near 1.3 cycles, marked in blue) generates k_1 and k_2 (peaks near 2.7 and 5.3 cycles, marked in green). Both sidebands show large day-to-day variability, similar to DE3 and the UFKW, and reach amplitudes up to 14 K for k_1 and 10 K for k_2, comparable to the amplitudes of the waves producing them (i.e., UFKW and DE3). Note: the horizontal dotted line indicates 95% confidence level.

Thus, even though the sideband waves cannot be directly resolved by the satellite sampling,

they appear in the pseudolongitude spectra. As emphasized by Moudden and Forbes [2010] [157], this methodology only provides insights for interactions between PWs and nonmigrating tides. Sideband peaks for PW interactions with migrating tides fall on top of the PW peak.

Evidence of secondary waves generated by DE3-UFKW interactions is found at both 110 km and 260 km, as presented in Figure 5.1 for SABER temperature, Figure 5.2 for GOCE density, and Figure 5.3 for GOCE wind. Figure 5.1a shows the 3-year-average pseudolongitude spectrum for SABER near-equatorial temperatures, followed by the daily amplitudes of DE3 (Figure 5.1b), UFKW (Figure 5.1c), k_1 (Figure 5.1d), and k_2 (Figure 5.1e). Looking at the spectrum in Figure 5.1a it is easy to detect the wave-4 peak at 4 cycles (mainly due to DE3), the UFKW peak near 1.3 cycles and the DE3-UFKW interaction near 2.7 cycles (k_1) and 5.3 cycles (k_2). These peaks are also evident in GOCE density (Figure 5.2a) and GOCE wind (Figure 5.3a). The peak at 1.0 cycle present in both SABER and GOCE could in principle be caused by D0, DW2, SW1 and SW3. D0, SW1, and SW3 are generally quite small around the equator at 110 km (see Truskowski et al., 2014 [209]), leaving DW2 as the probable cause of the observed wave-1 structure in SABER. It would be beyond the scope of this work to explore whether this wave component does in fact propagate from the lower to the middle thermosphere, similar to DE3. Its interaction with the UFKW would result in peaks around 0.3 and 2.3 cycles, which are not clearly identifiable in the spectra at either heights.

Figures 5.1a, Figure 5.2a, and Figure 5.3a present clear evidence of nonlinear interactions between DE3 and the UFKW both at 110 km and 260 km. Figure 5.1b-e, Figure 5.2b-e, and Figure 5.3b-e demonstrate that for certain periods of strong DE3 and UFKW (but not only), the interaction of the UFKW with DE3 produces sidebands that can reach amplitudes very much comparable to the amplitudes of the primary waves (14 K in the temperatures, 6% in the densities, and 10 m/s in the winds). This suggests that nonlinear wave-wave interactions are a type of complexity that needs to be taken into consideration to accurately model thermospheric variability.

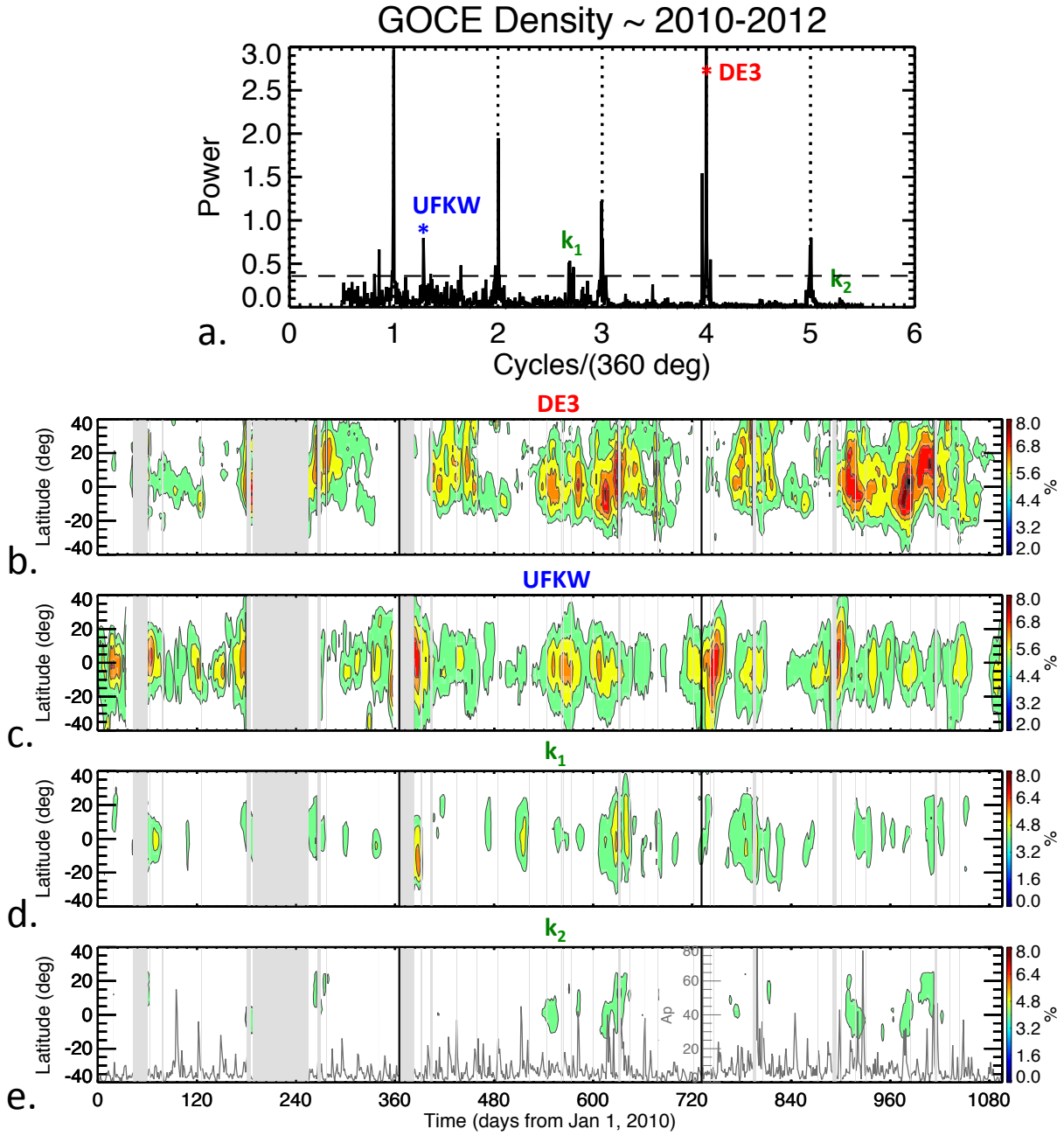

Figure 5.2: Same as Figure 5.1, but for GOCE density at 260 km. Gaps in the GOCE data are depicted in gray. Similar to SABER temperature, the sidebands due to the UFKW-DE3 interaction are clearly visible in GOCE density and reach amplitudes comparable to those of DE3 and the UFKW (i.e., up to ~6%). Note the Ap index plotted as a gray line in panel e.

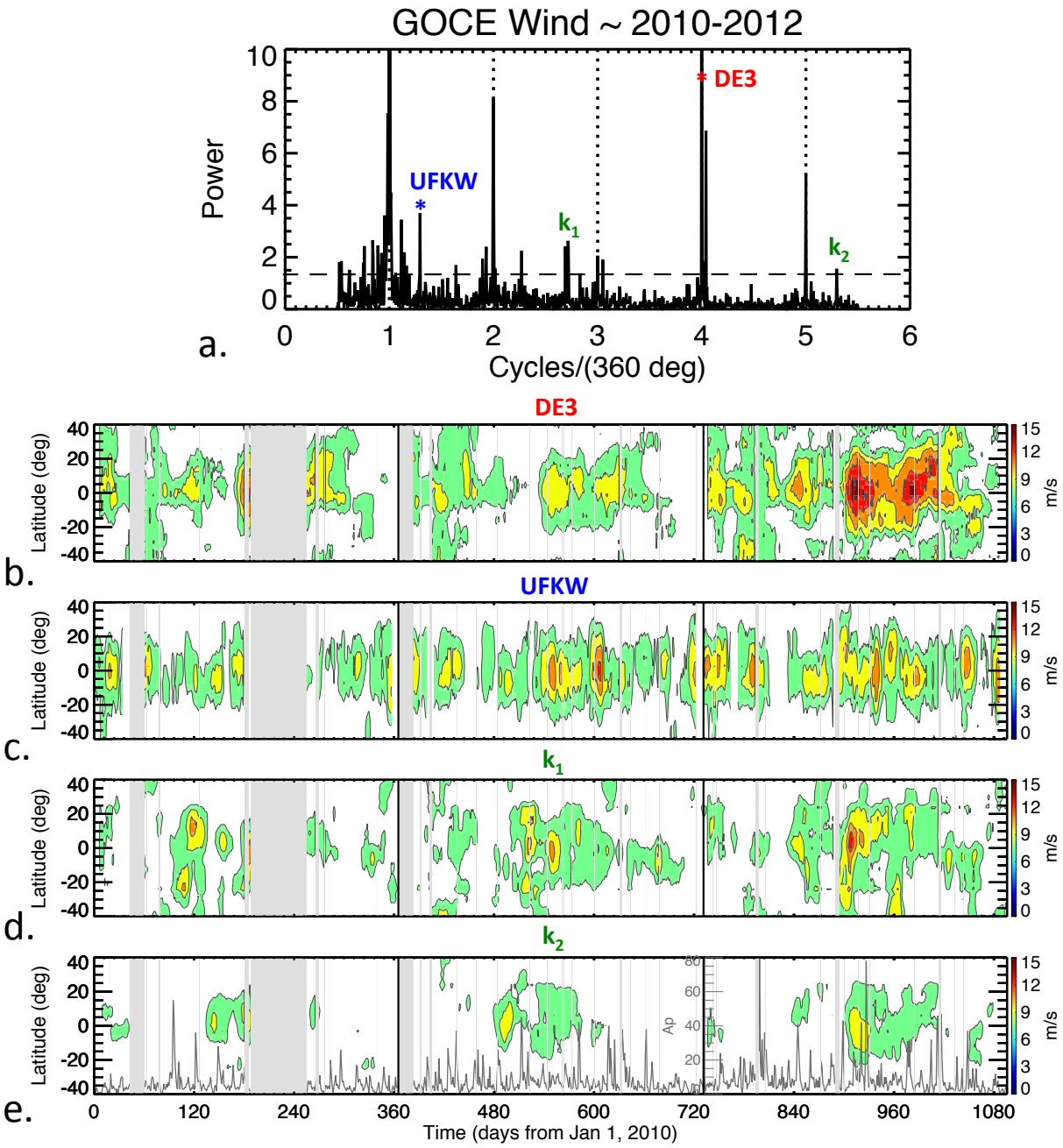

Figure 5.3: Same as Figure 5.1, but for GOCE wind at 260 km. Gaps in the GOCE data are depicted in gray. Similar to SABER temperature and GOCE density, the sidebands due to the UFKW-DE3 interaction are clearly visible in GOCE wind and reach amplitudes up to 11 m/s for k_1 and 9 m/s for k_2, comparable to the amplitudes of DE3 and the UFKW. Note the Ap index plotted as a gray line in panel e.

From Figures 5.1-5.3 (panels a, c, and d) one can see that k_1 generally possesses greater

amplitudes than k_2 both at 110 km and 260 km. As previously noted, k_2 has a period of 0.75 days and zonal wavenumber -4, whereas k_1 has a period of 1.5 days and zonal wavenumber -2. Since the nonlinear interaction between DE3 and the UFKW are likely to occur at altitudes lower than 110 km, the vertical propagation of the sidebands would depend on the wind field at altitudes below 110 km for SABER and below 260 km for GOCE. For eastward propagating waves (such as DE3 and the UFKW), the frequency is Doppler-shifted to higher absolute values in regions of westward wind and to lower absolute values in regions of eastward wind. As reviewed in Chapter 1, in regions where dissipation is important, waves with large Doppler-shifted frequency are less effectively damped than those with smaller Doppler-shifted frequency; all other things being equal, wave fields exhibit larger amplitudes where Doppler-shifting to higher absolute frequencies occurs. Generally higher zonal wavenumbers correspond to shorter vertical wavelengths and hence more susceptibility to dissipation. We have no definite explanation on why one sideband might be more readily excited than another, or why both might be excited during one period of time and not another, or why both might be excited during one period of time and not another. Concerning the latter, there may be a relationship to the cross-correlation between DE3 and UFKW. These issues are further investigated in Chapter 6 through the use of TIME-GCM model simulations.

5.3 Implications for Longitudinal Variability

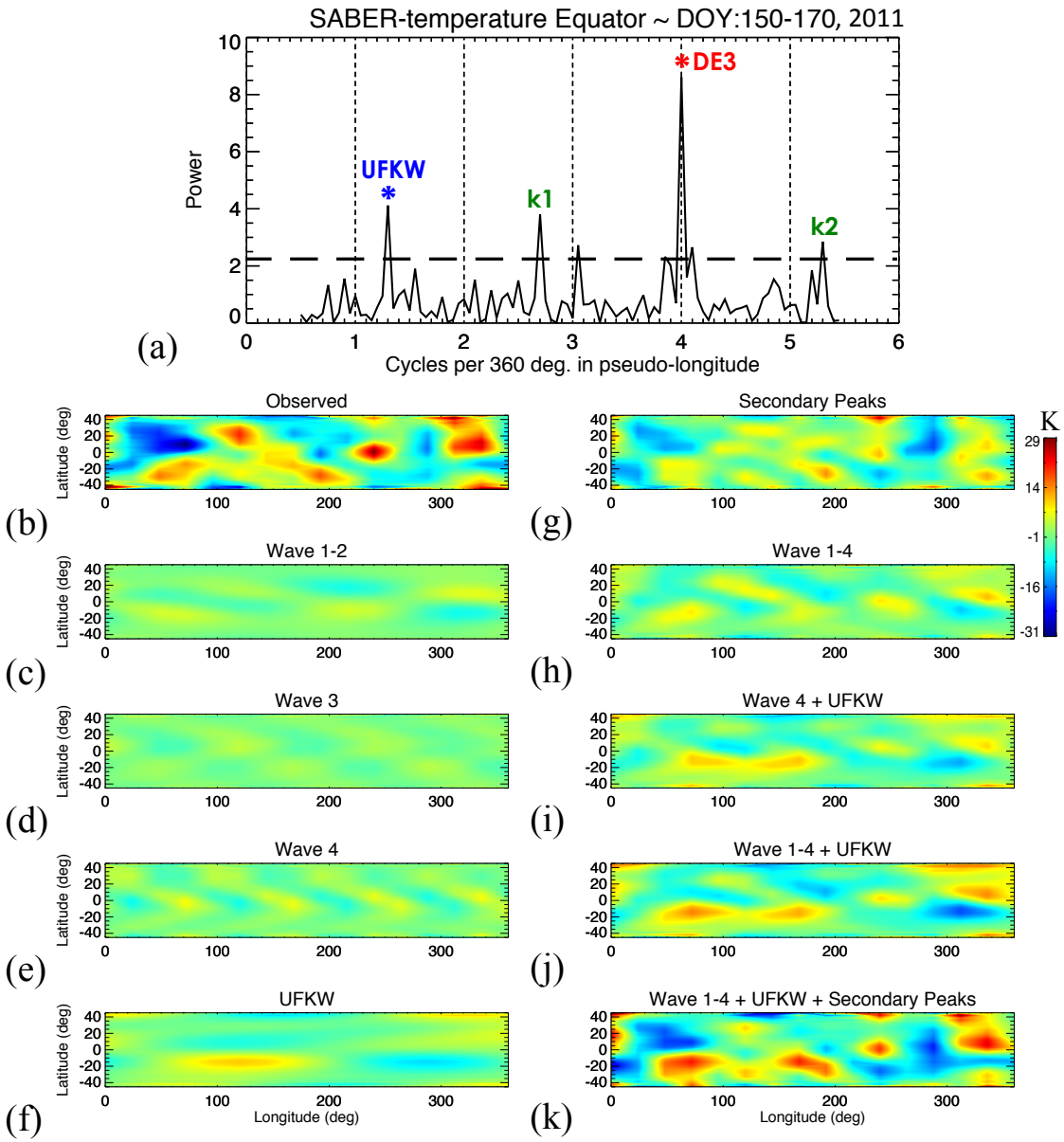

Figure 5.4: The top panel (a) contains the pseudolongitude spectrum centered on DOY 160 of 2011 and constructed using 21 days (from DOY 150 to DOY 170) of SABER temperatures. The UFKW peak near 1.3 cycles (marked in blue), the DE3 peak at 4 cycles (marked in red), and their sidebands near 2.7 and 5.3 (k_1 and k_2 marked in green) are all evident. Note: the horizontal dotted line indicates 95% confidence level. The reconstructed signal is shown in panels b-k: the observations (b), the sum of wave-1 and wave-2 (c), wave-3 (d), wave-4 (e), the UFKW (f), the secondary peaks (g), the sum of wave-1 to wave-4 (h), the sum of wave-4 and the UFKW (i), the sum of wave-1 to wave-4 and the UFKW (j), and the total fit that includes the DE3-UFKW interactions (k).

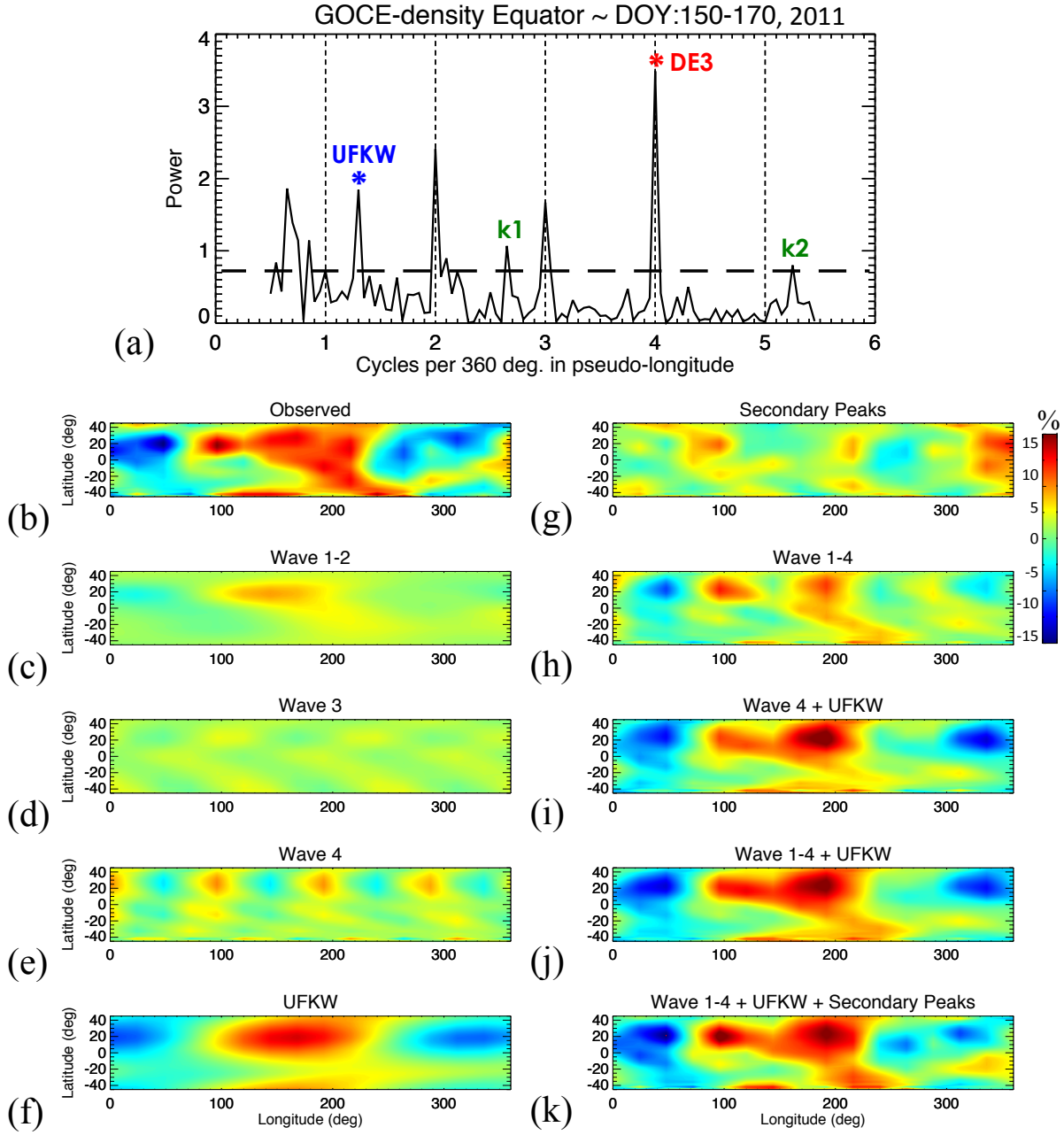

Figure 5.5: Same as Figure 5.4, but for GOCE density. Similar to SABER temperature, the total fit (k) reproduces well the observations (b), indicating that the sum of wave-1 to wave-4, the UFKW, and secondary waves due to the interaction between DE3 and the UFKW can adequately describe the latitude and longitude variability.

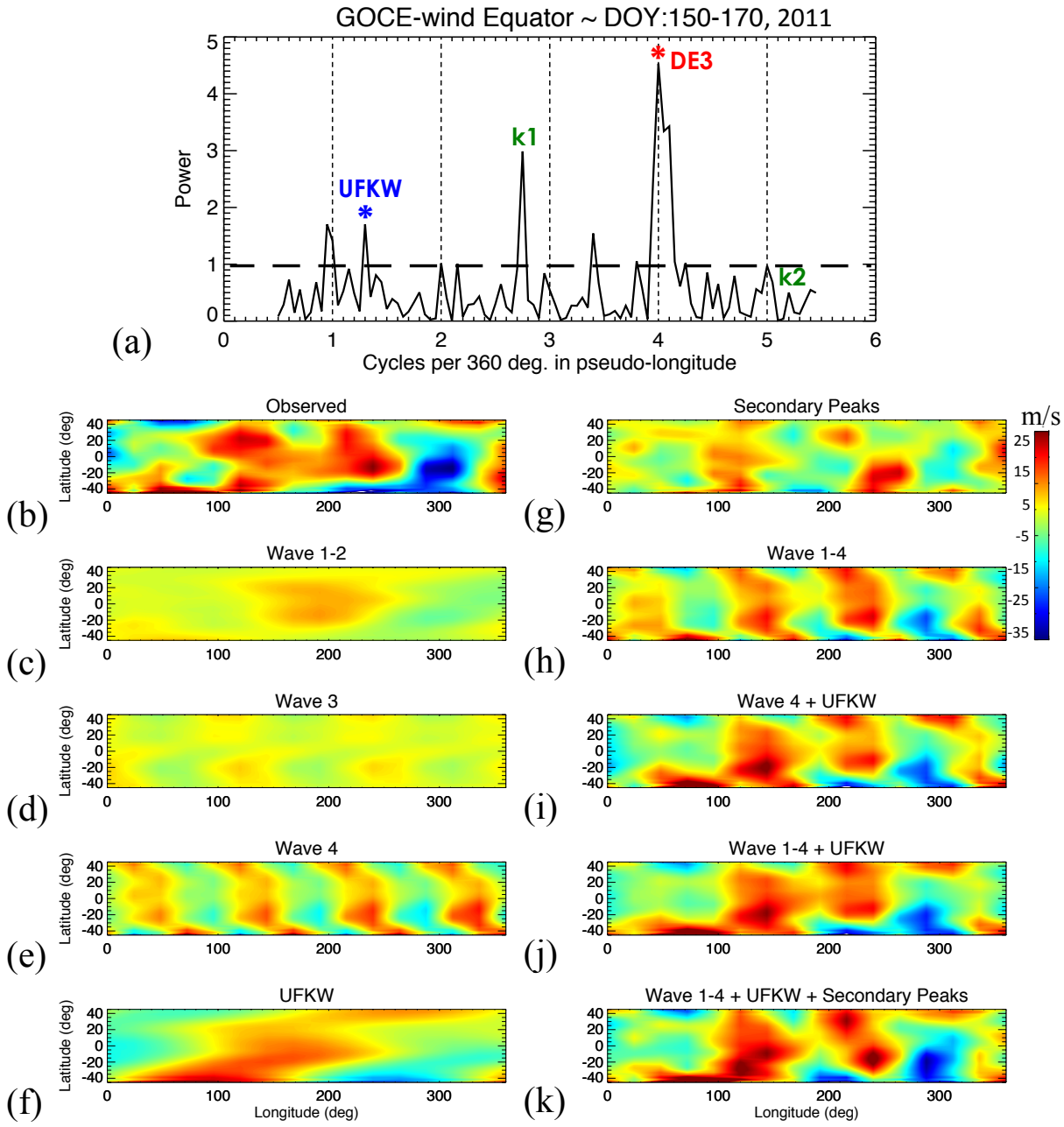

Figure 5.6: Same as Figure 5.4, but for GOCE wind. Similar to SABER temperature and GOCE density, the total fit (k) reproduces well the observations (b).

Figure 5.4a shows the 21-day-average pseudolongitude spectrum for SABER temperature residuals (data after the removal of the ap-S10.7 fits) centered on DOY 160 of 2011 (June 9, 2011). We selected this period because both DE3 and the UFKW have large amplitudes, thus offering the best opportunity to investigate the longitudinal variability due to their interaction. The UFKW peak near 1.3 cycles, the DE3 peak at 4 cycles, and their sideband peaks near 2.7 cycles (k_1) and 5.3 cycles (k_2) are all evident (and marked) in the spectrum displayed in Figure 5.4a. Figure 5.4 also presents the latitude-longitude view of SABER observations (Figure 5.4b), sum of wave-1 and wave-2 (Figure 5.4c), wave-3, wave-4, the UFKW, the secondary peaks (Figures 5.4d, 5.4e, 5.4f, 5.4g), the sum of wave-1 to wave-4 (Figure 5.4h), the sum of wave-4 and the UFKW (Figure 5.4i), the sum of wave-1 to wave-4 and the UFKW (Figure 5.4j), and the total fit including the DE3-UFKW interactions (Figure 5.4k). The total fit is the sum of wave-1 to wave-4, the UFKW, and the interaction between DE3 and the UFKW. Significant latitude-longitude variations are evident in the observations. The total fit (Figure 5.4k) reproduces well the observations (Figure 5.4b), indicating that the sum of wave-1 to wave-4, the UFKW, and the sidebands arising from the DE3-UFKW interaction can adequately describe the observed latitude-longitude variability. Comparing Figure 5.4k with Figure 5.4j, one can see the importance of the secondary waves in generating longitudinal variability. Figure 5.4i demonstrate the importance of the combined effect of wave-4 and the UFKW, while Figure 5.4c-h isolates the contribution due to wave-1,wave-2, wave-3, wave-4, the UFKW, and the sum wave-1 to wave-4.

Variance	SABER-temperature	GOCE-density	GOCE-wind
Wave 1-2	0.167	0.187	0.233
Wave 3	0.157	0.152	0.119
Wave 4	0.292	0.318	0.227
UFKW	0.253	0.356	0.159
Secondary Peaks	0.235	0.193	0.210
Wave 1-4	0.556	0.504	0.705
Wave 4 + UFKW	0.356	0.567	0.394
Wave 1-4 + UFKW	0.687	0.643	0.756
Total Fit	**0.814**	**0.922**	**0.925**

Table 5.1: Variance calculated around the equator (±12° latitude) for each wave component described in Figure 5.4, Figure 5.5, and Figure 5.6. The total fit includes wave-1 to wave-4, the UFKW, and the DE3-UFKW interactions. Note that, after the removal of ap-S10.7 fits, 80% (90%) of the variance in the latitude-longitude variability of SABER (GOCE) can be related to upward propagating waves.

Similar results are found in GOCE data at 260 km, as shown in Figure 5.5 for the density and Figure 5.6 for the wind. The variance for all the wave components calculated around the equator (±12° latitude) is listed in Table 5.1. Note that, after the removal of ap-S10.7 fits, around 65% of the variance in SABER temperature and around 75% in GOCE wind is due to the sum of wave-1 to wave-4 and the UFKW. If we include k_1 and k_2 this value increases to ∼80% for the temperatures and ∼92% for the winds. Although longitude variations due to the UFKW and waves 1-4 dominate, Figures 5.4-5.6, and Table 5.1 demonstrate that the contribution of secondary waves to the total longitude variation can be quite large and should be accounted for.

5.4 Upward Propagating Waves versus Geomagnetic-Solar Effects

In Sections 5.2 and 5.3 we demonstrated the importance of DE3, the UFKW, and their non-linear interactions in determining day-to-day and longitude variability. Here we seek to evaluate

the relative contributions of vertically propagating waves and geomagnetic-solar effects to the observed thermospheric variability. Since geomagnetic activity and solar flux effects are known to be relatively small at 110 km, we can confine ourselves to GOCE data in this context. Given the many gaps in the 2010 GOCE dataset and the fact that 2011 is intermediate between 2010 and 2012 in terms of geomagnetic activity and thus more generally representative, we performed our analysis on GOCE data for 2011 only.

Daily S10.7 and 3-hour ap values for the year 2011 are shown in Figure 5.7a. The variance due to S10.7/ap effects, DE3, UFKW, and the total fit is shown in Figure 5.7b for GOCE residual densities and in Figure 5.7c for GOCE residual winds. The total fit includes wave-1 to wave-4, the UFKW, and the sidebands produced by the DE3-UFKW interaction (k_1 and k_2). Individually, DE3 and the UFKW are responsible for 10% to 40% of the total variance, while their combined effect ranges from 20% to 60% during most of the year. What we discover by looking at Figure 5.7b and Figure 5.7c is that the ap/S10.7 contribution as embodied in the regression relationship is limited to 10-20%. As previously mentioned, geomagnetic and solar effects are likely underestimated by the ap/S10.7 fits. This would be caused by geomagnetic and solar EUV variability not captured by the ap and S10.7 indices (which are only a partial representation of the global geomagnetic and EUV variability). These errors are probably embedded in the unexplained variance (difference between the total fits and the unit), which varies from 10% to 40% during most of the year. Upward propagating migrating tides (and their interactions with the UFKW) are also candidates for some unexplained variance shown in Figure 5.7, but their effect is not the primary interest of this study. The variance of the total fits (i.e., 60-80%) indicates that during 2011 for solar low and geomagnetically quiet conditions the majority of thermospheric variability can be traced back to vertically propagating waves. This suggests that, in relatively quiet geomagnetic periods, waves coming from below (and their interactions) can significantly influence the dynamics of the thermosphere system, imposing even greater variability than that due to geomagnetic and solar effects. Note that these results are limited to solar and geomagnetic quiet conditions and one could envision that analysis of a set of observations characterized by a series of persistent and extreme

space weather events would lead to very different conclusions.

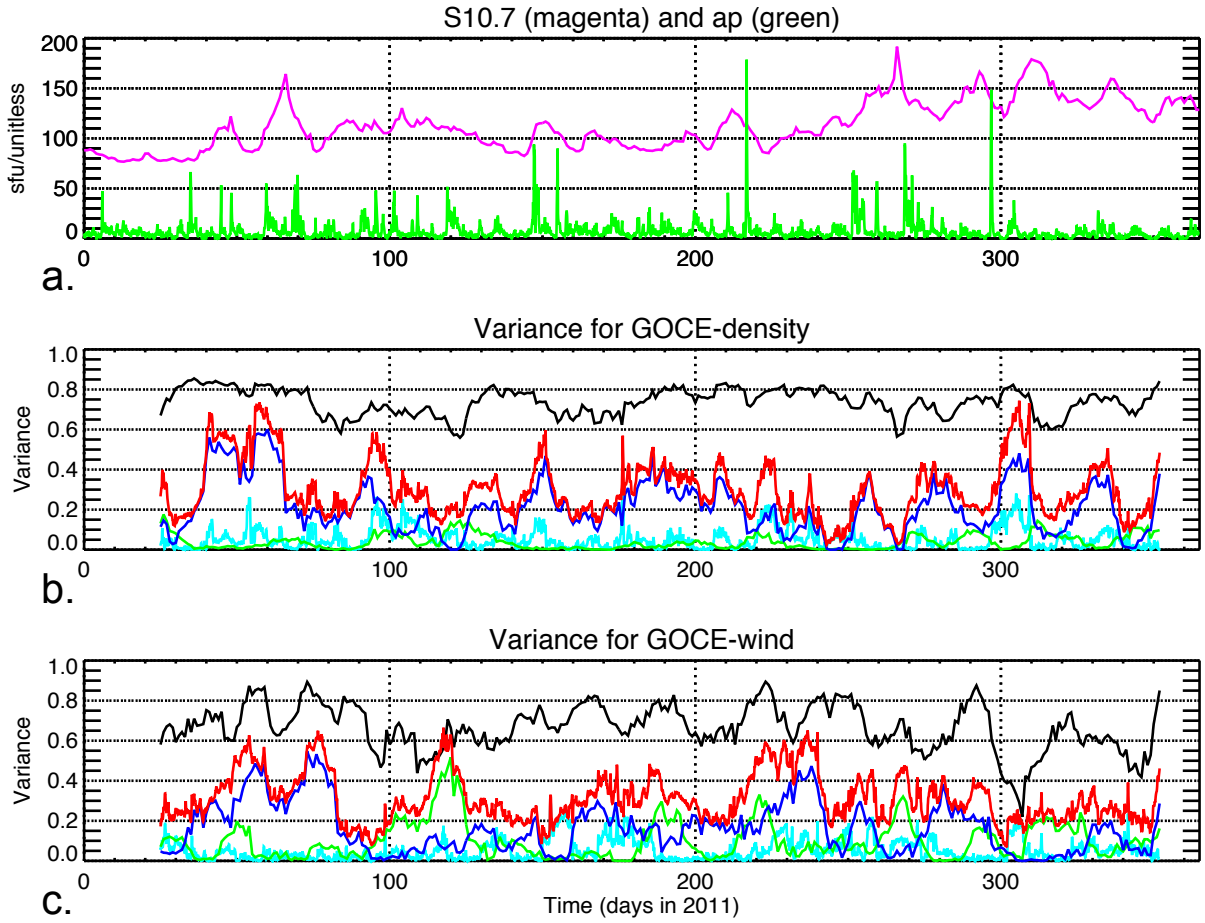

Figure 5.7: (a) Daily S10.7 (magenta line) and 3-hour ap (green line). (b) Variance of the total fit (black line), UFKW+DE3 (red line), DE3 (blue line), UFKW (green line), S10.7/ap (cyan line) for GOCE density. (c) Same as (b) except for GOCE wind. The total fit includes wave-1 to wave-4, the UFKW, and the sidebands produced by the DE3-UFKW interaction (k_1 and k_2). Individually, DE3 and the UFKW are responsible for 10% to 40% of the total variance, while their combined effect ranges from 20% to 60% during most of the year. The ap/S10.7 contribution is limited to 10-20%, while the variance of the total fits ranges between 60% and 80%.

5.5 Conclusions

Using SABER temperatures near 110 km and GOCE winds and densities near 260 km, we demonstrated the existence of secondary waves produced by nonlinear interactions between DE3 and the UFKW, two dominant sources of thermospheric variability as presented in Chapter 4. These sidebands are shown to be responsible for up to 10% to 20% of the day-to-day and longitudinal variability. In particular, we determined that at low- to mid-latitudes and for geomagnetically quiet and solar low conditions, the combined effect of DE3, the UFKW, and their interactions account for 20% to 60% of the total variability; while the combined effect of wave-1 to wave-4, the UFKW, and DE3-UFKW interactions explain 60-80% of the total variability, and only up to 20-40% may be ascribed to geomagnetic and solar effects.

To summarize our findings, for solar and geomagnetic quiet conditions we found:

(1) evidence of nonlinear interactions between DE3 and the UFKW both in the lower and middle thermosphere.

(2) that secondary waves due to DE3-UFKW interactions all combine to account for over 50% of the total short-term variability, while the sum of waves 1-4, the UFKW, and the secondary waves account for up to 80% of the observed variability.

(3) that during 2011 between 60% and 80% of the total thermospheric variability can be traced back to vertically propagating waves and their interactions, and up to ∼40% is due to geomagnetic and solar effects.

Nonlinear wave-wave interactions are shown to produce secondary waves with amplitudes that can be as large as the waves producing them. This demonstrates that wave-wave interactions are responsible for non-negligible spatial and temporal variability, and should be accounted for when analyzing thermospheric variability in nonlinear models and satellite data. Together with the results presented in Chapter 4, this study demonstrates that vertically propagating waves and their interactions represent an important contribution to thermosphere variability, and point to the

importance of lower atmosphere coupling as an important contributor to the thermosphere weather, at least in the absence of major solar-driven variability.

Chapter 6

WAVE COUPLING FROM MERRA/TIME-GCM

In Chapter 4 we demonstrated that vertically propagating waves and their nonlinear interactions constitute an important contribution to thermosphere variability. In particular, we showed that DE3 and UFKW propagate from 110 km to 260 km on daily-monthly time scales, and account for large day-to-day and longitudinal variability at both heights. Furthermore, in Chapter 5 we demonstrated the presence of secondary waves generated by nonlinear interactions between DE3 and the UFKW both in the lower and middle thermosphere, and that DE3, UFKW and the secondary waves due to their interaction all combine to account for over 50% of the total short term variability, while the sum of longitudinal waves 1-4, the UFKW, and the secondary waves account for up to 80% of the observed variability, and only up to 20-40% may be ascribed to geomagnetic and solar effects.

The discussion in Chapters 4 and 5 presented some outstanding questions regarding the effect of dissipation and zonal mean winds on the vertical coupling of waves between the lower and middle thermosphere. In this chapter we aim at addressing these issues using a state-of-the-art 2009 TIME-GCM run with the lower boundary condition based on ∼30-km MERRA reanalysis data (after Häusler et al. [2014] [76]). The purpose of this chapter is to delineate how the horizontal structures of upward propagating waves evolve with height and understand the processes responsible for this evolution. Section 6.1 presents an overview of the data employed, the methodology followed, and the objective of this study; Section 6.2 provides an analytic representation of upward propagating waves in a dissipative rotating atmosphere subject to the effect of zonal mean winds; Section 6.3

contains the model results; while Section 6.4 summarizes the conclusions.

6.1 Introduction

In this work we employ a TIME-GCM simulation covering all of 2009 that is forced by interpolated 3-hourly MERRA dynamical fields at the lower boundary of ∼30 km, as described in Häusler et al. [2014] [76]. This simulation uses the high-resolution version of the TIME-GCM, corresponding to 2.5° x 2.5° in latitude and longitude, four grid points per scale height in the vertical direction, and 60-second time step. The 3-hourly MERRA resolution inherently accounts for the variability in the diurnal and semidiurnal tides, as well as the PWs, generated in the troposphere. Since MERRA is physics-based and strongly constrained by assimilated global observations, we view MERRA as the most realistic specification possible of tides and planetary waves at the lower boundary of the TIME-GCM. As explained in Chapter 2, the MERRA lower boundary condition provides the best state-of-the-art specification of the upward-propagating wave spectrum at 30 km altitude, whereas the TIME-GCM provides the best state-of-the-art global simulation of the vertical evolution of this wave spectrum through the thermosphere.

Figure 6.1 presents the latitude versus zonal wavenumber (panels a and a') and latitude versus period (panels b and b') representation of the main diurnal tides and short-period (< 6 days) waves present at 260 km and 110 km in the 2009 model run. As one can see from Figure 6.1, the main non-migrating diurnal tides are DE3, DE2 (present at 110 km, but not at 260 km), and DE1, while the main short-period wave is the UFKW with zonal wavenumber -1 and period ranging from 2.5 to 3.5 days. In order to focus and confine this work to reasonable size, emphasis is placed on DE3 and UFKW, i.e., waves with horizontal phase speeds that are sufficiently large that critical levels, where the Doppler-shifted phase speed goes to zero, are not encountered (for more details on this topic, see discussion in Section 6.2).

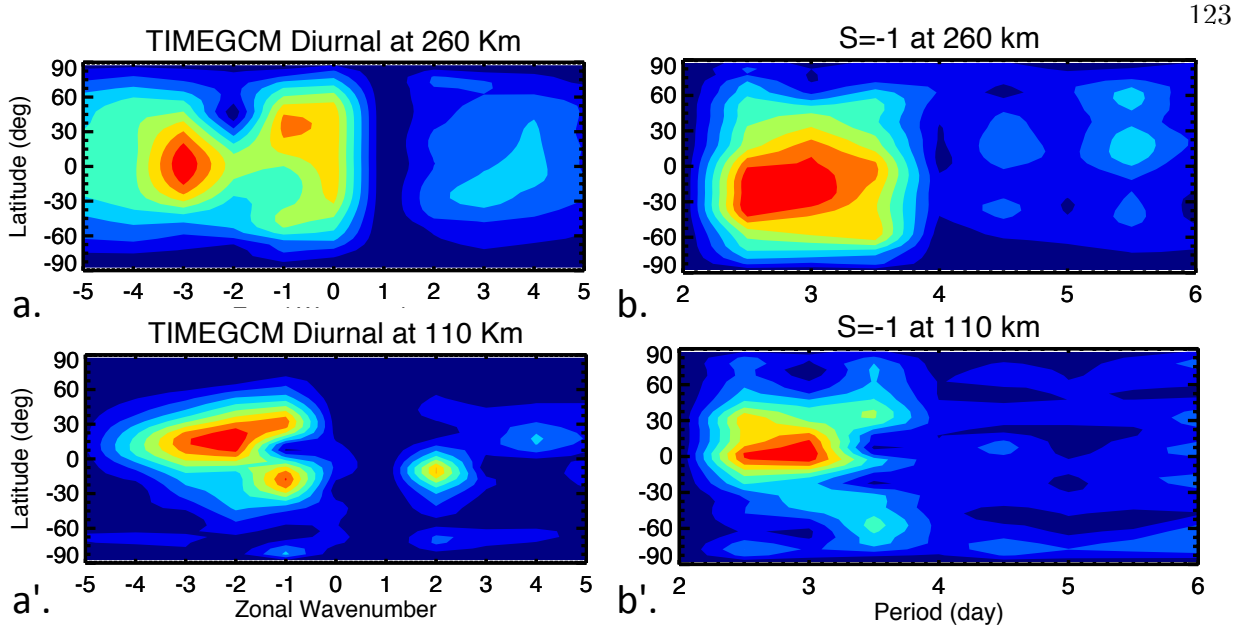

Figure 6.1: Latitude versus zonal wavenumber plot of the diurnal tide at 260 km (panel a) and 110 km (panel a′), and latitude versus period plot for zonal wavenumber -1 at 260 km (panel b) and 110 km (panel b′) for 2009 MERRA-forced TIME-GCM. Note strong DE3 amplitudes at both heights and the presence of a strong UFKW signal at a period ranging from 2.5 to 3.5 days.

Figure 6.2 shows output from the 2009 TIME-GCM simulation, which includes the latitude-temporal structures of DE3 and 3-day UFKW temperature amplitudes at 110 km and 260 km altitude during 2009. DE3 amplitudes are extracted on a daily basis, whereas UFKW amplitudes are obtained in 5-day moving windows (i.e., 2 full UFKW cycles). Note that DE3 and the UFKW possess similar amplitudes and intermittency to those shown in Figures 4.3 and 4.5 of Chapter 4, although the latter correspond to 2011 and not 2009. Similar to the results presented in Chapter 4, there is no exact one-to-one correspondence between the DE3 and UFKW latitude-time structures at 110 km and those at 260 km (see also Figure 6.3).

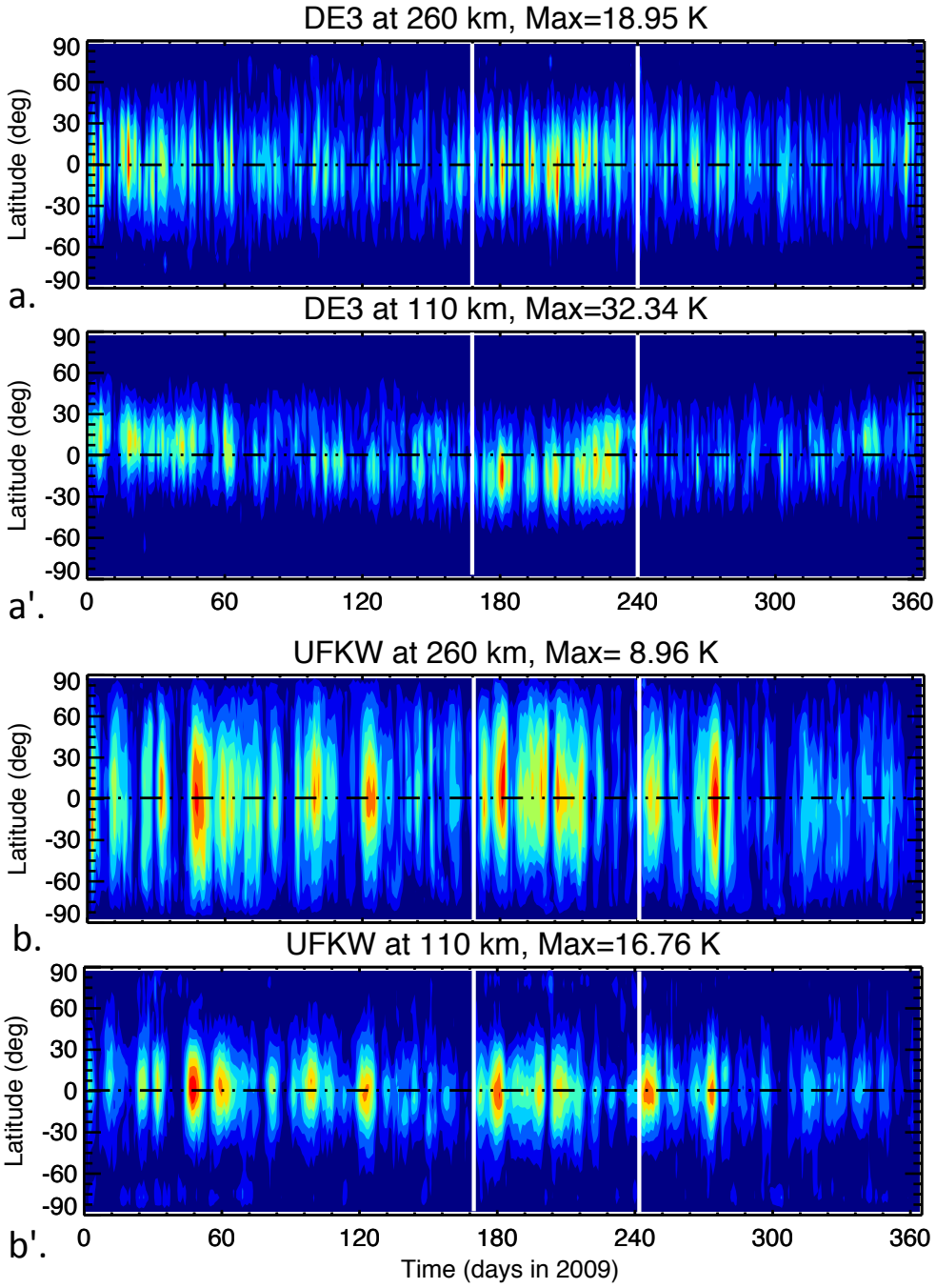

Figure 6.2: Time series of daily DE3 amplitudes at 260 km (panel a) and 110 km (panel a′), and 3-day UFKW amplitudes at 260 km (panel b) and 110 km (panel b′) during 2009. Large day-to-day and seasonal variability at both heights is present. Temperature amplitudes up to 32 K (17 K) are found in DE3 (UFKW) at 110 km and up to 19 K (9 K) in DE3 (UFKW) at 260 km. Similar intra- and inter-seasonal variability between the two heights, with some degree of asymmetry especially evident in DE3 at 110 km. Latitudinal broadening with height also evident. Note: the white vertical lines indicate the 70-day period analyzed in Figure 6.3.

Figure 6.2 also shows that while at 110 km DE3 amplitudes are largely latitudinally asymmetric, at 260 km these are much more symmetric about the equator; while UFKW tends to be symmetric at both heights, similar to what observed in SABER and GOCE data as presented in Chapter 4. This behavior is explained by the asymmetric component at 110 km that is dissipated by molecular diffusion during the course of its vertical propagation to 260 km due to its comparatively short vertical wavelength [Lindzen and Hong, 1974 [131]; Forbes and Garrett, 1979 [44]]. Additionally the latitude structures in DE3 and the UFKW shown in Figure 6.2 are broader at 260 km than at 110 km. This feature is also found in SABER and GOCE observations, as presented in Chapter 4, and is discussed in greater detail in Sections 6.2 and 6.3.

Further analyzing the MERRA-forced TIME-GCM run, evidence is found of nonlinear interactions between DE3 and a 3-day UFKW. As discussed in detail in Chapter 5, the modulation of DE3 by a 3-day UFKW produces two sidebands given by the sum and differences of the zonal wavenumbers and frequencies. In a UT-longitude frame [Teitelbaum and Vial, 1991 [205]] the sideband waves are the sum (K2) and difference (K1) waves with periods of 0.75 and 1.5 days and zonal wavenumbers -4 and -2, respectively. Figure 6.3 shows the time series of DE3 (panels a and a'), the 3-day UFKW (panels b and b'), sideband K1 with zonal wavenumber -2 and period 1.5 days (panels c and c'), and sideband K2 with zonal wavenumber -4 and period 0.75 days (panels d and d') for the 70-day period ranging from DOY 170 to DOY 240 (indicated by white vertical lines in Figure 6.2) at 110 km and 260 km. This period is chosen according to the large amplitudes found in DE3 and the UFKW. Amplitudes up to 32 K (18 K) and 16 K (8 K) are found at 110 km (260 km) in DE3 and UFKW, respectively; while K1 (K2) shows amplitudes up to 8 K (10 K) at 110 km and 4 K (4 K) at 260 km.

Using the vertical progression of the phases between 70 and 120 km, the vertical wavelengths of DE3, UFKW, K1, and K2 are calculated to be in the range 52-55 km for DE3, 59-61 km for the UFKW, 41-44 km for K1, and 39-42 for K2. These vertical wavelength values of DE3 are in line with the values of 56 km and 30 km for the first symmetric and anti-symmetric component reported by Truskowski et al. [2014] [209]. [Note that thermospheric DE3 is mainly due to its

symmetric mode, but also has some latitudinal asymmetry due to its anti-symmetric components, particularly at lower heights as previously discussed]. Vertical wavelengths of ∼60 km for UFKW are also similar to the 56 km reported by Forbes [2000] [40] for a 3-day Kelvin wave. Interestingly, and similar to the results presented in Chapter 5, there is no evident correlation between the maxima in the sidebands and the maxima in DE3 and the UFKW. This is likely due to the fact that the nonlinear interactions generating these secondary waves are occurring at lower heights, i.e., these waves propagate vertically from the low-middle atmosphere as independent waves and thus are affected by dissipation and mean winds differently than the primary waves. The modulation of DE3 by the 3-day UFKW is also evident in the time series of DE3 (see panels a and a'), where a clear 3-day modulation can be seen both at 110 km and 260 km. Figure 6.3e, showing the periodogram calculated around the equator of daily DE3 amplitudes at 110 km (red line) and 260 km (blue line), presents evidence of this 3-day modulation. Looking at panels b and b' of Figure 6.3, one can also see a ∼7-day modulation of the UFKW amplitudes, demonstrated by the periodogram in panel e'. Investigating the origin of this modulation, likely associated to the interaction of the UFKW with a longer period PW, is beyond the scope of this work and is left for future investigation.

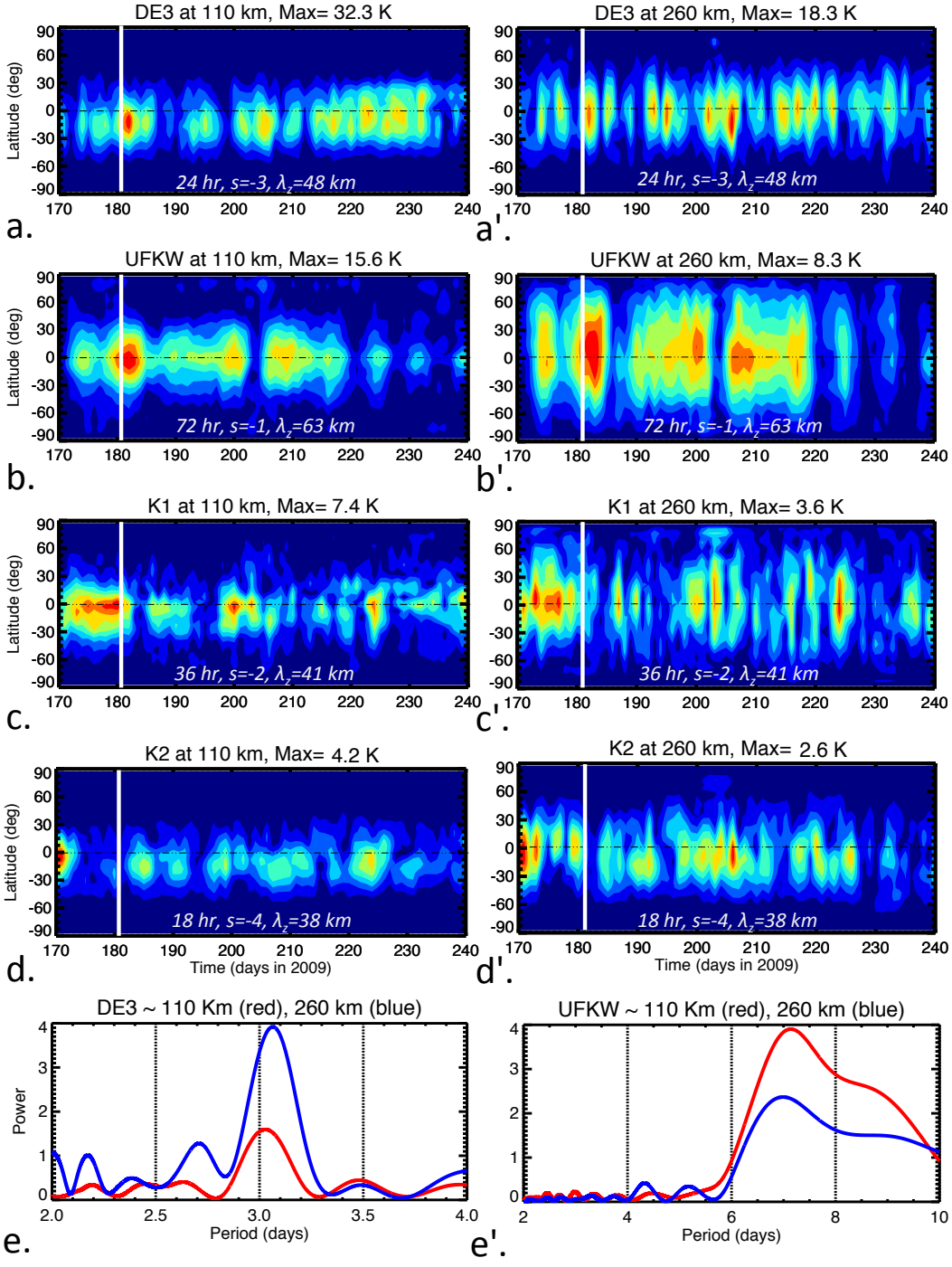

Figure 6.3: Latitude versus time representation for the 70-day period DOY 170-240 at 110 km (260 km) of: panels a (panel a′) DE3, panels b (panel b′) UFKW, panels c (panel c′) K1, panels d (panel d′) K2. The periodogram of DE3 and UFKW at 110 km (red line) and 260 km (blue line) is shown in panels e and e′, respectively. Note the strong 3-day modulation of DE3 amplitudes due to the interaction with the UFKW and a significant 7-day oscillation in the UFKW. The white vertical line indicates DOY 180, discussed in Figures 6.4 and 6.5.

In this chapter, we utilize the realism of the MERRA-forced TIME-GCM simulation, and a new analytic formulation of the latitudinal dependency on dissipation and mean winds for upward propagating waves, to gain new insights into the physics of the vertical wave coupling process in the thermosphere. Specifically, we aim at addressing the latitudinal asymmetries observed in DE3 and the UFKW and the broadening of latitude structures with altitude. The main objective of this chapter is to gain a better understanding on how waves subject to the combined effect of dissipation and zonal mean winds evolve with height in the thermosphere.

6.2 Mathematic Formulation

In the classical theory of atmospheric tides [Chapman and Lindzen, 1970 [18]], where the background atmosphere is assumed to be inviscid and independent of latitude, the linearized response to thermal or gravitational forcing reduces to an eigenfunction-eigenvalue problem where the eigensolutions (Hough functions) of Laplace's tidal equation describe the horizontal structures of each mode, and the eigenvalues (equivalent depths) fix each mode's vertical structure (see Appendix A). However, as explained in Chapter 1, for upper mesosphere and thermosphere global scale waves the effects of diffusion (momentum and heat) and planetary rotation renders the governing equations inseparable in height and latitude (meaning that the height structures vary with latitude, or equivalently, the horizontal structures vary with height), thus requiring a numerical solution to the problem.

In the following, we present the so-called f-plane [Forbes and Hagan, 1979 [44]] and beta-plane (or β-plane) [Lindzen, 1968 [125]] approximations. On a rotating sphere, such as Earth, the Coriolis parameter $f = 2\Omega sin\theta$ varies with the sine of latitude; in the f-plane approximation this variation is ignored and a value of f appropriate for a particular latitude is used throughout the domain (i.e., f is set to a constant value). This approximation can be visualized as a tangent plane touching the surface of the sphere at this latitude. In analogy with the f-plane, when f is set to vary lineally in the north-south direction this approximation is termed the β-plane, even though it no longer describes dynamics on a hypothetical tangent plane. Note: usually the β-

plane approximation is applied at the equator, while the f-plane is applied at other latitudes. The advantage of the f-plane and β-plane approximations over more accurate formulations is that they capture the most important dynamical effects of sphericity, without the complicating geometric effects, which are not essential to describe many phenomena.

Using the f-plane approximation, Section 6.2.1 shows that for equatorially-trapped waves, such as DE3 and the UFKW, some account must be taken of the wave's Doppler-shifted frequency and the local planetary rotation rate, which delineates whether a wave is vertically-propagating or evanescent below or above, respectively, a 'critical latitude' [Ekanakaye et al., 1997 [34]]. Additionally, using the β-plane approximation, Section 6.2.2 provides a solution to the momentum equations for equatorially-trapped waves with meridional velocity identical to zero (i.e., DE3 and UFKW), and derives an expression describing the latitude-height behavior of these waves in a rotating atmosphere subject to both dissipation and zonal mean winds.

6.2.1 F-Plane Approximation

In the absence of dissipation, the linearized eastward (u') and northward (v') momentum equations for a rotating planar atmosphere on a background state with only mean zonal wind U acting can be written as [Lindzen, 1972 [127]]:

$$\frac{\partial u'}{\partial t} + \frac{U}{acos\theta}\frac{\partial u'}{\partial \phi} + u' sin\theta\Big(2\Omega + \frac{U}{acos\theta}\Big) = -\frac{1}{acos\theta}\frac{\partial}{\partial \phi}\Big(\frac{\partial p}{\rho_0}\Big) \tag{6.1}$$

$$\frac{\partial v'}{\partial t} + \frac{U}{acos\theta}\frac{\partial v'}{\partial \phi} - 2v' sin\theta\Big(\Omega + \frac{U}{acos\theta}\Big) = -\frac{1}{a}\frac{\partial}{\partial \theta}\Big(\frac{\partial p}{\rho_0}\Big) \tag{6.2}$$

where ϕ and ρ are longitude and latitude. [Note: mean meridional winds can be omitted due to their small amplitude.]

If we assume a solution of the form u, v, $p \propto \hat{u}$, $\hat{v}$, $\hat{p}\ e^{i(\sigma t + kx + my)}$, where a is Earth's radius (i.e., R_E in Chapter 3), $k = s/a$ and m is the meridional wavenumber, then the terms $\frac{\partial}{\partial t} + \frac{U}{acos\theta}\frac{\partial}{\partial \phi}$ will be equal to $i\Big(\sigma + \frac{sU}{acos\theta}\Big) = -i\sigma_D$, where $\sigma_D = \sigma + \frac{s\bar{U}}{acos\theta}$ is the Doppler-shifted (or intrinsic)

frequency. If we then assume a constant Coriolis parameter $f = 2\Omega sin\theta$, Equations 6.1 and 6.2 can be expressed as:

$$(f^2 - \sigma_D^2)\hat{u} = \sigma_D k \frac{\partial p}{\rho_0} - imf\frac{\partial p}{\rho_0} \tag{6.3}$$

$$(f^2 - \sigma_D^2)\hat{v} = \sigma_D m \frac{\partial p}{\rho_0} + ikf\frac{\partial p}{\rho_0}. \tag{6.4}$$

and thus the divergence of the velocity field (X) is equal to

$$X = \nabla \cdot \vec{u} = \frac{\partial \hat{u}}{\partial x} + \frac{\partial \hat{v}}{\partial y} + \frac{\partial \hat{w}}{\partial z} = ik\hat{u} + im\hat{v} + \frac{\partial \hat{w}}{\partial z} \tag{6.5}$$

hence, solving for $\hat{u}$ and $\hat{v}$ in Equations 6.3 and 6.4 and substituting into Equation 6.5, we obtain

$$X = -\frac{i\sigma_D(k^2 + m^2)}{\sigma_D^2 - f^2}[\frac{\partial p}{\rho_0}] + \frac{\partial \hat{w}}{\partial z} \tag{6.6}$$

From Classical Theory [Chapman and Lindzen, 1970 [18]] we know that $X = \frac{i\sigma_D}{gh_n}\frac{\partial p}{\rho_0} + \frac{\partial \hat{w}}{\partial z}$, where h_n is equivalent depth, thus using Equation 6.6. we can write

$$gh_n = \frac{\sigma_D^2 - f^2}{k^2 + m^2} \tag{6.7}$$

For $f = 0$, gh_n is a measure of the square of the wave's Doppler-shifted phase speed. Alternatively, h_n is the depth of a fluid in which the phase speed of shallow-water gravity waves is $\sigma/K = \sqrt{gh_n}$, where $K = \sqrt{k^2 + m^2}$. However, for a rotating atmosphere interpretation of h_n as a depth can be non-physical since h_n is negative for $\sigma_D^2 < f^2$. As discussed in Chapter 1, negative equivalent depths correspond to exponentially decaying solutions (trapped waves), or non-propagating solutions, that are physically meaningful in the atmosphere.

The above approach can be used to reduce the spherical problem to a local one-dimensional problem by calculating the vertical propagation of a gravity wave 'equivalent' to that of the tide. For a rotating plane, for instance, one would take the frequency of the gravity wave to be identical to that of the tide (σ_D), the zonal wavenumber to be the same as that of the tide at the latitude

of the rotating plane ($m = s/(acos\theta)$), and the meridional wavenumber (k) is chosen so that the vertical wavelength of the gravity wave and tide are the same in the absence of dissipation [Lindzen and Blake, 1972 [127]].

The f-plane model can also be applied to trapped waves, i.e., tides with negative equivalent depths. In fact, consider the planar rotation rate to be equivalent to Earth's local rotation frequency $f = 2\Omega sin\theta$. Then, for a diurnal tide in the absence of zonal mean winds, $\sigma^2 - f^2 = \sigma^2 - 4\Omega^2 sin^2\theta$ implies a negative equivalent depth poleward of 30° latitude, and positive equivalent depth at lower latitudes, which furthermore implies that the diurnal tide is propagating at low latitudes and trapped or evanescent in its vertical structure at high latitudes. For semidiurnal and higher-frequency tides, there are no latitudes where negative equivalent depths or decaying solutions occur (they are all vertically-propagating). For the UFKW with a period of 2.5 days trapped modes are polarward of about 15° latitude. Note that any Doppler-shifting effects due to mean winds can change the latitudinal shape of upward propagating waves and modify the latitude at which the condition $\sigma_D^2 - 4\Omega^2 sin\theta^2 = 0$ occurs (see discussion in Section 6.3).

6.2.2 Beta-Plane Approximation

The momentum equations that include eddy and molecular dissipation and ion drag can be written as:

$$\frac{\partial u}{\partial t} - 2\Omega sin\theta v = -\frac{1}{a\rho_0 cos\theta}\frac{\partial p}{\partial \phi} + (\kappa_{eddy} + \frac{\mu}{\rho_0})\frac{\partial^2 u}{\partial z^2} - \lambda_{ion} u \tag{6.8}$$

$$\frac{\partial v}{\partial t} + 2\Omega sin\theta u = -\frac{1}{a\rho_0}\frac{\partial p}{\partial \theta} + (\kappa_{eddy} + \frac{\mu}{\rho_0})\frac{\partial^2 v}{\partial z^2} - \lambda_{ion} sin^2 I v \tag{6.9}$$

where we assumed isotropic ion drag λ_{ion} (note that this assumption will not have any implications, since later we impose the condition $v \equiv 0$).

Using the β-plane approximation, around the equator $sin\theta \simeq \theta = y/a$ and $cos\theta \simeq 1$, so $2\Omega sin\theta = \frac{2\Omega y}{a} = \beta y$, where $\beta = \frac{2\Omega}{a}$, thus Equations 6.8 and 6.9 can be written as

$$\frac{\partial u}{\partial t} - \beta y v = -\frac{1}{\rho_0}\frac{\partial p}{\partial x} + (\kappa_{eddy} + \frac{\mu}{\rho_0})\frac{\partial^2 u}{\partial z^2} - \lambda_{ion} u \tag{6.10}$$

$$\frac{\partial v}{\partial t} + \beta y u = -\frac{1}{\rho_0}\frac{\partial p}{\partial y} + (\kappa_{eddy} + \frac{\mu}{\rho_0})\frac{\partial^2 v}{\partial z^2} - \lambda_{ion} sin^2 I v \tag{6.11}$$

If we assume a solution of the form u, v, $p \propto \hat{u}$, $\hat{v}$, $\hat{p}\ e^{i(\sigma_D t + kx + k_z)}$ Equations 6.10 and 6.11 become

$$i\sigma_D \hat{u} - \beta y \hat{v} = -\frac{1}{\rho_0} ik\hat{p} - \left[(\kappa_{eddy} + \frac{\mu}{\rho_0})k_z^2 + \lambda_{ion}\right]\hat{u} \tag{6.12}$$

$$i\sigma_D \hat{v} + \beta y \hat{u} = -\frac{1}{\rho_0}\frac{\partial p}{\partial y} - \left[(\kappa_{eddy} + \frac{\mu}{\rho_0})k_z^2 + \lambda_{ion} sin^2 I\right]\hat{v} \tag{6.13}$$

We now want to verify whether there is a solution for which v is identical to 0 ($v \equiv 0$). For this case Equation 6.12 becomes

$$i\sigma_D \hat{u} = -\frac{1}{\rho_0} ik\hat{p} - \left[(\kappa_{eddy} + \frac{\mu}{\rho_0})k_z^2 + \lambda_{ion}\right]\hat{u} \tag{6.14}$$

and thus $i\left[\sigma_D \hat{u} - i[(\kappa_{eddy} + \frac{\mu}{\rho_0})k_z^2 + \lambda_{ion}]\right]\hat{u} = -\frac{1}{\rho_0} is\hat{p}$. Considering then $\nu_r = (\frac{2\pi}{\lambda_z})^2(\kappa_{eddy} + \frac{\mu}{\rho_0}) + \lambda_{ion}$, where ν_r is the 'Rayleigh friction coefficient' and k_z is expressed as $k_z = 2\pi/\lambda_z$, we can rewrite Equations 6.12 and 6.13 as

$$i(\sigma_D - i\nu_r)\hat{u} = -\frac{1}{\rho_0} ik\hat{p} \tag{6.15}$$

$$\beta y \hat{u} = -\frac{1}{\rho_0}\frac{\partial p}{\partial y} \tag{6.16}$$

Taking the y-derivative of Equation 6.15 yields the expression $i(\sigma_D - i\nu_r)\frac{\partial \hat{u}}{\partial y} = -\frac{1}{\rho_0} ik\frac{\partial \hat{p}}{\partial y}$, which can be written as

$$-\frac{1}{\rho_0}\frac{\partial \hat{p}}{\partial y} = \frac{1}{k}(\sigma_D - i\nu_r)\frac{\partial \hat{u}}{\partial y} \tag{6.17}$$

Note that although σ_D is latitude dependent, we ignore this dependence as a first order approximation around the equator. Substituting Equation 6.17 into Equation 6.16 we derive the expression:

$$\beta y\hat{u} = \frac{1}{k}(\sigma_D - i\nu_r)\frac{\partial \hat{u}}{\partial y} \tag{6.18}$$

which can be written as

$$\frac{\partial \hat{u}}{\partial y} - \frac{k\beta}{\sigma_D - i\nu_r} y\hat{u} = 0 \tag{6.19}$$

Equation 6.19 has a solutions of the form

$$\hat{u} = F \exp\left(\frac{k\beta}{2(\sigma_D - i\nu_r)} y^2\right) \tag{6.20}$$

If we manipulate the exponential as

$$e^{\frac{c}{a-ib}} = e^{\frac{c}{a-ib}\frac{a+ib}{a+ib}} = e^{\frac{c(a+ib)}{a^2+b^2}} = e^{\frac{ca}{a^2+b^2}} e^{\frac{icb}{a^2+b^2}} \tag{6.21}$$

where $a = \sigma_D$, $b = \nu_r$, and $c = k\beta/2$, and consider the Doppler-shifted frequency $\sigma_D = \sigma + \frac{s\bar{U}}{acos\theta}$ (with $cos\theta \sim 1$), we can write:

$$\hat{u} = F \exp\left(\frac{k\beta(\sigma + \frac{s\bar{U}}{a})}{2[(\sigma + \frac{s\bar{U}}{a})^2 + \nu_r^2]} y^2\right) \exp\left(\frac{ik\beta\nu_r}{2[(\sigma + \frac{s\bar{U}}{a})^2 + \nu_r^2]} y^2\right) \tag{6.22}$$

which, given that $k = s/a$ and s=-3 for DE3 and s=-1 for the UFKW, is Gaussian distribution with e^{-1} width equal to $\left|\frac{2[(\sigma+\frac{s\bar{U}}{a})^2+\nu_r^2]}{k\beta(\sigma+\frac{s\bar{U}}{a})}\right|^{1/2}$.

The relationship expressed in Equation 6.22 for $\hat{u}$ describes the latitudinal shape of an equatorial wave with zero meridional wind (i.e., UFKW and symmetric mode of DE3), which is a function of the Rayleigh friction coefficient ν_r and the zonal mean zonal wind $\bar{U}$. Both ν_r and $\bar{U}$ are strongly dependent on height and latitude, which means that the e^{-1} width of the gaussian and the latitude of maximum will vary with height (see Section 6.3 for estimations).

6.3 Model Results

In Section 6.2.2 we derived Equation 6.22, describing the combined effect of Rayleigh friction and Doppler-shifting due to zonal mean winds on the latitudinal shape of an equatorial wave with zero meridional wind (i.e., UFKW and symmetric mode of DE3). In this section, we use Equation 6.22, the model zonal mean zonal winds, and a vertical profile of a latitudinally-independent Rayleigh friction coefficient (where eddy diffusion is neglected as a first assumption) to highlight some characteristics of upward propagating waves in the thermosphere. As explained below the focus here is on the broadening of the latitude structures with height and on latitudinal asymmetries.

We start by looking at the model height versus latitude structures for DOY 180 of DE3 (i.e., panel *a*), 3-day UFKW (panel *b*), K1 (panel *c*), K2 (panel *d*) amplitudes in comparison to the zonal mean zonal winds extracted from the model (panel *e*), as shown in Figure 6.4. Note: DOY 180 is chosen since both DE3, UFKW, and secondary waves are present and show large amplitudes. As shown on Figure 6.4 the amplitude maxima of both of these waves tend to occur in the region where the zonal mean winds are maximum westward, and that the waves tend to follow the westward wind regime up to 260 km. Since DE3, the UFKW, and the secondary waves generated by their interactions, are eastward-propagating, they are Doppler-shifted to higher frequencies, i.e., where the mean winds are westward. The behavior depicted in Figure 6.4 is consistent with the concept that eastward (westward) propagating waves tend to be ducted towards westward (eastward) mean winds, and that Doppler-shifting to higher frequencies reduces the effects of dissipation, as extensively discussed before. This effect is further compounded by an increase in vertical wavelength, as discussed by Forbes [2000], [40] and Ekanakaye et al. [1997] [34]. The white dashed line in Figure 6.4 represents the region where $f^2 - \sigma_D^2 = 0$, which is this region where we would expect equivalent depth to change from being positive to negative (and vice-versa), and thus the waves would change from being propagating to being trapped or evanescent (see Section 6.2.1). As discussed in Section 6.2.1, this region is highly dependent on the zonal mean wind $\bar{U}$ and latitude θ. As one can see from Figure 6.4, the waves tend to exhibit larger amplitudes in regions where $\sigma_D > f$ (equatorward

of the white dashed lines), similar to what shown by Ekanakaye et al. [1997] [34] and Forbes [2000], [40]. Overall, the interactive effects of zonal mean winds and dissipation account for the behaviors depicted in Figure 6.4.

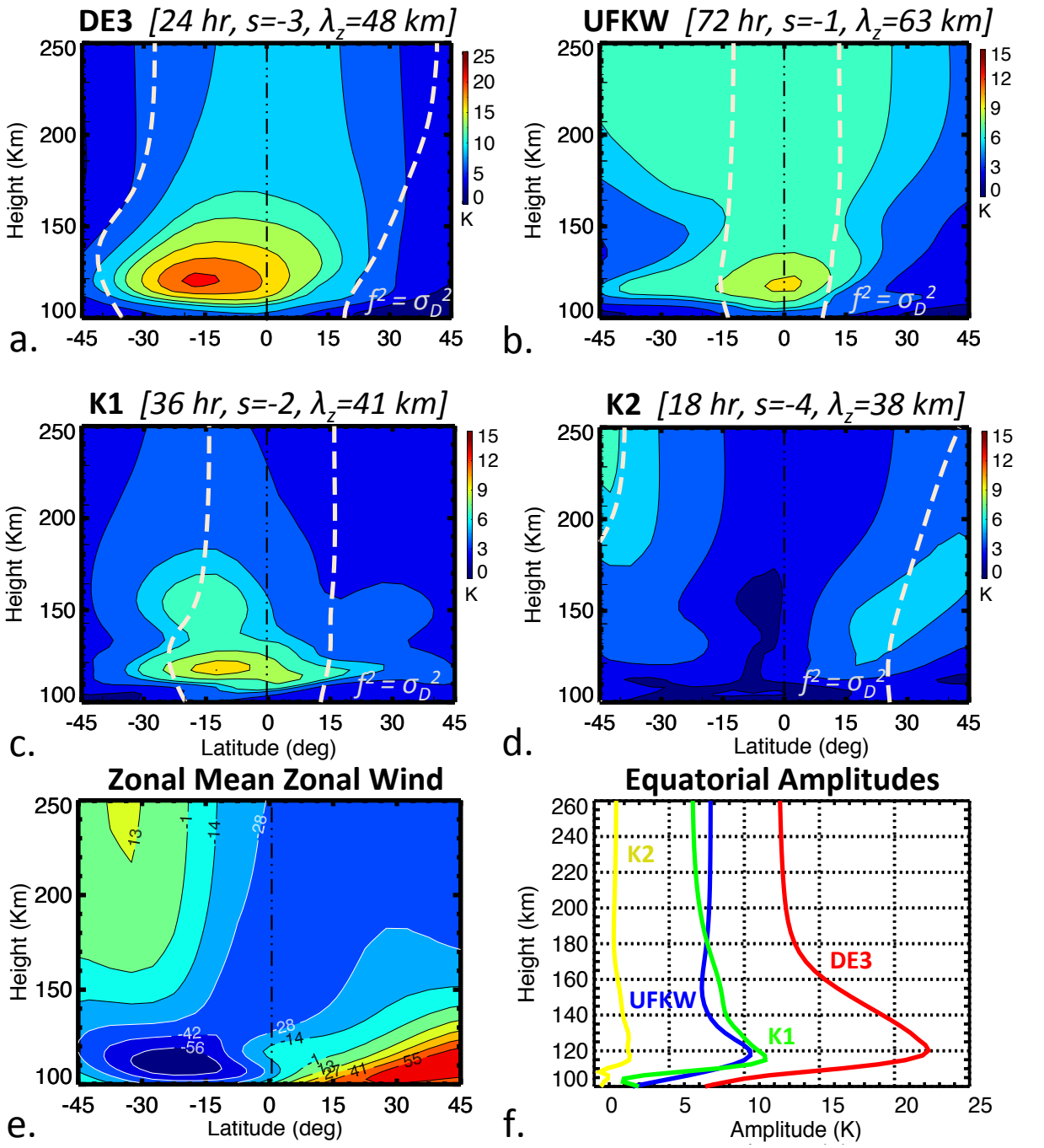

Figure 6.4: Height versus latitude structures for DOY 180 of DE3 (panel a), the UFKW (panel b), K1 (panel c), K2 (panel d) in comparison to the zonal-mean zonal winds extracted from the model (panel e). Note that the amplitude maxima of both of these waves tend to occur in the region where the zonal mean winds are maximum westward (negative), and that the waves tend to follow the westward wind regime up to 260 km. The white dashed line represents the region of $f^2 - \sigma_D^2 = 0$, i.e., where the equivalent depth changes sign and the waves becomes trapped. Panel f shows the vertical profile of DE3, UFKW, K1, and K2 equatorial amplitudes between 100 km and 260 km.

The vertical progression of equatorial DE3, UFKW, K1, and K2 amplitudes between 100 km and 260 km is presented in Figure 6.4f. All the waves grow exponentially up to ∼120 km, region where dissipation stops this growth and causes the amplitudes to decrease before reaching asymptotic values in the middle thermosphere. Note that K1 has large amplitudes (up to 12 K), even larger than the UFKW for altitudes between 110 km and 180 km, while K2 only reaches 3 K. Interestingly, this result, i.e., 'sum' sideband with smaller amplitudes than the 'difference' sideband, is similar to what is found in SABER and GOCE data (see discussion in Chapter 5). This is likely due to the shorter vertical wavelength of K2 (λ_z = 38 km) compared to K1 (λ_z = 41 km). Note that differential excitation at generation heights is also a possible cause of this feature. Further investigating the mechanisms responsible for this phenomenon is beyond the scope of this work.

Figure 6.5a shows the vertical profile between 100 km and 200 km of the ion drag coefficient (blue line), the molecular viscosity coefficient (green line), and Rayleigh friction coefficient (black line) for DE3 on DOY 180. The ion drag coefficient was derived by Forbes and Garrett [1979] [44], while the molecular viscosity coefficient was inferred by Hickey et al. [2011] [82] (using λ_z = 59 km for DE3), and both refer to solar medium conditions. Figure 6.5b shows the vertical profile for the equatorial zonal mean zonal winds also for DOY 180.

The region where $\nu_r \sim \sigma_D$ is the region where dissipation becomes important to the local physics of a wave propagating upwards from the lower atmosphere. Neglecting λ_{ion}, which is a good approximation around 100-120 km (well below the F-region ionospheric peak), one can show that the condition $\nu_r \sim \sigma_D$ is equivalent to $\chi = \left|\frac{4\pi^2}{\lambda_z^2}\frac{\nu_d}{\sigma_D}\right| \sim 1$ presented in Section 1.2.1 of Chapter 1, where χ represents the ratio between diffusive and inertial forces and ν_d is the molecular diffusion coefficient. As explained in Chapter 1, the dependence of χ on λ_z^2 and σ_D is such that the altitude at which the molecular processes dominate increases with vertical wavelength and wave frequency. The black dashed vertical line in Figure 6.5a illustrates where the frequency is equal to Earth's rotation rate Ω. For a diurnal tide in the absence of mean winds $\sigma_D \sim \sigma = \Omega$, thus the condition $\nu_r = \sigma_D$ is equivalent to $\nu_r = \Omega$, which in Figure 6.5a is the intercept between the black dashed vertical line and the black solid line. As shown in Figure 6.5a, this altitude occurs around 120 km,

which is consistent with what is found in the model, as mentioned when discussing Figure 6.4.

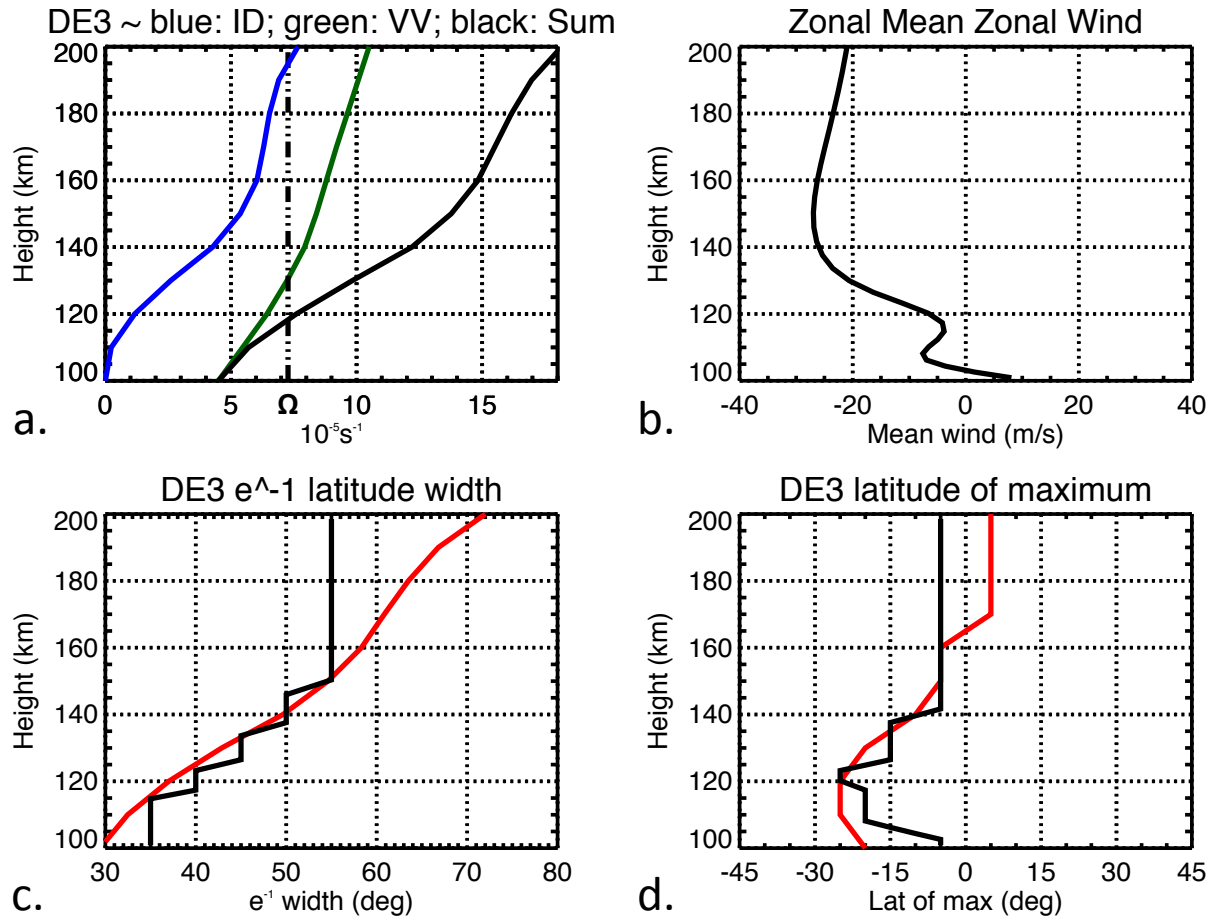

Figure 6.5: Panel a: ion drag (blue line, calculated from Forbes and Garrett [1979] [44]), vertical viscosity (green line, calculated from Hickey et al. [2011] [82] for DE3 with $\lambda_z = 59$ km), and their sum (black line, i.e., Rayleigh friction coefficient). The black dashed vertical line in panel a shows the location where the frequency is equal to Earth's rotation rate Ω. Panel b: zonal mean zonal winds from the model at the equator. Panels c and d: e^{-1} width and latitude of maximum of DE3 latitude amplitudes calculated according to Equation 6.22 (red line) and from the model (black line). Note the general agreement between the e^{-1} width and latitude of maximum predictions of Equations 6.22 and what is found in the model. Also note that the altitude where $\nu_r = \Omega$ (i.e., frequency of a diurnal tide in the absence of zonal mean winds) is ~120 km, same as the one found in the model (see Figure 6.4f).

Using the vertical profiles of Rayleigh friction coefficient and zonal mean winds shown in

Figure 6.5a and 6.5b, we calculated the e^{-1} width of the Gaussian distribution expressed in Equation 6.22, i.e., $\left|\frac{2[(\sigma+\frac{s\bar{U}}{a})^2+\nu_r^2]}{k\beta(\sigma+\frac{s\bar{U}}{a})}\right|^{1/2}$, as function of height (red line in Figure 6.5c) and compared this with the one calculated from the model (black line in Figure 6.5c). Using Equation 6.22, the e^{-1} width is found to be ∼30° around 100 km, increasing to around 70° at 200 km. The similarities between the e^{-1} width calculated using Equation 6.22 and the one found in the model are striking for heights less than ∼150 km. Around 150 km the model width and the one predicted using Equation 6.22 start differing, where the latter continues increasing and the former reaches an nearly asymptotic value of 55°. Figure 6.5c demonstrates that the latitudinal broadening observed in TIMED-SABER and GOCE data (Chapters 4 and 5) and in the TIME-GCM simulation (Sections 6.1 and 6.3) is due to the effect of molecular dissipation.

Figure 6.5d shows the latitude of maximum as function of height inferred using Equation 6.22 (red line) and calculated using model DE3 amplitudes (black line). Note that since ν_r is assumed to be latitude-independent the only source of asymmetry is in the background wind field. There are significant similarities between the two lines, with the latitude of maximum shifting to the southern hemisphere in the 100-120 km altitude range, shifting back toward the equator for heights of 120-140 km, and reaching a constant value for greats heights. This result demonstrates the strong effect of zonal winds on the latitude where DE3 amplitudes maximize.

Additional implications of Equation 6.22 are that for $\sigma_D \gg \nu_R$, the denominator of Equation 6.22 tends to 0 when σ_D goes to 0. This is related to the difference between phase speed $C_{ph} = d\lambda/dt$ (equal to $-n\Omega/s$ for a tide and $-\delta\Omega/m$ for a PW) and the mean wind $\bar{U}$. As explained by Salby [1984] [198], waves generally need to have this quantity be ≥ 0 in order to propagate; the line where $C_{ph} = \bar{U}$ is a critical line that that wave does not easily cross. For DE3, $C_{ph,DE3}$ = 154.6 m/s, while for a 2.5 day UFKW $C_{ph,UFKW}$ = 185.3 m/s, thus the critical wind speed for DE3 is $\bar{U}_{cr,DE3}$ = 154.6 m/s and $\bar{U}_{cr,UFKW}$=185.3 m/s (i.e., eastward wind). In the thermosphere this condition is not usually met for DE3 and the UFKW, since zonal mean eastward wind speeds (i.e., superotation speeds) do not generally exceed 50 m/s. On the other hand, at heights greater than ∼110-130 km $\nu_r > \sigma_D$, thus a wave entering this region transitions from an exponential growth (for propagating

waves) or decay (for trapped oscillations), to an asymptotically constant value in the thermosphere.

6.4 Conclusions

In this work we applied the f- and β-plane approximations to the momentum equations to show analytically how the vertical propagation of equatorially trapped waves with zero meridional velocity (e.g., DE3 and the UFKW) in a rotating atmosphere is affected by mean winds and dissipation. We then used a 2009 TIME-GCM simulation with the lower boundary based on MERRA reanalysis data (see Häusler et al. [2014] [76]) and a vertical profile of Rayleigh friction to show the effect of mean winds and dissipation on latitude-time and height-latitude structures. The main results presented in this chapter can be summarized as follows:

(1) DE3, a 3-day UFKW, and secondary waves due to their nonlinear interactions are found to be large source of day-to-day and latitude-longitude variability in both the lower to the middle thermosphere and to vertically propagate in this height regime.

(2) The effect of molecular dissipation on these oscillations is to broaden the latitudinal structures in accord with the theoretical predictions of Volland and Mayr (Volland and Mayr [1977] [212], Volland [1974] [210], and references contained therein) and satellite observations (see Chapters 4 and 5). In particular using our model shown in Equation 6.22 for DE3, we found the e^{-1} width around 100 km to be $\sim 30^\circ$ and to increase almost linearly to reach $\sim 70^\circ$ at 200 km.

(3) Doppler-shifting is very sensitive to the zonal mean wind distribution at low-mid latitudes. For DE3 and the UFKW (both eastward propagating waves), westward (eastward) zonal mean winds Doppler-shift the wave to higher (lower) frequencies, reducing (increasing) their susceptibility to dissipation. The amplitude maxima of both of these waves tend to occur in the region where the zonal mean winds are maximum westward (negative), and that the waves tend to follow the westward wind regime up to 260 km.

(4) Winds asymmetric about the equator are found to distort the latitudinal shapes. The distortion is shown to be imposed by relative changes in dissipation due to asymmetric Doppler-shifting of the wave. In particular the latitude of maximum is highly linked to the background zonal mean wind field.

(5) The altitude where upward propagating waves maximize is related to the ratio between the Rayleigh friction coefficient and the wave's Doppler-shifted frequency. For DE3 this height is found to be ∼120 km.

As demonstrated in this chapter, the combined effect of dissipation and Doppler-shifting associated with the zonal mean wind field explains several of the noted differences in the latitude-temporal variability of DE3 and UFKW between 110 km and 260 km shown in Chapters 4 and 5. Additional work is required to fully address outstanding issues regarding the effect of mean winds and dissipation on vertical wave coupling; below a list of next steps:

- Extend the analysis presented above to the UFKW, and sidebands K1 and K2.
- Use Rayleigh friction coefficients derived from data output from the MERRA/TIME-GCM simulation.
- Find a solution to Equation 6.22 using $sin\theta$ or linear distribution of mean winds about the equator.
- Decompose primary and secondary waves Hough modes to better understand the effect of mean winds and dissipation on their coupling characteristics.
- Use Ortland and Alexander's shape function to analyze the effects of mean winds on the spatial structures of the secondary waves.
- Define an index of refraction that takes into account the wave's Doppler-shifted frequency, zonal wavenumber, the Coriolis parameter, molecular dissipation, and ion drag, and that

describes the vertical and latitudinal evolution of a given wave as it propagates through the thermosphere.

Chapter 7

CONCLUSIONS

The massive amount of data collected by over a decade of satellite measurements has offered the unprecedented opportunity to gain a truly global perspective on the wave coupling problem. The dissertation herein investigated the vertical coupling of waves in the thermosphere using quasi-Sun-synchronous satellite measurements from recent low Earth orbiting missions (i.e., TIMED, CHAMP, and GOCE) and state-of-the-art numerical modeling simulations (i.e., MERRA/TIME-GCM). Particular attention was given to short-term (days to weeks) variability of DE3 and a 3-day ultra-fast Kelvin wave, two large thermospheric oscillations of tropospheric origin. Section 7.1 provides a summary of the main results and conclusions obtained in this dissertation, while Section 7.2 contains a list of next steps (post-dissertation) and recommendations for future work.

7.1 Summary

Chapter 1 provided a introduction to the wave coupling problem and background information on atmospheric tides, Kelvin waves, known effects of dissipation, mean winds, and EUV radiation on the vertical propagation, nonlinear wave-wave interactions, and the various methods (i.e., ground-based versus space-based) of observing atmospheric waves with their advantages and shortcomings. Chapter 1 also presented the main objective of this dissertation, i.e., reveal and understand the nature of vertical wave coupling in the thermosphere and quantify its role in determining the variability of the thermosphere system, and the science questions it sought to address.

Chapter 2 described the observational data used (i.e., quasi-Sun-synchronous satellite mea-

surements from the TIMED, CHAMP, and GOCE missions), reviewed the models implemented (i.e., TIME-GCM numerical simulations with GSWM-09 and MERRA lower boundary forcing), and explained the procedure adopted to extract daily tidal amplitudes and identify nonlinear wave-wave interactions from satellite measurements.

Chapter 3 discussed the importance of winds in the wave coupling problem and presented a new method of extracting low to mid-latitude zonal and meridional winds from CHAMP-measured neutral and electron densities at solar low and geomagnetically quiet conditions. The method was validated by showing that neutral and electron densities output from TIME-GCM could be used to derive solutions to the momentum equations replicating reasonably well (over 85% of the variance) the winds self-consistently calculated within the TIME-GCM. CHAMP cross-track winds were found to share over 65% of the variance with the synthetic zonal winds. Using this new wind product evidence was presented demonstrating: (1) a strong eastward jet (with equatorial superrotation speeds of 27 m/s) in the post-sunset hours around the geomagnetic equator due to depletion in ion drag; (2) HWM14 empirical model's inability to effectively capture much of the latitude, longitude, and local time variability in the winds; (3) vertical wave coupling due to DE3 and SE2; (4) non-negligible SE2 meridional winds supporting theories suggesting that SE2 transequatorial neutral winds can be responsible for the anti-symmetric component of the ionospheric wave-4; (5) strong seasonal and local time dependencies in both zonal and meridional winds.

In Chapter 4, TIMED-SABER temperature measurements at 110 km and GOCE neutral density and cross-track wind measurements around 260 km were employed to reveal the vertical coupling of waves during 2010-2012 for solar low and geomagnetic quiet conditions. For this 3-year period, DE3 and a 3-day UFKW were found to be prominent oscillations in both the lower and middle thermosphere and to vertically propagate in this height regime. Significant latitudinal asymmetry was found in both oscillations, and explained as due to the combined effect of dissipation and zonal mean winds.

Using SABER temperatures near 110 km and GOCE winds and densities near 260 km (i.e.,

same dataset as in Chapter 4), Chapter 5 demonstrated the existence of secondary waves produced by nonlinear interactions between DE3 and the UFKW. These sidebands were shown to be responsible for up to 10% to 20% of the day-to-day and longitudinal variability. In particular, at low to mid-latitudes and for geomagnetically quiet and solar low conditions, the combined effect of DE3, the UFKW, and their interactions was found to account for 20% to 60% of the total variability; while the combined effect of wave-1 to wave-4, the UFKW, and DE3-UFKW interactions was found to explain 60-80% of the total variability, with only up to 20-40% that could be ascribed to geomagnetic and solar effects. [Note: the analysis was limited to solar and geomagnetic quiet conditions, as one can envision that persistent and extreme space weather events would lead to different conclusions.] Nonlinear wave-wave interactions were found to be responsible for non-negligible spatial and temporal variability, demonstrating that these waves should be accounted for when analyzing thermosphere variability in nonlinear models and satellite data.

In Chapter 6, the f- and β-plane approximations to the momentum equations were used to show analytically how the vertical propagation of equatorially trapped waves with zero meridional velocity (e.g., DE3 and the UFKW) in a rotating atmosphere are affected by mean winds and dissipation. A 2009 TIME-GCM simulation with the lower boundary based on MERRA reanalysis data, with a vertical profile of Rayleigh friction, was then used to show the effect of mean winds and dissipation on latitude-time and height-latitude structures. With this study: (1) DE3, a 3-day UFKW, and secondary waves due to their nonlinear interactions were found to be large source of day-to-day and latitude-longitude thermospheric variability and to vertically propagate from the lower to the middle thermosphere (similar to satellite observations for 2010-2012); (2) molecular dissipation was found to be the main contributor to the observed broadening of latitudinal structures with height in accord with the theoretical predictions and satellite observations; (3) latitudinal asymmetries in DE3 were explained by the effect of zonal mean winds asymmetric about the equator distorting the latitudinal shapes due to relative changes in dissipation associated to asymmetric Doppler-shifting; (4) the peak height was found to be related to the ratio between the Rayleigh friction coefficient and the wave's Doppler-shifted frequency.

The dissertation herein showed the crucial role played by upward propagating waves in the dynamical coupling between the lower and middle thermosphere at low to mid-latitudes for solar and geomagnetically quiet conditions, while the background conditions (i.e., mean winds, dissipation) were found to significantly affect the vertical propagation. The following text provides a list of the original questions presented in the introduction of this dissertation (i.e., Chapter 1), and how they were answered in the context of this study.

Q1 What do satellite-based measurements reveal about the nature, origins, and consequences of wave coupling between the lower and middle thermosphere? In answering this question the unique perspectives of quasi-Sun-synchronous satellite observations are identified and applied to the wave coupling problem. Methods to investigate short-term tidal variability and the interactions with longer period waves are also presented. Additionally, a new method for deriving neutral winds from measured electron and neutral densities is presented. In this context, TIME-GCM output is used as mock data to validate the method, and wind products for a series for 10-day periods during 2007-2010 spanning a range of local times, seasons for quiet geomagnetic conditions are produced.

Q2 What are the most prominent low to mid-latitude global-scale waves participating in this coupling? To address this question, SABER temperatures near 110 km and GOCE winds and densities near 260 km are used to reveal wave coupling. DE3 and a 3-day UFKW are identified as dominant sources of longitudinal variability during 2010-2012, and evidence for the vertical propagation of DE3 and the UFKW from the lower to the middle thermosphere is presented.

Q3 What are the physical processes that determine the nature of this coupling? Significant latitudinal asymmetry is found in DE3 and UFKW extracted from SABER and GOCE data, this is explained as due to combined effect of dissipation and zonal mean winds. Also, by analyzing the ratio of DE3 density perturbations between 260 km and 110 km and S10.7, higher S10.7 is found to be associated with decreased propagation, pointing

to the importance of solar EUV radiation in the vertical propagation of waves in the thermosphere. Secondary waves due to nonlinear interactions between DE3 and the UFKW are identified and dissipation is found to broaden the latitudinal structures while mean winds are found to cause significant latitudinal asymmetries.

Q4 To what degree does vertical wave coupling contribute to the overall variability of the middle thermosphere? The thermosphere variability associated with solar and geomagnetic changes is quantified and compared with that due to upward-propagating waves. For 2011, at solar low and geomagnetically quiet conditions, vertically propagating waves are found to be the largest source of thermospheric variability (up to 60-80%).

7.2 Recommendations for Future Work

In order to further advance our understanding on how waves evolve in the thermosphere under the effect of mean winds and subject to dissipation additional steps are required that originate from the work presented in Chapter 7. These are: (1) extend the analysis on the vertical propagation of DE3 subject to background winds and dissipation effects to the UFKW, and sidebands K1 and K2; (2) model Rayleigh friction according to data output from the 2009 MERRA/TIME-GCM simulation; (3) find a solution to the derived expression describing the latitudinal profile of an equatorial wave with zero meridional velocity subject to mean winds and dissipation using a sine or linear distribution of mean winds about the equator; (4) decompose primary and secondary waves Hough modes to better understand the effect of mean winds and dissipation on their coupling characteristics; (5) use Ortland and Alexander's shape function to analyze the effects of mean winds on the spatial structures of the secondary waves; (6) define an index of refraction (taking into account the wave's Doppler-shifted frequency, zonal wavenumber, the Coriolis parameter, molecular dissipation, and ion drag) that describes the vertical and latitudinal evolution of a given wave as it propagates through the thermosphere (this new index will help to better understand and quantify how waves evolve in the thermosphere and thus contribute to our understanding of wave coupling).

This dissertation illustrated the impact of vertical wave coupling in the dynamics of the thermosphere systems, but also highlighted a number of areas where future research efforts are needed. For example, while the day-to-day variability of short-period waves is known to be very large according to ground-based observations, attribution of this variability to specific wave components on a global basis has been practically impossible due to inadequate latitude-longitude distribution of ground-based observing sites, and the slow local time precession of single satellites. For the latter, only wave fields averaged over 30-60 days or more can be retrieved, leading to observational wave climatologies with significant amplitude and day-to-day variability suppression. Additionally, the interactions between PW and tides are a major source of both tidal and longitude variability in the upper atmosphere. Yet the generation, manifestation and impacts of nonlinearly generated secondary waves are still poorly understood due to the difficulty of observing the short-term evolution of global scale waves with frequencies outside the Nyquist limits of a daily sampling. Some creative methods employed in this work allowed the determination of daily tidal variability and PW-tide interactions using space-based measurements, but introduced ambiguities in interpretation in terms of what the interacting waves are and resulted in errors of unknown amplitude.

Despite the significant progress made in the past decade on the vertical wave coupling problem, additional work is needed to improve our understanding of how waves act to change the zonal-mean composition and thermal structure of the ionosphere-termosphere (IT) system; the relative roles of PW, GW and tides in modifying the mean circulation, thermal structure, and composition of the thermosphere; and how this coupling translates to ionospheric variability. Global, simultaneous, and higher resolution measurements between 100-250 km of winds, temperature and composition, and their temporal evolution in response to measured external forcing, are what is really needed to truly understand these physical mechanisms, yet to date there are virtual no concurrent measurements of these fields.

Addressing these issues is important to understanding what might be involved in achieving a predictive capability that connects lower atmospheric weather with IT space weather, and what priorities might be placed on pursuing such a capability. Some advances in the field can be expected

with the recently launched Swarm mission, which comprises three satellites gathering pole-to-pole measurements of neutral densities, winds and electric and magnetic fields around 460-530 km. Even more exciting is the potential for future studies of wave coupling offered by the upcoming Ionospheric Connections (ICON) mission, due for launch in February 2017, which will obtain similar data to Swarm, but at lower altitudes and latitudes, as well as measurements of ionospheric emissions and chemical composition. The goal of the ICON mission is to understand the interplay between Earth's atmosphere and the space environment. ICON will allow a better investigation of the forces at play in the near-space environment, leading the way in understanding disturbances that can lead to severe interference with communications and GPS signals. At the same time, NASA will launch the Global-scale Observations of the Limb and Disk (GOLD) mission, which will measure densities and temperatures of Earths upper atmosphere. GOLD will examine how the neutral thermosphere shapes the evolution and structure of the ionosphere, in combination with the investigation into external forcing. One of the four science question that the GOLD mission will seek to address is one that is fundamental to the wave coupling problem: how significant are the effects of atmospheric waves and tides propagating from below on thermospheric temperature structure?

Bibliography

[1] D. N. Anderson and R. G. Roble. The effect of vertical e x b ionospheric drifts on f region neutral winds in the low-latitude thermosphere. J. Geophys. Res., 79:5231–5236, 1974.

[2] E. Becker. Dynamical control of the middle atmosphere. Space Sci. Rev., 168:283–314, 2011.

[3] R. Bernard. Variability of the semi-diurnal tide in the upper atmosphere. J. Atmos. Terr. Phys., 43:663–674, 1981.

[4] B. R. Bowman, W. K. Tobiska, F. Marcos, and C. Valladares. The jb2006 empirical thermospheric density model. J. Atmos. Sol. Terr. Phys., 70:774–793, 2008.

[5] S. L. Bruinsma, , and J. M. Forbes. Medium to large-scale density variability as observed by champ. Space Weather Journal, 6:S08002,, 2008.

[6] S. L. Bruinsma, , and J. M. Forbes. Anomalous behavior of the thermosphere during solar minimum observed by champ and grace. J. Geophys. Res., 115:A11323, 2010.

[7] S. L. Bruinsma, , and J. M. Forbes. Large-scale traveling atmospheric disturbances (lstads) in the thermosphere inferred from champ, grace and seta accelerometer data. J. Atmos. Solar-Terr. Phys., 72:1057–1066, 2010.

[8] S. L. Bruinsma, E. Doornbos, and B. R. Bowman. Validation of goce densities and thermosphere model evaluation. Adv. Space Res., 54:576–585, 2014.

[9] S. L. Bruinsma, C. Forste, O. Abrikosov, J. M. Lemoine, J. C. Marty, S. Mulet, M. H. Rio, and S. Bonvalot. Esa's satellite-only gravity field model via the direct approach based on all goce data. Geophys. Res. Lett., 41(21), 2014.

[10] S. L. Bruinsma, D. Tamagnan, and R. Biancale. Atmospheric densities derived from champ/star accelerometer observations. Planet. Space Sci., 52:297–312, 2004.

[11] M. J. Buonsanto. Observed and calculated f2 peak heights and derived meridional winds at mid-latitudes over a full solar cycle. J. Atmos. Sol. Terr. Phys., 52:223–240, 1990.

[12] M. J. Buonsanto. Neutral winds in the thermosphere at mid-latitude over a full solar cycle: A tidal decomposition. J. Geophys. Res., 96:3711–3724, 1991.

[13] P. O. Canziani, J. R. Holton, E. Fishbein, and L. Froidevaux. Equatorial kelvin wave variability during 1992 and 1993. J. Geophys. Res., 54:576–585, 2014.

[14] P. O. Canziani, J. R. Holton, E. Fishbein, L. Froidevaux, and J. W. Waters. Equatorial kelvin waves: a uars mls view. J. Atmos. Sc., 51:3053–3076, 1994.

[15] R. A. Challinor. Numerical-air winds in the ionospheric f-region for an asymmetric global pressure system. Plan. Space Sci., 17:1097–1106, 1969.

[16] C. P. Chang. Forcing of stratospheric kelvin waves by tropospheric heat sources. J. Atmos. Sci., 33:740–744, 1976.

[17] S. Chapman. The electrical conductivity of the ionosphere: A review. Nuovo Cimento, 4:1385–1412, 1956.

[18] S. Chapman and R. S. Lindzen. Atmospheric tides. D. Reidel Press, Dordrecht, Holland, 1970.

[19] R. R. Clark and J. S. Bergin. Bispectral analysis of mesosphere winds. Journal of Atmospheric and Solar-Terrestrial Physics, 59(6):629–639, 1997.

[20] J. H. Clemmons, R. L. Walterscheid, A. B. Christensen, and R. L. Bishop. Rapid, highly structured meridional winds and their modulation by non migrating tides: Measurements from the streak mission. J. Geophys. Res., 118:866–877, 2013.

[21] W. R. Coley, R. A. Heelis, and N. W. Spencer. Comparison of low- latitude ion and neutral zonal drift using de2 data. J. Geophys. Res., 99:341–348, 1994.

[22] D. L. Cooke, W. Turnbull, C. Roth, A. Morgan, and R. Redus. Ion drift-meter status and calibration, in first champ mission results for gravity, magnetic, and atmospheric studies. Springer, New York, pages 212–219, 2003.

[23] Y. Deng, G. Lu, Y.-S. Kwak, E. Sutton, J. M. Forbes, and S. Solomon. Reversed ionospheric convections during the november 2004 storm: Impact on the upper atmosphere. J. Geophys. Res., 114:A07313, 2009.

[24] R. E. Dickinson, E. C. Ridley, and R. G. Roble. A three-dimensional general circulation model of the thermosphere. J. Geophys. Res., 86:1499–1512, 1981.

[25] E. Doornbos. Thermospheric density and wind determination from satellite dynamics. PhD thesis, TU Delft, Netherlands, 2011.

[26] E. Doornbos, S. L. Bruinsma, B. Fritsche, G. Koppenwallner, P. Visser, J. van den IJssel, and J. de Teixeira de Encarnação. Data set user manual. ESA AO/1-6367/10/NL/AF, For data set version 1.4, July 2014.

[27] E. Doornbos, S. L. Bruinsma, B. Fritsche, G. Koppenwallner, P. Visser, J. van den IJssel, and J. de Teixeira de Encarnação. Air density and wind retrieval using goce data. ESA AO/1-6367/10/NL/AF, Final Report, June 2013.

[28] E. Doornbos, J. van den Ijssel, H. Lühr, M. Förster, and G. Koppenwallner. Neutral density and crosswind determination from arbitrarily oriented multi-axis accelerometers on satellites. J. Spacecr. Rockets, 47:580589, 2010.

[29] E. Doornbos, P. Visser, G. Koppenwallner, and B. Fritsche. Air density and wind retrieval using goce data. ESA AO/1-6367/10/NL/AF, Algorithm Theoretical Basis Document:1.1, 20 June 2013.

[30] M. R. Drinkwater, R. Floberghagen, R. Haagmans, D. Muzi, and A. Popescu. Goce: Esa's first earth explorer core mission. Kluwer Academic Publishers, 18:419–432, 2003.

[31] D. P. Drob and et al. An empirical model of the earths horizontal wind fields: Hwm07. J. Geophys. Res., 113:A12304, 2008.

[32] D. P. Drob and et al. An update to the horizontal wind model (hwm): The quiet time thermosphere. Earth Space Sci., 2:301–319, 2015.

[33] S. D. Eckermann and R. A. Vincent. First observations of intraseasonal oscillations in the equatorial mesosphere and lower thermosphere. Geophys. Res. Lett, 21:265–268, 1994.

[34] E. M. P. Ekanakaye, T. Aso, and S. Miyahara. Background wind effect on propagation of nonmigrating diurnal tides in the middle atmosphere. J. Atmos. Sol. Terr. Phys., 59:401–429, 1997.

[35] S. L. England, T. J. Immel, J. D. Huba, M. E. Hagan, A. Maute, and R. DeMajistre. Modeling of multiple effects of atmospheric tides on the ionosphere: an examination of possible coupling mechanisms responsible for the longitudinal structure of the equatorial ionosphere. J Geophys. Res., 115:A05308, 2010.

[36] S. L. England, T. J. Immel, E. Sagawa, S. B. Henderson, M. E. Hagan, S. B. Mende, H. U. Frey, C. M. Swenson, and L. J. Paxton. Effect of atmospheric tides on the morphology of the quiet time, postsunset equatorial ionospheric anomaly. J. Geophys. Res., 111, 2006.

[37] E. Doornbos et al. Processing of multi-satellite accelerometer data for thermospheric modelling. 37th COSPAR Scientific Assembly, 37:730, 2008.

[38] J. M Forbes. Atmospheric tides. i. model description and results for the solar diurnal component. J. Geophys. Res., 87:5222–5240, 1982.

[39] J. M. Forbes. Tidal and planetary waves, in the upper mesosphere and lower thermosphere: A review of experiment and theory. Geophysical Monograph, 87, 1995.

[40] J. M Forbes. Wave coupling between the lower and upper atmosphere: Case study of an ultra-fast kelvin wave. J. Atmos. Sol. Terr. Phys., 62(1718):1603–1621, 2000.

[41] J. M Forbes, S. Bruinsma, X. Zhang, and J. Oberheide. Surface-exosphere coupling due to thermal tides. Geophys. Res. Lett., 36:L15812, 2009.

[42] J. M. Forbes, S. L. Bruinsma, Y. Miyoshi, and H. Fujiwa. A solar terminator wave in thermosphere neutral densities measured by the champ satellite. Geophys. Res. Lett., 35, 2008.

[43] J. M. Forbes, M. Codrescu, and T. J. Hall. On the utilization of ionosonde data to analyze the latitudinal penetration of ionospheric storm effects. Geophys. Res. Lett., 15:249–252, 1988.

[44] J. M. Forbes and H. B. Garrett. The solar cycle variability of diurnal and semidiurnal thermospheric temperatures. J. Geophys. Res., 84:148–227, 1979.

[45] J. M Forbes, M. Hagan, S. Miyahara, Y. Miyoshi, and X. Zhang. Diurnal nonmigrating tides in the tropical lower thermosphere. Earth, Planets and Space, 55:419–426, 2003.

[46] J. M. Forbes and M. E. Hagan. Thermospheric extensions of the classical expansion functions for semidiurnal tides. J. Geophys. Res., 87:5253–5259, 1982.

[47] J. M Forbes, M. Kilpatrick, D. Fritts, A. H. Manson, and R. A. Vincent. Zonal mean and tidal dynamics from space: An empirical examination of aliasing and sampling issues. Ann. Geophys., 15:1158–1164, 1997.

[48] J. M Forbes and Y. Moudden. Quasi-two-day wave-tide interactions as revealed in satellite observations. J. Geophys. Res., 117:D12110, 2012.

[49] J. M. Forbes, R. G. Roble, and F. A. Marcos. Magnetic activity dependence of high-latitude thermospheric winds and densities below 200 km. J. Geophys. Res., 98:13693–13702, 1993.

[50] J. M. Forbes and R. A. Vincent. Effects of mean winds and dissipation on the diurnal propagating tide: An analytic approach. Planet. Space Sci., 37:197–209, 1989.

[51] J. M Forbes, X. Zhang, S. Bruinsma, and J. Oberheide. Lunar semidiurnal tide in the thermosphere under solar minimum conditions. J. Geophys. Res., 118:1788–1801, 2013.

[52] J. M. Forbes, X. Zhang, and S. L. Bruinsma. Middle and upper thermosphere density structures due to nonmigrating tides. J. Geophys. Res., 117, 2012.

[53] J. M. Forbes, X. Zhang, and S. L. Bruinsma. New perspectives on thermosphere tides - 2. penetration to the upper thermosphere. Earth, Planets and Space, 66:122, 2014.

[54] J. M Forbes, X. Zhang, S. E. Palo, and et al. Kelvin waves in stratosphere, mesosphere and lower thermosphere temperatures as observed by timed/saber during 2002-2006. Earth Planets and Space, 61:447–453, 2009.

[55] J. M Forbes, X. Zhang, W. Ward, and E. Talaat. Nonmigrating diurnal tides in the thermosphere. J. Geophys. Res., 108(A1):10–33, 2003.

[56] M. Förster, S. Rentz, W. Köhler, H. Liu, and S. E. Haaland. Imf dependence of high-latitude thermospheric wind pattern derived from champ cross-track measurements. Ann. Geophys., 26:1581–1595, 2008.

[57] D. C. Fritts and M. J. Alexander. Gravity wave dynamics and effects in the middle atmosphere. Rev. Geophys., 41:1003, 2003.

[58] T. J. Fuller-Rowell, M. V. Codrescu, B. G. Fejer, W. Borer, F. Marcos, and D. N. Anderson. Dynamics of the low-latitude thermosphere: Quiet and disturbed conditions. J. Atmos. Sol. Terr. Phys., 59:1533–1540, 1997.

[59] F. Gasperini and J. M. Forbes. Lunar-solar interactions in the equatorial electrojet. Geophys. Res. Lett., 41, 2014.

[60] F. Gasperini, J. M Forbes, E. Doornbos, and S. L. Bruinsma. Synthetic thermosphere winds based on champ neutral and plasma density measurements. J. Geophys. Res., 121:3699–3721, 2016.

[61] F. Gasperini, J. M. Forbes, E. N. Doornbos, and S. L. Bruinsma. Wave coupling between the lower and middle thermosphere as viewed from timed and goce. J. Geophys. Res., 120:5788–5804, 2015.

[62] J. E. Geisler. Atmosphere winds in the middle latitude f-region. J. Atm. Terr. Phy., 28:703–720, 1966.

[63] J. E. Geisler. A numerical study of the wind system in the middle thermosphere. J. Atm. Terr. Phy., 29:1469–1482, 1967.

[64] A. J. Gerrard. Application of the fabry-prot interferometer to thermospheric-ionospheric measurements. The Earths Ionosphere: Plasma Physics and Electrodynamics, Academic Press, 2009.

[65] J. M. Grebowsky and D. Sibeck. Nasa's formulation of two multiple spacecraft missions to explore the ionosphere and thermosphere. Rikkyo University Japan, Academic Press, 2009.

[66] S. Y. Gu, X. Dou, J. Lei, T. Li, X. Luan, W. Wan, and J. M. Russell III. Ionospheric response to the ultrafast kelvin wave in the mlt region. J. Geophys. Res., 119:1369–1380, 2014.

[67] J. Guo, W. Wan, J. M. Forbes, E. Sutton, R. S. Nerem, and S. Bruinsma. Interannual and latitudinal variability of the thermosphere density annual harmonics. J. Geophys. Res., 113:A08301, 2008.

[68] J. Guo, W. Wan, J. M. Forbes, E. K. Sutton, R. S. Nerem, T. Woods, S. Bruinsma, and L. Liu. Effects of solar variability on thermosphere density from champ accelerometer data. J. Geophys. Res., 112:A10308, 2007.

[69] M. E. Hagan. Comparative effects of migrating solar sources on tides in the mesosphere and lower thermosphere. J. Geophys. Res., 101:213–222, 1996.

[70] M. E. Hagan, M. D. Burrage, J. M. Forbes, J. Hackney, W. J. Randel, and X. Zhang. Gswm-98: Results for migrating solar tides. J. Geophys. Res., 104:6813–6827, 1999.

[71] M. E. Hagan, J. L. Chang, and S. K. Avery. Gswm estimates of non-migrating tidal effects. J. Geophys. Res., 102:439–452, 1997.

[72] M. E. Hagan and J. M. Forbes. Migrating and nonmigrating diurnal tides in the middle and upper atmosphere excited by tropospheric latent heat release. J. Geophys. Res., 107, 2002.

[73] M. E. Hagan and J. M. Forbes. Migrating and nonmigrating semidiurnal tides in the middle and upper atmosphere excited by tropospheric latent heat release. J. Geophys. Res., 108, 2003.

[74] M. E. Hagan, J. M. Forbes, and F. Vial. On modeling migrating solar tides. Geophys. Res. Lett., 22:893–896, 1995.

[75] M. E. Hagan, A. Maute, and R. G. Roble. Tropospheric tidal effects on the middle and upper atmosphere. J. Geophys. Res., 114:A01302, 2009.

[76] K. Häusler, M. E. Hagan, A. J. G. Baumgaertner, A. Maute, G. Lu, E. Doornbos, S. Bruinsma, J. M. Forbes, and F. Gasperini. Improved short-term variability in the thermosphere-ionosphere-mesosphere-electrodynamics general circulation model. J. Geophys. Res., 119:6623–6630, 2014.

[77] K. Häusler, M. E. Hagan, J. M. Forbes, X. Zhang, E. Doornbos, S. Bruinsma, and G. Lu. Intraannual variability of tides in the thermosphere from model simulations and in situ satellite observations. J. Geophys. Res., 120(8):751–765, 2015.

[78] K. Häusler and H. Lühr. Nonmigrating tidal signals in the upper thermospheric zonal wind at equatorial latitudes as observed by champ. Ann. Geophys., 27:2643–2652, 2009.

[79] K. Häusler, H. Lühr, S. Rentz, and W. Köhler. A statistical analysis of longitudinal dependencies of upper thermospheric zonal winds at dip equator latitudes derived from champ. J. Atm. Sol. Terr. Phys., 69:1419–1430, 2007.

[80] M. He, L. Liu, W. Wan, and Y. Wei. Strong evidence for couplings between the ionospheric wave structure and atmospheric tides. Geophys. Res. Lett., 388:L14101, 2011.

[81] A. E. Hedin and et al. Revised global model of thermosphere winds using satellite and ground-based observations. J. Geophys. Res., 96(A5):7657–7688, 1991.

[82] M. P. Hickey, R. L. Walterscheid, and G. Schubert. Gravity wave heating and cooling of the thermosphere: Sensible heat flux and viscous flux of kinetic energy. J. Geophys. Res., 116:A12326, 2011.

[83] C. O. Hines. Internal gravity waves at ionospheric heights. J. Phys., 38:1441–1481, 1960.

[84] M. Hitchman and C. Leovy. Diurnal tide in the equatorial middle atmosphere as seen in lims temperatures. Amer. Meteor. Soc., 42:557–561, 1985.

[85] J. R. Holton. The influence of mean wind shear on the propagation of kelvin waves. Tellus, 22:186–193, 1970.

[86] J. R. Holton. Waves in the equatorial stratosphere generated by tropospheric heat sources. J. Atmos. Sci., 29:368–375, 1972.

[87] J. R. Holton. On the frequency distribution of atmospheric kelvin waves. J. Atmos. Sci., 30:499–501, 1973.

[88] J. R. Holton. An introduction to dynamic meteorology. New York: Academic Press, 1992.

[89] F. T. Huang and C. A. Reber. Nonmigrating semidiurnal and diurnal tides at 95 km based on wind measurements from the high resolution doppler imager on uars. Journal of Geophysical Research: Atmospheres, 109(D10):2156–2202, 2004.

[90] A. Huuskonen, T. S. Virdi, G. O. L. Jones, and P. J. S. Williams. Observations of the day-to-day variability in the meridional semi-diurnal tide at 70 degrees n. Ann. Geophy., 9:407–415, 1991.

[91] T. J. Immel, E. Sagawa, S. L. England, S. B. Henderson, M. E. Hagan, S. B. Mende, H. U. Frey, C. M. Swenson, and L. J. Paxton. Control of equatorial ionospheric morphology by atmospheric tides. Geophys. Res. Lett., 33, 2006.

[92] L. G. Jacchia. Revised static models of the thermosphere and exosphere with empirical temperature profiles. Smithson. Astrophys. Obs. Spec., 332:B10091, 1971.

[93] L. G. Jacchia and J. Slowey. Temperature variations in the upper atmosphere during geomagnetically quiet intervals. J. Geophys. Res., 69(19):4145–4148, 1964.

[94] G. Jiang, W. Wang, J. Xu, J. Yue, A. G. Burns, J. Lei, M. G. Mlynczak, and J. M. Rusell III. Responses of the lower thermospheric temperature to the 9 day and 13.5 day oscillations of recurrent geomagnetic activity. J. Geophys. Res., 119:4841–4859, 2014.

[95] H. Jin, Y. Miyoshi, H. Fujiwara, and H. Shinagawa. Electrodynamics of the formation of ionospheric wave number 4 longitudinal structure. J. Geophys. Res., 113:A09307, 2008.

[96] E. S Johnson and R. A. Heelis. Characteristics of ion velocity structure at high latitudes during steady southward interplanetary magnetic field conditions. J. Geophys. Res., 110:148–227, 2005.

[97] M. Jr. Jones, J. M. Forbes, and M. E. Hagan. Tidal-induced net transport effects on the oxygen distribution in the thermosphere. Geophys. Res. Lett., 41:GL060698, 2014.

[98] M. Jr. Jones, J. M. Forbes, and M. E. Hagan. Tidal-induced net transport effects on the oxygen distribution in the thermosphere. Geophys. Res. Lett., 41, 2014.

[99] M. Jr. Jones, J. M. Forbes, M. E. Hagan, and A. Maute. Non-migrating tides in the ionosphere-thermosphere: In situ versus tropospheric sources. J. Geophys. Res., 118, 2013.

[100] M. Jr. Jones, J. M. Forbes, M. E. Hagan, and A. Maute. Impacts of vertically propagating tides on the mean state of the ionosphere-thermosphere system. J. Geophys. Res., 119:2197–2213, 2014.

[101] E. Kazimirovsky, M. Herraiz, and B. de la Morena. Effects on the ionosphere due to phenomena occurring below it. Surv. Geophys., 24:139–184, 2003.

[102] H. Kil, S.-J. Oh, M. C. Kelley, L. J. Paxton, S. L. England, E. Talaat, K.-W. Min, and S.-Y. Su. Longitudinal structure of the vertical e x b drift and ion density seen from rocsat-1. Geophys. Res. Lett., 34:L14110, 2007.

[103] H. Kil, E. R. Talaat, S. J. Oh, L. J. Paxton, S. L. England, and S. J. Su. Wave structures of the plasma density and vertical e x b drift in low-latitude f region. J. Geophys. Res., 113:A09312, 2008.

[104] T. L. Killeen and R. G. Roble. An analysis of the high-latitude thermospheric wind pattern calculated by a thermospheric general circulation model: 1. momentum forcing. J. Geophys. Res., 89:7509–7522, 1984.

[105] D. G. King-Hele. The rotational speed of the upper atmosphere determined from changes in satellite orbits. Planet. Space Sci., 12:835–853, 1964.

[106] D. G. King-Hele and D. M. C. Walker. Upper-atmosphere zonal winds from satellite orbit analysis. Planet. Space Sci., 31:509–535, 1983.

[107] D. Knipp, L. Kilcommons, L. Hunt, M. Mlynczak, V. Pilipenko, B. Bowman, Y. Deng, and K. Drake. Thermospheric damping response to sheath-enhanced geospace storms. Geophys. Res. Lett., 40:1263–1267, 2013.

[108] G. Kopp and J. L. Lean. A new, lower value of total solar irradiance: Evidence and climate significance. Geophys. Res. Lett., 38, 2011.

[109] S. Kovalam, R. A. Vincent, I. M. Reid, T. Tsuda, T. Nakamura, K. Ohnishi, A. Nuryanto, and H. Wiryosumarto. Longitudinal variations in planetary wave activity in the equatorial mesosphere. Earth Planets Space, 51:665–674, 1999.

[110] W. K.Tobiska, S. Bouwer, and B. R. Bowman. The development of new solar indices for use in thermospheric density modeling. J. Atmos. Sol. Terr. Phys., 70:803–819, 2008.

[111] Y.-S. Kwak, K. H. Kim, Y. Deng, and J. M. Forbes. Response of thermosphere density to changes in interplanetary magnetic field sector polarity. J. Geophys. Res., 116:A11316, 2011.

[112] Y.-S. Kwak, A. D. Richmond, Y. Deng, J. M. Forbes, and K.-H. Kim. Dependence of the high-latitude thermospheric densities on the interplanetary magnetic field. J. Geophys. Res., 114:A05304, 2009.

[113] J. Lastovicka. Forcing of the ionosphere by waves from below. J. Atmos. Sol.-Terr. Phys., 68:479–497, 2006.

[114] J. Lei, J. P. Thayer, and J. M. Forbes. Longitudinal and geomagnetic activity modulation of the equatorial thermosphere anomaly. J. Geophys. Res., 115:A08311, 2010.

[115] J. Lei, J. P. Thayer, J. M. Forbes, E. K. Sutton, and R. S. Nerem. Rotating solar coronal holes and periodic modulation of the upper atmosphere. Geophys. Res. Lett., 35:L10109, 2008.

[116] J. Lei, J. P. Thayer, J. M. Forbes, E. K. Sutton, R. S. Nerem, M. Temmer, and A. M. Veronig. Global thermospheric density variations caused by high-speed solar wind streams during the declining phase of solar cycle 23. J. Geophys. Res., 113:A11303, 2008.

[117] J. Lei, J. P. Thayer, J. M. Forbes, Q. Wu, C. She, W. Wan, and W. Wang. Ionosphere response to solar wind high-speed streams. Geophys. Res. Lett., 35:L19105, 2008.

[118] J. Lei, J. P. Thayer, W. Wang, and R. L. McPherron. Impact of cir storms on thermosphere density variability during the solar minimum of 2008. Sol. Phys., 274(1-2):427–437, 2011.

[119] R. S. Lieberman. Nonmigrating diurnal tides in the equatorial middle atmosphere. J. Atmos. Sci., 48:1112–1123, 1991.

[120] R. S. Lieberman, R. A. Akmaev, T. J. Fuller-Rowell, and E. Doornbos. Thermospheric zonal mean winds and tides revealed by champ. Geophys. Res. Lett., 40:2439–2443, 2013.

[121] R.S. Lieberman and D. Riggin. High resolution doppler imager observations of kelvin waves in the equatorial mesosphere and lower thermosphere. J. Geophys. Res., 102(D22):26117–26130, 1997.

[122] M. A. Lima and J. W. Wilson. Convective storm initiation in a moist tropical environment. Monthly Weather Review, 136, 2008.

[123] C. H. Lin, W. Wang, M. E. Hagan, C. C. Hsiao, T. J. Immel, M. L. Hsu, J. Y. Liu, L. J. Paxton, T. W.Fang, and C. H. Liu. Plausible effect of atmospheric tides on the equatorial ionosphere observed by the formosat-3/cosmic: Three-dimensional electron density structures. Geophys. Res. Lett., 34, 2007.

[124] R. Lindsay, M. Wensnahan, A. Schweiger, and J. Zhang. Evaluation of seven different atmospheric reanalysis products in the arctic. J. Climate, 27:2588–2606., 2014.

[125] R. S. Lindzen. Vertically propagating waves in an atmosphere with newtonian cooling inversely proportional to density. Can. J. Phys., 46:1835–1840, 1968.

[126] R. S. Lindzen. Internal equatorial planetary scale waves in shear flow. J. Atmos. Sci., 27:394–407, 1970.

[127] R. S. Lindzen. Atmospheric tides. in structure and dynamics of the upper atmosphere. Elsevier, 46:21–88, 1972.

[128] R. S. Lindzen. Turbulence and stress owing to gravity wave and tidal breakdown. J. Geophys. Res., 86(C10), 1981.

[129] R. S. Lindzen and D. Blake. Lamb waves in the presence of realistic distributions of temperature and dissipation. J. Geophys. Res., 77, 1972.

[130] R. S. Lindzen and S. Chapman. Atmospheric tides. Space Sci. Rev., 10:3–188, 1969.

[131] R. S. Lindzen and S. S. Hong. Effects of mean winds and horizonal temperature gradients on solar and lunar semidiurnal tides in the atmosphere. J. Atmos. Sci., 31:1421–1446, 1974.

[132] R. S. Lindzen, S. S. Hong, and J. M. Forbes. Semidiurnal hough mode extensions in the thermosphere and their application, memo. Rep. 3442, Nav. Res. Lab., Washington, D. C., 1977.

[133] H. Liu, H. Lühr, , and S. Watanabe. Climatology of the equatorial thermospheric mass density anomaly. J. Geophys. Res., 112:A05305, 2007.

[134] H. Liu and H. Lühr. Strong disturbances of the upper thermospheric density due to magnetic storms: Champ observations. J. Geophys. Res., 110:A09829, 2005.

[135] H. Liu, H. Lühr, V. Henize, and W. Köhler. Global distribution of the thermospheric total mass density derived from champ. J. Geophys. Res., 110:A04301, 2005.

[136] H. Liu, H. Lühr, W. Köhler, V. Henize, and P. Visser. Zonal winds in the equatorial upper thermosphere: Decomposing the solar flux, geomagnetic activity, and seasonal dependencies. J. Geophys. Res., 111:A07307, 2006.

[137] H. Liu, H. Lühr, and S. Watanabe. A solar terminator wave in thermospheric wind and density simultaneously observed by champ. Geophys. Res. Lett., 36:L10109, 2009.

[138] H. Liu, C. Stolle, M. Förster, and S. Watanabe. Solar activity dependence of the electron density at 400 km at equatorial and low latitudes observed by champ. J. Geophys. Res., 112:A11311, 2007.

[139] H. Liu and S. Watanabe. Seasonal variation of the longitudinal structure of the equatorial ionosphere: Does it reflect tidal influences from below? J. Geophys. Res., 113:A08315, 2008.

[140] L. Liu, X. Luan, W. Wan, J. Lei, and B. Ning. Seasonal behavior of equivalent winds over wuhan derived from ionospheric data in 2000-2001. Adv. Space Res., 32:1765–1770, 2003.

[141] L. Liu, X. Luan, W. Wan, J. Lei, and B. Ning. Solar activity variations of equivalent winds derived from global ionosonde data. J. Geophys. Res., 109, 2004.

[142] L. Lomidze and L. Scherliess. Estimation of thermospheric zonal and meridional winds using a kalman filter technique. Space Weather, 13:747–760, 2015.

[143] L. Lomidze, L. Scherliess, and R. W. Schunk. Magnetic meridional winds in the thermosphere obtained from global assimilation of ionospheric measurements (gaim) model. J. Geophys. Res., 120:8025–8044, 2015.

[144] M. S. Longuet-Higgins. The eigenfunctions of laplace's tidal equation over a sphere. Philosophical Transactions of the Royal Society of London, pages 511–607, 1968.

[145] X. Luan and S. C. Solomon. Meridional winds derived from cosmic radio occultation measurements. J. Geophys. Res., 113, 2008.

[146] H. Lühr, K. Häusler, and C. Stolle. Longitudinal variation of f region electron density and thermospheric zonal wind caused by atmospheric tides. Geophys. Res. Lett., 34:L16102, 2007.

[147] H. Lühr, S. Rentz, P. Ritter, H. Liu, and K. Häusler. Average thermospheric wind pattern over the polar regions, as observed by champ. Ann. Geophys., 25:1093–1101, 2007.

[148] H. Lühr, M. Rother, W. Köhler, P. Ritter, and Grunwaldt. Thermospheric upwelling in the cusp region: Evidence from champ observations. Geophys. Res. Lett., 31:6, 2004.

[149] F. Marcos and J. M. Forbes. Thermospheric winds from the satellite electrostatic triaxial accelerometer system. J. Geophys. Res., 90:6543–6552, 1985.

[150] A. H. Mason, C. E. Meek, J. B. Gregory, and D. K. Chakrabarty. Fluctuations in tidal (24-,12-h) characteristics and oscillations (8-h 5-d) in the mesosphere and lower thermosphere (70-100 km): Saskatoon (52 deg. n, 107 deg. w),1979-1981. Planet. Space Sci., 30:1283–1294, 1982.

[151] A. H. Mason, C. E. Meek, H. Teitelbaum, F. Vial, R. Schminder, D. Kurschner, M. J. Smith, G. J. Fraser, and R. R. Clark. Climatologies of semi-diurnal and diurnal tides in the middle atmosphere (70 - 110 km) at middle latitudes (40 - 55 degrees). J. Atmos. Terr. Phys., 51:579–593, 1989.

[152] L. F. McNamara, D. L. Cooke, C. E. Valladares, and B. W. Reinisch. Comparison of champ and digisonde plasma frequencies at jicamarca, peru. Radio Sci.., 42:RS2005, 2007.

[153] J. W. Meriwether. Studies of thermospheric dynamics with a fabry-perot interferometer network: A review. J. Atmos. Sol. Terr. Phys., 68:1576–1589, 2006.

[154] C. J. Mertens and et al. Retrieval of mesospheric and lower thermospheric kinetic temperature from measurements of co2 15μm earth limb emission under non-lte conditions. Geophys. Res. Lett., 28:1391–1394, 2001.

[155] Y. Miyoshi and H. Fujiwara. Excitation mechanism of intraseasonal oscillation in the equatorial mesosphere and lower thermosphere. J. Geophys. Res., 111, 2006.

[156] Y. Miyoshi, H. Fujiwara, H. Jin, H. Shinagawa, , and H. Liu. Numerical simulation of the equatorial wind jet in the thermosphere. J. Geophys. Res., 117, 2012.

[157] Y. Moudden and J. M. Forbes. A new interpretation of mars aerobraking variability: Planetary wave-tide interactions. J. Geophys. Res., 115:E09005, 2010.

[158] Y. Moudden and J. M. Forbes. A decade-long climatology of terdiurnal tides using timed/saber observations. J. Geophys. Res., 118:4534–4550, 2013.

[159] P. Mukhtarov, D. Pancheva, and B. Andonov. lobal structure and seasonal and interannual variability of the migrating diurnal tide seen in the saber/timed temperatures between 20 and 120 km. J. Geophys. Res., 114, 2009.

[160] S. Müller, H. Lühr, and S. Rentz. Solar and magnetospheric forcing of the low latitude thermospheric mass density as observed by champ. Ann. Geophys., 27:2087–2099, 2009.

[161] V. A. Nguyen, S. E. Palo, R. S. Liebermann, J. M. Forbes, D. A. Ortland, and D. E. Siskind. Generation of secondary waves arising from nonlinear interaction between the quasi 2 day wave and the migrating diurnal tide. J. Geophys. Res. Atmos., 121:7762–7780, 2016.

[162] J. Oberheide and J. M. Forbes. Tidal propagation of deep tropical cloud signatures into the thermosphere from timed observations. Geophys. Res. Lett., 35, 2008.

[163] J. Oberheide, J. M. Forbes, and S. L. Bruinsma. Climatology of upward propagating diurnal and semidiurnal tides in the thermosphere. J. Geophys. Res., 116, 2011.

[164] J. Oberheide, J. M. Forbes, Q. Wu K. Häusler, and S. L. Bruinsma. Tropospheric tides from 80 to 400 km: Propagation, interannual variability, and solar cycle effects. J. Geophys. Res., 114, 2009.

[165] J. Oberheide, J. M. Forbes, X. Zhang, and S. L. Bruinsma. Wave-driven variability in the ionosphere-thermosphere-mesosphere system from timed observations: What contributes to the wave 4? J. Geophys. Res., 116:A01306, 2011.

[166] J. Oberheide and O. A. Gusev. Observation of migrating and nonmigrating diurnal tides in the equatorial lower thermosphere. Geophys. Res. Lett., 29(24):2167, 2002.

[167] J. Oberheide, M. E. Hagan, W. E. Ward, M. Riese, and D. Offermann. Modeling the diurnal tide for the cryogenic infrared spectrometers and telescopes for the atmosphere (crista) 1 time period. J. Geophys. Res., 105:24917–24929, 2000.

[168] J. Oberheide, M.E. Hagan, A.D. Richmond, and J.M. Forbes. Atmospheric tides. Encyclopedia of Atmospheric Sciences, page 287, 2015.

[169] S. E. Palo, R. G. Roble, and M. E. Hagan. Middle atmosphere effects of the quasi-two-day wave determined from a general circulation model. Earth Planets Space, 51:629–647, 1999.

[170] S. E. Palo, R. G. Roble, and M. E. Hagan. Middle atmosphere effects of the quasi-two-day wave determined from a general circulation model. Earth Planets Space, 51:629–647, 1999.

[171] D. Pancheva and et al. Global-scale tidal variability during the psmos campaign of juneaugust 1999: interaction with planetary waves. J. Atmos. Sol.-Terr. Phys., 64:1865–1896, 2002.

[172] D. Pancheva, Y. Miyoshi, P. Mukhtarov, H. Jin, H. H. Shinagawa, and H. Fujiwara. Global response of the ionosphere to atmospheric tides forced from below: comparison between cosmic measurements and simulations by atmosphere-ionosphere coupled model gaia. J. Geophys. Res., 117, 2012.

[173] D. Pancheva and P. Mukhtarov. Strong evidence for the tidal control on the longitudinal structure of the ionospheric f-region. Geophys. Res. Lett., 37, 2010.

[174] D. Pancheva and Pl. Mukhtarov. Variability of mesospheric dynamics observed at yambol (42 degrees n, 26.6 degrees e) by meteor radar. J. Atm. Terr. Phys., 56(10):1271–1278, 1994.

[175] N. M. Pedatella and J. M. Forbes. Evidence for stratosphere sudden warming-ionosphere coupling due to vertically propagating tides. Geophys. Res. Lett., 37, 2010.

[176] N. M. Pedatella, J. M. Forbes, and J. Oberheide. Intra-annual variability of the low-latitude ionosphere due to nonmigrating tides. Geophys. Res. Lett., 35, 2008.

[177] N. M. Pedatella, H.-L. Liu, and M. E. Hagan. Day-to-day migrating and nonmigrating tidal variability due to the six-day planetary wave. J. Geophys. Res., 117, 2012.

[178] G. W. Prölss. Density perturbations in the upper atmosphere caused by the dissipation of solar wind energy. Surv. Geophys., 31, 2011.

[179] H. Rebhan, M. Aguirre, and J. Johannessen. The gravity field and steady-state ocean circulation explorer mission. GOCE, ESA Earth Obs. Q., 66:6–11, 2000.

[180] S. Rentz and H. Lühr. Climatology of the cusp-related thermospheric mass density anomaly, as derived from champ observations. Ann. Geophys., 26:2807–2823, 2008.

[181] A. D. Richmond. Tidal winds at ionospheric heights. Radio Sci., 6:175–189, 1971.

[182] A. D. Richmond, E. C. Ridley, and R. G. Roble. A thermosphere/ionosphere general circulation model with coupled electrodynamics. Geophys. Res. Lett., 19:601–604, 1992.

[183] A. D. Richmond and R. G. Roble. Electrodynamic effects of thermospheric winds from the ncar thermospheric general circulation model. J. Geophys. Res., 92:148–227, 1987.

[184] M. M. Rienecker and et al. Merra: Nasa's modern-era retrospective analysis for research and applications. J. Climate, 24:3624–3648, 2011.

[185] D. M. Riggin, D. C. Fritts, T. Tsuda, T. Nakamura, and R. A. Vincent. Radar observations of a 3-day kelvin wave in the equatorial mesosphere. J. Geophys. Res., 102:141–158, 1997.

[186] H. Rishbeth. The effect of winds on the ionospheric f2-peak. J. Atmos. Sol. Terr. Phys., 29:225–238, 1967.

[187] H. Rishbeth. The f-layer dynamo. Planet. Space Sci., 19:263267, 1971.

[188] H. Rishbeth. The equatorial f-layer: Progress and puzzles. Ann. Geophys., 18:730–739, 2000.

[189] H. Rishbeth. Whatever happened to superrotation. J. Atmos. Sol. Terr. Phys., 64:1351–1360, 2002.

[190] H. Rishbeth, S. Ganguly, and J. C. G. Walker. Field-aligned and field-perpendicular velocities in the ionospheric f2 layer. J. Atmos. Sol. Terr. Phys., 40:767–784, 1978.

[191] H. Rishbeth and O. K. Garriott. Introduction to ionospheric physics. Academic, New York, page 331, 1969.

[192] R. G. Roble and E. C. Ridley. A thermosphere-ionosphere-mesosphere-electrodynamics general circulation model (time-gcm): Equinox solar cycle minimum simulations (30500 km). Geophys. Res. Lett., 21:417–420, 1994.

[193] R. G. Roble, E. C. Ridley, A. D. Richmond, and R. E. Dickinson. A coupled thermosphere/ionosphere general circulation model. Geophys. Res. Lett., 15:1325–1328, 1988.

[194] C. J. Roth. Idm-2 sensor commanding, data collection processing and analysis. Air Force Res. Lab., AFRL-Rep. VS-HA-TR-2004- 1204:Hanscom Air Force Base, Mass, 2004.

[195] E. Sagawa, T. J. Immel, H. U. Frey, and S. B. Mende. Longitudinal structure of the equatorial anomaly in the nighttime ionosphere observed by image/fuv. J. Geophys. Res., 110, 2005.

[196] J. E. Salah and J. M. Holt. Midlatitude thermospheric winds from incoherent scatter radar and theory. Radio Sci., 9:301–313, 1974.

[197] M. L. Salby and R. R. Garcia. Transient response to localized episodic heating in the tropics. part i: Excitation and short-time near-field behavior. J. Atmos. Sci., 44:458–498, 1987.

[198] M. L. Salby, D. L. Hartmann, P. L. Bailey, and J. C. Gille. Evidence for equatorial kelvin modes in nimbus-7 lims. J. Atm. Sci., 41:220–235, 1984.

[199] A. Spizzichino. Etude des interactions entre less differentes composantes du vent dans la haute atmosphere. Ann. Geophys., 25:693–720, 1969.

[200] R. Sridharan, C. V. Devasia, N. Jyoti, D. Tiwari, K. S. Viswanathan, and K. S. V. Subbarao. Effects of solar eclipse on the electrodynamical processes of the equatorial ionosphere: a case study during 11 august 1999 dusk time total solar eclipse over india. Ann. Geophys., 20:1977–1985, 2002.

[201] E. K. Sutton, J. M. Forbes, and R. Nerem. Global thermospheric neutral density and wind response to the severe 2003 geomagnetic storms from champ accelerometer data. J. Geophys. Res., 110:A09S40, 2005.

[202] A. A. Svoboda, J. M. Forbes, and S. Miyahara. A space-based climatology of mlt winds, temperatures and densities from uars wind measurements. J. Atmos. Solar-Terr. Phys., 67:1533–1543, 2005.

[203] E. R. Talaat and R. S. Lieberman. Nonmigrating diurnal tides in mesospheric and lower thermospheric winds and temperatures,. J. Atmos. Sci., 56:4073–4087, 1999.

[204] E. R. Talaat and R. S. Lieberman. Direct observations of nonmigrating diurnal tides in the equatorial thermosphere. Geophys. Res. Lett., 37, 2010.

[205] H. Teitelbaum and F. Vial. On tidal variability induced by nonlinear interaction with planetary waves. J. Geophys. Res., 96:169–178, 1991.

[206] H. Teitelbaum, F. Vial, A. H. Manson, R. Giraldez, and M. Massebeuf. Nonlinear interaction between the diurnal and semidiurnal tides: Terdiurnal and diurnal secondary waves. J. Atmos.Terr. Phys., 51:627–634, 1989.

[207] J. P. Thayer, J. Lei, J. M. Forbes, E. K. Sutton, and R. S. Nerem. Thermospheric density oscillations due to periodic solar wind fast streams. J. Geophys. Res., 113:A06307, 2008.

[208] J. P. Thayer and J. Semeter. The convergence of magnetospheric energy flux in the polar atmosphere. J. Atmos. Sol. Terr. Phys., 66:807–824, 2004.

[209] A. O. Truskowski, J. M. Forbes, X. Zhang, and S. E. Palo. New perspectives on thermosphere tides: 1. lower thermosphere spectra and seasonal-latitudinal structures. Earth, Planets and Space, 136:66, 1, 2014.

[210] H. Volland. Solutions of laplaces tidal equation for complex frequencies. J. Atmos. Sol.-Terr. Phys., 36:445–460, 1974.

[211] H. Volland. Atmospheric tidal and planetary waves. Kluwer Academic Publishers, Boston, page 348, 1988.

[212] H. Volland and H. G. Mayr. Theoretical aspects of tidal and planetary wave propagation at thermospheric heights. Reviews of Geophysics and Space Physics, 15:203–226, 1977.

[213] J. M. Wallace and V. E. Kousky. Observational evidence of kelvin waves in the tropical stratosphere. J. Atmos. Sci., 25:900–907, 1968.

[214] R. L. Walterscheid and G. Crowley. Thermal cell structures in the high-latitude thermosphere induced by ion drag. J. Geophys. Res., 120:6837–6850, 2015.

[215] R. L. Walterscheid, J. G. de Vore, and S. V. Venkateswaran. Influence of mean zonal motion and meridional temperature gradients on the solar semidiurnal tide: A revised spectral study with improved heating rates. J. Atmos. Sci., 37:455–470, 1980.

[216] R. L. Walterscheid and S. V. Venkateswaran. Influence of mean zonal motion and meridional temperature gradients on the solar semidiurnal atmospheric tide: A spectral study, i, numerical results. J. Atmos. Sci., 36:1636–1662, 1979.

[217] R. L. Walterscheid and S. V. Venkateswaran. Influence of mean zonal motion and meridional temperature gradients on the solar semidiurnal atmospheric tide: A spectral study, i, theory,. J. Atmos. Sci., 36:1623–1635, 1979.

[218] H. T. Wang, J. Fuller-Rowell, R. A. Akmaev, M. Hu, D. T. Kleist, and M. D. Iredell. First simulations with whole atmosphere data assimilation and forecast system: The january 2009 major sudden stratospheric warming. J. Geophys. Res., 116:A12321, 2011.

[219] D. R. Weimer, E. K. Sutton, M. G. Mlynczak, and L. A. Hunt. Intercalibration of neutral density measurements for mapping the thermosphere. J. Geophys. Res., 121:5975–5990, 2016.

[220] L. E. Wharton, N. W. Spencer, and H. G. Mayr. The earth's thermospheric superrotation from dynamics explorer 2. Geophys. Res. Lett., 11:531–533, 1984.

[221] M. Wheeler and G. N. Kiladis. Convectively coupled equatorial waves: analysis of clouds and temperature in the wavenumber-frequency domain. J. Atmos. Sci., 56:374–399, 1999.

[222] M. Yanowitch. Effect of viscosity on gravity waves and the upper boundary condition. J. Fluid Mechanics, 29:209–231, 1967.

[223] E. Yigit and A. S. Medvedev. Internal wave coupling processes in earth's atmosphere. Adv. Space Res., 55:983–1003, 2015.

[224] E. Yigit and A. S. Medvedev. Internal wave coupling processes in earths atmosphere. Advances in Space Research, 55:983–1003, 2015.

[225] S. Yoshida, T. Tsuda, A. Shimizu, and T. Nakamura. Seasonal variations of 3.0-3.8 day ultra-fast kelvin waves observed with a meteor wind radar and radiosonde in indonesia. Earth Planets Space, 51:675–684, 1999.

[226] X. Zhang, J. M. Forbes, and M. E. Hagan. Longitudinal variation of tides in the mlt region: 1. tides driven by tropospheric net radiative heating. J. Geophys. Res., 115, 2010.

[227] X. Zhang, J. M. Forbes, and M. E. Hagan. Longitudinal variation of tides in the mlt region: 1. tides driven by tropospheric net radiative heating. J. Geophys. Res., 115:A06316, 2010.

[228] X. Zhang, J. M. Forbes, and M. E. Hagan. Longitudinal variation of tides in the mlt region: 2. relative effects of solar radiative and latent heating. J. Geophys. Res., 115, 2010.

[229] X. Zhang, J. M. Forbes, M. E. Hagan, J. M. Russell III, S. E. Palo, C. J. Mertens, and M. G. Mlynczak. Monthly tidal temperatures 20-120 km from timed/saber. J. Geophys. Res., 111:A10S08, 2006.

Appendix A

THE CLASSICAL THEORY OF GLOBAL-SCALE ATMOSPHERIC WAVES

The basic characteristics of global-scale atmospheric waves are described by the classical tidal theory. By neglecting mechanical forcing and dissipation, the classical tidal theory assumes that atmospheric wave motions can be considered as linear perturbations of an initially motionless zonal mean state that is horizontally stratified and isothermal. Specifically, the following assumptions are made [Longuet-Higgins, 1968 [144]; Chapman and Lindzen, 1970 [18]; Volland, 1988 [211]; Forbes, 1995 [39]]:

- the solutions to the momentum, thermal energy, continuity, and state equations for a specified forcing represent linearized perturbations on a horizontally stratified motionless background state;
- the solutions are hydrostatic and periodic in longitude and time;
- a spherical rotating planet;
- dissipative processes are neglected, or simply parameterized by through a complex frequency.

Under the above assumptions, the solutions to the linearized dynamical equations have a form which is separable in height and latitude, i.e.,

$$e^{i(s\lambda-\sigma t)}y_n(x)\Theta_n(\theta, f, s) \tag{A.1}$$

where σ is the wave frequency, t the time, s the zonal wavenumber ($s \geq 0$), λ the longitude, $x = \int \frac{dz}{H}$, z the geometric height, H the scale height, $f = \frac{\sigma}{2\Omega}$, Ω the planetary rotation rate, Θ_n the nth eigenfunction, and n denotes the nth solution to the eigenvalue-eigenfunction problem ($\sigma > 0$ implies eastward propagation and $\sigma < 0$ implies westward propagation).

A.1 Horizontal Structure

The Θ_n are the solutions to Laplace's Tidal Equation $F(\Theta) = \epsilon_n \Theta_n$, where ϵ_n are the eigenvalues and

$$F(\Theta) = \frac{d}{d\mu}\left[\frac{(1-\mu^2)}{(f^2-\mu^2)}\frac{d\Theta_n}{d\mu}\right] - \frac{1}{f^2-\mu^2}\left[-\frac{s}{f}\frac{(f^2+\mu^2)}{(f^2-\mu^2)} + \frac{s^2}{(1-\mu^2)}\right]\Theta_n \tag{A.2}$$

where $\mu = sin\theta$. The eigenvalues are usually expressed in terms of the equivalent depths h_n, where $\epsilon_n = (4R_E^2\Omega^2)/(gh_n)$, and g is the acceleration due to gravity, and $\epsilon_n \sim 88$ km$/h_n$ (on Earth). For each choice of s and σ, there exists sets of ϵ_n and Θ_n satisfying Equation (A.2) and the condition of boundedness at the poles. The ϵ_n and σ are generally related parametrically for a given s in diagrams like Figure A.1 for s=1 (diagrams for s=2 and s=3 are very similar).

Identified in Figure A.1, for both eastward-propagating and westward-propagating solutions, are the 'gravity-type' or 'Class I' modes; the 'Rossby-type' or 'Class II' modes; the 'Rossby-Haurwitz' waves for which $\epsilon_n = 0$; normal modes, identified by the horizontal line where $\epsilon_n = 8.4$ ($h_n = 10.5$ km) for a 256 K isothermal atmosphere; the series of diurnal tidal modes along an imaginary vertical line where $\sigma/\Omega = -1$; the series of eastward-propagating waves with period = 3 days along an imaginary vertical line where $\sigma/\Omega = 1/3$.

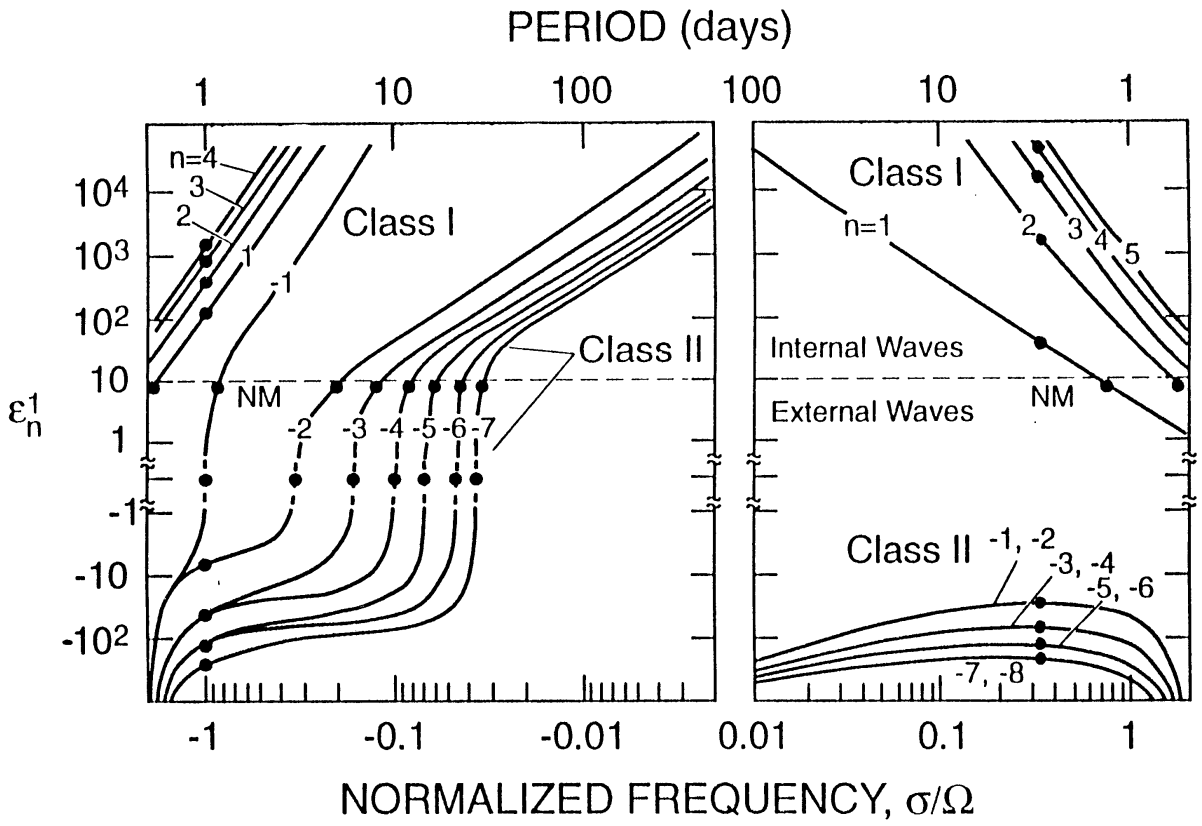

Figure A.1: Eigenvalue ϵ of wave modes of zonal wave number $s = 1$ vs. normalized frequency σ/Ω where Ω is the Earth's rotation rate. Waves with positive (negative) frequencies propagate to the east (west). The horizontal dashed line at $\epsilon_n^1 \sim 11$ indicates the transition from internal to external waves. The horizontal series of dots corresponding to $\epsilon_n^1 = 0$ denote the so-called Rossby-Haurwitz waves. The dots corresponding to NM refer to the normal modes ($\epsilon_n^1 \sim 8.4$). The vertical series of dots at $\sigma/\Omega = -1$ and $\sigma/\Omega = 1/3$ define the ϵ_n^1 for the westward-propagating diurnal tide and the eastward-propagating 3-day wave, respectively. The gravest (n=1) of the eastward-propagating gravity-type (Class I) modes is the Kelvin wave. Figure and caption adapted from Volland [1988] [211].

A.2 Vertical Structure

Atmospheric waves are eigenoscillations (eigenmodes) of Earth's atmosphere with eigenfunctions Θ_n, called Hough functions, and eigenvalues ϵ_n. The vertical structure $y_n(x)$ of each Hough mode for a thermally forced oscillation is given by

$$\frac{d^2 y_n}{dx^2} + \alpha^2 y_n = \frac{\kappa J_n(x)}{\gamma g h_n} e^{-x/2} \tag{A.3}$$

where $\alpha^2 = [(1/h_n)(\kappa H + dH/dx) - 1/4]$, $\kappa = (\gamma - 1)/\gamma$ where γ is the ratio of specific heats C_p/C_v, and the eigenvalue is now introduced as h_n, and $x = \int \frac{dz}{H}$ (see beginning of this appendix). When

- $h_n > 4(\kappa H + dH/dx)$ or $h_n < 0$, then $\alpha^2 < 0$, and the solution decays exponentially with height $y_n(x) \sim e^{(|\alpha|)}$ above the source region.

- $0 < h_n < 4(\kappa H + dH/dx)$, then $\alpha^2 > 0$, and vertically propagating solutions $y_n(x) \sim e^{i\alpha x}$ exist; for this case a vertical wavelength $\lambda_z = 2\pi/\alpha$ can be defined.

- In the absence of any forcing on the right-hand side of Equation (A.3), the only nontrivial solution satisfying boundedness and zero vertical velocity at the lower boundary is one for which $y_n(x) \sim e^{(\kappa - 0.5)x}$, and a single eigenvalue emerges with value $h_n = H/(1 - \kappa)$ (h_n =10.5 km for H = 7.5 km). This free (unforced) solution corresponds to a resonant response of the atmosphere, known as a 'normal mode'.

For propagating solutions ($\alpha_n^2 > 0$), the vertical group velocity $c_{gz,n} = H\frac{\partial \sigma}{\partial \alpha_n}$ becomes positive (upward energy propagation) only if $\alpha_n > 0$ for westward ($\sigma < 0$) or if $\alpha_n < 0$ for eastward ($\sigma > 0$) propagating waves.

Each eigenfunction/eigenvalue pair, Θ_n and ϵ_n (or h_n), represents a 'mode'. Generally modes are expressed in terms of s, the zonal wavenumber, and n, the meridional index, providing information on the number of latitudinal nodes and symmetry characterizing Θ_n. Thus one can refer to particular mode as the Θ_n^s mode or just the (s, n) mode, and to add some information on wave period, as in the '(1,1) diurnal tide' or 'first symmetric propagating diurnal tide'.

For forced modes we generally know the frequency of forcing. By drawing a vertical line at σ/Ω = -1 in Figure A.1, the points of intersection define the ϵ_n values corresponding to the modes which comprise the response at the diurnal frequency. We see that the diurnal response can possibly consist of a mixture of trapped ($\epsilon_n < 0$) modes (i.e., (1, -1); (1, -2)) and propagating

($\epsilon_n > 0$) modes (i.e., (1, 1); (1, 2)). As a result, heating in the lower atmosphere may result in (a) modes vertically propagating, and/or (b) a response contained at the level of excitation. Figure A.2 shows examples of common Hough functions and velocity expansion functions.

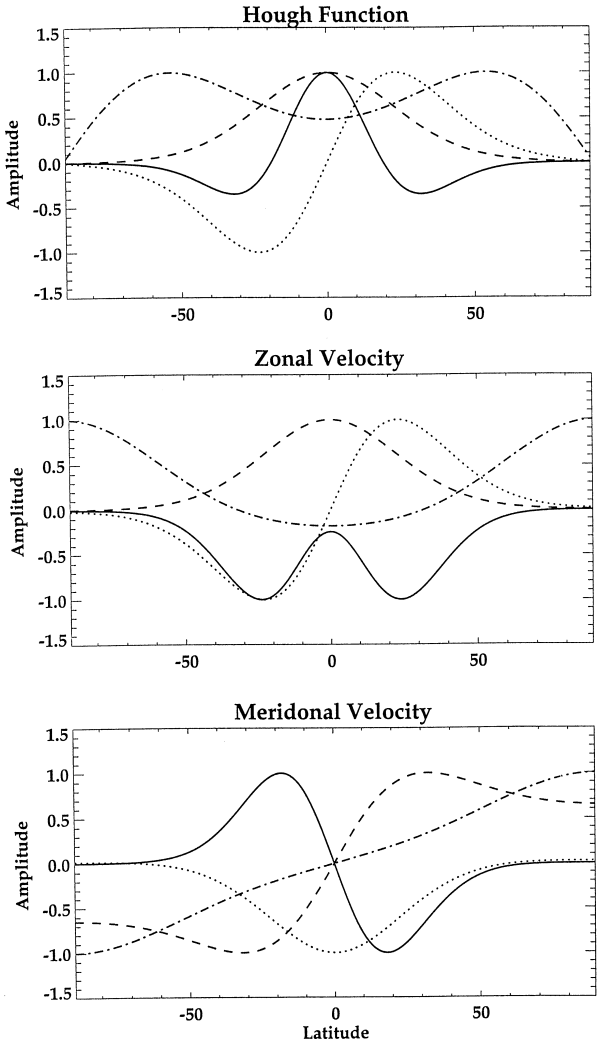

Figure A.2: Hough functions (top) and zonal (middle) and meridional (bottom) velocity expansion functions, normalized to unity, for the following $s = 1$ oscillations, ($\pm\ \sigma/\Omega$, s, n): the first symmetric propagating diurnal tide (-1, 1, 1) (solid line); the first symmetric westward trapped diurnal tide (-1, 1, -2) (dash-dot line); the first asymmetric eastward propagating diurnal tide (1, 1, 2) (dotted line); and the eastward-propagating Kelvin wave with 3-day period (1/3, 1, 1) (dashed line). Figure and caption adapted from Forbes [2000] [40].

A.3 Modeling Dissipation

In linear wave theory, dissipative terms appear on the right-hand side of the horizontal momentum and thermal energy equations and can be written as:

$$\frac{\partial}{\partial t}\begin{pmatrix}u'\\v'\end{pmatrix}+\frac{U}{R_E cos\theta}\frac{\partial}{\partial\lambda}\begin{pmatrix}u'\\v'\end{pmatrix}+...=\frac{1}{\rho_0}\frac{\partial}{\partial z}(\mu_0+\rho_0\mu_{eddy})\frac{\partial}{\partial z}\begin{pmatrix}u'\\v'\end{pmatrix}-\Lambda_1^0\begin{bmatrix}1 & 0\\0 & sin^2 I\end{bmatrix}\begin{pmatrix}u'\\v'\end{pmatrix} \tag{A.4}$$

$$\frac{\partial T'}{\partial t}+\frac{U}{R_E cos\theta}\frac{\partial T'}{\partial\lambda}+...=\frac{1}{\rho_0}\frac{\partial}{\partial z}(\kappa_0+\rho_0\kappa_{eddy})\frac{\partial T'}{\partial z}-\alpha T' \tag{A.5}$$

where u' is the eastward wind perturbation, v' the northward wind perturbation, T' the temperature perturbation, U the mean zonal wind, R_E the radius of the Earth, θ the latitude, ρ_0 the background density, Λ_1^0 the diurnal mean ion drag coefficient, I the dip angle of the magnetic field, μ_0 the molecular viscosity coefficient, κ_0 the molecular thermal conductivity, κ_{eddy} the eddy thermal conductivity, ν_{eddy} the kinematic eddy viscosity, and α is the Newtonian cooling coefficient.

If we assume isotropic ion drag ($I = 90°$), replace the diffusion terms with terms of the form $\nu_{diff}=\frac{\partial^2}{\partial z^2}\binom{u'}{v'}$ and $\kappa_{diff}=\frac{\partial^2 T'}{\partial z^2}$ (where ν_{diff} and κ_{diff} describe the effects of molecular and eddy diffusion), and assuming solutions of the form $(u', v', T') = (\hat{u}, \hat{v}, \hat{T})e^{i(s-\sigma t)}$, Equations (A.4) and (A.5) can be written as

$$i\sigma_D\begin{pmatrix}u'\\v'\end{pmatrix}+...=\nu_{diff}\frac{\partial^2}{\partial z^2}\begin{pmatrix}u'\\v'\end{pmatrix}-\nu_{ion}\begin{pmatrix}u'\\v'\end{pmatrix} \tag{A.6}$$

$$i\sigma_D T'+...=\kappa_{diff}\frac{\partial^2 T'}{\partial z^2}-\alpha T' \tag{A.7}$$

where σ_D is the Doppler-shifted frequency $\sigma_D = -\sigma + sU/(R_E cos\theta)$.

The 3 terms in the above momentum and thermal energy equations (A.6) and (A.7) can then be approximated in terms of a complex frequency, and wherein the equations begin to look like those for a windless atmosphere and no dissipation:

$$i(\sigma_D - i\nu_R(z))\begin{pmatrix} u' \\ v' \end{pmatrix} + ... = 0 \tag{A.8}$$

$$i(\sigma_D T' - ia(z))T' + ... = 0 \tag{A.9}$$

and $\nu_R(z) = \frac{\nu_{diff} 4\pi}{\lambda_z^2} + \nu_{ion}$ is Rayleigh friction, and $a(z) = \frac{\kappa_{diff} 4\pi}{\lambda_z^2} + \alpha$ is radiative cooling (units of s^{-1}). Lindzen [1968, 1970] [125][126] showed that the windless tidal equations still remained separable when including a height-dependent Newtonian cooling coefficient, and used this formulation to reveal some basic characteristics of waves propagating into a thermosphere where the dissipative time scale increases as ρ_0^{-1}.

For more details on the horizontal structure, vertical structure, and influence of dissipation an interested reader may refer to Chapman and Lindzen [1970] [18].

Appendix B

VALIDATION OF THE WIND DERIVATION METHOD

This appendix provides the complete validation of the methodology outlined in Section 3.3. In order to validate the winds derived from CHAMP neutral and electron densities, we implement TIME-GCM simulations with horizontal resolution of 2.5° x 2.5° (longitude x latitude), vertical resolution of 4 points per scale height, and 60-second time step for September at solar minimum (F10.7 value of 70 sfu) and December at solar medium (F10.7 value of 120 sfu). The simulations are static monthly values i.e., the TIME-GCM is run for one day in the middle of the month of interest until the model reaches a diurnally-reproducible state, and uses GSWM-09 to specify tidal components at the lower boundary (i.e., 10 mb or 30 km). GSWM-09 includes updated background temperature and wind fields derived from TIMED-SABER measurements, as well as new radiative and latent heating rates derived from the International Satellite Cloud Climatology Project (ISCPP) and Tropical Rainfall Measuring Mission (TRMM) data, respectively [Zhang et al., 2010a,b [226][228]]. The GSWM-09 boundary used in the TIME-GCM simulations include migrating and non-migrating diurnal and semidiurnal tidal components with zonal wavenumbers ranging between ±6. The results are presented for the single height of 350 km, comparable to CHAMP average altitude around 2007.

The validation outlined in this appendix consists of 3 parts: (B.1) scale analysis of the momentum equation in the zonal (eastward) direction, (B.2) error analysis for each of the 3 steps in the wind derivation method, and (B.3) summary of errors, including errors due to fix local time assumptions and uncertainties in the raw data.

B.1 Scale Analysis of the Zonal Momentum Equation

Starting from the zonal momentum equation in its complete form (as presented in Section 3.3):

$$\frac{\partial u}{\partial t} = \frac{\mu}{\rho}\frac{\partial^2 u}{\partial z^2} + f^{cor}v + \lambda_x(u^e - u) + \lambda_y(v^e - v) - \vec{v}\cdot\vec{\nabla}u + \frac{uv}{R_E}tan\theta - \frac{1}{\rho R_E cos\theta}\frac{\partial p}{\partial \phi} - w\frac{\partial u}{\partial z} \quad \text{(B.1)}$$

and considering the linear relationship between universal time (UT) and local time (LT), such that $\delta t_{UT} = \delta t_{LT} - \frac{\delta\phi}{\Omega}$, we can rewrite Equation B.1 from a fixed local time perspective ($\delta t_{LT} \approx 0$, so $\delta t_{UT} \approx -\frac{\delta\phi}{\Omega}$), similar to that of a quasi-Sun-synchronous satellite, as:

$$-\Omega\frac{\partial u}{\partial \phi} = \frac{\mu}{\rho}\frac{\partial^2 u}{\partial z^2} + f^{cor}v + \lambda_x(u^e - u) + \lambda_y(v^e - v) - \vec{v}\cdot\vec{\nabla}u + \frac{uv}{R_E}tan\theta - \frac{1}{\rho R_E cos\theta}\frac{\partial p}{\partial \phi} - w\frac{\partial u}{\partial z} \quad \text{(B.2)}$$

In other words, the temporal variability for a satellite in a Sun-synchronous orbit is perceived as longitude variability. If we write the rate of change of the zonal wind $-\Omega\frac{\partial u}{\partial \phi}$ as $-\Omega u_\phi$, and consider vertical viscosity $\frac{\mu}{\rho}\frac{\partial^2 u}{\partial z^2} = VV$, the Coriolis force $f^{cor}v = CF$, ion drag $\lambda_x(u^e - u) + \lambda_y(v^e - v) = ID$, horizontal advection $\vec{v}\cdot\vec{\nabla}u = HA$, the momentum force $\frac{uv}{R_E}tan\theta = MF$, pressure gradient $\frac{1}{\rho R_E cos\theta}\frac{\partial p}{\partial \phi} = PG$, and vertical advection $w\frac{\partial u}{\partial z} = VA$, we can rewrite (B.2) as (in the units of acceleration ms^{-2}):

$$-\Omega u_\phi = CF + ID + PG + VA + VV + HA + MF \quad \text{(B.3)}$$

In order to quantify the relative importance of each term in the zonal momentum equation, we use TIME-GCM simulations for December at solar medium conditions. Figure B.1 shows the latitude-longitude structures for VA, VV, the sum VA+VV+HA+MF, ID, PG, CF, the sum ID+PG+CF and the dU/dt ($= \Omega u_\phi$) term. Figure B.2 shows the same results as Figure B.1, but with a fixed colorbar scale for the primary terms (PG, ID, CF) and the second order terms (VA, MF, HA, VV).

The terms VA, HA, ID, and PG are an output of the model, MF is computed using u and v from the model, and VV is calculated assuming $\mu = 0.266 K_0/R$ (where $K_0 = 0.15 T^{2/3}/M$) [Forbes, 1982 [46]] and computing $\frac{\partial^2 u}{\partial z^2} = \frac{u_{z+1} - 2u_z + u_{z-1}}{\Delta z^2} = \frac{u_{355km} - 2u_{350km} + u_{345km}}{5^2}$ (using the temperature array inferred from model neutral densities.)

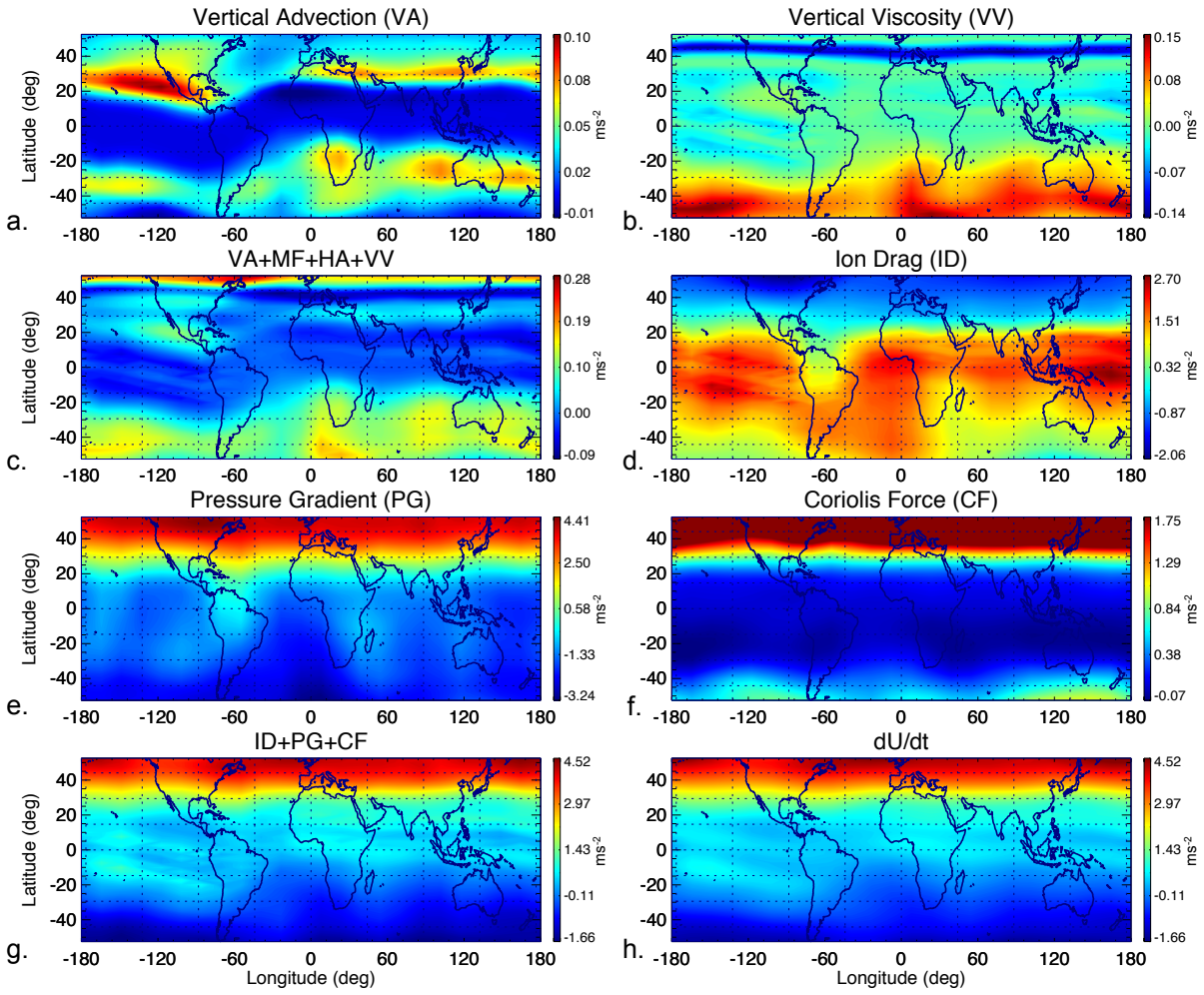

Figure B.1: Latitude vs. longitude plot for: (a) vertical advection (VA), (b) vertical viscosity (VV), (c) the sum VA+MF+HA+VV, (d) ion drag (ID), (e) pressure gradient (PG), (f) Coriolis force (CF), (g) the sum ID+PG+CF, and (h) the dU/dt term. Note that values are ±4 ms^{-2} for pressure gradient, up to 2 ms^{-2} for ion drag, and up to 2 ms^{-2} for the Coriolis force, while the sum of the other terms (VA+MF+HA+VV) only accounts for -0.1 to 0.3 ms^{-2}.

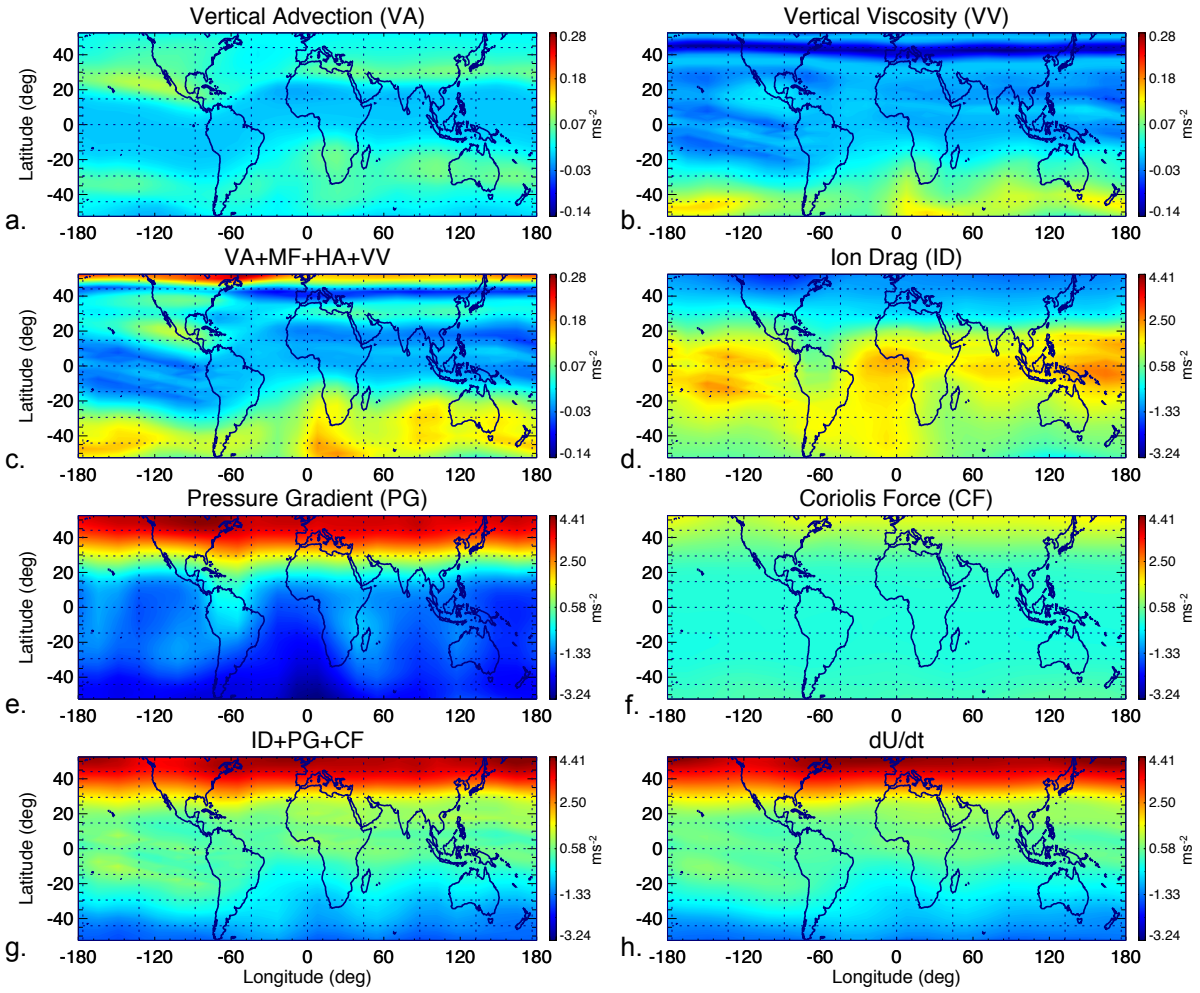

Figure B.2: Latitude vs. longitude plot for: (a) vertical advection (VA), (b) vertical viscosity (VV), (c) the sum VA+MF+HA+VV, (d) ion drag (ID), (e) pressure gradient (PG), (f) Coriolis force (CF), (g) the sum ID+PG+CF, and (h) the dU/dt term. To note how the ion drag force tends to oppose to the pressure gradient force and reduce the overall amplitude of the dU/dt term. The ion drag, pressure gradient, and Coriolis force account for almost all the longitude-latitude variability, as can be seen comparing (g) and (h).

Figures B.1 and B.2 show that the amplitude of VA, MF, HA, and VV is an order of magnitude smaller than that of PG, CF, and ID. This can be seen by comparing the amplitude of VA+MF+HA+VV (panel c) $\sim \pm$ 0.2 ms^{-2} to that of ID+PG+CF (panel g) $\sim \pm 4$ ms^{-2} (the latter is $\sim$20 times larger than the former), as well as by comparing ID+PG+CF (panel g) with

the dU/dt term (panel h).

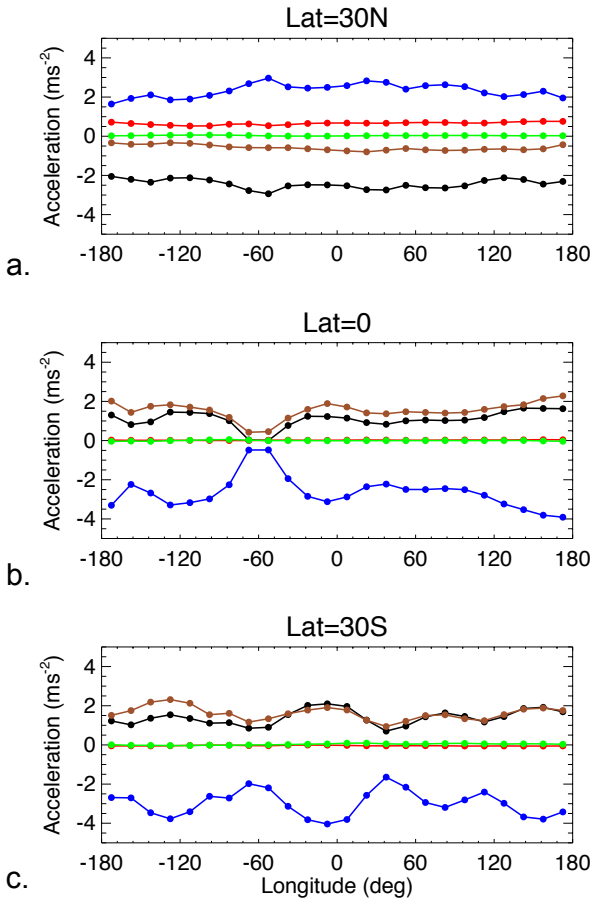

Figure B.3: Longitudinal variability due to PG (black line), ID (brown line), CF (red line), VA+MF+HA+VV (green line), and dU/dt term (blue line) for 30N (panel a), equator (panel b), and 30S (panel c). To note the large contribution of pressure gradient and ion drag force (that tend to oppose to each other), as opposed to the very small values attained by VA+MF+HA+VV.

Figure B.3 shows the longitudinal variability of PG (black line), ID (brown line), CF (red line), dU/dt (blue line), and the sum VA+MF+HA+VV (green line) at different latitudes: +30° (panel a), equator (panel b), and -30° (panel c). From Figure B.3, and similar to what shown by Figures B.1 and B.2, one can see that the terms VA, MF, HA, VV play a secondary role in generating longitude variability. Additionally, Figure B.3 shows the tendency of the ion drag force

to oppose to the pressure gradient force, resulting in a more balanced momentum equation and thus a smaller dU/dt term.

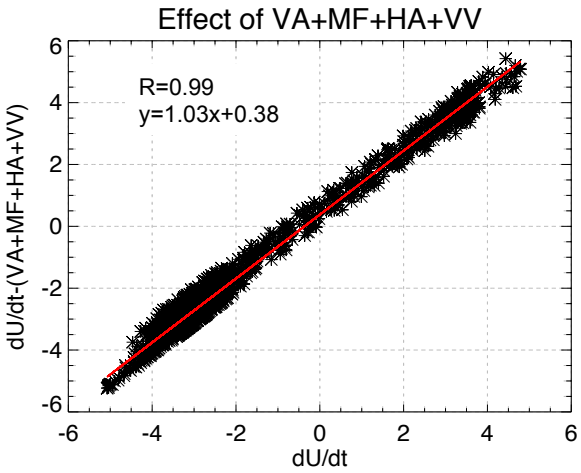

Figure B.4: Scatter plot of all the terms in the momentum equation (dU/dt, x-axis) vs. only pressure gradient, Coriolis force, and ion drag for ±50° latitude. The correlation between the the two datasets is very high, with a correlation coefficient of 0.99.

Figure B.4 shows the scatter plot of the resulting acceleration due to PG+ID+CF vs. the total acceleration (dU/dt). From Figure B.4 we report a correlation coefficient of 0.99, which translates to a variance of ∼0.98. This means that including only PG, ID, CF in the momentum equation leads to an estimated error of only ∼ ±2%, mainly due to the omission of VA, MF, HA, and VV.

B.2 Errors in the Winds Derived from CHAMP Densities

In this section we provide a step by step error analysis of the method used to derive horizontal winds from neutral and electron densities. This full analysis is performed in the zonal direction and using the December solar medium model simulation, but the final comparisons between the derived winds and the model winds are made in both the zonal and meridional directions as well as for the September solar minimum run. First, we compare ion drag values calculated from model

electron densities with the ones self-consistently calculated within TIME-GCM. Second, we compare the temperatures derived from the model neutral density with the temperatures self-consistently output by TIME-GCM, and we compare the pressure gradient values calculated from the derived temperatures with the TIME-GCM pressure gradients. Third, we compare the winds derived from electron densities and ion drag values with the ones self-consistently calculated within TIME-GCM.

B.2.1 Ion Drag values from Electron Densities

Ion drag values are derived from electron densities assuming the absence of ion drifts, and a single ion drag coefficient for the x-direction (y-direction) for the zonal (meridional) component. With these assumptions, the ion drag acceleration can be expressed as:

$$ID = \lambda_x(u^e - u) + \lambda_y(v^e - v) = -u\lambda_x \approx \frac{n_e}{N}\frac{\nu_{in}}{1 + (\nu_{in}/\omega_{in})^2} \tag{B.4}$$

where we approximate $\lambda_x \approx \frac{n_e}{N}\frac{\nu_{in}}{1+(\nu_{in}/\omega_{in})^2}$ and $\nu_{in} = 2.610^{-9}(N/M^{0.5})$ [Chapman, 1956 [17]; Rishbeth and Garriott, 1969 [191]; Forbes and Garrett, 1979 [44]].

Figure B.5 shows a comparison between the model ion drag values and those derived using Equation B.4, both by including and not including the model ion drift velocities. Starting from electron densities and ignoring ion drifts and using the crude approximation in Equation B.4 we capture over 86% of the variance of the model ion drag. When including ion drift values this value increases to 98% (panel b$''$). From Figure B.5 we conclude that ion drifts play a non-negligible role in determining ion drag longitudinal variability (accounting up to 12%).

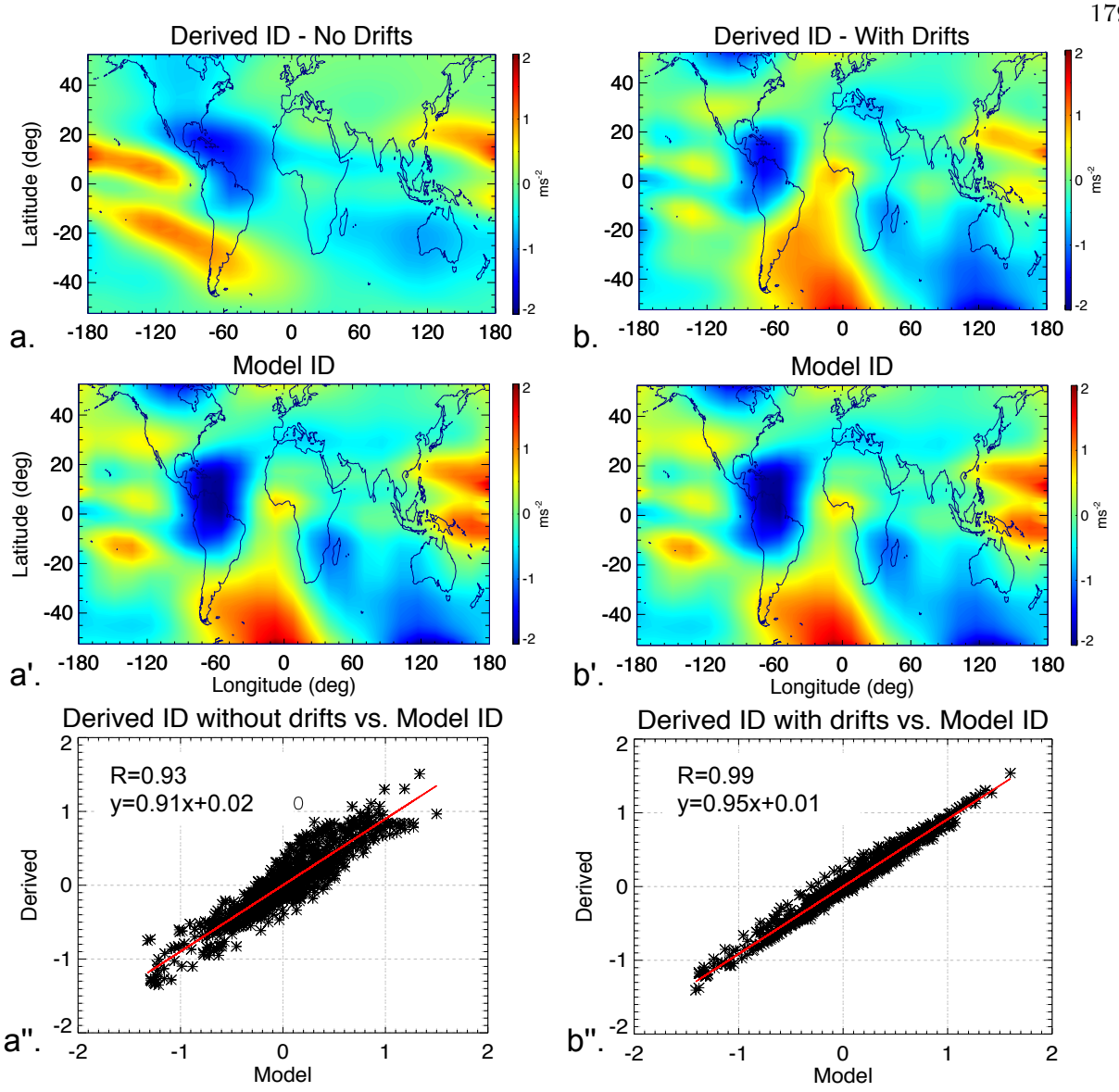

Figure B.5: Latitude-longitude structures for ID derived by not including (panel a) and including (panel b) ion drift velocities; model ID (panels a′ and b′); scatter plots (panels a′′ and b′′) between derived and model values. Note how including ion drift values leads to a much better comparison (correlation coefficients of 0.99 with drifts, compared to 0.93 without the drifts). Note that these plots have the zonal mean removed to help the comparison.

B.2.2 Pressure Gradients from Temperatures

Starting from TIME-GCM neutral density values we use NRLMSISE-00 to derive temperatures consistent with TIME-GCM neutral densities by iterating on the F10.7 index. Starting from an F10.7 value of 120 sfu, we increase or decrease this value in steps of 1 sfu, until the MSISE neutral densities and TIME-GCM neutral densities match with an error less than 5%. For this value of F10.7, we output the MSISE temperature and use the IDL smoothing function 'SMOOTH' to remove some of the noise introduced by this procedure. Figure B.6 (panels a and a′) shows a comparison between the latitude-longitude structures (with zonal mean removed) in the derived temperatures and those in the model temperatures. Figure B.6 shows how well we can replicate the longitudinal variability in the model temperature starting from model densities, with a correlation coefficient (see panel a″) of 0.97 corresponding to a variance of ∼0.94.

We then use these derived temperatures and TIME-GCM neutral densities to calculate pressures using the ideal gas law $p = \rho RT$, and pressure gradients in the zonal and meridional direction by calculating the derivative with respect to longitude and latitude, respectively. The comparison between model pressure gradients (in the zonal direction) and derived pressure gradients is presented in Figure B.6 (panels b and b′). As shown by the scatter plot in panel b″, the derived pressure gradients replicate very well the TIME-GCM pressure gradients, and a correlation coefficient of 0.98 is found between the two. This means that we can capture over 96% of the latitude-longitude variability in the zonal pressure gradients starting exclusively from neutral densities. This value is even greater than the one found for the derived temperatures (∼94%); this is likely due to biases in the MSISE-derived temperature field that are removed by applying longitude/latitude derivatives.

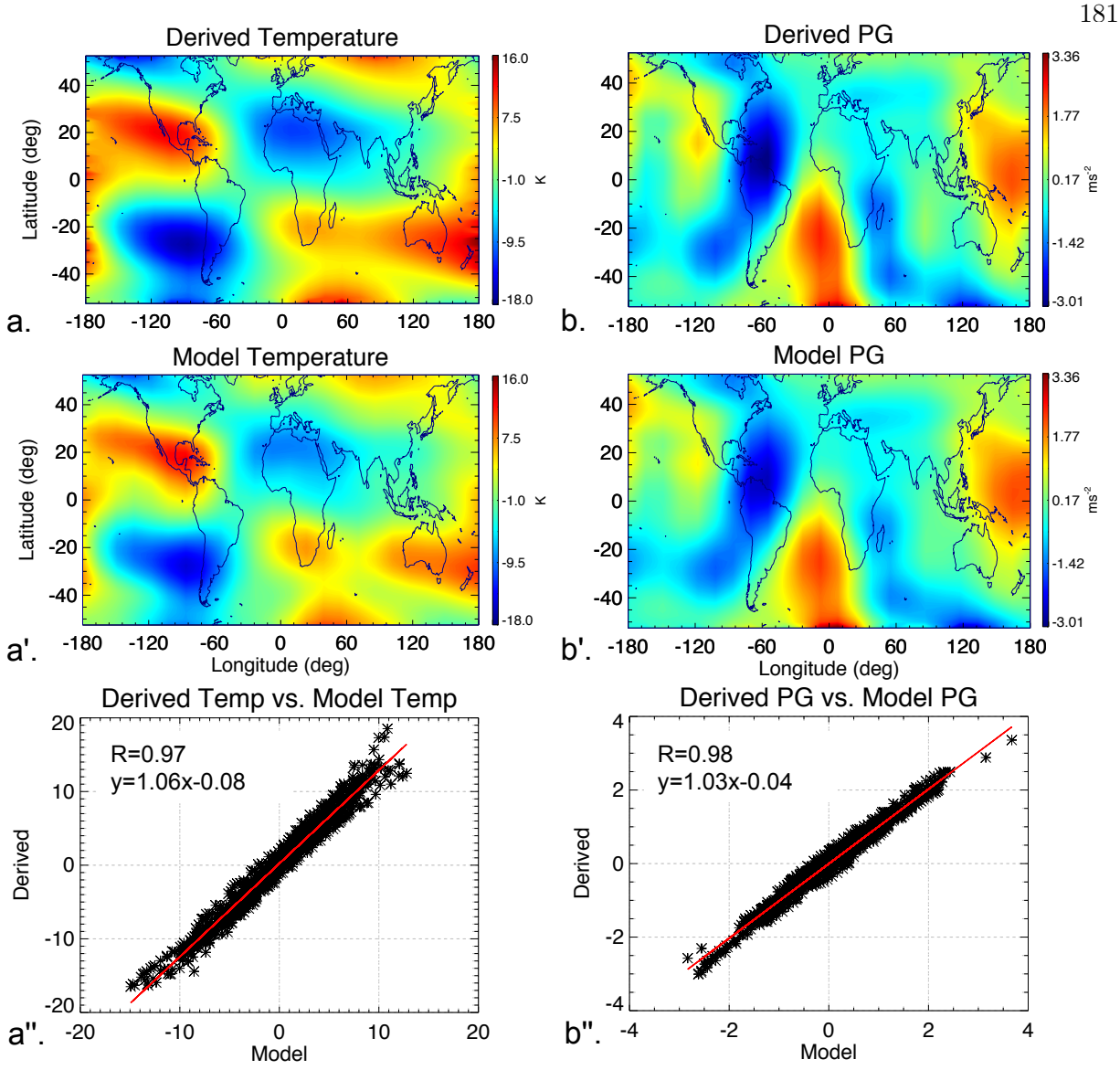

Figure B.6: Latitude vs. longitude plot of derived temperatures (panel a), model temperatures (panel a′), derived pressure gradient values (panel b) and model pressure gradient values (panel b′). The scatter plot of derived vs. model temperatures (panel a′′) shows a correlation coefficient of 0.97, while the scatter plot of derived vs. model pressure gradient values (panel b′′) shows a correlation coefficient of 0.98. Similar to Figure B.5 the zonal mean was removed to facilitate the comparisons.

B.2.3 Winds from Pressure Gradients and Ion Drag Values

Comparisons between model winds and winds derived from electron and neutral densities at different local times are presented in Figure B.7 (Figure B.9) for 4 LT, 8 LT, 12 LT and Figure B.8 (Figure B.10) for 16 LT, 20 LT, 24 LT for the zonal (meridional) wind component. These results show correlation coefficients greater than 0.9 for all the local times analyzed. This means that we are able to capture over 80% of the latitude-longitude variability by starting from neutral and electron densities alone. Most of the error (up to 14% as presented in Section B.2.1 for the ion drag coefficient) is likely caused by neglecting ion drift velocities (discussed at the end of Section B.2.3), while very little is due to neglecting VA, VV, HA, and MF (less then 2%). The results for September are shown in Figure B.11 (Figure B.12) for the zonal (meridional) component at 12 and 24 local time. For these we report correlation coefficients greater than 0.92, very similar to the results for December. For this run one can see greater longitudinal variability ($\sim \pm 50\ ms^{-1}$) in the wind data due to the effect of upward propagating tides, stronger for the month of September at solar minimum than for December at solar medium.

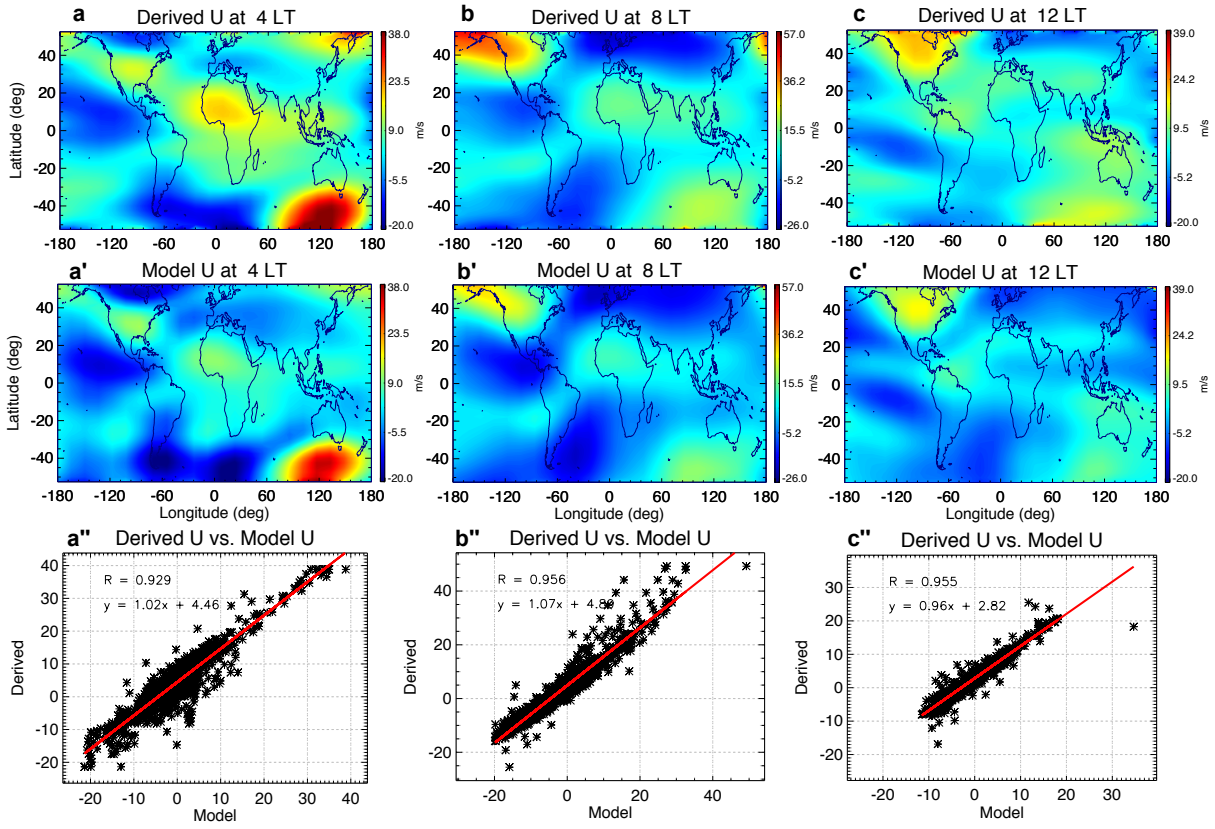

Figure B.7: Zonal wind latitude vs. longitude structures derived from neutral and electron densities (panels a, b, c) and from the model (panels a′, b′, c′), and their scatter plot (panels a′′, b′′, c′′) for 4 LT (a, a′, a′′), 8 LT (b, b′, b′′) and 12 LT (c, c′, c′′). These plots are for December at solar medium conditions with tides at the lower boundary. Note: the zonal mean was removed to facilitate the comparison.

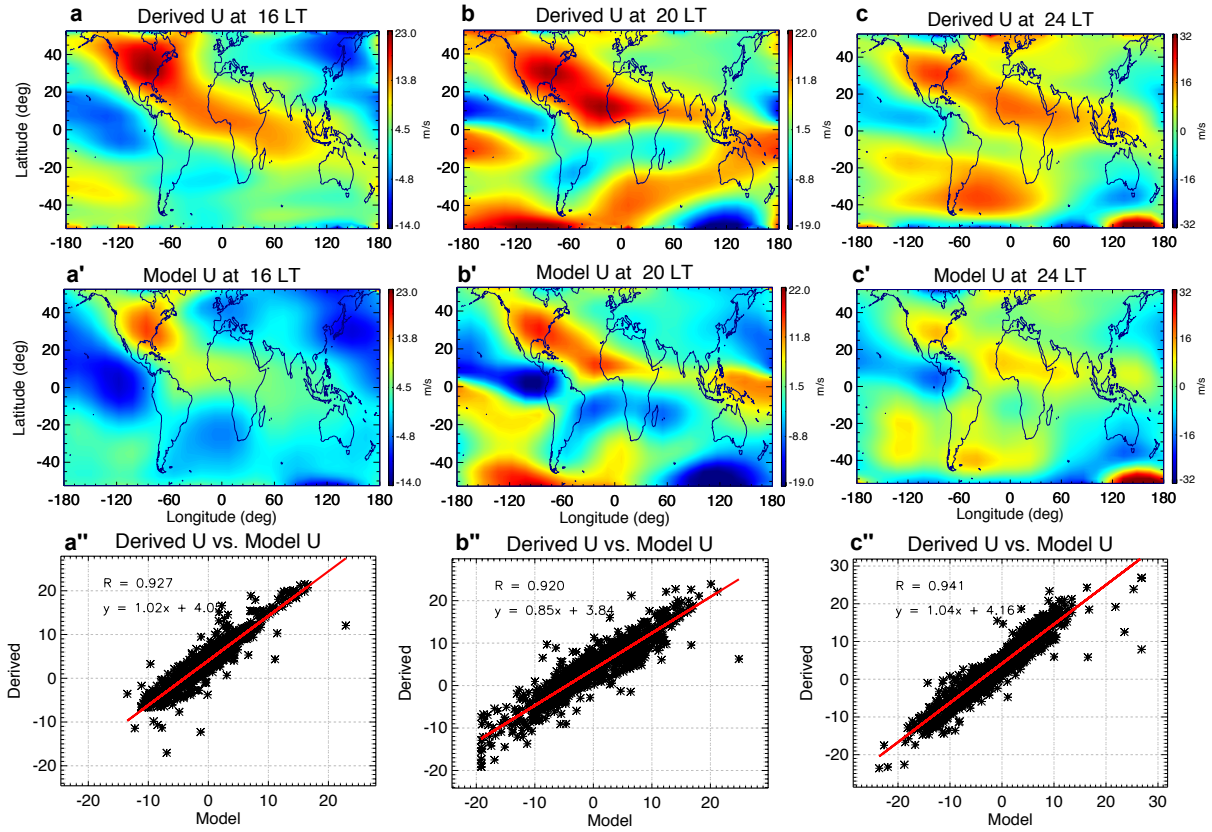

Figure B.8: Similar to Figure B.7, but for 16 LT, 20 LT, 24 LT (panels a-a′′, b-b′′, and c-c′′, respectively).

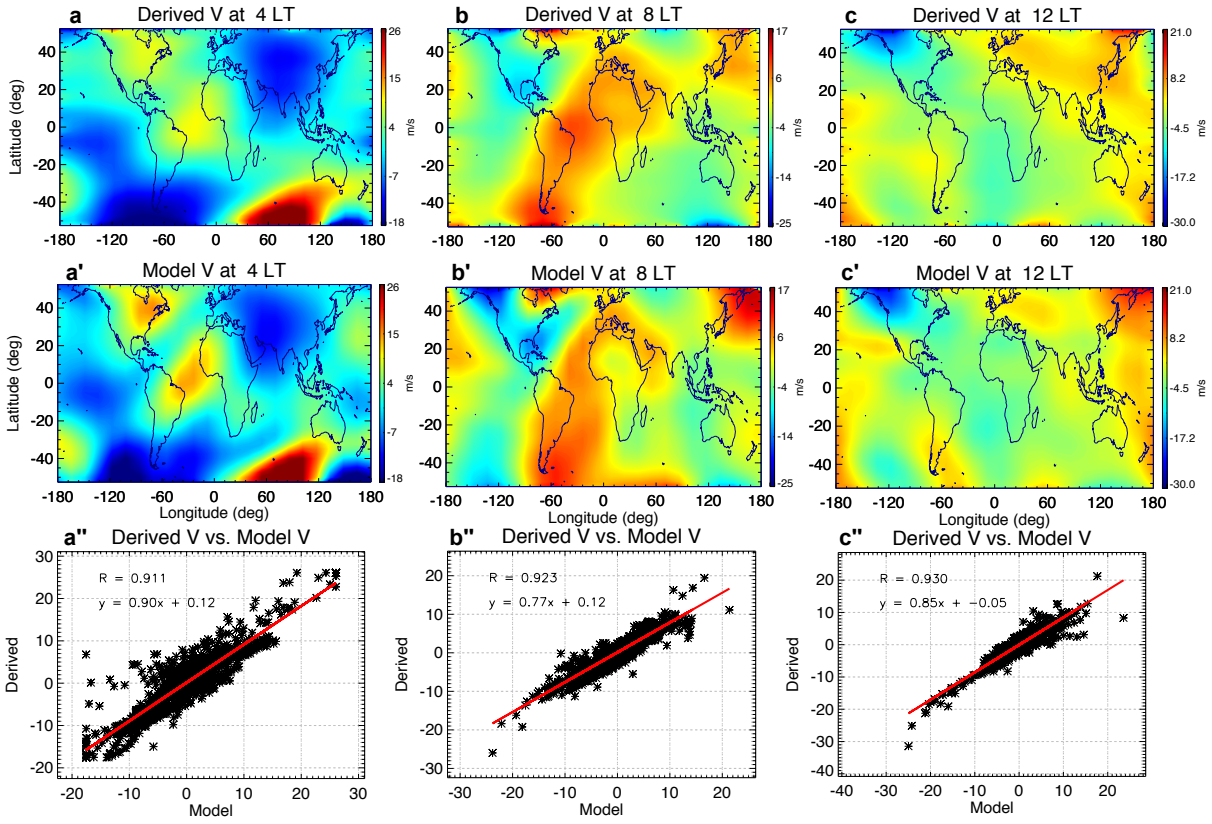

Figure B.9: Similar to Figure B.7, but for the meridional wind component V.

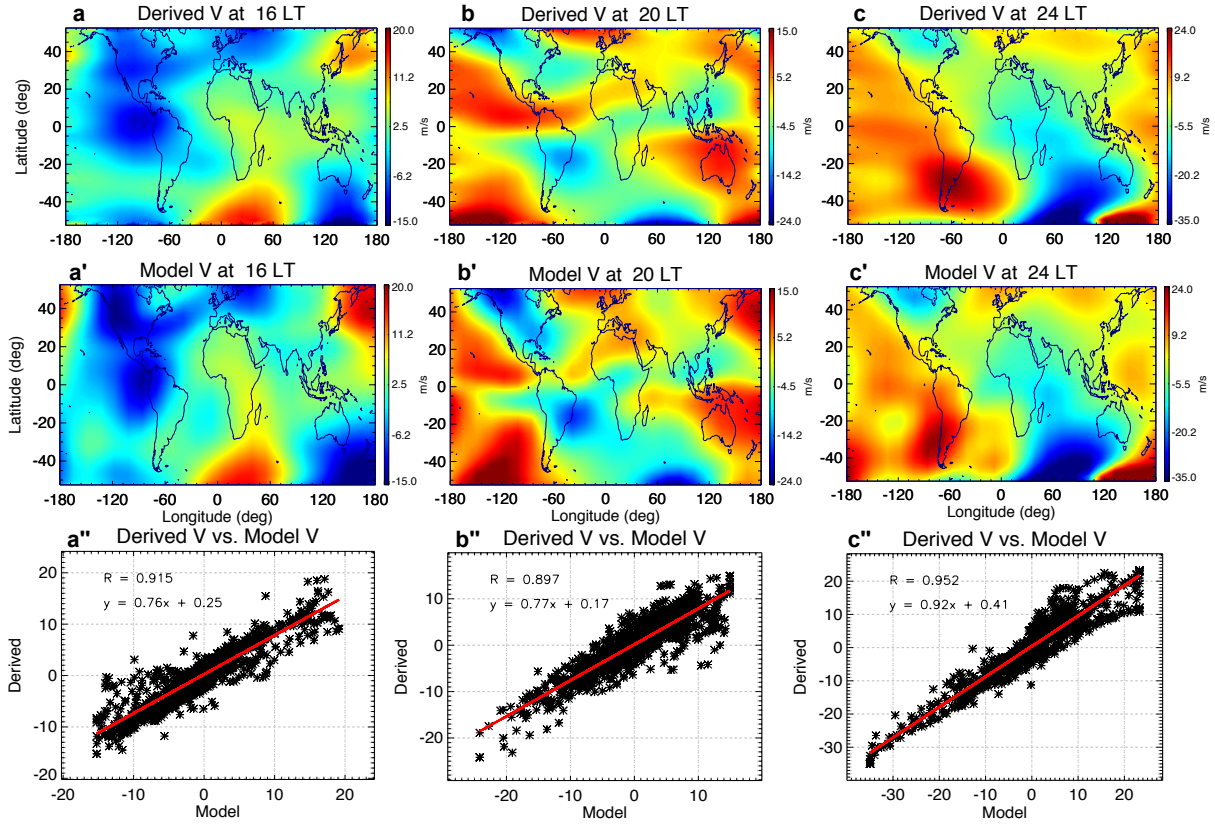

Figure B.10: Similar to Figure B.8, but for the meridional wind component V.

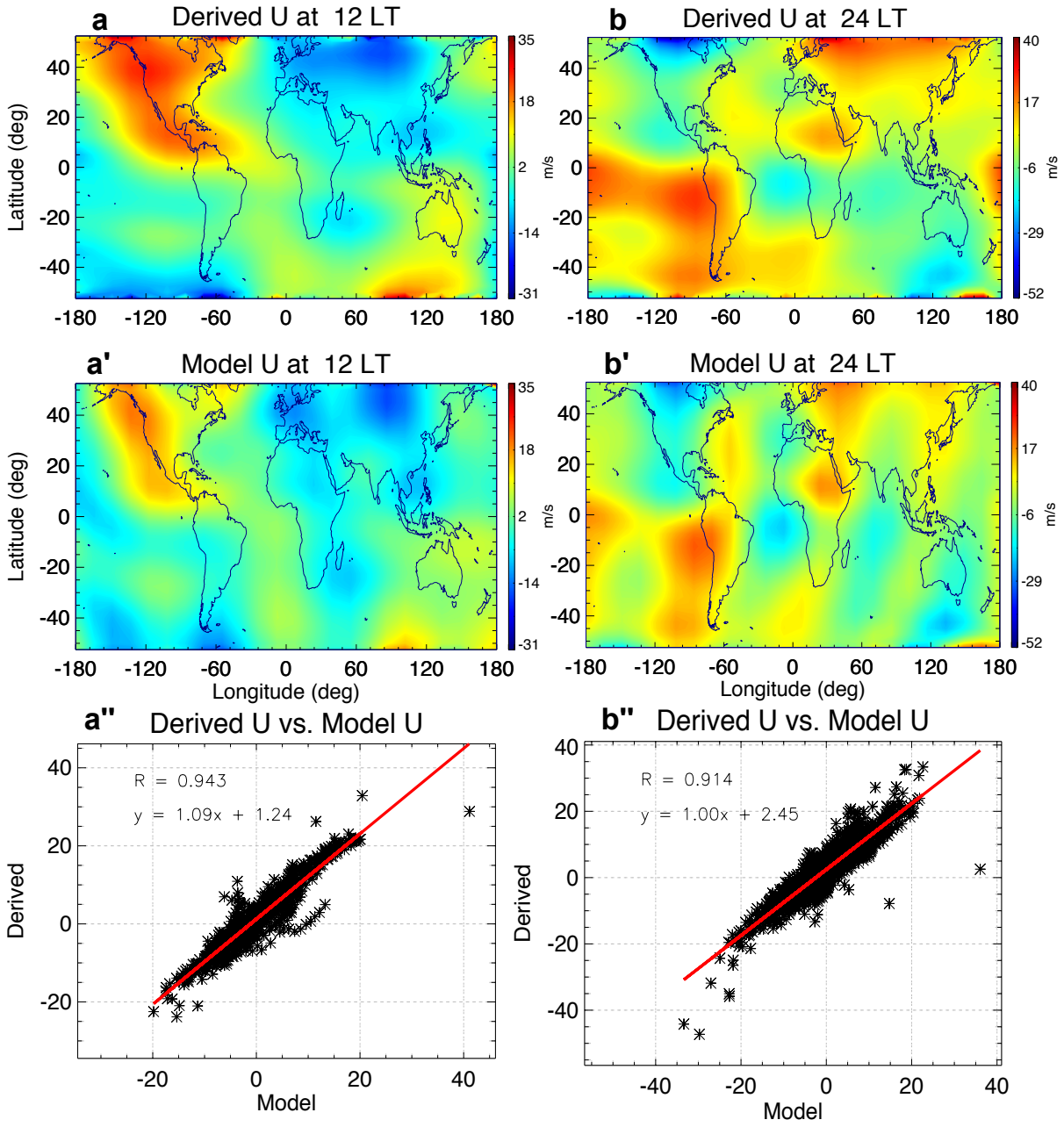

Figure B.11: Zonal wind latitude vs. longitude structures derived from neutral and electron densities (panels a and b) and from the model ′ and b′), and their scatter plot (panels a′′ and b′′) for 12 LT (a, a′, a′′) and 24 LT (b, b′, b′′). These plots are for September as solar minimum with tides at the lower boundary. Note: the zonal mean was removed to facilitate the comparison.

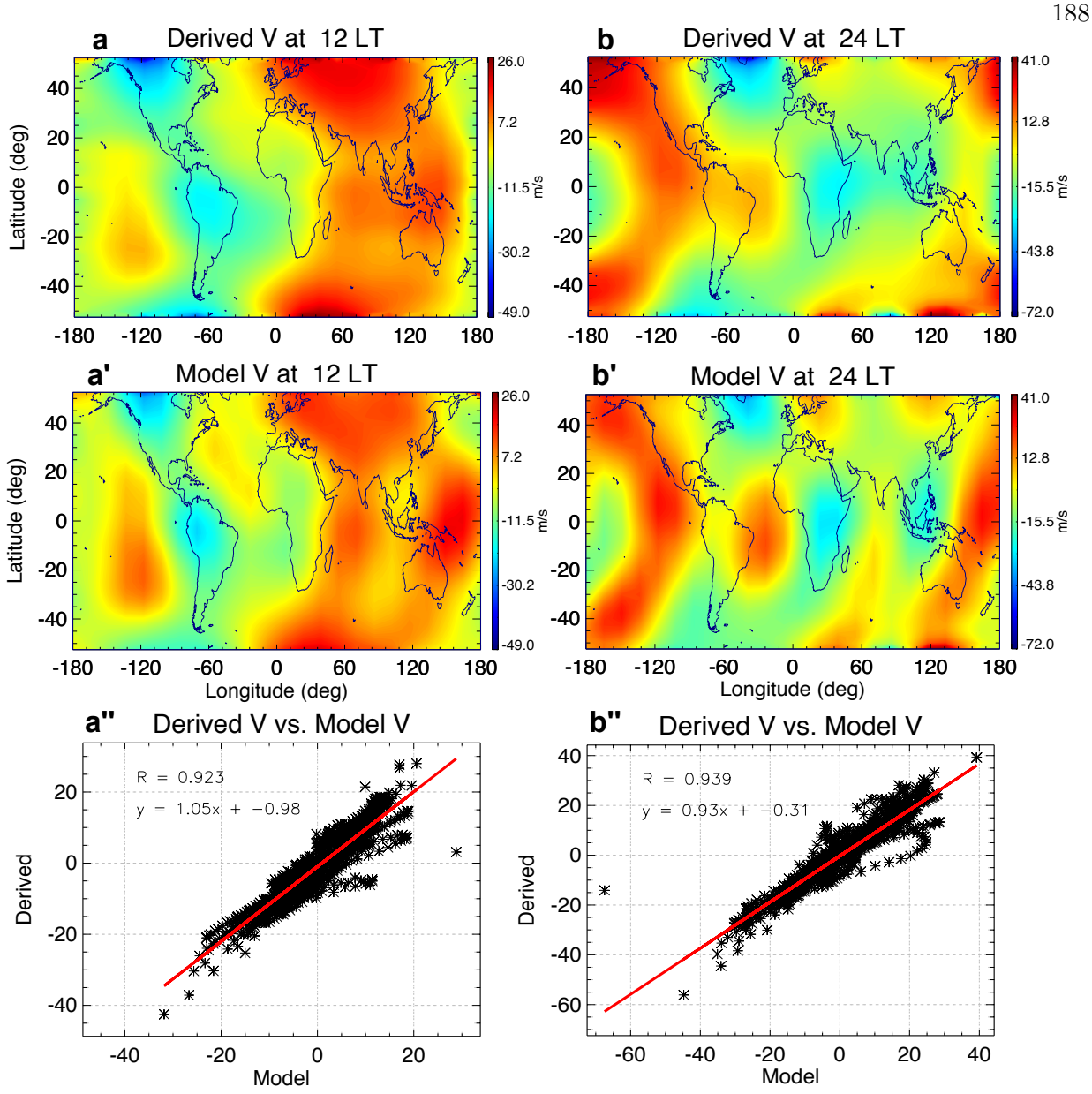

Figure B.12: Similar to Figure B.11, but for the meridional wind component.

Figure B.13 shows zonally-averaged latitude vs. local time wind comparisons for December. For this case we report correlation coefficients of ∼0.98 and ∼0.93 for the zonal and meridional wind component, respectively. The results in Figure B.13 confirm our ability to successfully reproduce most of the latitude-local time variability in the winds, with errors in the 5-15% range.

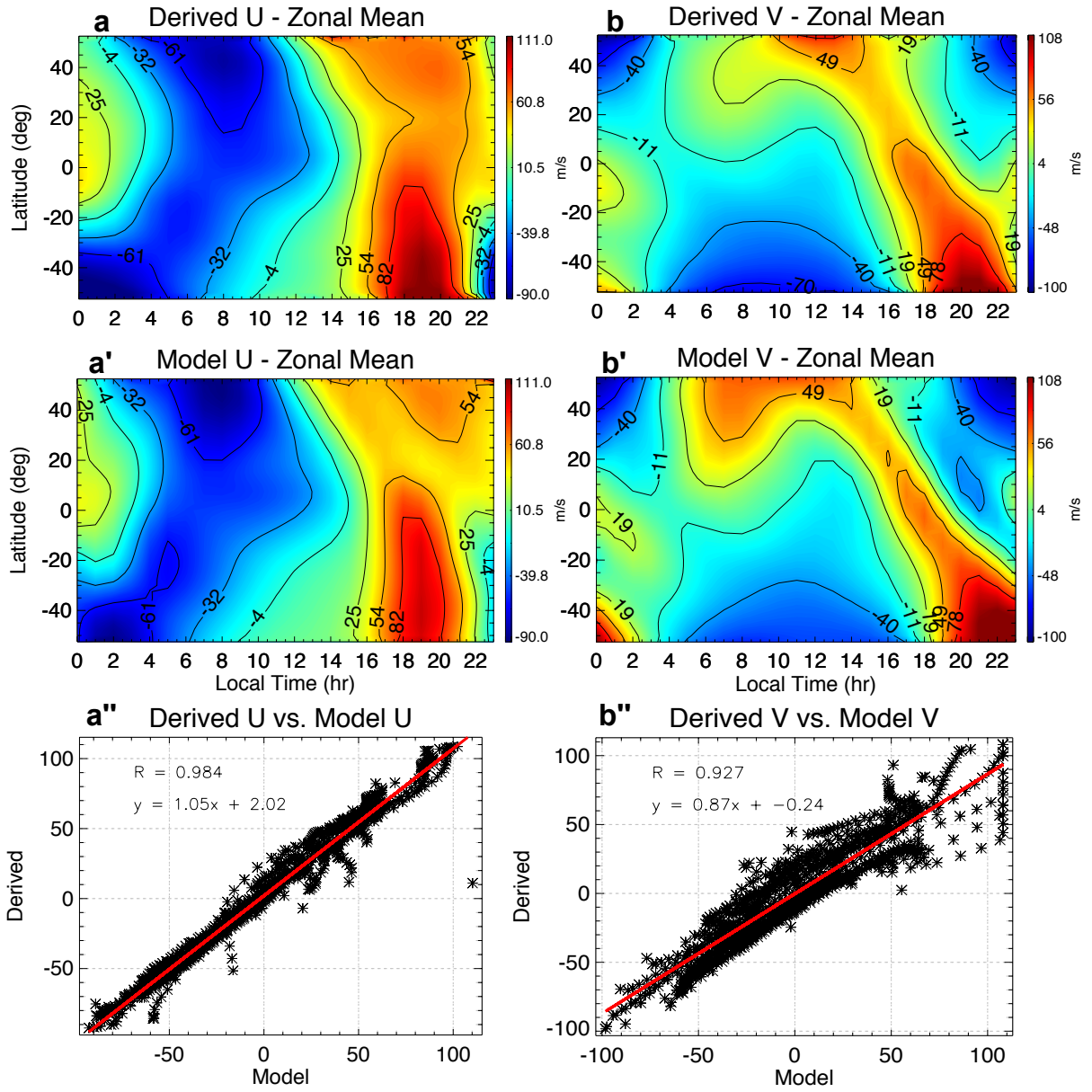

Figure B.13: Comparisons in latitude vs. local time for the December run for the zonal wind component of derived (panel a) and model (panel a′), and meridional derived (panel b) and model (panel b′) wind components. The scatter plot is shown in panels a′′ and b′′, for the zonal and meridional wind components, respectively. Note a correlation coefficients of ∼0.98 (∼0.93) for the zonal (meridional) wind.

Figures B.14 and B.15 show the latitude vs. longitude wind comparisons for December at 12 LT and 24 LT using the model ion drift velocities (in addition to the electron densities) to

calculate ion drag values. The difference between these wind values and the ones calculated in Figures B.7 and B.8 (panels c-c″) and Figures B.9 and B.10 (panels c-c″) show the importance of ion drifts in generating latitude-longitude variability. From Figures B.14 and B.15 we report correlation coefficients of ∼0.96-0.97 for the zonal wind and ∼ 0.94-0.97 for the meridional wind. Comparing these values with the ∼0.94-0.96 (∼0.93-0.95) for the zonal (meridional) wind calculated neglecting ion drift velocities, we can assert that ion drifts are responsible for over 3% of the zonal and meridional wind variability.

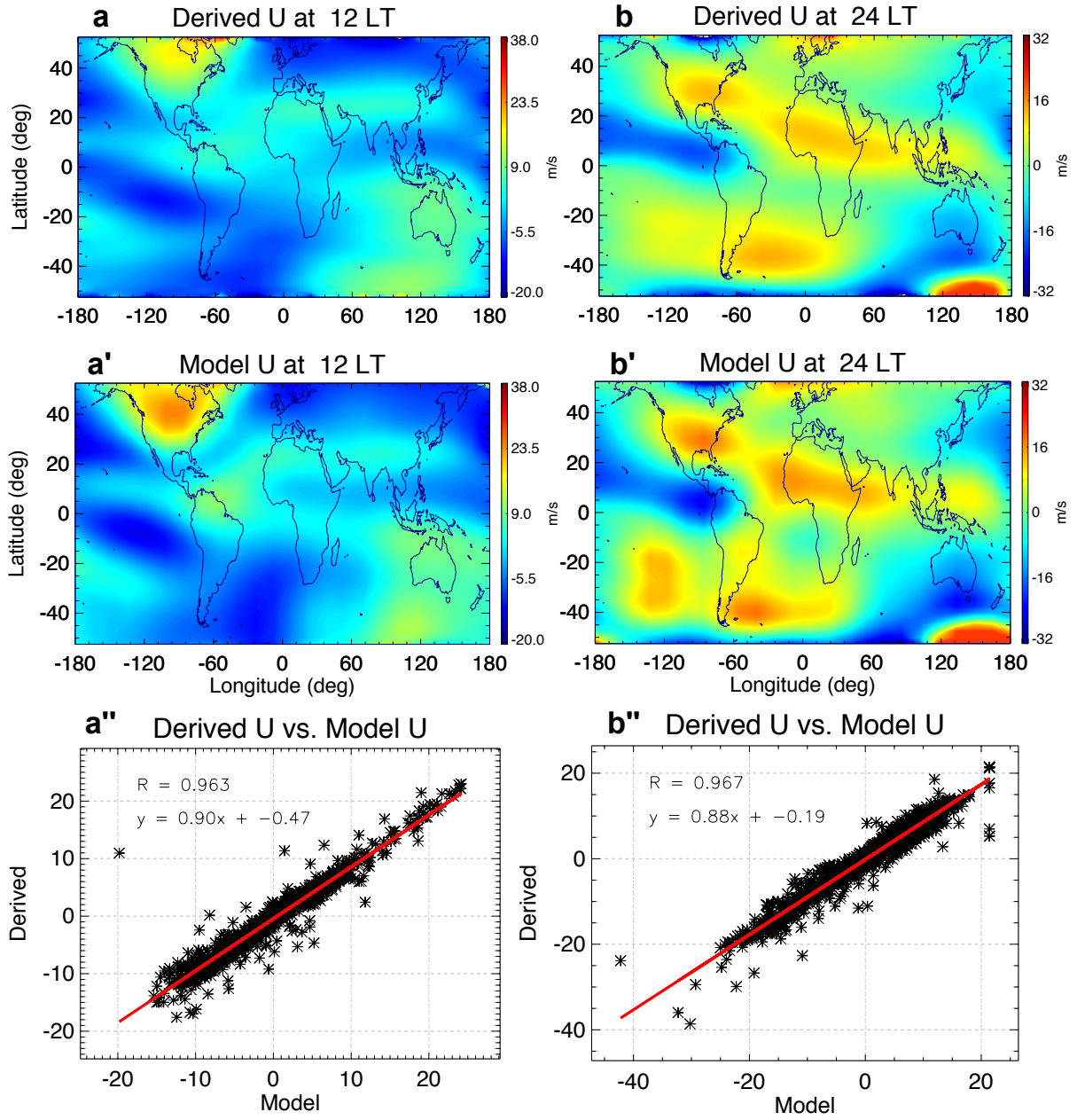

Figure B.14: Similar to Figure B.11, but including ion drift velocities in calculating ion drag coefficients and for December at solar minimum with tides at the lower boundary (and zonal mean removed).

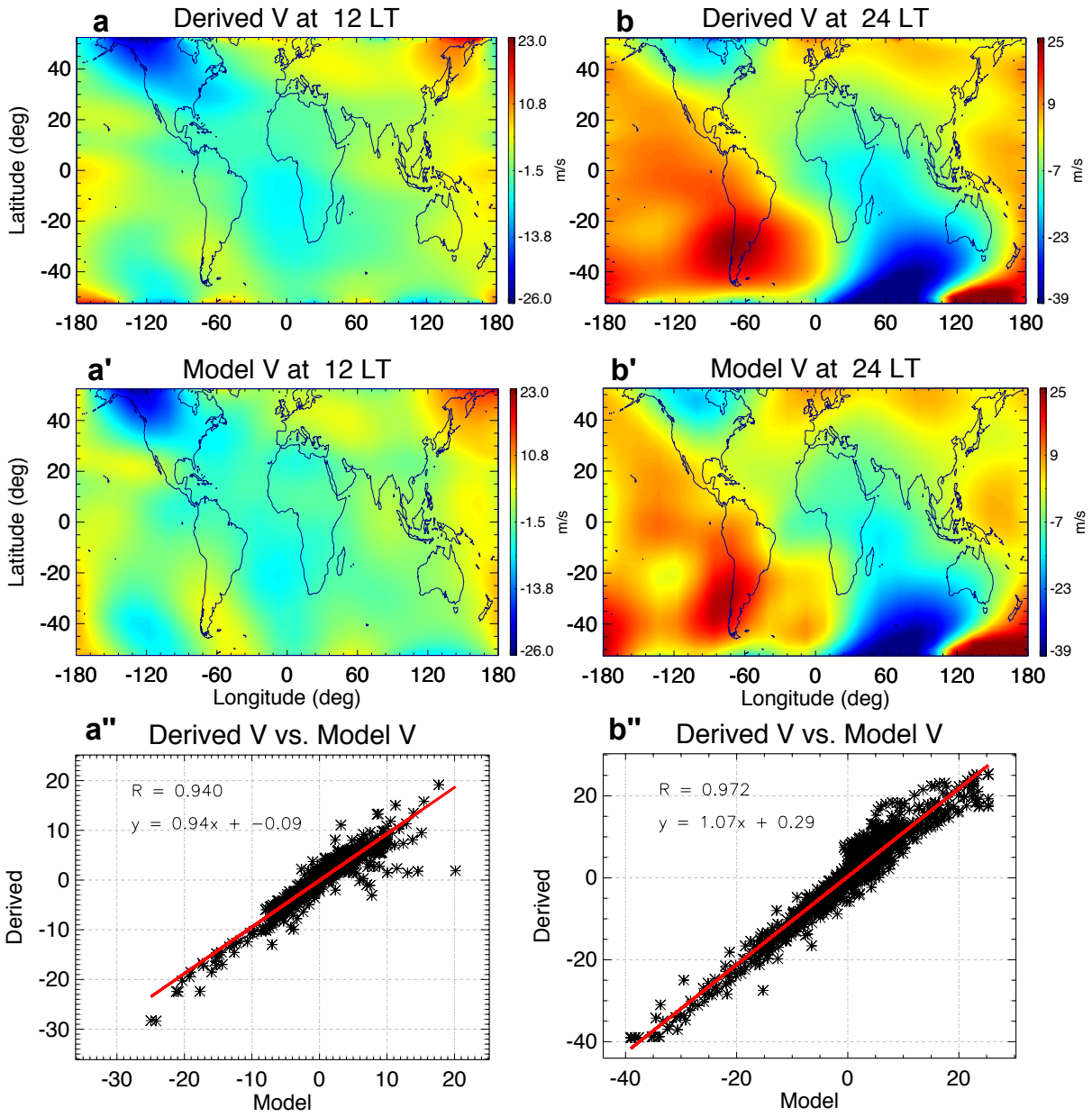

Figure B.15: Similar to Figure B.14, but for the meridional wind component.

In the following section we provide a summary of the errors associated with each step of the wind derivation and Table B.1 summarizes the results shown in Figures B.7-B.15 . We conclude with a discussion of the additional errors introduced by deriving winds from CHAMP measurements (i.e., fixed local time assumptions and errors in density retrieval).

B.3 Summary of Errors

In Section B.1 we discussed the errors due to the approximations made on the zonal momentum equation. These results are presented only for the zonal component, but similar conclusions can be made for the meridional component. Summarizing, we determined that pressure gradient, ion drag and the Coriolis force are by far the largest terms in the momentum equations, and that neglecting horizontal and vertical advection, vertical viscosity, and momentum force causes errors no greater than $\sim \pm 2\%$ in the derived winds.

Additional errors are introduced in the retrieval of ion drag from electron density and pressure gradient from neutral density. Comparing model ion drag values with the ones calculated using model electron densities we determined that ignoring ion drifts leads to $\sim \pm 14\%$ uncertainties in the derivation of ion drag. This value is reduced to $\sim \pm 2\%$ when including ion drifts, suggesting that ion drifts determine up to 12% of total ion drag force. The errors in the retrieval of pressure gradients from neutral densities and temperatures are estimated to be $\sim \pm 4\%$.

Comparing the model winds with the winds derived using model neutral and electron densities for December at solar medium and September at solar minimum (both including and ignoring ion drifts in the derivation) we estimated the overall errors in the wind estimates. The correlation coefficients between model and derived winds for the different cases are summarized in Table B.1.

		Corr. Coeff. for U	Corr. Coeff. for V
December	4 LT	*0.93*	*0.91*
	8 LT	*0.96*	*0.92*
	12 LT	*0.95*	*0.93*
	16 LT	*0.93*	*0.92*
	20 LT	*0.92*	*0.90*
	24 LT	*0.94*	*0.95*
September	12 LT	*0.94*	*0.92*
	24 LT	*0.91*	*0.94*
December with drifts	12 LT	*0.96*	*0.94*
	24 LT	*0.97*	*0.97*
December (local time)	Zonal Mean	*0.98*	*0.93*

Table B.1: Correlation coefficients between the derived and model winds for December at solar medium ignoring ion drifts, for September at solar minimum ignoring ion drifts, for December with ion drift velocities, and for December in latitude vs. local time frame as zonal mean and ignoring ion drifts.

From Table B.1 we conclude that starting from neutral and electron density values we can reproduce the model winds with errors generally less than ±10%, mainly caused by neglecting VA, HA, VV, MF (±2%), ion drift velocities (±5%), and pressure gradient values (±4%).

As previously mentioned, in addition to the errors in derivation of winds from neutral and electron densities, there are other errors due to (a) uncertainties in the retrieval of densities from CHAMP measurements and (b) introduced by assuming the local time to be exactly constant within the 10-day period used for solving the momentum equations. For (a), the errors in the retrieval of electron densities from Planar Langmuir Probe measurements are estimated to be up to ±4%, while the errors in neutral density and cross-wind derived from accelerometer measurements are estimated to be up to ±10%. For (b), assuming the 10-day period used in the derivation of the

latitude-longitude wind structures to be at a fixed local time (while in reality CHAMP precesses ∼5 min each day) causes the mixing of data with up to 1 hour of local time difference. For this case, local time changes can be perceived as longitudinal variability and lead to errors up to $\sim \pm 4\%$ (1 hour over 24 hour in the $\frac{\partial u}{\partial t} = \Omega \frac{\partial u}{\partial \phi}$ term).

Summarizing our findings, the estimated errors in the derivation of winds from electron and neutral densities are ±5-10%, errors in the 'raw' neutral and electron densities are up to ±10% and ±4%, respectively, while errors due to the local time precession are up to ±4%. In conclusion, the overall expected errors in the derived wind product is estimated to be up to approx. ±28%. [Note that we expect the combined error in the electron and neural density measurements to be lower than 14%, because of some biases in the density measurements removed by applying derivatives. This would lead us to estimate the errors in the derived wind product to be closer to ±20% than ±30%.]